

---

---

DISSERTATION

INDEPENDENT MEASUREMENT OF THE T2K NEAR DETECTOR CONSTRAINT  
USING THE OFF-AXIS PI-ZERO DETECTOR

Submitted by

Matthew Gregory Hogan

Department of Physics

In partial fulfillment of the requirements

For the Degree of Doctor of Philosophy

Colorado State University

Fort Collins, Colorado

Fall 2019

Doctoral Committee:

Advisor: Walter Toki

Robert Wilson

Norman Buchanan

Wen Zhou

---

---

Copyright by Matthew Gregory Hogan 2019

---

All Rights Reserved

---

---

ABSTRACT

---

INDEPENDENT MEASUREMENT OF THE T2K NEAR DETECTOR CONSTRAINT  
USING THE OFF-AXIS PI-ZERO DETECTOR

The Tokai to Kamioka (T2K) experiment is a long-baseline neutrino oscillation experiment hosted in Japan in search for electron neutrino appearance in a high purity muon neutrino beam. In order to constrain the systematic uncertainties in the oscillation analysis, a dedicated near detector (ND) complex called ND280 is located 280 meters from the neutrino production source in line of the beam. To date, the Fine Grain Detector (FGD) in ND280 has provided the ND constraint using a binned maximum likelihood estimate fit. This thesis describes the effort to validate the ND constraint using the same framework, but with an independent data set from the ND280 Pi-Zero Detector (PØD). Expanding on previously developed PØD selections, new selections have been developed to select neutrino and antineutrino events in one and multiple track topologies on water and carbon. These selections are shown to have similar sensitivity to the T2K flux and cross section systematic uncertainties. Using the same parameterization as the official ND constraint result, a hypothesis test was conducted between the PØD-only and FGD-only data fit results. A p-value of 0.2865 was obtained indicating the two data sets are likely describing the same population of neutrinos and their interactions in T2K.

---

---

## ACKNOWLEDGEMENTS

I would like to first thank Elliott Forney for making a publicly accessible L<sup>A</sup>T<sub>E</sub>X template. I also thank the T2K BANFF group and the T2K collaboration for supporting this analysis.

I give thanks to my loving wife Hannah who has supported me through my graduate career. I want to acknowledge the support from family, friends, and my dogs. I could not have made it this far without them.

I graciously acknowledge the support of the United States Department of Energy for providing the grant money to support my research. Additionally, I thank my advisors for supporting me with grant proposals and guiding me on my journey through graduate school.

---

# Contents

ABSTRACT . . . . .	ii
ACKNOWLEDGEMENTS . . . . .	iii
Contents . . . . .	iv
List of Tables . . . . .	vii
List of Figures . . . . .	viii
Chapter 1 Introduction . . . . .	1
1.1 Introduction to Neutrinos . . . . .	1
1.1.1 Neutrinos in the Standard Model . . . . .	3
1.1.2 Neutrino Oscillations . . . . .	13
1.1.3 CP Violation: Origins of Matter . . . . .	24
1.1.4 Long-Baseline Neutrino Oscillation Experiments . . . . .	25
1.2 Tokai to Kamioka Experiment . . . . .	26
1.2.1 Neutrino Production at J-PARC . . . . .	28
1.2.2 Neutrino Near Detectors: ND280 . . . . .	34
1.2.3 Neutrino Far Detector: Super-Kamiokande . . . . .	46
1.2.4 ND Constraint . . . . .	48
1.2.5 Contributions to the T2K Experiment . . . . .	51
1.3 Summary . . . . .	52

Chapter 2	BANFF Likelihood . . . . .	53
2.0.1	Introduction to Conditional PDFs and Likelihoods . . . . .	54
2.1	BANFF Fit Test Statistic . . . . .	55
Chapter 3	The PØD Selections and Samples . . . . .	60
3.1	Global Reconstruction . . . . .	61
3.2	PØD Selection Cuts . . . . .	62
3.2.1	Precuts . . . . .	62
3.2.2	The $\nu_\mu$ CC Inclusive in FHC Cut . . . . .	65
3.2.3	The $\bar{\nu}_\mu$ CC Inclusive in RHC Cuts . . . . .	65
3.2.4	The $\nu_\mu$ Background CC Inclusive in RHC Cuts . . . . .	66
3.3	Selection Kinematics . . . . .	67
3.3.1	$\nu_\mu$ in FHC CC 1-Track . . . . .	72
3.3.2	$\nu_\mu$ in FHC CC N-Tracks . . . . .	77
3.3.3	$\bar{\nu}_\mu$ in RHC CC 1-Track . . . . .	81
3.3.4	$\bar{\nu}_\mu$ in RHC CC N-Tracks . . . . .	83
3.3.5	$\nu_\mu$ Background in RHC CC 1-Track . . . . .	85
3.3.6	$\nu_\mu$ Background in RHC CC N-Tracks . . . . .	87
3.4	Summary of Selections . . . . .	89
Chapter 4	The PØD-Only in BANFF Parameterization . . . . .	93
4.1	Fit Binning . . . . .	94
4.1.1	Fit Binning Determination . . . . .	95
4.2	Penalty Terms and Systematic Uncertainties . . . . .	96
4.2.1	Flux Model . . . . .	97
4.2.2	Detector Inefficiencies Model . . . . .	104
4.2.3	Cross Section Model . . . . .	120
4.3	BANFF Fit Parameterization Summary . . . . .	128

Chapter 5	Fitter Validation . . . . .	130
5.1	Asimov Data Fit . . . . .	130
5.1.1	Event Rate . . . . .	132
5.1.2	One Sigma Variation of Cross Section Parameters . . . . .	134
5.1.3	Log-Likelihood Scans . . . . .	134
5.1.4	Fit Results . . . . .	134
5.2	Fake Data . . . . .	141
5.2.1	High Energy $\nu_\mu$ in FHC Flux Variation . . . . .	141
5.2.2	Single Pion Event Rate Variation . . . . .	143
5.3	Validation Summary . . . . .	146
Chapter 6	Fitter Results . . . . .	148
6.1	Prefit Sample Distributions . . . . .	148
6.2	Postfit Results . . . . .	149
6.2.1	Postfit Sample Distributions . . . . .	162
6.2.2	Parameter Value and Correlation Comparisons . . . . .	163
6.2.3	P-Value Between PØD and FGD Fits . . . . .	179
6.3	Summary . . . . .	189
Chapter 7	Discussion . . . . .	190
7.1	Potential Impacts on the T2K Oscillation Analysis . . . . .	191
7.2	Analysis Improvements . . . . .	191
7.2.1	Regularization Strength . . . . .	191
7.2.2	Alternative Penalty . . . . .	193
7.3	Future Prospects . . . . .	196
Bibliography	. . . . .	200

---

# List of Tables

1.1	Sensitivity of Different Oscillation Experiments . . . . .	20
1.2	Table of Best Fit MNSP Parameters Split by Normal and Inverted hierarchy . . . . .	23
1.3	PØD Water Target Mass Composition . . . . .	44
3.1	The PØD WT FV and Corridor Definition . . . . .	64
3.2	POT Used in This Analysis . . . . .	67
3.3	The Expanded $\nu$ NEUT Reactions Table . . . . .	69
3.4	The Expanded $\bar{\nu}$ NEUT Reactions Table . . . . .	70
4.1	Flux Binning and Uncertainties Used in the BANFF Fit . . . . .	100
4.1	Flux Binning and Uncertainties Used in the BANFF Fit . . . . .	101
4.1	Flux Binning and Uncertainties Used in the BANFF Fit . . . . .	102
4.1	Flux Binning and Uncertainties Used in the BANFF Fit . . . . .	103
4.2	List of Detector Systematic Effects and Treatment . . . . .	105
4.3	Cross Section Model Fit Parameters in the BANFF Fit . . . . .	127
4.3	Cross Section Model Fit Parameters in the BANFF Fit . . . . .	128
5.1	Event Rate Table for Asimov Set . . . . .	133
6.1	Neutrino-Nucleon Exposure on Target Elements . . . . .	177
7.1	Neutrino-Nucleon Exposure on Target Elements in a Run 2 - 8 PØD+FGD Joint Fit . . . . .	198

---

---

# List of Figures

1.1	The Elementary Particles of the Standard Model of Particle Physics . . . . .	3
1.2	CC and NC Feynman Diagrams . . . . .	6
1.3	Helicity of the Neutrino . . . . .	7
1.4	A Schematic of $\theta$ in $\nu_e + e^-$ Scattering . . . . .	11
1.5	A $\nu_\mu$ -Induced CCQE Interaction . . . . .	13
1.6	Depiction of Two Neutrino Flavor Change of Basis . . . . .	15
1.7	Survival and Disappearance Probability . . . . .	17
1.8	Semi-logarithmic Plot of the Two Flavor Survival Probability . . . . .	19
1.9	Neutrino Mass Hierarchy Problem and MNSP Representation . . . . .	22
1.10	The Matter and Energy Content of the Universe . . . . .	25
1.11	Birds Eye View of the T2K experiment on the Japanese Archipelago . . . . .	27
1.12	The T2K Experiment Unoscillated $\nu_\mu$ Flux at SK . . . . .	27
1.13	Bird's eye view of the J-PARC center . . . . .	28
1.14	Schematics of the J-PARC Accelerators . . . . .	30
1.15	The Neutrino Beamline at J-PARC . . . . .	31
1.16	Photographs of the Target Station . . . . .	32
1.17	T2K Accumulated Protons on Target . . . . .	33
1.18	Schematic of INGRID . . . . .	36
1.19	Photographs of the T2K MPPC . . . . .	37
1.20	INGRID Beam Profile . . . . .	38

1.21	INGRID Event Rate . . . . .	39
1.22	Schematic of the Off-Axis Near Detector ND280 . . . . .	40
1.23	ND280 Magnetic Field Deviations from a Data Fit . . . . .	41
1.24	Schematic of the PØD . . . . .	43
1.25	A cross section of a PØD scintillating bar . . . . .	44
1.26	Cut-Away Drawing of a TPC Volume in ND280 . . . . .	46
1.27	Diagram of the Super-Kamiokande Detector . . . . .	47
1.28	Representative T2K Events in Super-Kamiokande . . . . .	48
1.29	Predicted and Best Fit Measurements for the SK Flux . . . . .	49
1.30	Predicted CCInc Cross Section at T2K Energies . . . . .	50
3.1	Data and MC distributions of the $\nu_\mu$ and $\bar{\nu}_\mu$ water-in CC signal selections . . . . .	61
3.2	The NEUT Interaction CCQE and non-CCQE Legend . . . . .	69
3.3	True Particle Selected Legend . . . . .	70
3.4	NEUT $\nu$ Interaction Legend . . . . .	71
3.5	NEUT $\bar{\nu}$ Interaction Legend . . . . .	71
3.6	Reconstructed Kinematics for the $\nu_\mu$ in FHC CC 1-Track Selection for CCQE and non-CCQE Interactions . . . . .	73
3.7	Reconstructed Kinematics for the $\nu_\mu$ in FHC CC 1-Track Selection for the True Selected Particle . . . . .	74
3.8	Vertex Z Position of the $\nu_\mu$ in FHC CC 1-Track Selection . . . . .	75
3.9	Efficiency and Purity of $\nu_\mu$ CCQE Interactions in the $\nu_\mu$ in FHC CC 1-Track Selection . . . . .	75
3.10	The $\nu_\mu$ in FHC CC 1-Track True Kinematics . . . . .	76
3.11	Lepton Candidate Reconstructed Kinematics for the $\nu_\mu$ in FHC CC N-Tracks Selection for CCQE and non-CCQE Interactions . . . . .	77
3.12	Lepton Candidate Reconstructed Kinematics for the $\nu_\mu$ in FHC CC N-Tracks Selection for the True Selected Particle . . . . .	78

3.13	Vertex position of the $\nu_\mu$ in FHC CC N-Tracks Selection . . . . .	78
3.14	Efficiency and Purity of $\nu_\mu$ CCQE Interactions in the $\nu_\mu$ in FHC CC N-Tracks Selection . . . . .	79
3.15	The $\nu_\mu$ in FHC CC N-Tracks True Kinematics . . . . .	80
3.16	Reconstructed Kinematics for the $\bar{\nu}_\mu$ in RHC CC 1-Track Selection for CCQE and non-CCQE Interactions . . . . .	81
3.17	Reconstructed Kinematics for the $\bar{\nu}_\mu$ in RHC CC 1-Track Selection for the True Selected Particle . . . . .	82
3.18	Efficiency and Purity of $\bar{\nu}_\mu$ CCQE Interactions in the $\bar{\nu}_\mu$ in RHC CC 1-Track Selection . . . . .	82
3.19	The $\bar{\nu}_\mu$ in RHC CC 1-Track True Kinematics . . . . .	83
3.20	Lepton Candidate Reconstructed Kinematics for the $\bar{\nu}_\mu$ in RHC CC N-Tracks Selection for CCQE and non-CCQE Interactions . . . . .	84
3.21	Lepton Candidate Reconstructed Kinematics for the $\bar{\nu}_\mu$ in RHC CC N-Tracks Selections for the True Selected Particle . . . . .	84
3.22	Efficiency and Purity of $\bar{\nu}_\mu$ CC non-QE Interactions in the $\bar{\nu}_\mu$ in RHC CC N-Tracks Selection . . . . .	85
3.23	The $\bar{\nu}_\mu$ in RHC CC N-Tracks True Kinematics . . . . .	86
3.24	Reconstructed Kinematics for the $\nu_\mu$ in RHC CC 1-Track Selection for CCQE and non-CCQE Interactions . . . . .	87
3.25	Reconstructed Kinematics for the $\nu_\mu$ in RHC CC 1-Track Selection for the True Selected Particle . . . . .	88
3.26	Efficiency and Purity of $\nu_\mu$ CCQE Interactions in the $\nu_\mu$ in RHC CC 1-Track Selection . . . . .	88
3.27	The $\nu_\mu$ in RHC CC 1-Track True Kinematics . . . . .	89
3.28	Reconstructed Kinematics for the $\nu_\mu$ in RHC CC N-Tracks Selection for CCQE and non-CCQE Interactions . . . . .	90

3.29	Reconstructed Kinematics for the $\nu_\mu$ in RHC CC N-Tracks Selection for the True Selected Particle . . . . .	90
3.30	Efficiency and Purity of $\nu_\mu$ CC non-QE Interactions in the $\nu_\mu$ in RHC CC N-Tracks Selection . . . . .	91
3.31	The $\nu_\mu$ in RHC CC N-Tracks True Kinematics . . . . .	92
4.1	The PØD Momenta Resolutions Used for Fit Binning . . . . .	96
4.2	The PØD Angular Residuals Used for Fit Binning . . . . .	97
4.3	BANFF Pre-fit Flux Covariance Matrix . . . . .	98
4.4	The T2K Unoscillated Neutrino Flux Prediction at SK . . . . .	99
4.5	Bin Normalization Edges for the $\nu_\mu$ in FHC Selections . . . . .	110
4.6	Bin Normalization Edges for the $\bar{\nu}_\mu$ in RHC Selections . . . . .	111
4.7	Bin Normalization Edges for the $\nu_\mu$ in RHC Selections . . . . .	113
4.8	Event Variations in Observable Normalization Bins . . . . .	115
4.9	Vertex Distribution Showing Evidence of PØD Bulging . . . . .	117
4.10	Detector Covariance Matrix . . . . .	119
4.11	Cross Section Parameters Prefit Covariance Matrix . . . . .	126
5.1	Complete Prefit Correlation Matrix for the BANFF Fit. . . . .	131
5.2	Test Statistic Scans for Variations of Fit Parameters in the Asimov Set . . . . .	135
5.3	Asimov Fit Results for the Flux at ND280 . . . . .	136
5.4	Asimov Fit Results for the Flux at Super-K . . . . .	137
5.5	Asimov Fit Results for the Bin Normalization Parameters . . . . .	138
5.6	Asimov Fit Results for the Cross Section and FSI Parameters . . . . .	139
5.7	Complete Postfit Correlation Matrix for the Asimov Data Fit . . . . .	140
5.8	Flux and Cross Section Postfit Correlation Matrix for the Asimov Data Fit . . . . .	140
5.9	Neutrino Flux in the High Energy Neutrino Flux Variation Fake Data Set . . . . .	142
5.10	Postfit Parameters for the High Energy $\nu_\mu$ in FHC Flux Fake Data fit . . . . .	144

5.11	Lepton Candidate Momentum in the Single Pion Event Rate Variation Fake Data Set	145
5.12	Postfit Parameters for the $C_A^5$ Fake Data Fit	147
6.1	Data and Prefit Legend	149
6.2	Prefit for the Water-In $\nu_\mu$ in FHC CC 1-Track Sample	150
6.3	Prefit for the Water-In $\nu_\mu$ in FHC CC N-Tracks Sample	151
6.4	Prefit for the Water-In $\bar{\nu}_\mu$ in RHC CC 1-Track Sample	152
6.5	Prefit for the Water-In $\bar{\nu}_\mu$ in RHC CC N-Tracks Sample	153
6.6	Prefit for the Water-In $\nu_\mu$ in RHC CC 1-Track Sample	154
6.7	Prefit for the Water-In $\nu_\mu$ in RHC CC N-Tracks Sample	155
6.8	Prefit for the Water-Out $\nu_\mu$ in FHC CC 1-Track Sample	156
6.9	Prefit for the Water-Out $\nu_\mu$ in FHC CC N-Tracks Sample	157
6.10	Prefit for the Water-Out $\bar{\nu}_\mu$ in RHC CC 1-Track Sample	158
6.11	Prefit for the Water-Out $\bar{\nu}_\mu$ in RHC CC N-Tracks Sample	159
6.12	Prefit for the Water-Out $\nu_\mu$ in RHC CC 1-Track Sample	160
6.13	Prefit for the Water-Out $\nu_\mu$ in RHC CC N-Tracks Sample	161
6.14	Postfit for the Water-In $\nu_\mu$ in FHC CC 1-Track Sample	164
6.15	Postfit for the Water-In $\nu_\mu$ in FHC CC N-Tracks Sample	165
6.16	Postfit for the Water-In $\bar{\nu}_\mu$ in RHC CC 1-Track Sample	166
6.17	Postfit for the Water-In $\bar{\nu}_\mu$ in RHC CC 1-Track Sample	167
6.18	Postfit for the Water-In $\nu_\mu$ in RHC CC 1-Track Sample	168
6.19	Postfit for the Water-In $\nu_\mu$ in RHC CC N-Tracks Sample	169
6.20	Postfit for the Water-Out $\nu_\mu$ in FHC CC 1-Track Sample	170
6.21	Postfit for the Water-Out $\nu_\mu$ in FHC CC N-Tracks Sample	171
6.22	Postfit for the Water-Out $\bar{\nu}_\mu$ in RHC CC 1-Track Sample	172
6.23	Postfit for the Water-Out $\bar{\nu}_\mu$ in RHC CC N-Tracks Sample	173
6.24	Postfit for the Water-Out $\nu_\mu$ in RHC CC 1-Track Sample	174

---

6.25 Postfit for the Water-Out $\nu_\mu$ in RHC CC N-Tracks Sample . . . . .	175
6.26 Legend Used to Compare PØD-only and FGD-only Fit Results . . . . .	176
6.27 Postfit ND280 Flux Parameters for the PØD-only BANFF Fit . . . . .	180
6.28 Postfit Super-K Flux Parameters for the PØD-only BANFF Fit . . . . .	181
6.29 Postfit Cross Section Parameters for the PØD-only BANFF Fit . . . . .	182
6.30 Prefit and Postfit Bin Normalization Parameters . . . . .	183
6.31 The 2p2h Shape Mirrored Spline . . . . .	184
6.32 Postfit Correlation Matrix . . . . .	185
6.33 Prefit and Post Flux and Cross Section Parameter Correlations . . . . .	186
6.34 Prefit and Post Flux and Cross Section Parameter Correlations . . . . .	187
6.35 P-Value for the PØD vs FGD ND Constraint . . . . .	189
7.1 The Lasso vs Elastic Net Constraint . . . . .	196



---

# Chapter 1

## Introduction

*Chose trop vue n'est chère tenue*

A thing too much seen is little prized – French proverb

### 1.1 Introduction to Neutrinos

The history of the neutrino can be traced back to the electron energy spectrum observed in neutron  $\beta$ -decay. While measurements of the  $\alpha$ - and  $\gamma$ -decay of atomic nuclei showed discrete spectral lines, the electron ( $\beta$  particle) exhibited a continuous energy spectrum. Experimentally, there were two observed particles in each decay process and classical physics dictated that the outgoing daughter particles should have discrete energies. The fact that the  $\beta$ -decay spectrum was very different posed a fundamental problem for physicists in the mid-1910s, which was that energy was not conserved. Two solutions were postulated: either the “energy conservation law is only valid statistically in such a process [...] or an additional undetectable new particle [...] carrying away the additional energy and spin [...] is emitted” [77]. The latter solution was proposed by Wolfgang Pauli in a letter dated 4 December 1930 to a group of physicists meeting in Tübingen, modern Germany, where he

---

first proposed the neutrino<sup>1</sup>. Pauli's solution also predicted that the undetected neutrino would have half-integer spin, a quantum mechanical property of matter, since the observed particles in  $\beta$ -decay did not conserve angular momentum. The existence of the neutrino and validation of Pauli's predictions would not be experimentally verified for another 20 years.

The neutrino was first observed in 1953 by Clyde Cowan and Frederick Reines using a nuclear reactor in South Carolina, United States of America. Since then three types or "flavors" of neutrinos and antineutrinos have been observed using accelerators and also from unique sources like the Sun and a supernova. Neutrino physics continues to be an active area of fundamental research since the neutrino is a truly unique probe to subatomic processes. For instance they are observed to originate from the depths of the Sun's core (over  $10^7$  degrees Kelvin) where fusion occurs.

Neutrinos rarely interact with normal matter, meaning that they travel essentially unimpeded towards one's particle detector. The rarity of such interactions can be illustrated by the fact that over a typical human lifetime, only one solar neutrino interaction with an individual is expected out of the  $7.0 \times 10^{10}$  neutrinos/cm<sup>2</sup>/sec incident on the Earth.<sup>2</sup>. So this begs the question: how does one detect a neutrino? The short answer is that one requires a large enough flux of neutrinos passing through a large dense volume of matter just to detect a single neutrino with today's technology.

Scientists continue to be interested in neutrinos due to the unusual properties they exhibit. One of the more recent and surprising aspects of neutrinos is their ability to undergo "flavor oscillations" where a neutrino of definite flavor (type) is created and later observed as a different flavor. The impact of differences between neutrino and antineutrino oscillations

---

<sup>1</sup>In W Pauli's December 1930 letter, he referred to his proposed particle as the "neutron", which is not the same neutron that we know of today. At that point in time, the neutral particles inside the atomic nucleus, also called "neutrons", had not been discovered, let alone understood. The neutron, which was discovered in 1932 by James Chadwick, has been formally associated as the neutral, cousin particle to the proton. It would be Enrico Fermi who would coin the particle in W Pauli's letter and solution to the  $\beta$ -decay spectrum as a "neutrino" meaning in Italian *little neutral one*.

<sup>2</sup>To give some perspective to this number, this means 70 billion neutrinos are traveling every second through an area similar to one's own thumb nail.

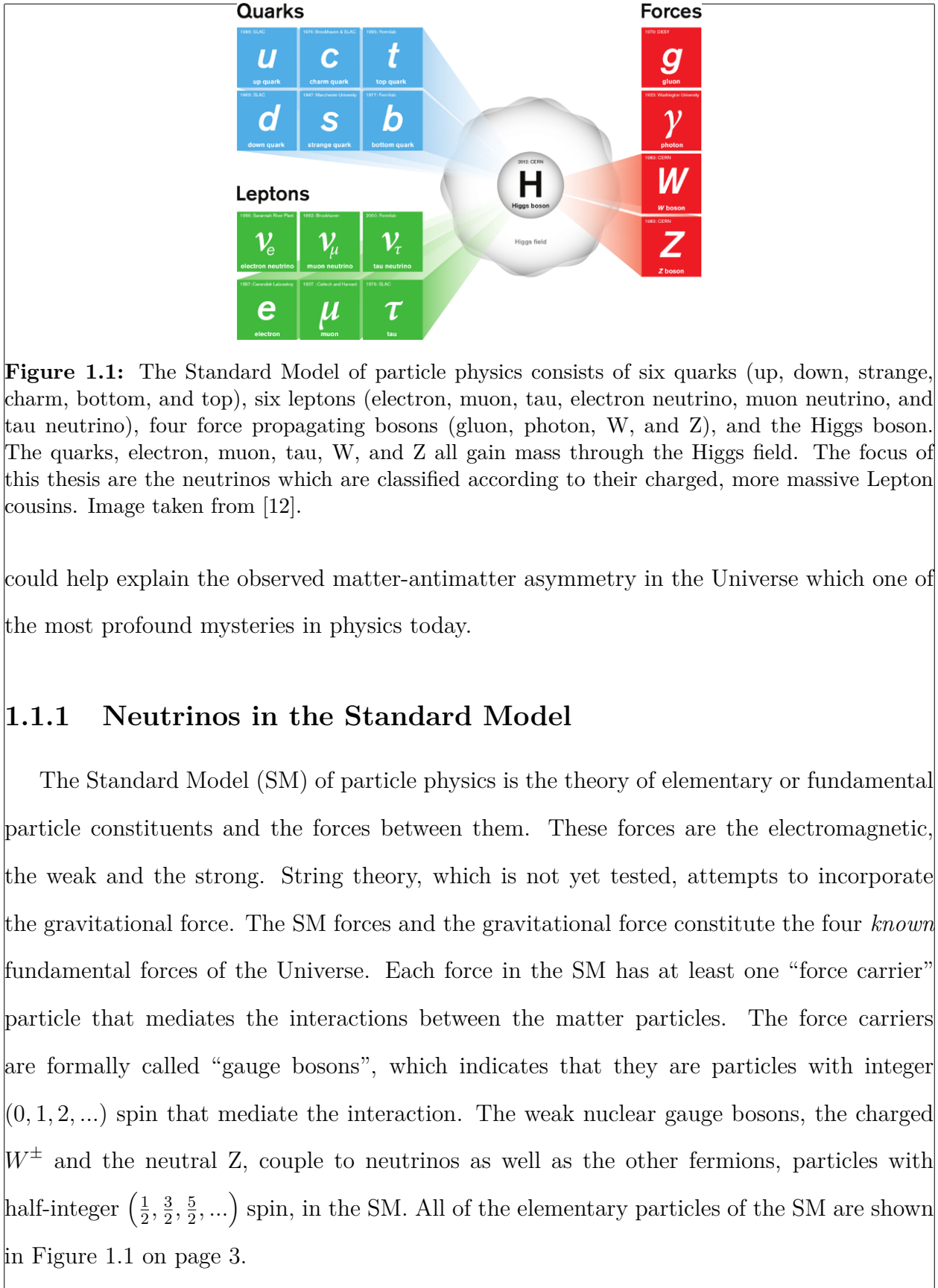


**Figure 1.1:** The Standard Model of particle physics consists of six quarks (up, down, strange, charm, bottom, and top), six leptons (electron, muon, tau, electron neutrino, muon neutrino, and tau neutrino), four force propagating bosons (gluon, photon, W, and Z), and the Higgs boson. The quarks, electron, muon, tau, W, and Z all gain mass through the Higgs field. The focus of this thesis are the neutrinos which are classified according to their charged, more massive Lepton cousins. Image taken from [12].

could help explain the observed matter-antimatter asymmetry in the Universe which one of the most profound mysteries in physics today.

### 1.1.1 Neutrinos in the Standard Model

The Standard Model (SM) of particle physics is the theory of elementary or fundamental particle constituents and the forces between them. These forces are the electromagnetic, the weak and the strong. String theory, which is not yet tested, attempts to incorporate the gravitational force. The SM forces and the gravitational force constitute the four *known* fundamental forces of the Universe. Each force in the SM has at least one “force carrier” particle that mediates the interactions between the matter particles. The force carriers are formally called “gauge bosons”, which indicates that they are particles with integer  $(0, 1, 2, \dots)$  spin that mediate the interaction. The weak nuclear gauge bosons, the charged  $W^\pm$  and the neutral Z, couple to neutrinos as well as the other fermions, particles with half-integer  $(\frac{1}{2}, \frac{3}{2}, \frac{5}{2}, \dots)$  spin, in the SM. All of the elementary particles of the SM are shown in Figure 1.1 on page 3.

---

Neutrinos in the SM are electrically neutral, massless particles categorized into three generations based on their charged, more massive lepton cousins. In the SM, the three neutrinos and the three antineutrinos are the only spin  $1/2$  particles that experience only weak interactions. The neutrino and its associated charged cousin of the same flavor pair into a “weak isospin doublet” in the SM. These doublets are locally gauge invariant under a  $SU(2) \times U(1)$  symmetry which leads to the postulated existence of the photon, the  $W^\pm$  and  $Z$  bosons. They are necessary to enable local gauge invariance<sup>3</sup>.

What follows is a brief introduction to weak interactions. This is followed by a exploration on the nature of neutrino handedness. Then this is proceeded by a discussion on neutrino scattering with matter.

## Weak Interactions

The name “weak force” comes from the fact that this force is much weaker than the electromagnetic and strong nuclear forces. This is due to the weak mediating bosons, the  $W^\pm$  and  $Z$ , being massive particles unlike the massless gluon ( $g$ ) and photon ( $\gamma$ ). The  $W^\pm/Z$  have masses of  $80/90 \text{ GeV}/c^2$ , which is more massive than all the other elementary particles except for the top quark.

For weak interactions to occur at energies far below the masses (also called “off-shell”) of the  $W^\pm$  and  $Z$ , the interaction time must be infinitesimally small as dictated by the Heisenberg Uncertainty Principle

$$\Delta E \Delta t \gtrsim \hbar \quad (1.1)$$

---

<sup>3</sup>A gauge theory describes ways to measure physical forces or fields through interactions between elementary particles. The electric or magnetic fields for example can only be probed by charged particles. In the realm of quantum field theories, fields are postulated to permeate everywhere and it is excitations of these fields that produce experimental observables. Fields are constructed using the Lagrangian formalism and altered using gauge transformations. If altering the Lagrangian in some way does not affect the observables, this is referred to as a gauge invariance. Local gauge invariance means that under the constraints of the experiment, certain gauge transformations do not affect the observables. The allowed locally gauge invariant transformations require knowledge of its underlying Lie, or symmetry, group. With the weak isospin doublets, the Lie groups are  $SU(2) \otimes U(1)$  where  $SU(2)$  is the special unitary group of  $2 \times 2$  unitary matrices, and  $U(1)$  is the unitary (circle) group consisting of complex numbers of magnitude 1.

where  $\Delta E$  is the energy of the particle and  $\Delta t$  is the time during which the particle exists. As an example, consider a neutrino emitting a Z-boson as shown in Figure 1.2 on page 6. If the energy of the neutrino is 1 GeV, the lifetime of the  $Z$  boson is about  $10^{-25}$  seconds according to ( 1.1). In general, the probability that a massive particle of mass  $M$  will be created from the collision of two particles is given by a relativistic Breit–Wigner distribution

$$f(M) \propto \frac{1}{(M^2 - M_0^2)^2 c^4 + M_0^2 \Gamma^2}, \quad (1.2)$$

where  $M_0$  is the rest mass and  $\Gamma$  is the decay width of the particle. For  $M \ll M_0$ , the probability of creating that particle will be infinitesimally small. Therefore to observe a single weak interaction requires a large number of weakly interacting particles.

Weak interactions are classified into two classes: charged current (CC) and neutral current (NC). The CC interactions involve a charged W boson and changes the incident neutrino into an electrically charged lepton of flavor  $l$  where the flavor of the neutrino  $\nu_l$  is inferred from the charged lepton. The same is not true for NC interactions, in which the exchange a neutral Z boson occurs. The NC interactions are flavor agnostic since they do not produce a charged lepton nor change the neutrino's flavor. An example of each interaction type is shown in Figure 1.2 on page 6.

### Chirality: How Neutrinos are Left Handed

Neutrinos are observed to have their spin direction vectors  $\sigma$  opposite to their momentum  $\mathbf{P}$  and this is reversed for antineutrinos. This property is called helicity and is given by ( 1.3)

$$\mathcal{H} = \frac{\sigma \cdot \mathbf{P}}{|\mathbf{P}|}. \quad (1.3)$$

Although neutrino detection is difficult, the neutrino helicity is readily inferred from the daughter muon's helicity in pion decay,  $\pi^+ \rightarrow \mu^+ + \nu_\mu$ . The  $\mu^+$  has negative helicity ( $\mathcal{H} = -1$ ) and to converse spin, the neutrino's helicity must also be negative as shown in Figure 1.3

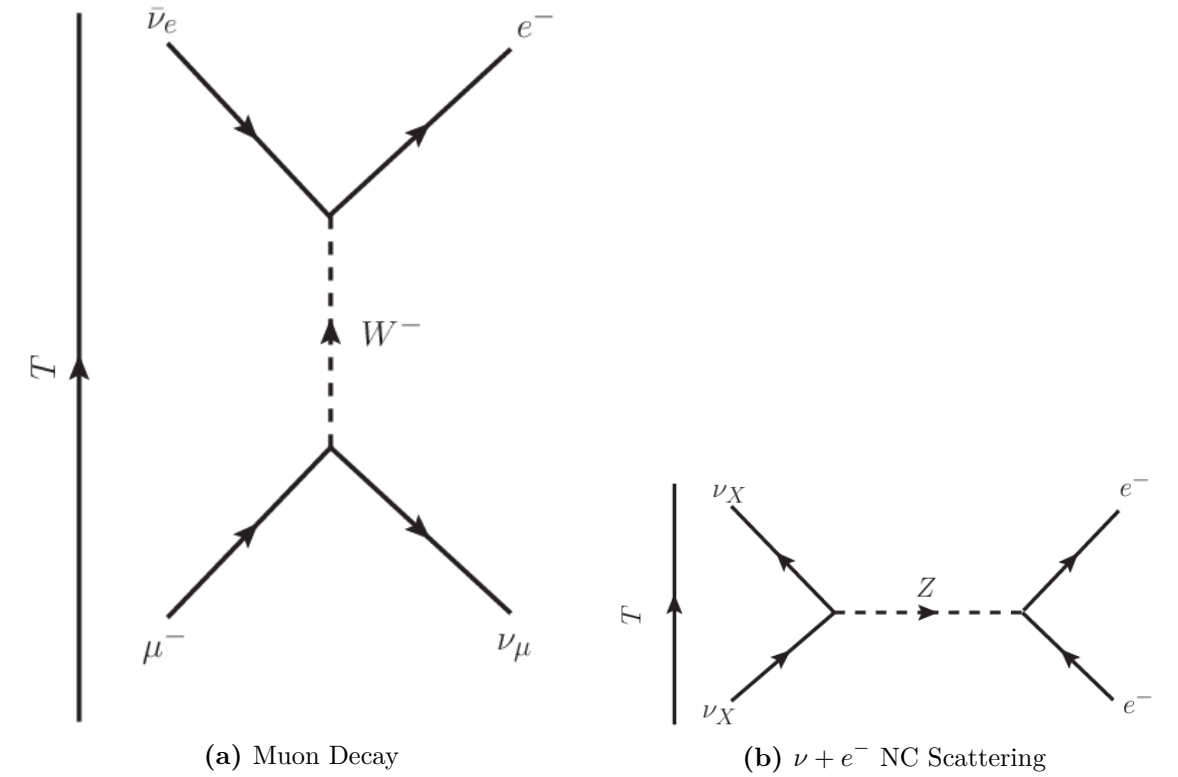


**Figure 1.2:** Feynman diagrams illustrating a CC and a NC interaction with time axis increasing from bottom to top in both. (a) Feynman diagram of a muon decay ( $\mu^- \rightarrow \nu_\mu \bar{\nu}_e e^-$ ). This is a charged current process that converts a charged muon into a muon neutrino via the emission of a  $W^-$  boson. Due to a conserved quantum number called lepton number, the  $W^-$  must emit an electron and electron neutrino pair. (b) Feynman diagram of NC scattering between a neutrino of arbitrary flavor  $X$  scatters off an electron via the emission of a  $Z$  boson.

on page 7. The antineutrino's helicity is positive (+1) as shown in Figure 1.3 on page 7 through use of the charge (C) conjugation and parity (P) transformations. A C conjugation is a linear transformation that transforms all particles into their corresponding antiparticles while the P transformation inverts all spatial coordinates. Thus neutrinos are referred to as *left-handed* (LH) particles while antineutrinos are referred to as *right-handed* (RH) particles. It turns out that helicity is a useful quantum number to describe neutrinos and coincides with a property called chirality. To understand chirality and its relationship to helicity requires an analysis of the Dirac Lagrangian and Dirac equation.

The Dirac Lagrangian for a free particle field  $\psi(x)$  with half-integer spin can be written as

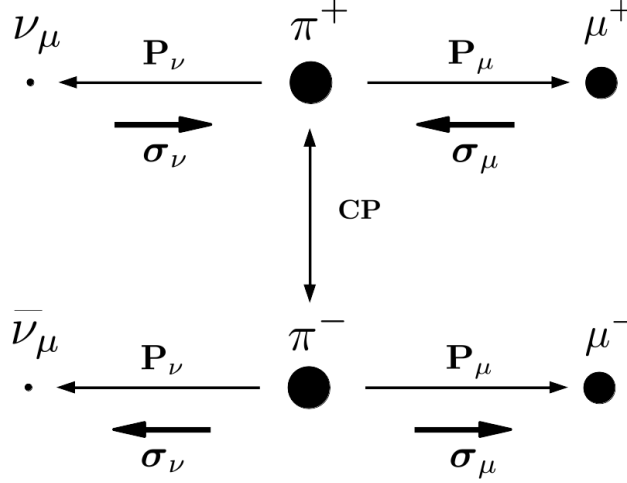


**Figure 1.3:** The helicity of the neutrino as inferred from pion decay. Since a pion at rest has zero (0) angular momentum, the system of daughter particles must have also net zero angular momentum. By measuring the muon's helicity, the helicity of neutrino is inferred. A neutrino (antineutrino) is a left- (right-) handed helicity particle since its spin is anti-parallel (parallel) to its momentum.

$$\mathcal{L} = \bar{\psi}(x) \left[ \frac{i\hbar}{2} \sum_{\mu=0}^3 \gamma^\mu (\overrightarrow{\partial}_\mu - \overleftarrow{\partial}_\mu) - mc \right] \psi(x) \quad (1.4)$$

where  $\psi(x)$  is a four-component vector (spinor) describing a particle field and  $\gamma^\mu$  are a set of four 4x4 matrices. The adjoint field  $\bar{\psi}(x)$  is defined as

$$\bar{\psi}(x) \equiv \psi^\dagger(x) \gamma^0 \quad (1.5)$$

where  $\dagger$  denotes the conjugate and transpose operations. The  $\overrightarrow{\partial}_\mu$  operator is a four-vector defined as

$$\partial_0 = \frac{1}{c} \frac{\partial}{\partial t}, \partial_1 = \frac{\partial}{\partial x}, \partial_2 = \frac{\partial}{\partial y}, \partial_3 = \frac{\partial}{\partial z} \quad (1.6)$$

that acts only to the right while  $\overleftarrow{\partial}_\mu$  only acts to the left (i.e.  $\overline{\psi} \overleftarrow{\partial}_\mu = \partial_\mu \overline{\psi}$ ). The  $\gamma^\mu$  matrices are not unique and different representations are more appropriate for different kinematic regimes. The field equations are extracted from the Lagrangian using the Euler-Lagrange procedure. In general for a set of  $M$  fields, the field equations are given by

---


$$\partial_\mu \frac{\partial \mathcal{L}}{\partial (\partial_\mu \psi_r)} - \frac{\partial \mathcal{L}}{\partial \psi_r} = 0 \quad (r = 0, 1, 2, \dots, M-1, M). \quad (1.7)$$

For the Dirac Lagrangian, the field equation for  $\psi$  is given by

$$\partial_\mu \frac{\partial \mathcal{L}}{\partial (\partial_\mu \bar{\psi})} - \frac{\partial \mathcal{L}}{\partial \bar{\psi}} = 0 \quad (1.8)$$

which yields the Dirac equation

$$\left[ i\hbar \sum_{\mu=0}^3 \gamma^\mu \partial_\mu - mc \right] \psi(x) = 0. \quad (1.9)$$

The representation of the  $\gamma^\mu$  matrices that is useful to describe neutrinos is the *Chiral representation* (also called the *Weyl representation*) where

$$\gamma^0 = \begin{bmatrix} 0 & I_2 \\ I_2 & 0 \end{bmatrix}, \gamma^1 = \begin{bmatrix} 0 & \sigma_x \\ -\sigma_x & 0 \end{bmatrix}, \gamma^2 = \begin{bmatrix} 0 & \sigma_y \\ -\sigma_y & 0 \end{bmatrix}, \gamma^3 = \begin{bmatrix} 0 & \sigma_z \\ -\sigma_z & 0 \end{bmatrix}, \quad (1.10)$$

$I_2$  is the  $2 \times 2$  identity matrix,  $\sigma_{x,y,z}$  are the Pauli Spin matrices given by

$$\sigma_x = \sigma_1 = \begin{pmatrix} 0 & 1 \\ 1 & 0 \end{pmatrix}, \quad \sigma_y = \sigma_2 = \begin{pmatrix} 0 & -i \\ i & 0 \end{pmatrix}, \quad \sigma_z = \sigma_3 = \begin{pmatrix} 1 & 0 \\ 0 & -1 \end{pmatrix}.$$

Using the Chiral representation, the chirality matrix,  $\gamma^5$  (the fifth gamma matrix), is defined as

$$\gamma^5 = i\gamma^0\gamma^1\gamma^2\gamma^3 = \begin{bmatrix} -I_2 & 0 \\ 0 & I_2 \end{bmatrix}, \quad (1.11)$$

which is diagonal as well as Hermitian, meaning that its eigenvalues are real and observable. Let the eigenfunctions of the chirality matrix be denoted with subscripts  $P$  and  $M$  such that the eigenvalue equations are

---

$$\begin{aligned}\gamma^5 \psi_P &= +1\psi_P, \\ \gamma^5 \psi_M &= -1\psi_M.\end{aligned}\tag{1.12}$$

The field equation solutions to ( 1.9) can be decomposed into  $\psi_P$  and  $\psi_M$  projections using two chiral projection operators  $\hat{O}_{P,M}$  where

$$\psi = (\hat{O}_P + \hat{O}_M) \psi = \psi_P + \psi_M.\tag{1.13}$$

The chiral operators are explicitly given by

$$\begin{aligned}\hat{O}_M &= \frac{1}{2} (I_4 - \gamma^5) = \begin{pmatrix} 0 & 0 \\ 0 & I_2 \end{pmatrix}, \\ \hat{O}_P &= \frac{1}{2} (I_4 + \gamma^5) = \begin{pmatrix} I_2 & 0 \\ 0 & 0 \end{pmatrix},\end{aligned}\tag{1.14}$$

where  $I_4$  is the  $4 \times 4$  identity matrix. Taken together ( 1.13) and ( 1.14) indicate the free neutrino field is a vector  $\psi$  minus axial vector  $\gamma^5\psi$ , also referred to as V-A, under P transformations. This feature is what allows for the weak force to violate P-symmetry and CP-symmetry. Referring back to( 1.4) and ( 1.7), the Dirac equation becomes a set of coupled equations

$$\begin{aligned}i\hbar \sum_{\mu=0}^3 \gamma^\mu \partial_\mu \psi_P &= mc\psi_M, \\ i\hbar \sum_{\mu=0}^3 \gamma^\mu \partial_\mu \psi_M &= mc\psi_P\end{aligned}\tag{1.15}$$

where dynamics are set by the mass.

Since the chiral projection operators are decompositions of the identity matrix, the simplest nontrivial solution to  $\psi$  is

$$\psi = \begin{pmatrix} \chi_P \\ \chi_M \end{pmatrix}\tag{1.16}$$

where  $\chi$  represent two-component spinors. Using 1.16 the Dirac equation in ( 1.15) can again be rewritten as

$$\begin{aligned} i\hbar \left[ \frac{1}{c} \frac{\partial}{\partial t} + \boldsymbol{\sigma} \cdot \boldsymbol{\nabla} \right] \chi_P &= -mc\chi_M, \\ i\hbar \left[ \frac{1}{c} \frac{\partial}{\partial t} - \boldsymbol{\sigma} \cdot \boldsymbol{\nabla} \right] \chi_M &= -mc\chi_P, \end{aligned} \quad (1.17)$$

where

$$\boldsymbol{\sigma} \cdot \boldsymbol{\nabla} = \sigma_x \frac{\partial}{\partial x} + \sigma_y \frac{\partial}{\partial y} + \sigma_z \frac{\partial}{\partial z}. \quad (1.18)$$

In the limiting case of vanishing mass ( $m \rightarrow 0$ ), as is in the SM, the free particle field equations in ( 1.17) decouple into

$$\begin{aligned} \left( \frac{E}{c} + \boldsymbol{\sigma} \cdot \boldsymbol{P} \right) \chi_P &= 0, \\ \left( \frac{E}{c} - \boldsymbol{\sigma} \cdot \boldsymbol{P} \right) \chi_M &= 0, \end{aligned} \quad (1.19)$$

where the differential operators have been evaluated as the particle's energy  $E$  and momentum three-vector  $\boldsymbol{P}$ . For massless neutrinos,  $\chi_P$  and hence  $\psi_P$ , describe particles of negative energy  $E = -|\boldsymbol{P}|c$  in the context of quantum field theory are interpreted as antiparticles traveling backwards in time. Conversely,  $\psi_M$  have positive energy  $E = |\boldsymbol{P}|c$  and which means they are particles traveling forward in time.

If one also multiplies ( 1.15) by  $\gamma^5\gamma^0$  and uses the fact that the spin operator  $\boldsymbol{\sigma}$  is given by

$$\boldsymbol{\sigma} = i(\gamma^2\gamma^3, \gamma^3\gamma^1, \gamma^1\gamma^2) = \gamma^0\gamma^k\gamma^5 \quad (k = 1, 2, 3) \quad (1.20)$$

each decoupled equation becomes

$$\frac{\boldsymbol{\sigma} \cdot \boldsymbol{P}}{|\boldsymbol{P}|} \psi_{P,M} = \gamma^5 \psi_{P,M} = \pm \psi_{P,M}, \quad (1.21)$$

where one recognizes that the helicity and chiral states are the same for  $m \rightarrow 0$  only. Thus the labels  $M$  and  $P$  actually are identical to the LH and RH helicity labels, respectively.

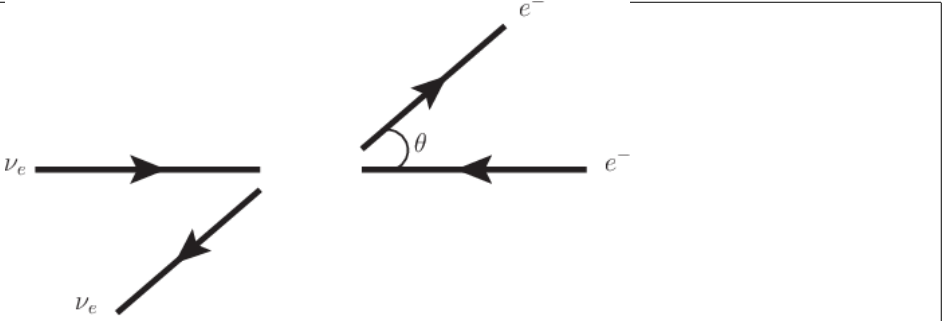


**Figure 1.4:** A schematic of  $\theta$  in  $\nu_e + e^-$  scattering. The same diagram is used to describe  $\bar{\nu}_e + e^-$  scattering with  $\nu_e \rightarrow \bar{\nu}_e$ .

Using the results above, a neutrino is always observed as a LH particle while the antineutrino is always observed as a RH antiparticle.

The observation of only LH neutrinos and RH antineutrinos is an important feature in the SM. However, since neutrinos are known to have mass, given that neutrinos oscillate, it is theoretically possible to observe a RH neutrino and a LH antineutrino. That would require boosting to a highly relativistic reference frame with respect to the laboratory.

### Neutrino Scattering with Matter

Charged current (CC) neutrino interactions on nuclear particles are the interactions investigated in this thesis. These interactions produce an outgoing charged lepton and a variety of hadronic states. While interactions with valence electrons is possible, they are far less common in large, subatomic particle detectors. However, the physics of neutrino-electron scattering is very similar to neutrino-nucleus scattering.

Consider neutrino-electron scattering, the cross section for  $\nu_e + e^-$  is given by

$$\frac{d\sigma}{d\Omega} = \left( \frac{G_F \hbar c}{2\pi} \right)^2 s, \quad (1.22)$$

where  $G_F$  is the Fermi constant and  $s$  is the center of mass energy squared. Due to the V-A nature of the weak force, neutrinos couple to LH particles and to RH antiparticles. The outgoing particles are isotropically distributed in the center-of-mass frame since the initial

and final spin state of the system is  $J = 0$ . Compare ( 1.22) with the cross section for  $\bar{\nu}_e + e^-$

$$\frac{d\sigma}{d\Omega} = \left( \frac{G_F \hbar c}{4\pi} \right)^2 (1 - \cos \theta)^2 s, \quad (1.23)$$

where  $\theta$  is the observed scattering angle of the electron as shown in Figure 1.4 on page 11. Since the total spin of the  $\bar{\nu}_e + e^-$  system is  $J = 1$  with z-projection  $J_z = 1$ , the antineutrino is preferentially forward scattered. Integrating over all angles, the cross sections are related to each other by

$$\sigma(\bar{\nu}_e + e^-) = \frac{1}{3} \sigma(\nu_e + e^-).$$

The factor  $1/3$  arises from the fact that angular momentum conservation forbids the  $J_z = -1$  and  $0$  states for  $\bar{\nu}_e + e^-$  scattering. The same  $1/3$  factor arises between  $\nu_\mu + d \rightarrow \mu^- + u$  and  $\bar{\nu}_\mu + u \rightarrow \mu^+ + d$  scattering.

In neutrino-nuclear scattering, the simple picture of free quarks must be replaced with the reality of the nuclear medium. Interactions with a single quark are still possible, but nuclear effects can alter the products of the interactions. The kinematics of the particles involved can be altered as well depending on the initial state of the nucleus. Distinctions must be made in neutrino physics between primary interactions ( $\nu_e + e^-$ ) and “final state interactions” (FSI) observables.

There are three neutrino-nuclear scattering classes presented in this thesis: quasi-elastic (CCQE), deep inelastic scattering (CC-DIS), and single pion production (CC- $1\pi$ ). The  $\nu_\mu$  CCQE interaction refers to the process where an incoming neutrino and neutron (udd) scatter to produce a charged lepton and proton (uud) as shown in Figure 1.5 on page 13. For  $\bar{\nu}_\mu$  CCQE, the proton is converted to a neutron instead. The CCQE interaction is the lowest energy CC interaction with a nucleon and has approximate mass conservation between the proton-neutron states ( $\Delta m = 1.29 \text{ MeV}/c^2$ ). The CC-DIS interaction is a high energy transfer process that shatters the nucleus apart. Finally, CC- $1\pi$  interactions refer to processes where a post-FSI charged pion is experimentally observed presumably from the

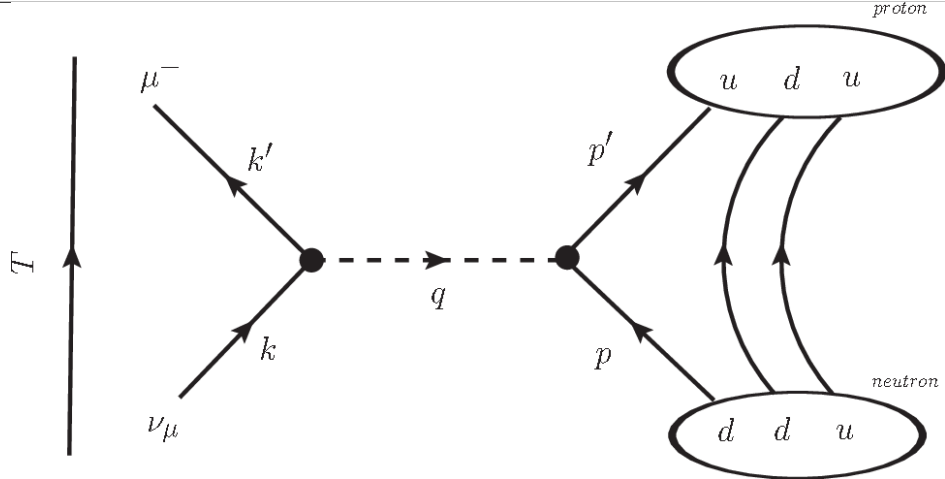


**Figure 1.5:** A  $\nu_\mu$ -induced CCQE interaction.

decay of resonance state like the  $\Delta(1232)$  baryon. These interactions are not well understood currently since they occur in the transition between CCQE and CC-DIS interaction modes.

### 1.1.2 Neutrino Oscillations

Neutrino oscillations is the physical process of a neutrino produced with a particular, definite flavor and later observed as a different flavor. This phenomenon was first observed as a deficit of neutrinos for a number of atmospheric and solar neutrino experiments. The deficit also seemed more pronounced for atmospheric neutrinos as the distance from their source increased. For neutrino oscillations to occur, at most one neutrino can be massless. This observation firmly established that the SM is incorrect with its assumption of massless neutrinos.

The first indication of neutrino oscillations was from the Ray Davis Homestake Mine experiment [26] which began operation in the 1960s. Ray Davis was an expert chemist and designed a radiochemical experiment to measure the flux of neutrinos from sun. The purpose of this experiment was to test John Bahcall's prediction of the fusion rate in the Sun and neutrino flux from it as well. Davis' experiment would need to operate for many years to collect enough statistics due to expected low capture rate. Measurements continued into the 1980s and showed that the flux of neutrinos was about  $1/3$  the expected rate and this

---

became known as the “Solar Neutrino Problem.” The primary explanations were either that the solar model was incorrect or the neutrino capture cross section was incorrect. The Sudbury Neutrino Observatory (SNO) was able to resolve this problem by making a model-independent measurement of the solar neutrino flux. SNO observed a  $\nu_e$  CC-to-NC ratio of  $0.301 \pm 0.033$ , which confirmed that only about 30% of neutrinos arrive as  $\nu_e$  flavors on Earth. In other words, the majority of neutrinos arrive as the wrong flavor [77].

Another outstanding problem emerged with measurements of atmospheric neutrinos, in particular muon and electron types. Atmospheric neutrinos are produced when high energy cosmic rays strike atmospheric particles. These cosmic ray collisions generate mostly pions and kaons that decay into neutrinos. When trying to measure the  $\nu_\mu/\nu_e$  ratio, there was another significant deficit. This was particularly apparent for the Super-Kamiokande (SK) experiment, which is a 50 kt tank of pure water lined with thousands of photomultiplier tubes designed to observe solar and atmospheric neutrinos. It was the first experiment to perform a neutrino oscillation analysis that successfully explained the deficit.

The observation of neutrino oscillations is a relatively new discovery. Bruno Pontecorvo [57] first proposed such a mechanism in 1957 between neutrinos and antineutrinos much like known neutral K-mesons oscillations. However, oscillations between flavored neutrinos was not expected since it requires the neutrino to have mass. The reasons why are explained in the next subsection.

## Two Flavor Derivation of Neutrino Oscillations

The phenomenon of neutrino oscillations can be described with elementary, non-relativistic quantum mechanics. Beginning with the Schrödinger Equation in ( 1.24)

$$-\frac{\hbar}{i} \frac{d}{dt} |\nu(\mathbf{r}, t)\rangle = \hat{H} |\nu(\mathbf{r}, t)\rangle, \quad (1.24)$$

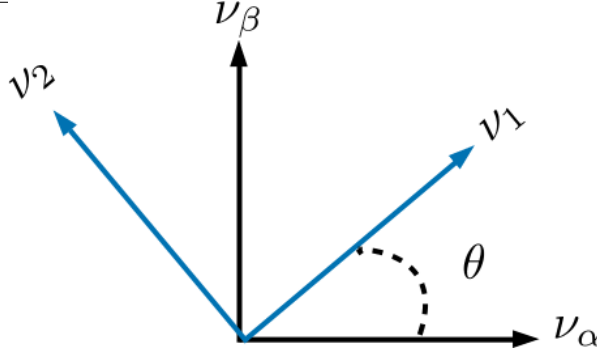


**Figure 1.6:** The depiction of two neutrino flavor change of basis using a rotation matrix, defined in ( 1.29).

where  $\hat{H}$  is the Hamiltonian for the physical system. Here we consider massive neutrinos of mass  $m_j$  in its rest frame (free particle). The Hamiltonian is diagonal in this case, which acting on  $|\nu_j\rangle$  results in the eigenvalue equation

$$\hat{H} |\nu_j(\mathbf{r}, t)\rangle = E_j |\nu_j(\mathbf{r}, t)\rangle, \quad (1.25)$$

where  $E_j$  is the energy of the neutrino  $|\nu_j\rangle$ . Substituting ( 1.25) into ( 1.24) and solving for  $|\nu(\mathbf{r}, t)\rangle$ , one obtains the following

$$|\nu_j(\mathbf{r}, t)\rangle = e^{-iE_j t/\hbar} |\nu_j(\mathbf{r}, t=0)\rangle, \quad (1.26)$$

where  $|\nu_j(\mathbf{r}, t=0)\rangle$  is created with momentum  $\mathbf{p}$  at the origin  $\mathbf{r} = 0$ . The time-independent solution to ( 1.24) is a plane-wave given by

$$|\nu_j(\mathbf{r}, t=0)\rangle = e^{i\mathbf{p} \cdot \mathbf{r}/\hbar} |\nu_j\rangle. \quad (1.27)$$

Before being able to describe neutrino oscillations, the basis states must be defined. For this example, consider that there are only two eigenstates, labeled  $\nu_1$  and  $\nu_2$ , in the “mass” basis with definite mass  $m_1$  and  $m_2$ , respectively. However, experiments can produce neutrinos, as well as probe them, only in a definite flavor state, denoted by a Greek letter subscript  $\lambda$ . Let the generated neutrino, which is a linear superposition of mass states 1 and

2, have momentum  $\mathbf{p}$  and flavor  $\alpha$ . Since both mass eigenstates share the same momentum  $\mathbf{p}$  (but not energy!), the exponential term in ( 1.27) is an overall phase that will cancel out later. One can postulate a linear transformation,  $U$ , between the basis states given by ( 1.28).

$$\begin{bmatrix} \nu_\alpha \\ \nu_\beta \end{bmatrix} = \begin{bmatrix} U_{11} & U_{12} \\ U_{21} & U_{22} \end{bmatrix} \begin{bmatrix} \nu_1 \\ \nu_2 \end{bmatrix} \quad (1.28)$$

This linear transformation must be a unitary matrix ( $U^{-1} = U^\dagger$ ,  $\dagger$  = transpose conjugate) since the states  $\nu_{1,2}$  constitute a complete orthonormal basis in the mass basis. With this unitary property,  $U$  can be written as a rotation matrix

$$\begin{bmatrix} \nu_\alpha \\ \nu_\beta \end{bmatrix} = \begin{bmatrix} \cos(\theta) & \sin(\theta) \\ -\sin(\theta) & \cos(\theta) \end{bmatrix} \begin{bmatrix} \nu_1 \\ \nu_2 \end{bmatrix}, \quad (1.29)$$

where  $\theta$  is the angle between the two bases. One can imagine this transformation between bases as shown in Figure 1.6 on page 15. The probability of creating a neutrino of flavor  $\alpha$  and later observing it as flavor  $\beta \neq \alpha$  at time  $t = T > 0$  is given by

$$\begin{aligned} \mathcal{P}(\nu_\alpha \rightarrow \nu_\beta) &= |\langle \nu_\alpha(t=0) | \nu_\beta(t=T) \rangle|^2 \\ &= |\{\cos(\theta) \langle \nu_1(t=0) | + \sin(\theta) \langle \nu_2(t=0) |\} \\ &\quad \times \{-\sin(\theta) |\nu_1(t=T)\rangle + \cos(\theta) |\nu_2(t=T)\rangle\}|^2. \end{aligned} \quad (1.30)$$

Evaluating all inner products and simplifying terms in ( 1.30) results in ( 1.31) below.

$$\mathcal{P}(\nu_\alpha \rightarrow \nu_\beta) = \sin^2(2\theta) \sin^2\left(\frac{E_1 - E_2}{2\hbar}T\right) \quad (1.31)$$

The terminology of “neutrino oscillations” should be more apparent now since ( 1.31) demonstrates that the probability changes sinusoidally as a function of time  $T$ . This equation is not, however, terribly useful in the laboratory frame since it is hard to design an experiment

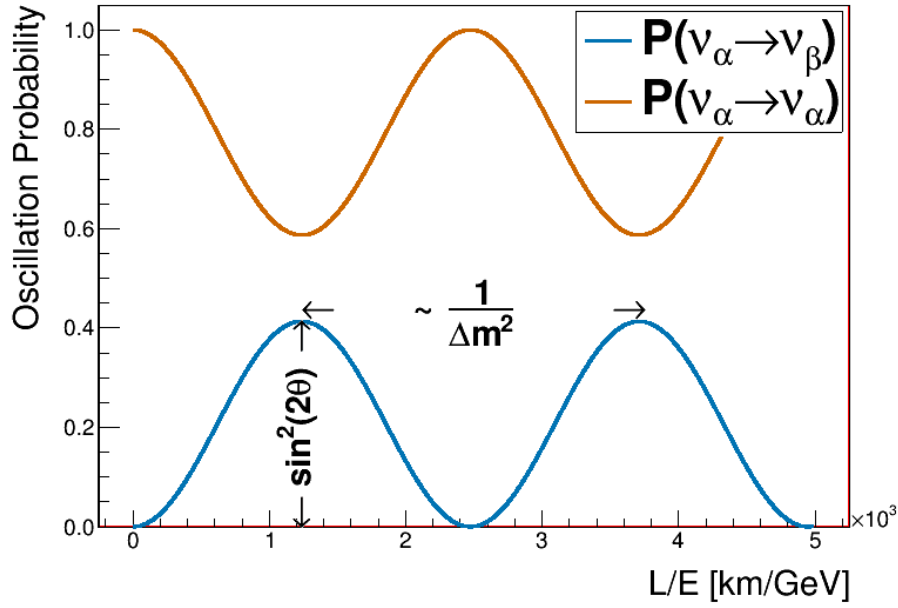


**Figure 1.7:** Two flavor oscillation probability as a function  $L/E$  is shown using  $\theta = 20^\circ$  and  $\Delta m^2 = 10^{-3} \text{ eV}^2/c^4$ . The spacing between adjacent peaks/troughs is proportional to the inverse of  $\Delta m^2$ . Note that  $\mathcal{P}(\nu_\alpha \rightarrow \nu_\alpha) = 1 - \mathcal{P}(\nu_\alpha \rightarrow \nu_\beta)$  since the oscillation probability must always sum to 1.

where the travel time an individual neutrino is actually measured. Since neutrinos are nearly massless, they travel very close to the speed of light. Therefore time  $T$  is replaced with  $L/c$  where  $L$  is the distance between the neutrino origin and detection and  $c$  is now the speed of light in vacuum. One can also approximate the energy of the mass eigenstate as

$$\begin{aligned}
E_j &= \left( m_j^2 c^4 + p_j^2 c^2 \right)^{\frac{1}{2}} = p_j c \left( 1 + \frac{m_j^2 c^2}{p_j^2} \right)^{\frac{1}{2}} \\
&\approx p_j c \left( 1 + \frac{m_j^2 c^2}{2p_j^2} + \mathcal{O} \left( \frac{m_j c}{p_j} \right)^4 \right) \\
&\approx E_\nu + \frac{m_j^2 c^4}{2E_\nu},
\end{aligned} \tag{1.32}$$

where for oscillation experiments  $p_j \gg m_j c$  and  $p_j c \approx E_\nu$  where  $E_\nu$  is the neutrino energy as measured in the laboratory. Substituting these assumptions in (1.31), the oscillation probability is given by

---


$$\mathcal{P}(\nu_\alpha \rightarrow \nu_\beta) = \sin^2(2\theta) \sin^2\left(\frac{\Delta m^2 c^3}{4\hbar} \frac{L}{E_\nu}\right), \quad (1.33)$$

where  $\Delta m^2 = m_2^2 - m_1^2$  is the mass-squared difference between the mass states. For a moment consider evaluating all the physical constants in natural units ( $c = \hbar = 1$ ), the  $\Delta m^2$  in  $\text{eV}^2$ ,  $L$  in km, and  $E_\nu$  in GeV, . The oscillation probability from between states  $\nu_\alpha$  to  $\nu_\beta$  is given by

$$\mathcal{P}(\nu_\alpha \rightarrow \nu_\beta) = \sin^2(2\theta) \sin^2\left(1.27 \frac{\Delta m^2}{[\text{eV}^2]} \frac{L/E_\nu}{[\text{km}/\text{GeV}]}\right) \text{ [natural units]} \quad (1.34)$$

which more clearly illustrates the physics of neutrino oscillations. The oscillation probability has an amplitude of  $\sin^2(2\theta)$  and varies with frequency inversely proportional to  $\Delta m^2$  as shown in Figure 1.7 on page 17. Since  $L$  and  $E_\nu$  are the only controllable parameters for an oscillation experiment, probing  $\theta$  or  $\Delta m^2$  can be difficult unless the experiment can probe a large range of  $L/E_\nu$  as shown in Figure 1.8 on page 19.

### Three Flavor Oscillations

In the general case of oscillations using a  $n \times n$  mixing matrix, the unitary transformation can be written as a rotation matrix with  $\frac{n}{2}(n-1)$  weak mixing angles with  $\frac{1}{2}(n-2)(n-1)$  Charge-Parity (CP) violating phases. In addition, oscillations are dictated by a total of  $n-1$  mass-squared splittings [77]. This all assumes that neutrinos obey the Dirac Equation, or that they are not their own antiparticles. The favored mixing model is a  $3 \times 3$  matrix since there are three known neutrino flavors,  $\nu_e$ ,  $\nu_\mu$ , and  $\nu_\tau$ . This means that there are three (3) mixing angles, one (1) CP violating phase, and three (3) mass-squared splittings.

The most frequently used matrix parameterization is the MNSP (MNSP: Maki-Nakagawa-Sakata-Pontecorvo) matrix. Pontecorvo is credited with first conceiving of neutrino oscillations, albeit between neutrino and antineutrinos [56]. It was Maki, Nakagawa, and Sakata who conceived of the parameterization based on the ideas of Pontecorvo [52]. The MNSP matrix is decomposed into separate rotation matrices as given by ( 1.35)

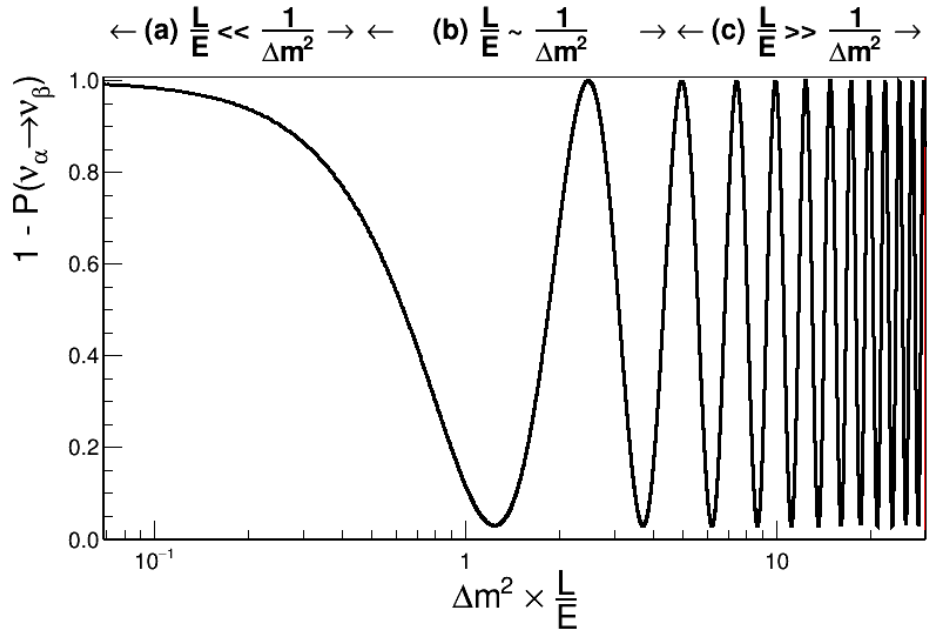


**Figure 1.8:** Semi-logarithmic plot of the survival probability of flavor  $\alpha$  ( $1 - \mathcal{P}(\nu_\alpha \rightarrow \nu_\beta) = \mathcal{P}(\nu_\alpha \rightarrow \nu_\alpha)$ ) over a wide range of  $L/E$  values for  $\theta = 40^\circ$ . The arrows above the plot coarsely denote three possible cases: (a) no oscillations ( $L/E \ll 1/\Delta m^2$ ); (b) sensitivity to oscillations ( $L/E \sim 1/\Delta m^2$ ); (c) only average measurement ( $L/E \gg 1/\Delta m^2$ ). Image originally inspired by [66].

$$U_{\text{MNSP}} = \underbrace{\begin{bmatrix} 1 & 0 & 0 \\ 0 & c_{32} & s_{32} \\ 0 & -s_{32} & c_{32} \end{bmatrix}}_{U_{32}=U_{\text{atm}}} \times \underbrace{\begin{bmatrix} c_{31} & 0 & s_{31}e^{i\delta_{\text{CP}}} \\ 0 & 1 & 0 \\ -s_{31}e^{-i\delta_{\text{CP}}} & 0 & c_{31} \end{bmatrix}}_{U_{31}=U_{\text{rea}}} \times \underbrace{\begin{bmatrix} c_{21} & s_{21} & 0 \\ -s_{21} & c_{21} & 0 \\ 0 & 0 & 1 \end{bmatrix}}_{U_{21}=U_{\text{sol}}}, \quad (1.35)$$

where

$$c_{ij} = \cos \theta_{ij}, \quad s_{ij} = \sin \theta_{ij}, \quad (1.36)$$

and  $\delta_{\text{CP}}$  represents the CP violating phase. Each rotation matrix  $U_{ij}$  represents the different sources for neutrino oscillations experiments with “atm”, “rea”, and “sol” representing atmospheric  $\nu$ ’s, nuclear reactor  $\nu$ ’s, and solar  $\nu$ ’s, respectively. The sensitivity of neutrino oscillations for different sources is given in Table 1.1 on page 20.

Source	Species	Baseline [km]	Mean Energy [GeV]	$\min(\Delta m^2)$ [eV $^2$ ]
Reactor	$\bar{\nu}_e$	1	$\sim 10^{-3}$	$\sim 10^{-3}$
Reactor	$\bar{\nu}_e$	100	$\sim 10^{-3}$	$\sim 10^{-5}$
Accelerator	$\nu_\mu, \bar{\nu}_\mu$	1	$\sim 1$	$\sim 1$
Accelerator	$\nu_\mu, \bar{\nu}_\mu$	$10^3$	$\sim 1$	$\sim 10^{-3}$
Atmospheric $\nu$ 's	$\nu_{e,\mu}, \bar{\nu}_{\mu,e}$	$10^4$	$\sim 1$	$\sim 10^{-4}$
Sun	$\nu_e$	$1.5 \times 10^8$	$\sim 10^{-3}$	$\sim 10^{-11}$

**Table 1.1:** Sensitivity of different oscillation experiments originally published in [70].

If neutrinos are their own antiparticles, they are not described by the Dirac Equation but instead are described the Majorana Equation. This adds two (in general  $n - 1$ ) more CP violating Majorana phases,  $\alpha$  and  $\beta$ , to the MNSP matrix

$$U_{\text{MNSP}} \rightarrow U_{\text{MNSP}} \times \underbrace{\begin{bmatrix} 1 & 0 & 0 \\ 0 & e^{i\alpha} & 0 \\ 0 & 0 & e^{i\beta} \end{bmatrix}}_{U_{\text{Majorana}}} . \quad (1.37)$$

Unfortunately, neutrino oscillations are not able to probe the Majorana phases since the Majorana matrix is diagonal. The question of as to whether neutrinos are Majorana ( $\nu = \bar{\nu}$ ) or Dirac ( $\nu \neq \bar{\nu}$ ) particles is an open question that is being explored by neutrino-less double beta decay experiments [65].

The full three flavor oscillation probability is given by

$$\begin{aligned} \mathcal{P}(\nu_\alpha \rightarrow \nu_\beta) = & \delta_{\alpha\beta} - 4 \sum_{j=1}^3 \left[ \sum_{i>j}^3 \text{Re}(K_{\alpha\beta,ij}) \sin^2(\phi_{ij}) \right] \\ & + 4 \sum_{j=1}^3 \left[ \sum_{i>j}^3 \text{Im}(K_{\alpha\beta,ij}) \sin(\phi_{ij}) \cos(\phi_{ij}) \right] \end{aligned} \quad (1.38)$$

where

$$K_{\alpha\beta,ij} = U_{\alpha i} U_{\beta i}^* U_{\alpha j}^* U_{\beta j} \quad (1.39)$$

encapsulates the MNSP matrix elements and

$$\phi_{ij} = \frac{\Delta m_{ij}^2 c^3}{4\hbar} \frac{L}{E_\nu}. \quad (1.40)$$

Since CP violation means that  $\mathcal{P}(\nu_\alpha \rightarrow \nu_{\beta \neq \alpha}) \neq \mathcal{P}(\bar{\nu}_\alpha \rightarrow \bar{\nu}_{\beta \neq \alpha})$ , CP violating terms must be odd function of  $\delta_{\text{CP}}$ . Consider the following examples, muon neutrino survival and muon neutrino to electron neutrino appearance.

**Muon Neutrino Survival** The probability of a muon type neutrinos (antineutrinos) surviving is given by

$$\begin{aligned} \mathcal{P}\left(\overset{(-)}{\nu}_\mu \rightarrow \overset{(-)}{\nu}_\mu\right) &= 1 - 4s_{23}^2 c_{13}^2 \left(V_{\cos \delta_{\text{CP}}}\right) \sin^2 \phi_{31} \\ &\quad - 4s_{23}^2 c_{13}^2 \left(Z_{\cos \delta_{\text{CP}}}\right) \sin^2 \phi_{32} \\ &\quad - 4 \left(V_{\cos \delta_{\text{CP}}}\right) \left(Z_{\cos \delta_{\text{CP}}}\right) \sin^2 \phi_{21} \end{aligned} \quad (1.41)$$

where

$$V_{\cos \delta_{\text{CP}}} = s_{12}^2 c_{23}^2 + s_{13}^2 s_{23}^2 c_{12}^2 + 2s_{12}s_{13}s_{23}c_{12}c_{23} \cos \delta_{\text{CP}} \quad (1.42)$$

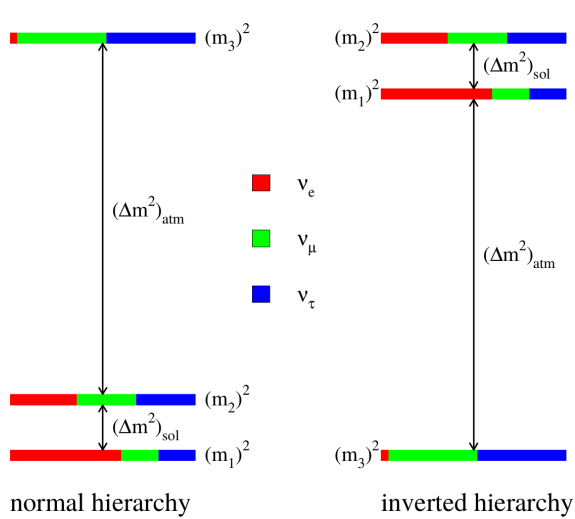
$$Z_{\cos \delta_{\text{CP}}} = c_{12}^2 c_{23}^2 + s_{13}^2 s_{23}^2 s_{12}^2 - 2s_{12}s_{13}s_{23}c_{12}c_{23} \cos \delta_{\text{CP}} \quad (1.43)$$

and  $\overset{(-)}{\nu}_\mu$  represents either  $\nu_\mu$  or  $\bar{\nu}_\mu$ . If a definitive measurement of  $\mathcal{P}(\nu_\mu \rightarrow \nu_\mu) \neq \mathcal{P}(\bar{\nu}_\mu \rightarrow \bar{\nu}_\mu)$  in vacuum occurs, it implies that the combined C, P and time (CPT) symmetry is violated<sup>4</sup>.

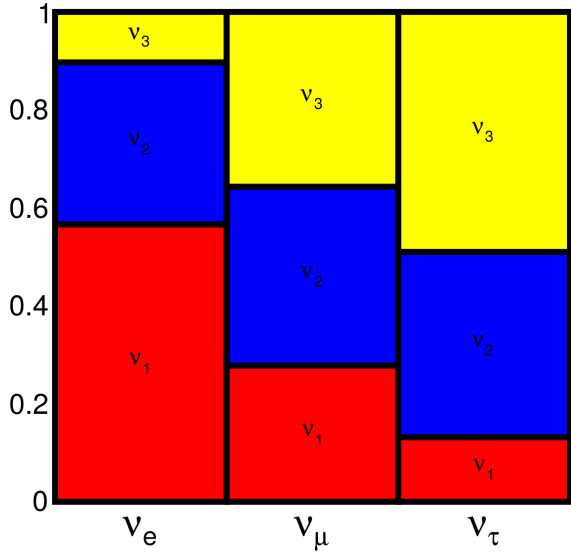
**Electron Neutrino Appearance** The previous subsection briefly explored the muon disappearance probability, which is not tested as a channel for CP violation. Electron neutrino appearance, however, does provide insight into CP violation in the lepton sector. The appearance probability of electron neutrino types from muon neutrino types is given by

---

<sup>4</sup>When going to through matter however, the oscillation probability is affected. This is explained more in Section 1.1.2.



(a) Mass hierarchy as shown in [30]



(b) Mass eigenstate components as shown in [12]

**Figure 1.9:** Neutrino mass hierarchy problem and MNSP representation. Left: the mass hierarchy problem is shown. The colored bars for each mass eigenstate correspond to the approximate flavor content of the neutrino. For example, state “2” has about equal three portions of all three flavors. Right: the mass eigenstate components of each flavor eigenstate. This is a complementary demonstration of the MNSP matrix.

$$\begin{aligned}
 \mathcal{P} \left( \overset{(-)}{\nu}_\mu \rightarrow \overset{(-)}{\nu}_e \right) = & 4 c_{13}^2 s_{13}^2 s_{23}^2 \sin^2 \phi_{31} \\
 & + 8 \left( X_{\cos \delta_{CP}} \right) \cos \phi_{23} \sin \phi_{31} \sin \phi_{21} \\
 & - \underbrace{8 \left( Y_{\sin \delta_{CP}} \right)}_{CP \text{ violating}} \sin \phi_{32} \sin \phi_{31} \sin \phi_{21} \\
 & + 4 \left( Z_{\cos \delta_{CP}} \right) s_{12}^2 c_{13}^2 \sin^2 \phi_{21}
 \end{aligned} \tag{1.44}$$

where

$$X_{\cos \delta_{CP}} = c_{13}^2 s_{12} s_{13} s_{23} (c_{12} c_{23} \cos \delta_{CP} - s_{12} s_{13}) \tag{1.45}$$

$$Y_{\sin \delta_{CP}} = \frac{1}{8} \sin(2\theta_{12}) \sin(2\theta_{13}) \sin(2\theta_{23}) c_{13} \sin \delta_{CP} \tag{1.46}$$

and (+) represents the sign change from neutrinos to antineutrinos. The CP violating term (1.46) is also known as the Jarlskog Invariant and is a measure of CP violation independent

Parameter	Normal Hierarchy	Inverted Hierarchy	Units
$\Delta m_{32}^2$	$2.51 \pm 0.05$	$-2.56 \pm 0.04$	$10^{-3}$ eV <sup>2</sup>
$\Delta m_{21}^2$		$7.53 \pm 0.18$	$10^{-5}$ eV <sup>2</sup>
$\sin^2(\theta_{21})$		$0.307^{+0.013}_{-0.012}$	1
$\sin^2(\theta_{32})$	$\begin{cases} 0.417^{+0.025}_{-0.028} & \theta_{32} \in (0, \frac{\pi}{2}) \\ 0.597^{+0.024}_{-0.030} & \theta_{32} \in (\frac{\pi}{2}, \frac{\pi}{4}) \end{cases}$	$\begin{cases} 0.421^{+0.033}_{-0.025} & \theta_{32} \in (0, \frac{\pi}{2}) \\ 0.592^{+0.023}_{-0.030} & \theta_{32} \in (\frac{\pi}{2}, \frac{\pi}{4}) \end{cases}$	1
$\sin^2(\theta_{31})$		$2.12 \pm 0.08$	$10^{-2}$
$\delta_{\text{CP}}$	$217^{+40}_{-28}$	$280^{+25}_{-28}$	degrees

**Table 1.2:** Table of best fit MNSP parameters split by normal and inverted hierarchy. All values except for  $\delta_{\text{CP}}$  are combined values from the Particle Data Group and  $\delta_{\text{CP}}$  is from the 2018 NuFit analysis [31, 70].

of the mixing parameterization [46]. This oscillation channel is of primary importance in current and future proposed accelerator and atmospheric neutrino oscillation experiments.

Current and next generation experiments aim to improve knowledge of the mixing parameters. There are a couple of degeneracies to unravel as well as precise measurement of  $\delta_{\text{CP}}$ . While the two defined mass-squared splittings  $\Delta m_{21}^2 = \Delta m_{\text{sol}}^2$  and  $\Delta m_{32}^2 = \Delta m_{\text{atm}}^2$  are known, it is unknown which eigenstates are more massive. This problem is known as the mass hierarchy problem and is illustrated in Figure 1.9a on page 22. Normal hierarchy refers to the case where  $m_3 > m_2 > m_1$  whereas the inverted hierarchy has  $m_2 > m_1 > m_3$ . Also distinguishing if  $\theta_{23}$  is in the first octant  $\theta \in (0, \pi/2)$  or second octant  $\theta \in (\pi/2, \pi/4)$  of the unit circle requires large statistics. Finally the value of  $\delta_{\text{CP}}$  is quite uncertain with values in the 3rd and 4th quadrants. Best fit measurements of the oscillations parameters are given in Table 1.2 on page 23.

## Matter Effects

Traveling through matter has the potential to increase the sensitivity of neutrino oscillation measurements if the baseline is long enough. Known as the Mikheyev-Smirnov-

Wolfenstein (MSW) effect [74], all oscillations are affected by coherent forward scattering of neutrinos with electrons in the media. Taking the example of  $(\bar{\nu}_\mu \rightarrow \bar{\nu}_e)$  from ( 1.41), the MSW effect to first order is

$$\begin{aligned} \mathcal{P}((\bar{\nu}_\mu \rightarrow \bar{\nu}_e)) \rightarrow & \mathcal{P}((\bar{\nu}_\mu \rightarrow \bar{\nu}_e)) + \frac{8\alpha}{\Delta m_{31}^2} (c_{13}^2 s_{13}^2 s_{23}^2) (1 - 2s_{13}^2) \\ & \times \left( \sin^2 \phi_{31} - \underbrace{\left( \frac{\Delta m_{31}^2 c^3}{4\hbar} \frac{L}{E_\nu} \right)}_{\phi_{31}} \cos \phi_{32} \sin \phi_{31} \right), \end{aligned} \quad (1.47)$$

where

$$\alpha = 2\sqrt{2}G_F n_e E_\nu, \quad (1.48)$$

and  $n_e$  is the average electron density of the Earth through which the neutrinos travel [15]. Carefully studying ( 1.47) reveals that the MSW effect alters the oscillation probability as a function of the electron density and increases in magnitude with baseline.

### 1.1.3 CP Violation: Origins of Matter

To conclude the introduction on neutrinos, it is important to examine the implications of CP violation. The observation of CP violation in the lepton sector might provide critical insight into the origins of the matter. CP violation dictates that certain interactions behave differently between matter or antimatter like  $\mathcal{P}(\nu_\mu \rightarrow \nu_e) \neq \mathcal{P}(\bar{\nu}_\mu \rightarrow \bar{\nu}_e)$ . The Big Bang Theory suggests that in the first fractions of a second of the Universe, equal amounts of matter and antimatter were created. However, observational evidence shows the Universe consists of only 4.5% baryonic matter (i.e. protons and neutrons) from cosmological models as shown in Figure 1.10 on page 25. The anti-baryonic fraction of the baryonic matter is infinitesimally low from external constraints on data from gamma-ray telescopes like Fermi-GLAST [72]. This problem is known as the Baryon Asymmetry of the Universe (BAU).

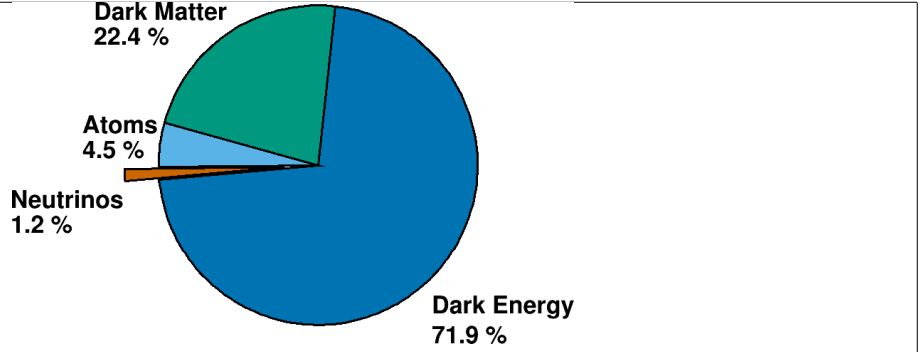


**Figure 1.10:** The matter and energy content of the Universe. The observable Universe contains about 4.5% of atoms (baryons and electrons) and an estimated neutrino content less than 1.2%. The rest of the Universe consists of Dark Matter at 22.4% and a form of energy called Dark Energy at 71.9%. These inferred parameters are taken from the  $\Lambda$ CDM model, the simplest model that describes the cosmos [48].

The process of Baryogenesis<sup>5</sup> is a favored model to explain the BAU and lacks a necessary precursor mechanism. One of the necessary conditions for Baryogenesis [63] is C symmetry violation and CP violation. Evidence of CP violation has been experimentally confirmed in the quarks, but not to the level which resolves the BAU. Baryogenesis can be achieved by having Leptogenesis<sup>6</sup> occur first through the decay of very heavy, right handed Majorana neutrino ( $\nu = \bar{\nu}$ ) through the *see-saw* mechanism. Detailed discussions on Leptogenesis and the *see-saw* mechanism can be found in [12].

#### 1.1.4 Long-Baseline Neutrino Oscillation Experiments

The KEK to Kamioka (K2K) experiment was the first neutrino oscillation experiment where researchers controlled the production and observation of neutrinos. In K2K, a beam of muon neutrinos were directed from the 12 GeV proton synchotron at KEK to the Kamioka Observatory at a distance of 250 km. While travelling through the Earth, the neutrinos

<sup>5</sup>Baryogenesis is the mechanism by which matter and antimatter baryons are created in the early Universe.

<sup>6</sup>Leptogenesis is the mechanism by which leptons and anti-leptons are created in the early Universe.

---

oscillate before they are observed at Kamioka. Prior to K2K, neutrino sources included the atmosphere, the Sun, and one supernova.

The K2K experiment established the experimental methods for current and planned next generation long-baseline neutrino oscillation experiments from accelerators. The accelerator neutrinos are produced when a high energy proton beam hits a target. The secondary particles are then forward focused using electrically pulsed magnets and allowed to decay in a large decay volume. This procedure produces a highly pure muon neutrino beam with order 1% electron neutrino contamination. Prior to any oscillations, a “near” detector is used to measure the neutrino flux as function of neutrino energy and study detector systematic uncertainties associated at the “far” detector at Kamioka. The successor experiment to K2K called Tokai to Kamioka (T2K), closely followed this design methodology. Other notable accelerator-based long-baseline experiments include MINOS [77] and NO $\nu$ A [11], both in the United States.

## 1.2 Tokai to Kamioka Experiment

The Tokai to Kamioka (T2K) experiment is a long-baseline, neutrino oscillation experiment hosted in Japan [1] as shown in Figure 1.11 on page 27. It is the successor experiment to the K2K neutrino oscillation experiment also hosted in Japan. The T2K experiment produces a high intensity, relatively pure muon neutrino beam at the Japan Proton Accelerator Complex (J-PARC) which is a world class particle accelerator facility. The beam is directed at the Super-Kamiokande (SK) [36] detector, which is 295 km away from the source. Additionally, the beam is designed to maximize the  $\nu_\mu \rightarrow \nu_e$  probability at the far detector  $L = 295$  km baseline using a neutrino energy spectrum sharply peaked at  $E_\nu = 0.6$  GeV as shown in Figure 1.12 on page 27. This spectrum is achieved by directing the center of the beam axis 2.5 degrees off center from SK. Along the beamline at 280 m from the beam source is the near detector facility called ND280 [33], whose data is used in thesis.

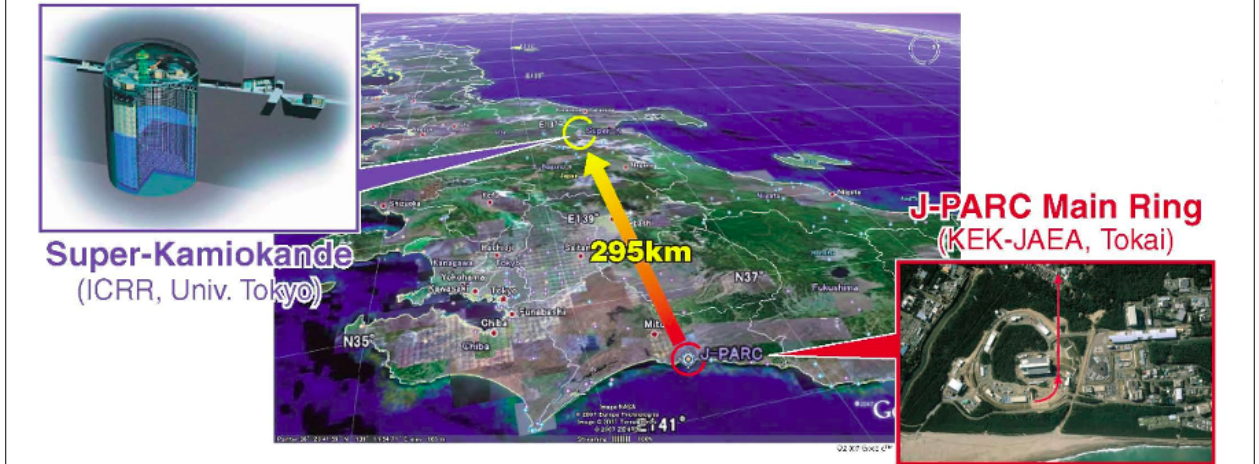


**Figure 1.11:** Birds eye view of the T2K experiment on the Japanese archipelago. An intense beam of neutrinos is produced at the J-PARC site (bottom right red box) using high energy protons. The beam is directed towards the Super-Kamiokande detector (top left blue box) at a distance of 295 km away from J-PARC.

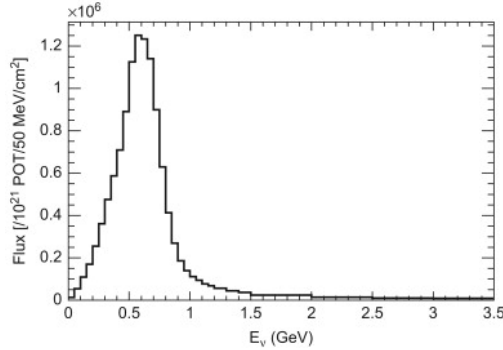


**Figure 1.12:** The T2K unoscillated  $\nu_\mu$  flux at SK at the off-axis angle of  $2.5^\circ$ .

The ND280 facility is designed to observe and characterize the unoscillated neutrino beam. There are two detectors at ND280: the primary, off-axis detector and on-axis detector. The measurement in this thesis uses data collected from the off-axis near detector.

The T2K experiment was primarily designed to measure the last unknown MNSP mixing angle  $\theta_{13}$ , which was thought to be nearly zero, via the  $\nu_\mu \rightarrow \nu_e$  channel. In addition it aims to make a precision measurement the atmospheric mixing parameters,  $\theta_{23}$  and  $\Delta m_{23}^2$  via the  $\nu_\mu \rightarrow \nu_\mu$  channel. An early landmark for the T2K experiment was a  $7.3\sigma$  measurement excluding non-zero  $\theta_{13}$  in 2013 [3]. It continues to be a world leader in oscillation physics and as of 2018 rejects CP conserving values ( $\delta_{\text{CP}} = 0, \pi$ ) at the  $2\sigma$  level [8].



**Figure 1.13:** Bird's eye view of the J-PARC center showing the primary components of its accelerator programs. To generate the high intensity neutrino beam, first the linear accelerator (Linac, red) accelerates hydrogen ions (protons) into the 3 GeV Synchrotron (also red) called the rapid-cycle synchrotron (RCS). The RCS then injects some of its protons into the 50 GeV Synchrotron (yellow) called the main ring (MR), which currently runs at 30 GeV. Finally the MR protons are directed into a target material along the neutrino beamline (teal) [23].

The following topics will be discussed in the following order. First a look how neutrinos are produced at J-PARC. Next a detailed look at the T2K near detectors which are used in this thesis. This is followed by a discussion on Super-Kamiokande, the T2K far detector.

### 1.2.1 Neutrino Production at J-PARC

To facilitate the high intensity neutrino beam requirements for T2K, the J-PARC site generates a high intensity proton beam through a series of particle accelerators. A bird's eye view of J-PARC can be seen in Figure 1.13 on page 28 which highlights its accelerators and other facilities. For this section, note that all beam energies are kinetic energies.

---

Protons for the T2K beamline are first accelerated in the J-PARC linear accelerator<sup>7</sup> (linac) and then the rapid cycle synchrotron<sup>8</sup> (RCS). Hydrogen ions ( ${}_1^1\text{H}^-$ ) are extracted from plasma in a electrical discharge chamber and fed through a series of linac elements as shown in Figure 1.14a on page 30. Each linac element, except for the initial quadrupole magnet, accelerates the ions using carefully synchronized oscillating electric fields generated by radio frequency pulses. After traveling 240 m along the linac, the ions have been boosted to 181 MeV of kinetic energy and transported into the RCS. While in transit to the RCS, the ions are stripped of their electrons via charge stripping foils. The 348 m circumference RCS then further boosts the protons to 3 GeV at an operating frequency of 25 Hz. While being accelerated, protons are aggregated into two bunches and focused using particle collimators as shown in Figure 1.14b on page 30.

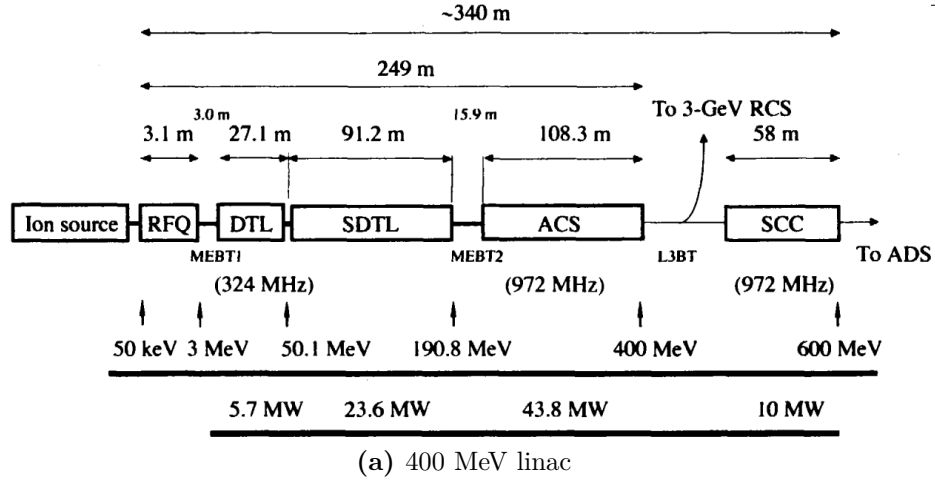
The next stage for the protons intended for the neutrino beamline is the much larger main ring (MR) synchrotron as shown in Figure 1.14c on page 30 which has a circumference of 1567m. While nominally designed to boost protons to 50 GeV, it currently operates at 30 GeV. Protons are injected into the MR to form eight proton bunches (spill), initially six when T2K first ran, before entering the neutrino beamline. The total temporal width of the spill is approximately  $0.5\mu\text{s}$  [1]. At a spill cycle frequency of 0.5Hz, the bunches are extracted from the MR into the neutrino beamline.

The neutrino beamline is designed to direct the protons toward SK and generate neutrinos by striking them into the end of a cylindrical target. Figure 1.15a on page 31 shows the process of proton extraction from the MR for both primary and secondary neutrino beamlines. In the primary beamline, a series of normal and superconducting magnets steer the proton beam away from the MR first along a 54 m preparation section and then a 147 m arc

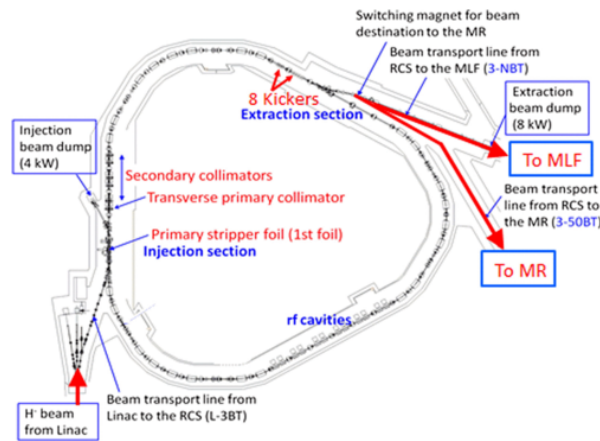
---

<sup>7</sup>A linear accelerator accelerates particles using time varying electric fields along a one direction, terminal beamline. Linear accelerators are also used in the medical field to generate X-rays.

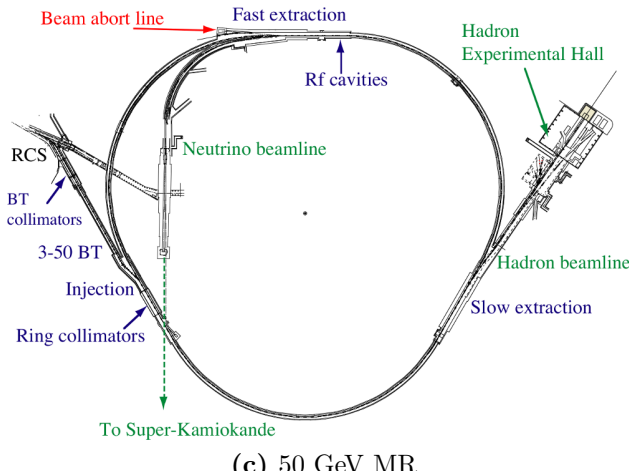
<sup>8</sup>A synchrotron is cyclic particle accelerator that relies on time varying magnetic fields to accelerate particles. Since they require many magnets and large spaces to operate, they are usually operated at national laboratories for others uses like material and life sciences.



(a) 400 MeV linac

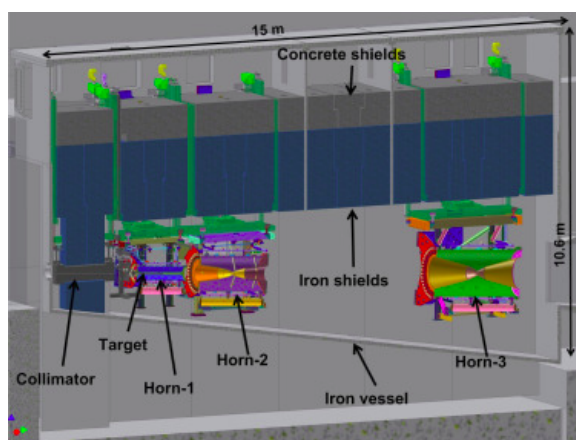
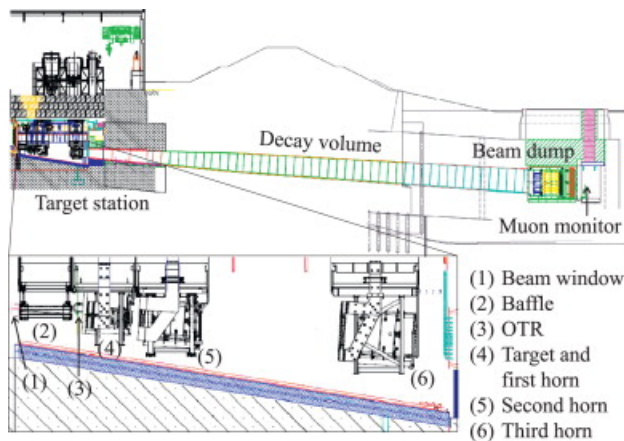
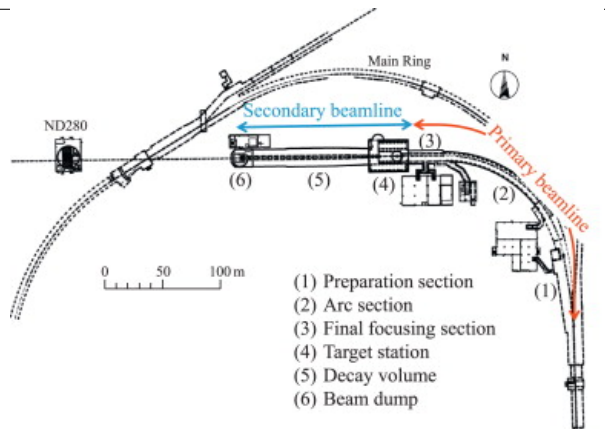


(b) 3 GeV RCS



(c) 50 GeV MR

**Figure 1.14:** Schematics of the J-PARC accelerators. (a) The linac accelerates hydrogen ions to 181 MeV of kinetic energy, designed for 400 MeV, from the ion source [76]. (b) Protons from the linac are collected into the RCS and accelerated to 3 GeV [62]. (c) Protons from the RCS are injected into the MR synchrotron. While the MR is designed for 50 GeV, it currently operates at 30 GeV.



(c) Beamlime horns

**Figure 1.15:** The neutrino beamline at J-PARC consists of a primary and secondary beamline. (a) The primary beamline redirects the protons towards the secondary beamline [1]. (b) In the secondary beamline, the protons are impinged on a cylindrical target producing mostly pions. The pions are focused using in sequence horns and decay in a long decay volume. Any non-decayed particles are stopped at the beam dump. (c) A further zoomed in cross section of the target station showing the target and focusing horns [68].



(a) A graphite target at the target station



(b) A magnetic focusing horn

**Figure 1.16:** Shown are photos of work performed on the target station. (a) The graphite rod being extracted from the target station is shown in the black-dashed box. (b) One focusing horn in T2K.

section to bend the beam towards SK. A final focusing section in the primary beamline focuses the protons into the secondary beam while directing it downwards  $3.637^\circ$  with respect to the local horizontal. Since a well-tuned and stable proton beam is necessary for neutrino production, numerous beam monitors are installed along the primary beamline to measure any losses.

The secondary beamline marks the end of the proton beam and production of a neutrino beam as shown in Figure 1.15b on page 31. It consists of a target station, a decay volume for the outgoing particles from the target station, and a beam dump for any remaining particles. The target station houses a 91.4 cm long, 2.6 cm diameter, and  $1.8 \text{ g/cm}^3$  graphite rod, which corresponds to 1.9 radiation lengths. When the protons strike the target, strong (nuclear) interactions produce  $\pi(\pi)$ -mesons (pions) and K-mesons (kaons) like those produced from cosmic ray collisions in the upper atmosphere. To enhance the flux of neutrinos, a series of three current pulsed, focusing magnets called horns<sup>9</sup> as shown in Figure 1.15c on page 31 are used to focus the mesons of the correct charge towards SK. Photographs of a graphite target and focusing horn are shown in Figure 1.16 on page 32. The horns are pulsed at

<sup>9</sup>The name horn derives from the fact that the focusing magnets are shaped like brass horns in a music ensemble or marching band. One can think of these horns like a focusing lens for charged particles.

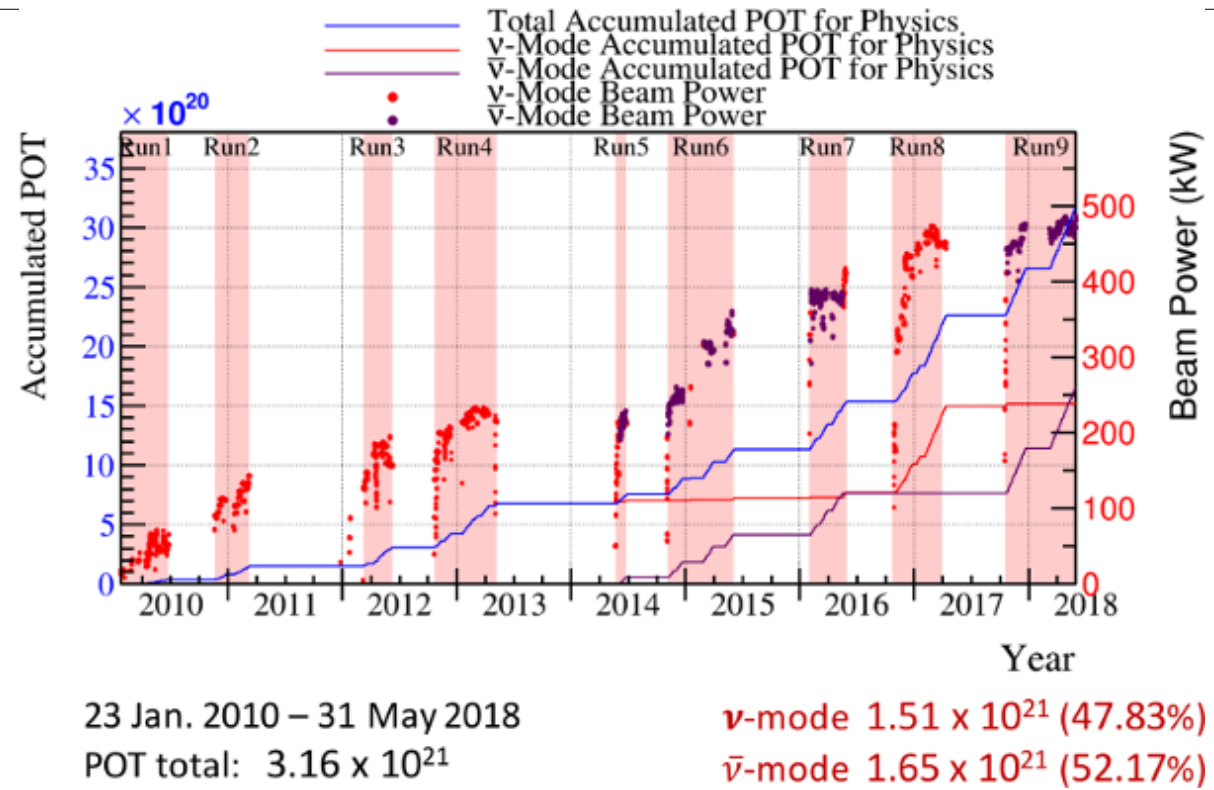


**Figure 1.17:** T2K accumulated protons on target since 2010 shows a steady increase in beam power over time.

+250 kA (-250 kA) to select positively (negatively) charged pions. The focused pions then decay in the 96 m long decay volume creating a neutrino beam boosted along the secondary beamline direction. For safety reasons, the decay volume is filled with gaseous helium at 1 atm of pressure which has a low pion absorption rate. A beam dump is placed at the end of the decay volume to stop particles like muons that have not yet decayed from contaminating the beam with their decay neutrinos.

Along both beamlines are numerous monitors and timing systems to ensure stable production of neutrinos. Proton beam monitors are placed along the primary beamline to ensure the proton beam is properly steered into the secondary beamline. An optical transition radiation monitor is situated around the target to observe any protons not intersecting with the target region itself. The last monitor along the secondary beamline is the a muon mon-

---

itor (MUMON), which is placed downstream of the beam dump to characterize the flux of daughter muons of  $> 5$  GeV/c momentum [1].

In order to provide timing information for the neutrino beam at SK, a global positioning system (GPS) is used to synchronize clocks at SK and J-PARC. Any event outside the beam timing window is rejected in the T2K oscillation analysis, and so having precise timing information for the neutrino beam is critical for the experiment. The GPS has an internal accuracy of 50 ns, or about  $\sim 150$  m assuming that the neutrinos are traveling near the speed of light. This is well within the time it takes for a neutrino to travel the 295 km between J-PARC and SK.

J-PARC continues to improve the proton delivery and neutrino flux intensity since T2K begin in 2010. T2K has run in two horn current modes:  $\nu$ -mode and  $\bar{\nu}_\mu$ -mode. Focusing positively charged pions with +250 kA horn current is called forward horn current (FHC) mode. Similarly, using -250 kA horn current is called reverse horn current (RHC) mode. The aggregate running of T2K for both FHC and RHC modes is shown in Figure 1.17 on page 33 in units of protons on target (POT).

In addition the proton beam intensity, as measured in kW (energy/proton/second), has been increased over time which increases the number of neutrino interactions observed at SK. Note that while  $\pm 250$  kA is the preferred horn current in both FHC and RHC modes, the horns were run briefly at +205 kA when operations resumed after 2011 Tōhoku earthquake.

### 1.2.2 Neutrino Near Detectors: ND280

T2K has a near detector (ND) site at J-PARC that is designed specifically to observe the neutrino beam in flight aimed at Super-K. The primary purpose of a ND site is to constrain the neutrino flux and interaction rate at SK in order to reduce the impact of their systematic uncertainties on the oscillation analysis. The analysis in this thesis uses the data collected by the off-axis ND. The site is called ND280 and is located 280m away from the production target. The primary detector is an off-axis, magnetized tracking detector

---

consisting of different subdetectors. A separate detector array called the Interactive Neutrino Grid (INGRID) measures the neutrino beam profile. Both on-axis and off-axis detectors extensively utilize a commercial light sensor called a multi-pixel photon counter (MPPC) for the light collection in the scintillator-based detectors.

The following subsections begin with a description of the MPPC technology used in T2K. Next is a description of INGRID and its purpose at ND280. This is followed by a general description primary off-axis, magnetized detector. The last two subsections are descriptions of two primary subdetectors in the off axis detector. The first and second being the pi-zero detector (PØD) and time projection chamber (TPC), respectively.

From here on, unless specified, INGRID will refer only to the on-axis ND and ND280 will refer only to off-axis ND.

## On-Axis Detector

The on-axis near detector called the Interactive Neutrino Grid (INGRID) is a tracking scintillator detector designed to directly measure the neutrino beam profile. As shown in Figure 1.18 on page 36, it is a cross grid of tracking modules centered at the designed neutrino beam center ( $\theta = 0$ ). Each module consists of alternating layers of iron plates and scintillator bars except for the two most downstream scintillating layers which lack iron plates. To monitor any beam asymmetry, two separate modules are placed off the grid axis.

Each scintillating bar consists of scintillator-doped polystyrene which emits light when a charged particle deposits energy in the media. Each bar contains a single wavelength-shifting (WLS) fiber to collect and shift the light to a different energy. The light from the fiber is then collected using a device called a multipixel photon counter (MPPC) and converted into an electrical signal. A MPPC is a compact device containing many sensitive avalanche photodiode pixels that act as Geiger micro-counters as shown in Figure 1.19 on page 37. The MPPCs are well matched with the spectral emission of the WSL fibers and operate in a strong magnetic fields, unlike traditional photomultiplier tubes. In order to enhance

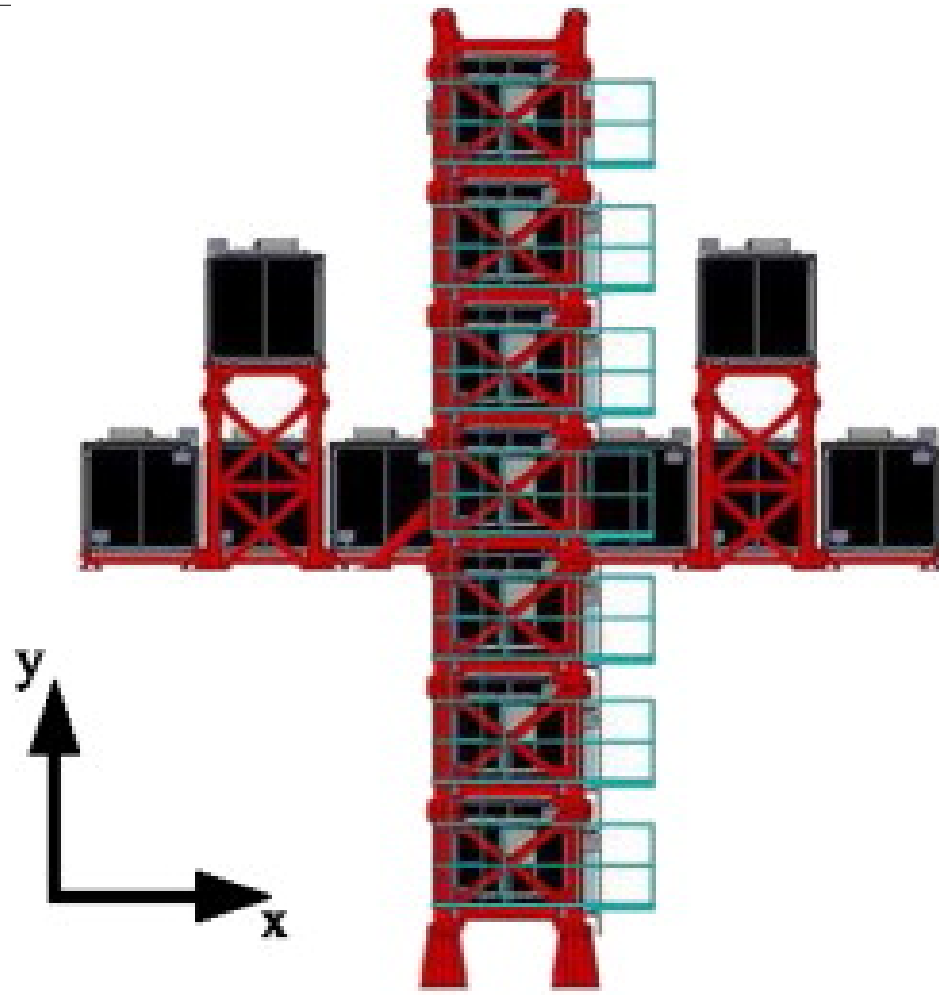


**Figure 1.18:** A schematic of INGRID shows the arrangement of the tracking scintillating modules. There are 16 identical modules total with seven in the vertical row, seven in the horizontal row, and two at off-axis positions. INGRID is capable of measuring the neutrino beam in a transverse area of  $10\text{m} \times 10\text{ m}$ . With the vertical row upstream of the horizontal row, the designed beam center intersects each row's center module [2].

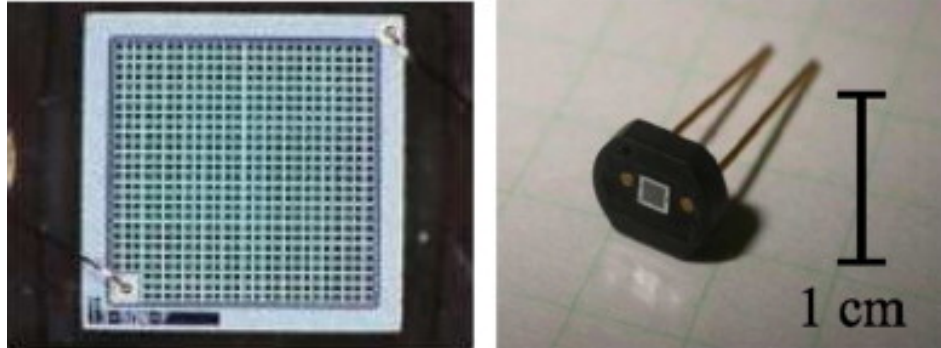


**Figure 1.19:** Photographs of the specially designed MPPC used in T2K. A magnified face view is shown on the left with an entire unit shown on the right. T2K utilizes specialized 667-pixel MPPCs with an effective area of  $1.3\text{ mm} \times 1.3\text{ mm}$  [1].

the collection efficiency, a reflective  $\text{TiO}_2$  doped polystyrene shell surrounds each bar. Bars are assembled into planes to provide tracking capabilities. Veto planes also surround each module to prevent false signals to trigger.

INGRID is continuously operated to check that the neutrino beam center was properly aligned at its designed center. Diagnostic plots such as Figure 1.20 on page 38 are collected on a monthly basis to ensure that the neutrino flux at Super-Kamiokande (SK) is consistent with T2K's design. A history of the beam profile and event rate on INGRID between January 2010 and October 2016 is shown in Figure 1.21 on page 39.

### Off-Axis Detector Summary

The near detector in T2K is ND280, which is an off-axis, magnetized tracking detector. It is a collection of different detector technologies designed to facilitate three primary measurements:

1.  $\nu_\mu$  flux at SK,
2. Irreducible  $\nu_e$  background flux at SK, and
3.  $\nu_\mu$  interaction backgrounds and cross sections for the  $\nu_\mu \rightarrow \nu_e$  search.

ND280 consists of the pi-zero detector (PØD), the tracker region consisting of a fine grain detector (FGD) and time projection chamber (TPC), an electromagnetic calorimeter (ECal),

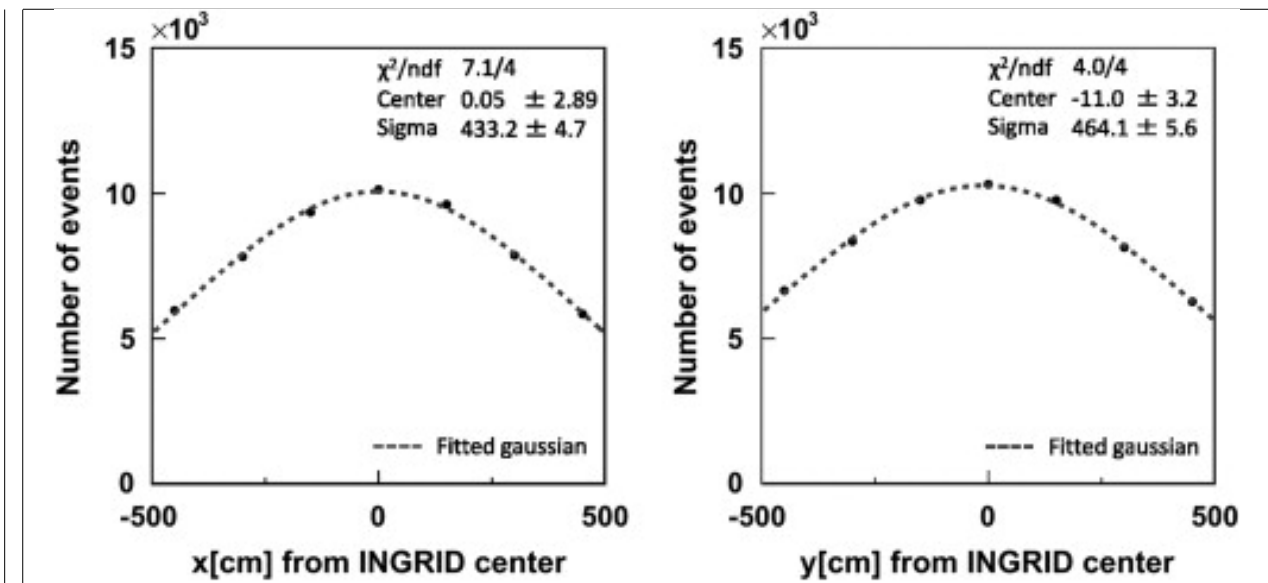


**Figure 1.20:** A beam profile taken with INGRID in April 2010 shows the Gaussian nature of the beam. The errors on the data points are about 1%. [2]

and side muon range detector (SMRD). The ND280 subdetectors are instrumented inside the recycled UA1/NOMAD magnet with the SMRD in the magnetic field return yoke itself. All but the FGD is instrumented with the same scintillating-bar bar technology collected by MPPCs. A schematic of the different detector components of ND280 is shown in Figure 1.22 on page 40.

The analysis in this thesis use measurements from the primary subdetectors, the PØD and the TPC. The PØD serves as a massive target for the incident neutrino beam and the TPC serves to measure the charge and momentum of the outgoing particles.

The ND280 magnetic field is generated using electrical current fed through solenoid coils to generate a dipole field of strength  $0.2 \text{ T}^{10}$  in the x direction. The field is highly uniform near the center of the detector which is where the majority of the TPC system is located. However, it has significant deviations from 0.2 T near the solenoid edges. In order to fully understand the field inside ND280, a precise 3D model was generated using a machine

<sup>10</sup>This is a powerful magnetic field. According to the The US/UK World Magnetic Model for 2015-2020, the magnetic field strength on the surface of the Earth is about 0.294385 Gauss or  $2.94385 \times 10^{-5} \text{ T}$ . So the field inside ND280 is about 6800 times more forceful than the Earth's influence [25].

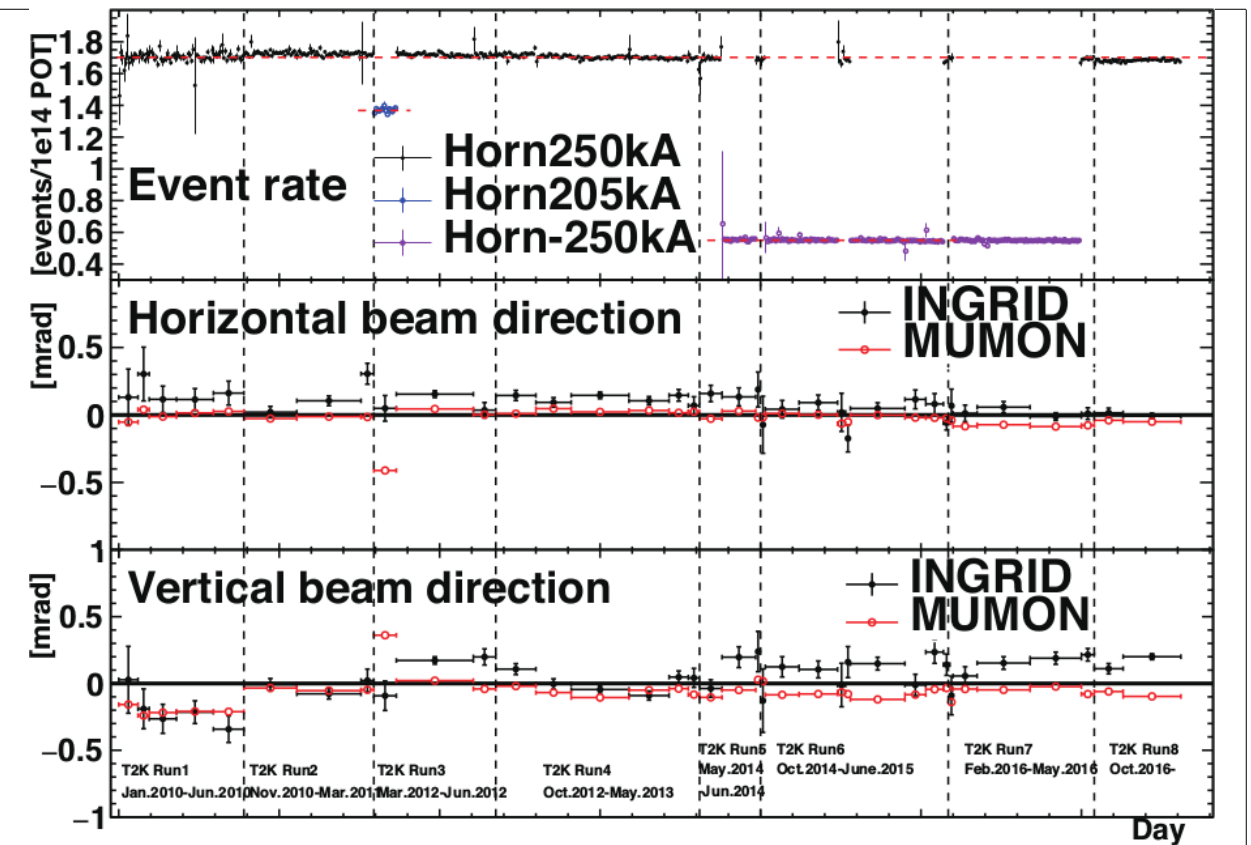


**Figure 1.21:** INGRID interaction event rate and beam profiles are shown. The top panel shows the event rate for the three different horn currents. The middle and bottom panels show the horizontal and vertical beam directions with respect to the beam center, respectively. A deviation of 1 mrad corresponds to a little under 30 cm. The error bars shown are the statistical errors on the mean.

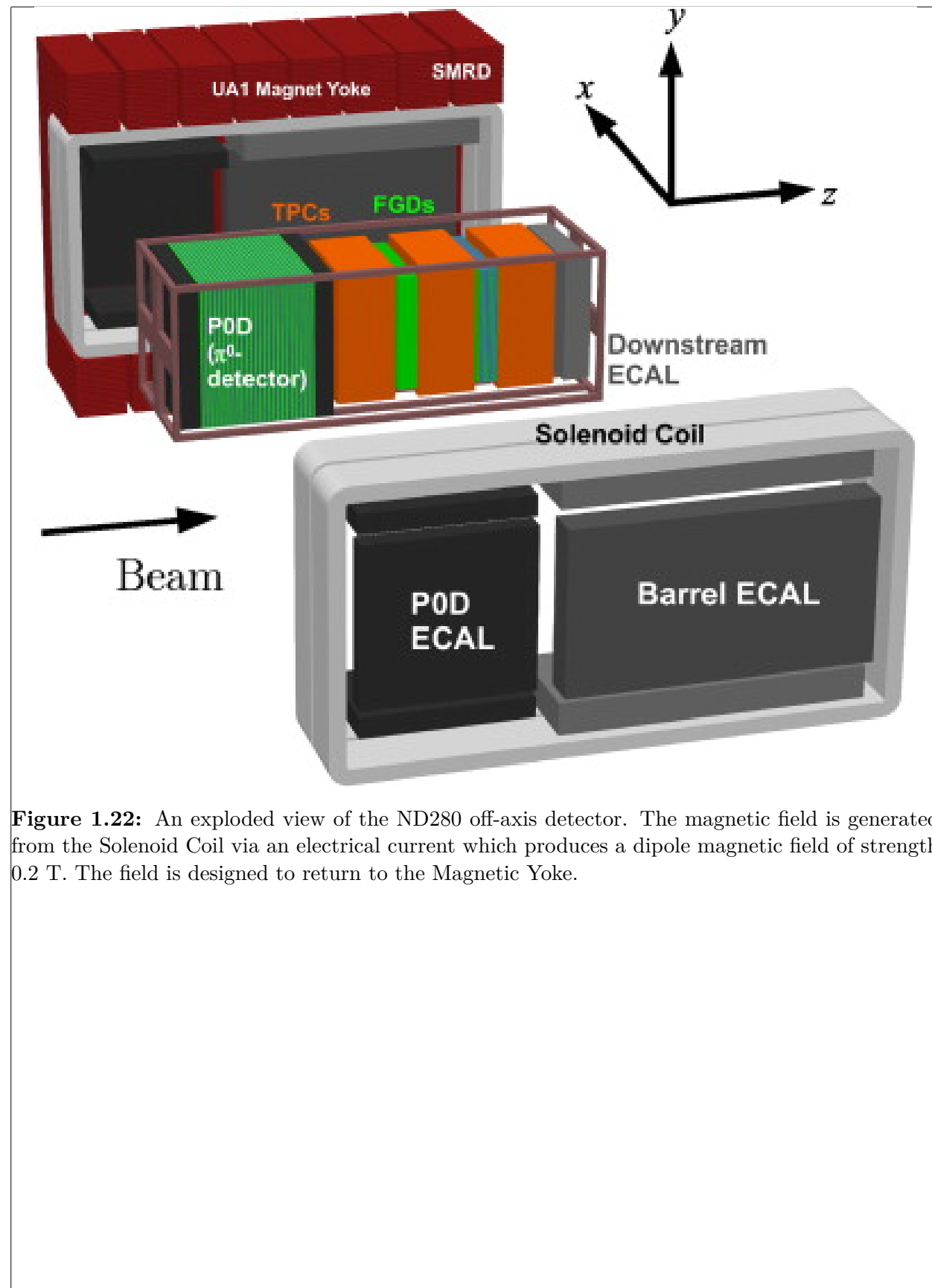


**Figure 1.22:** An exploded view of the ND280 off-axis detector. The magnetic field is generated from the Solenoid Coil via an electrical current which produces a dipole magnetic field of strength 0.2 T. The field is designed to return to the Magnetic Yoke.

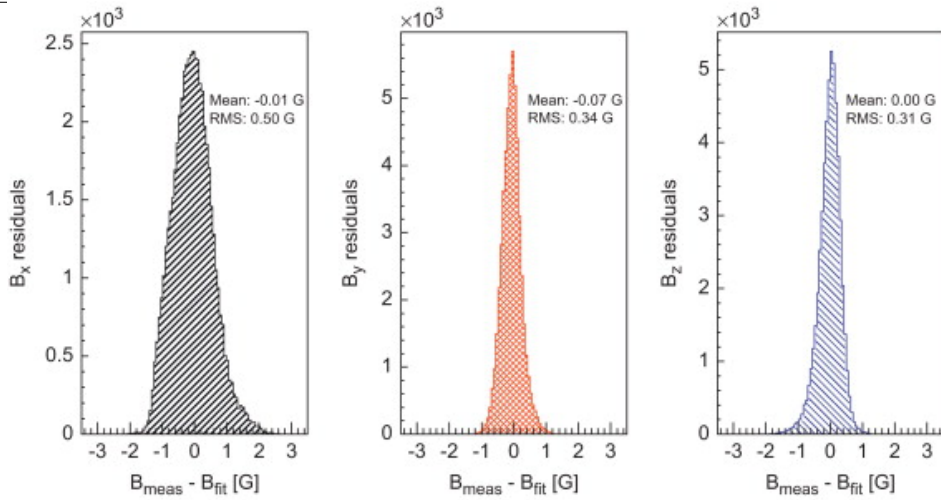


**Figure 1.23:** Each of the magnetic field components (x, y and z, respectively) are compared between a fit of the data and the actual measurements near the center of ND280. The systematic uncertainty on the field is extracted from the RMS of the mapping [1].

controlled Hall probe. The operating field strength during the mapping process was 0.07 T due to power restrictions at the time. The model was then compared with measurements in the TPC region as shown in Figure 1.23 on page 41. After scaling the model to the nominal operating strength of 0.2 T, a fractional uncertainty of  $10^{-3}$  or uncertainty of 2 Gauss in each direction was obtained.

The ND280 magnetic field permits the measurements of particle charge and momentum. A particle of charge  $q$ , rest mass  $m_0$ , and velocity  $\mathbf{v}$  under the influence of an external electric and magnetic fields,  $\mathbf{E}$  and  $\mathbf{B}$ , respectively, experiences a force  $\mathbf{F}$  given by the Lorentz force equation

$$\mathbf{F} = q(\mathbf{E} + \mathbf{v} \times \mathbf{B}). \quad (1.49)$$

Assuming for now that there is no external electric field, the force on the particle is

$$\mathbf{F} = q\mathbf{v} \times \mathbf{B}, \quad (1.50)$$

which is both orthogonal to  $\mathbf{v}$  and  $\mathbf{B}$ . Since the mechanical work on a particle in a magnetic field is zero, the particle's energy is unchanged ( $|\mathbf{v}| = v = \text{constant}$ ). Newton's Second Law

---

allows us to rewrite the force as an change in momentum  $\mathbf{P}$

$$\begin{aligned}
 \mathbf{F} &= \frac{d\mathbf{P}}{dt} \\
 &= \frac{d}{dt} (\gamma(v)m_0\mathbf{v}) \\
 &= m_0\mathbf{v} \left( \frac{d\gamma(v)}{dt} \right) + \gamma(v)m_0 \left( \frac{d\mathbf{v}}{dt} \right) \\
 &= m_0\mathbf{v} \left( \frac{d\gamma(v)}{dv} \right) \cancel{\left( \frac{dv}{dt} \right)}^0 + \gamma(v)m_0\mathbf{a} \\
 &= \gamma(v)m_0\mathbf{a},
 \end{aligned} \tag{1.51}$$

where  $\mathbf{P} = \gamma(v)m_0\mathbf{v}$  is the relativistic momentum and  $\gamma(v) = (1 - (v/c)^2)^{-1/2}$  is the Lorentz factor for relativistic particles. For uniform circular motion, the magnitude of the acceleration is given by

$$|\mathbf{a}| = v^2/R, \tag{1.52}$$

where  $R$  is the radius of curvature for the circle. Combining ( 1.52) and ( 1.51) with some algebra yields

$$R = \frac{\gamma(v)m_0v}{q|\mathbf{B}|\sin\theta_{\mathbf{vB}}}, \tag{1.53}$$

where  $\theta_{\mathbf{vB}}$  is the angle between  $\mathbf{v}$  and  $\mathbf{B}$ . The numerator of ( 1.53) is recognized as the magnitude of the momentum  $|\mathbf{P}|$ . Some further rearrangement yields

$$|\mathbf{P}| = q|\mathbf{B}|R\sin\theta_{\mathbf{vB}}, \tag{1.54}$$

and thus measuring the direction and radius of curvature inside the field provides the charge and momentum, respectively, as desired.

### Off Axis pi-zero detector (PØD)

The PØD is the primary detector used as the neutrino target in this thesis. It is a plastic scintillator based tracking calorimeter inside the ND280 magnet region. It was designed to

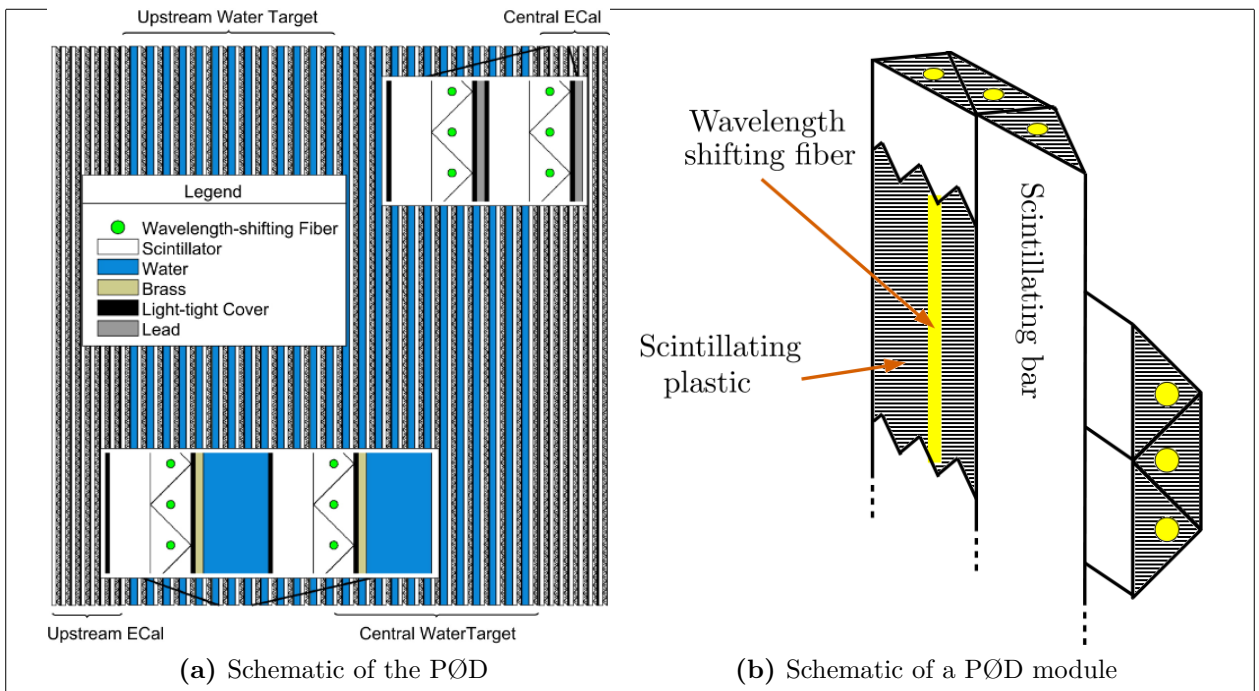


**Figure 1.24:** Schematics of the PØD. Left: insets detail the Water Target and ECal layers. Right: A view of a PØD module illustrating the orthogonal layout of the scintillating planes. Both: the neutrino beam is coming from the left.

measure the neutral current (NC) process  $\nu_\mu + N \rightarrow \nu_\mu + N + \pi^0 + X$  on water where  $N$  is a nucleus and  $X$  is any set of final state particles. The NC  $\pi^0$  process was expected to be a significant background in the  $\nu_e$  appearance search in the likelihood that  $\theta_{13} \approx 0$ . The PØD is a modifiable detector which can be filled or drained of water during data taking, enabling the determination of water target (WT) cross sections by comparing water-in data with water-out data.

A representation of the PØD is shown in Figure 1.24 on page 43. The active detector components are very similar to INGRID's design where scintillation light is captured by a WSF and counted by a MPPC. Each bar is triangular in shape as shown in Figure 1.25 on page 44. A plane of 134 horizontal and 129 vertical bars together to form a PØD module (PØDule) as shown in 1.24b. The PØD dimensions are  $2.298 \times 2.468 \times 2.350\text{m}^3$ , in XYZ respectively, with a fiducial mass of  $\sim 1900$  kg for water and 3570 kg for other materials. The total mass of the PØD is approximately 15,800 kg when the bags are full of water. PØDules

Element	Symbol	Fraction [%]
Carbon	C	45.0
Oxygen	O	29.9
Copper	Cu	14.3
Hydrogen	H	8.0
Zinc	Zn	1.6
Chlorine	Cl	1.1
Titanium	Ti	0.1

**Table 1.3:** Elemental composition of PØD water target region. The table is sorted from top to bottom by fraction of mass. This table was originally produced in Reference [6]

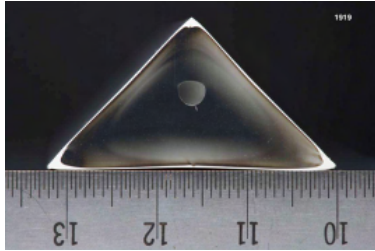


**Figure 1.25:** A cross section of a PØD scintillating bar. The base and height is 33 mm long and 17 mm high. The wavelength shifting fiber is inserted in the bored hole which is half-way between the base and tip.

are arranged into three primary regions. The water target (WT) region contains 26 PØDules interleaved between bags of water 2.8 cm thick when filled and 1.3 mm thick brass sheets designed to help contain  $\pi^0$  decay photons. The last two regions are the upstream ECal (USECal) central ECal (CECal). Each ECal region contains 7 PØDules with steel sheets clad with lead between them [6]. An elemental composition of the WT is shown in Table 1.3 on page 44.

The readout electronics for the PØD is based on the Trip-T application specific integrated circuit (ASIC) shared among the SMRD, ECals, and INGRID. Signals from 64 MPPCs are routed to Trip-T front end boards (TFB) that each house 4 Trip-T ASICs. Each Trip-T collects the MPPC charge in 23 programmable integration cycles.

The TFB are readout to back-end electronics which control the TFBs and synchronize clocks. A total of six readout merger module (RMM) electronics receive TFB the data and control each TFB ASIC. RMM timing are synchronized with a cosmic trigger module and

---

a slave clock module (SCM), of which both are synchronized with a master clock module from the beamline. Synchronizing the RMMs with the SCM allows for the Trip-T ASIC integration windows to match with the beam. The RMMs are responsible for distributing the TFB data to the data acquisition (DAQ) system for storage.

The ND280 DAQ consists of a MIDAS framework to monitor and control data collection. The primary client of the DAQ is to merge data and package it for long term storage. In parallel to it is the Global Slow Control (GSC) system which measures temperatures, voltages, and other physical quantities. Together the DAQ and GSC help scientists consistently produce high quality data and maintain the overall stability of the detector.

### **Off Axis Time Projection Chamber (TPC)**

The ND280 TPC is designed to provide momenta measurements of charged particle tracks as discussed above, high resolution particle counting capabilities, and particle identification based on energy deposition. The latter most aspect is not utilized in this thesis. The TPC is divided into three volumes separated by the two FGD volumes. Each TPC volume ( $2.3 \times 2.4 \times 1.0 \text{ m}^3$ ) consists of an inner box that holds an argon-based gas and an outer box that holds an insulating CO<sub>2</sub> gas. The inner gas mixture is 3000 L of Ar:CF<sub>4</sub>:iC<sub>4</sub>H<sub>10</sub> (95:3:2) gas. It was selected for its high speed, low diffusion, and good performance with the micromegas [1]. A simplified schematic of the TPC is shown in Figure 1.26 on page 46.

As charged particles traverse the inner TPC volume, they create ionization electrons in the gas which drift towards readout planes away from a central cathode. The electron drift acceleration is rapid due to the strong 5 kV/cm electric field present. Drift electrons are multiplied and sampled by micromega detectors that line the sides of the TPC, providing nearly 3 m<sup>2</sup> of active surface coverage. Arrival times of the electrons provide timing information to give a full three dimensional portrait of the events.

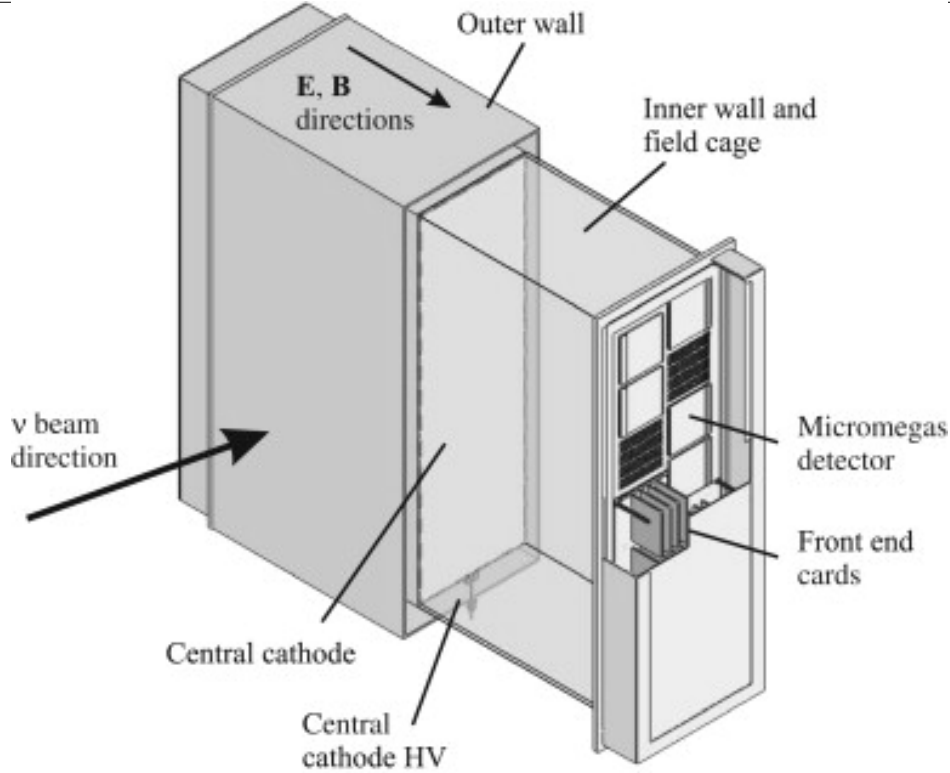


**Figure 1.26:** Cut-away drawing of a TPC volume in ND280 [1].

### Track Reconstruction in ND280

The goal of track reconstruction software is to capture the shape and history of energy deposited in the detector. Since ND280 is collection of different technologies, highly specific algorithms and models are used to identify track-like patterns. Since this analysis uses neutrino events incident in the PØD and cross into the TPC, an unified and coherent reconstruction model is needed. A reconstruction package called “Global” is designed to combine all ND280 information for this purpose. The Global reconstruction will be revisited in Chapter 3.

### 1.2.3 Neutrino Far Detector: Super-Kamiokande

The Super-Kamioka neutrino detection experiment (Super-Kamiokande) is the dedicated far detector for the T2K experiment. Positioned at 295 km away from the neutrino source with a 1 km overburden, it is well designed to detect the elusive neutrino. Containing about

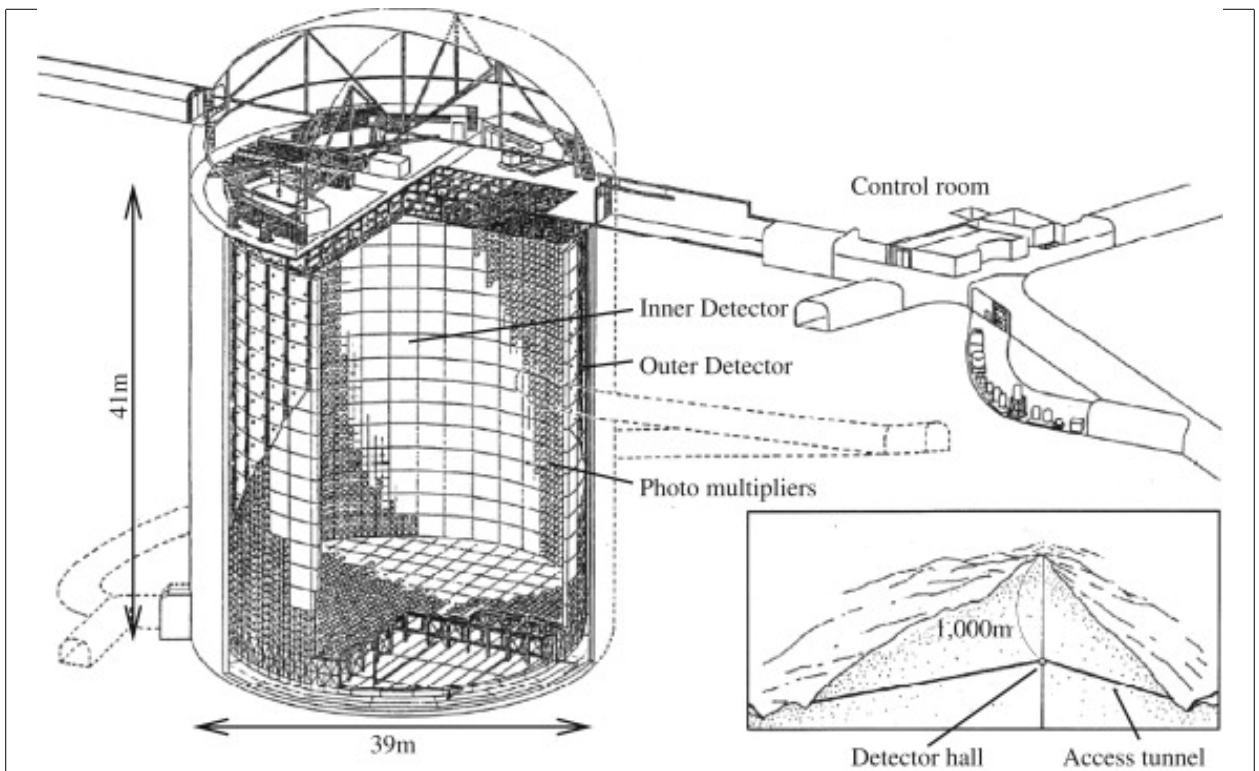


**Figure 1.27:** Diagram of the Super-Kamiokande detector consisting mainly of the inner and outer detector segments. The boundary between the two segments is cylindrical scaffolding used to mount photomultiplier tubes and optically isolate the segments.

50 kt of pure water, is it lined with PMTs in both an inner and veto outer detector as shown in Figure 1.27 on page 47.

When charged particles travel through the water, a Cherenkov radiation cone is produced. The sharpness of the cone edge is an unique ID for the particle species that produced it. An electron produces a fuzzy edge since it experiences many large multiple scatterings off the water molecules. A muon on the other hand produces a sharp edge since it is much more massive and thus less perturbed by the water molecules. Both types of events are shown in Figure 1.28 on page 48. By determining the particle that produced it and isolating the event during the T2K beam, the neutrino flavor is deduced.

While events from SK are not used in this analysis, the goal is to try to improve T2K's parameters which depend on comparing the Near Detector neutrino measurements to the

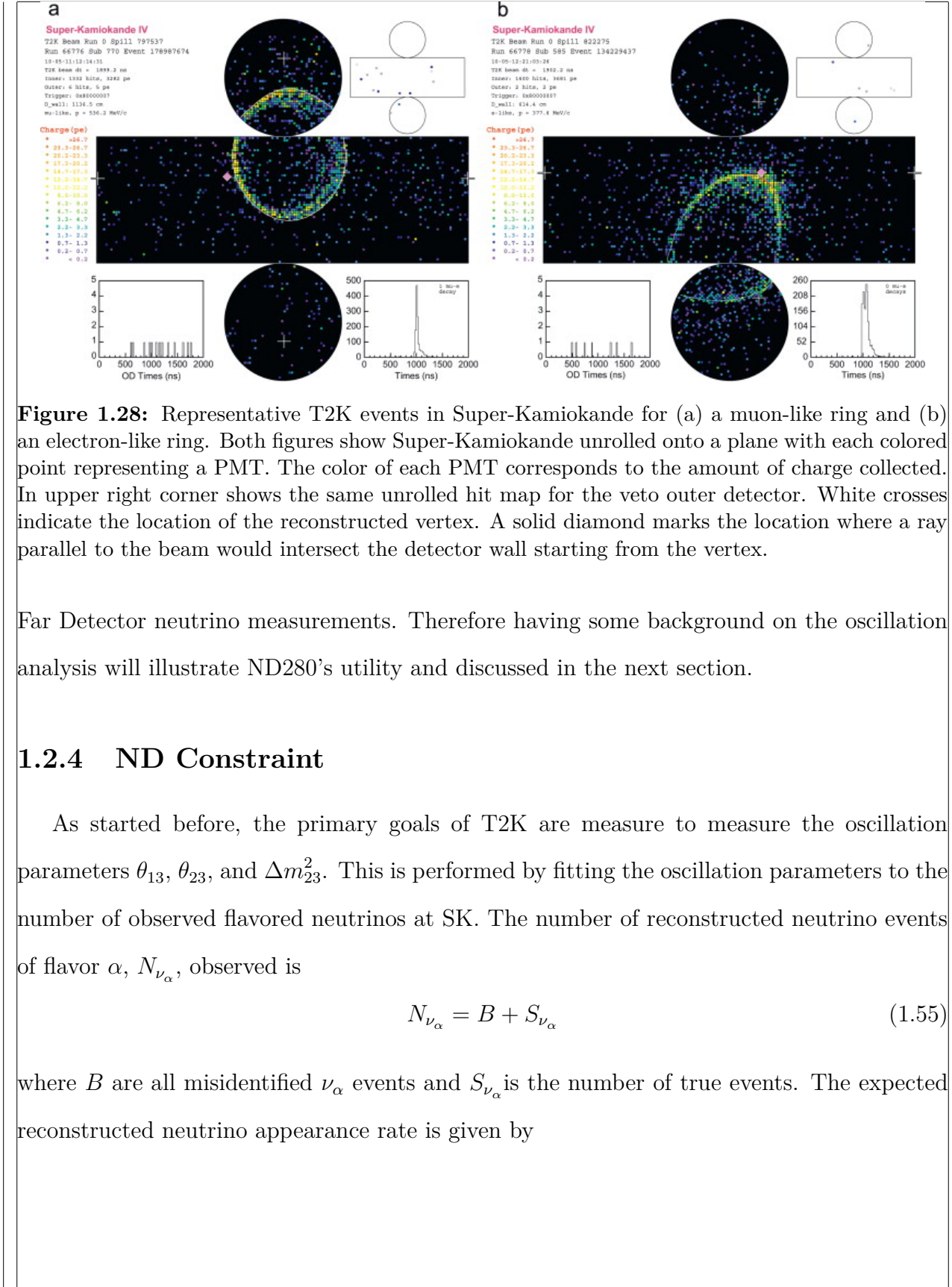


**Figure 1.28:** Representative T2K events in Super-Kamiokande for (a) a muon-like ring and (b) an electron-like ring. Both figures show Super-Kamiokande unrolled onto a plane with each colored point representing a PMT. The color of each PMT corresponds to the amount of charge collected. In upper right corner shows the same unrolled hit map for the veto outer detector. White crosses indicate the location of the reconstructed vertex. A solid diamond marks the location where a ray parallel to the beam would intersect the detector wall starting from the vertex.

Far Detector neutrino measurements. Therefore having some background on the oscillation analysis will illustrate ND280's utility and discussed in the next section.

### 1.2.4 ND Constraint

As started before, the primary goals of T2K are measure to measure the oscillation parameters  $\theta_{13}$ ,  $\theta_{23}$ , and  $\Delta m_{23}^2$ . This is performed by fitting the oscillation parameters to the number of observed flavored neutrinos at SK. The number of reconstructed neutrino events of flavor  $\alpha$ ,  $N_{\nu_\alpha}$ , observed is

$$N_{\nu_\alpha} = B + S_{\nu_\alpha} \quad (1.55)$$

where  $B$  are all misidentified  $\nu_\alpha$  events and  $S_{\nu_\alpha}$  is the number of true events. The expected reconstructed neutrino appearance rate is given by

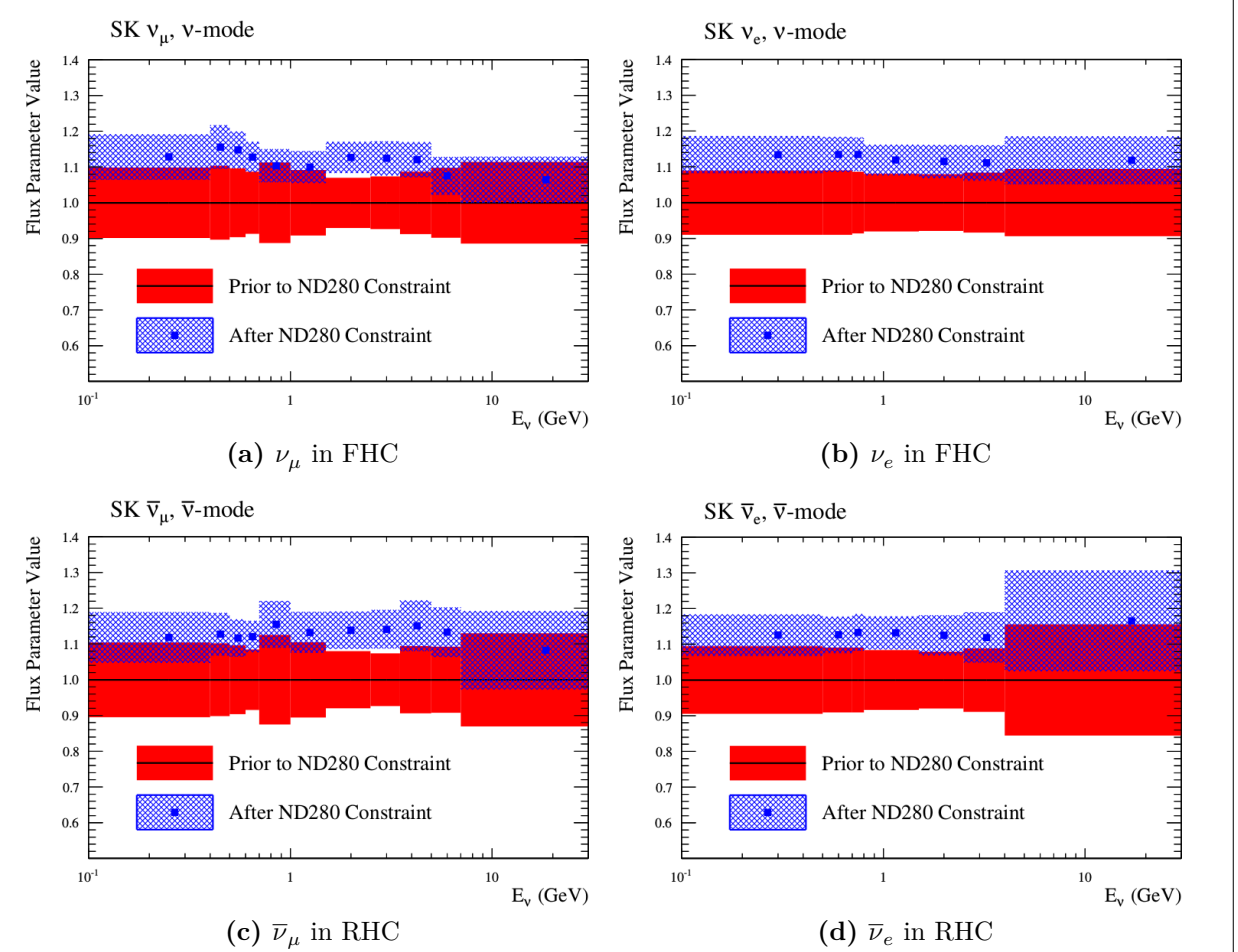


**Figure 1.29:** Predicted and best fit measurements for the SK flux. The horizontal axes are the neutrino energy and the vertical axes are the fractional change in the flux normalization. These figures were taken from the 2017 T2K oscillation analysis [4]. A value 1.1 corresponds to a 10% increase in the number of predicted events.

$$S_{\nu_\alpha} = \sum_{\lambda=e,\mu} \left[ \mathcal{P}_{\nu_\lambda \rightarrow \nu_\alpha} (E_\nu; \vec{\sigma}) \right] \times \sum_t \left[ \sigma_{\nu_\alpha}^t (E_\nu) \cdot t_N \right] \\ \times \Phi_{\nu_\alpha} (E_\nu) \times \epsilon(p_\alpha, \theta_\alpha), \quad (1.56)$$

where  $\vec{\sigma}$  is a vector of the oscillation parameters from (1.38),  $\sigma_{\nu_\alpha}^t$  is the cross section for  $\nu_\alpha$  on target  $t$ ,  $t_N$  is the number of targets of type  $t$ ,  $\Phi_{\nu_\alpha}$  is the flux of neutrinos, and  $\epsilon(p_\alpha, \cos \theta_\alpha)$  is the efficiency of reconstructing and correctly categorizing the event as a function of momentum  $p$  and angle  $\theta$ .

*Having a large, sensitive off-axis ND like ND280 provides critical constraints to the neutrino flux in the oscillation analysis.* This includes the oscillation channel  $\nu_\mu \rightarrow \nu_e$ , but also

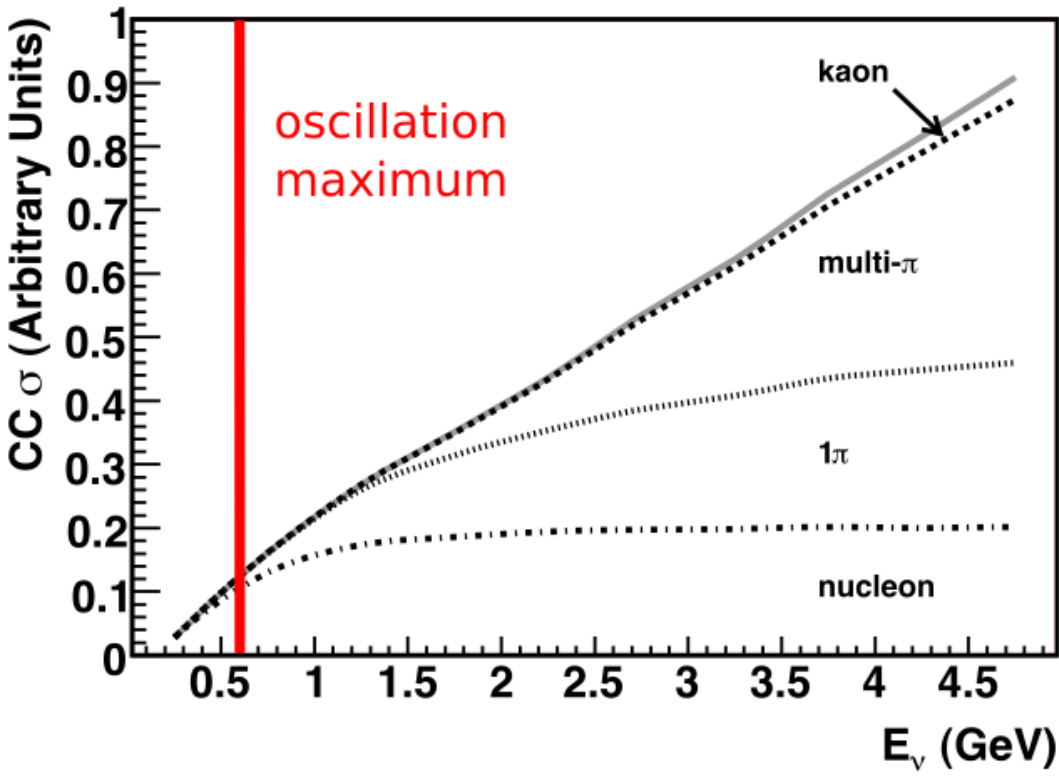


**Figure 1.30:** Predicted CC inclusive scattering cross section at T2K relevant energies. Only the most common final state modes are shown. A thick, red line indicates the T2K  $\nu_e$  appearance probability maximum. For CCQE-like interactions, they usually include the emission of one or more nucleons. Resonance states and DIS interactions produce  $1\pi$ ,  $N\pi$  (multi- $\pi$ ) and kaon final states as well. Combined, the inclusive cross section increases linearly with energy. This image was edited and originally produced by Formaggio and Zeller [34].

the intrinsic  $(\bar{\nu}_e)$  background in the T2K beam. These neutrinos interact the same way an oscillated neutrino would at SK. Without ND280, the fractional uncertainty on the flux rate is about  $\sim 10\%$  per energy bin. These constraints are obtained from MUMON discussed above and the NA61/SHINE experiment [10]. Adding the ND constraint reduces the uncertainty to about  $\sim 5\%$  as seen in fig. 1.29 on the preceding page.

T2K uses the NEUT<sup>11</sup> [45] program library to simulate neutrino interactions with nucleons and the nucleus. It was originally designed to simulate atmospheric neutrinos for the Kamioka Nucleon Decay Experiment (Kamiokande). Included in NEUT are numerous

<sup>11</sup>NEUT is neither an initialism nor acronym

---

models for neutrino interactions on matter and intra-medium hadron transport within the nucleus.

*Using the ND280 constraint can tune the NEUT cross section model to best match the T2K data.* The canonical T2K cross section model in NEUT is problematic due to depending on older neutrino-nuclear scattering models developed for low-Z nuclear targets like deuterium. The models implemented in NEUT, while being well studied in previous neutrino-nuclear Physics experiments, are known as effective models in T2K. In particular, large disparities exist in recent, high statistics CCQE measurements [34] which is forcing T2K to explore other and new Nuclear Physics models in this analysis.

### 1.2.5 Contributions to the T2K Experiment

Since joining the T2K experiment five years ago, I have played a critical role in analysis that is currently in preparation for publication. This analysis was a second generation measurement of the  $\nu_\mu$  CC single pion production cross section on water in the PØD. I am a co-author of that paper and its internal T2K technical document that outlines the analysis procedure and studies. In particular, I developed the momentum calibration and event selection using machine learning. Further details on these two contributions are found in Appendix ??.

Outside of analysis work, the majority of my contributions to the experiment include on-site PØD and ND280 expertise. I was involved in the 2015 work to replace two PØD water bags when they showed evidence of leaking. Additionally, I helped measure the PØD water mass and its “bulging” due to the water. During data taking periods, I signed up at least once a year to perform shifts. I am certified as a TTD expert, PØD water system and calibration expert, and experienced DAQ shifter. As TTD and PØD expert, this included daily reporting and point of contact for the SMRD, ECals, and PØD along with the PØD water target system whenever problems arose. My most recent contribution was participating in the 2018 Super-K open tank work at the Kamioka Observatory. That work included

---

removing any found oxidation, diesel fumes from the initial construction, and glass shards remaining after a significant multi-PMT implosion in 2001. When not cleaning, the other important task was to install light-tight Tyvek sheets to insulate the inner detector.

### 1.3 Summary

The neutrino is an elusive particle to detect. The relatively new neutrino oscillation phenomenon has opened up the possibility of exploring fundamental questions of the Universe like CP violation. In the T2K experiment, some of the uncertainties associated with neutrino oscillations are being explored. To facilitate these goals, constraining all forms of uncertainty in neutrino-nuclear interactions and flux help improve its sensitivity to the oscillation predictions.

The next chapters in this thesis are presented in the following order. First is the ND280 constraint on the flux and cross section models using the BANFF maximum likelihood fit. Next is the description of the analysis samples that are used in the BANFF fit. With the samples defined, the parameterization of the fit bins and penalty terms are defined for this analysis. This is followed by the validation of the BANFF fit in a few scenarios. Then the BANFF postfit results will be analyzed in relation to previous analyses. The final chapter is a discussion of the results and prospects for the future.

---

# Chapter 2

## BANFF Likelihood

The BANFF likelihood maximization procedure is a binned likelihood maximization fitting of the ND280 data. This fit is done separately from the fitting the Super-Kamiokande (SK) data for the oscillation analysis. In a joint fit, the measurements from both detectors are considered along with their respective nuisance parameters. This joint-fit approach is more computationally expensive since the time to perform a fit increases non-linearly with increasing the number of fit parameters. However it is developed in an alternate method called the Markov Chain Monte Carlo analysis (MaCh3) and this will not be explained here. The BANFF likelihood maximization, hitherto referred to as the “BANFF-fit”, includes nuisance parameters that affect the measurement of the oscillation parameters, but are not physics goals of the T2K experiment. The BANFF-fit parameters and their respective covariances are then used as inputs in the oscillation analysis. This “divide-and-conquer” approach allows for more rapidly completed studies on the effects of model parameters and biases present. Also this approach should provide the same result with a joint ND280 and SK analysis as is performed in MaCh3. However, information encoded in the ND280 measurements for shared nuisance parameters like the neutrino flux is inevitably lost in the BANFF-fit.

The modern BANFF-fit likelihood is described in detail in detail in [Insert PRD instead](#)TN-220 [42]. It uses a frequentist approach to find the best nuisance parameter set to maximize a

---

binned likelihood. Subsequent updates to the BANFF-fit have increased the sample sizes and systematic parameterizations.

### 2.0.1 Introduction to Conditional PDFs and Likelihoods

Curve fitting is commonly found in the particle physics community literature due to the need to compare two models or constrain unknown model parameters using one or more histograms. For the first case, this involves two competing hypotheses or models,  $H_0$  and  $H_1$ , in order to establish if the data supports new Physics ( $H_1$ ) not predicted in the Standard Model ( $H_0$ ). The second case finds the “best” set of the model predictions,  $\theta$ , that match the data as is the case for the BANFF-fit. In both cases, chi-squared tests are performed to provide goodness of fit, parameter estimation (also referred to as “best fit parameters”), and error/confidence estimation.

Consider the problem of extracting physics parameters  $\vec{y}$  given some data vector  $\vec{N}$ . The conditional probability density function (PDF)  $\mathcal{P}$  to measure these parameters is given as

$$\mathcal{P}(\vec{y}|\vec{N}) = \frac{\mathcal{L}(\vec{N}|\vec{y})\mathcal{P}(\vec{y})}{\int \mathcal{L}(\vec{N}|\vec{x})\mathcal{P}(\vec{x})d\vec{x}}, \quad (2.1)$$

where anything right of a vertical line represents a condition on the probability.  $\mathcal{L}(\vec{N}|\vec{y})$  is the likelihood of the model with parameters  $\vec{y}$ ,  $\mathcal{P}(\vec{y})$  is the probability for the model, and the denominator is the normalization over all possible constraints on the observations. A frequentist interpretation of a PDF is a proportion of outcomes of repeated trials or experiments. A likelihood function is an expression of the probability of observing data as a function of the model parameters in their appropriate ranges.

One arrives at ( 2.1) by using the definition of compound probabilities

$$\mathcal{P}(A, B) = \mathcal{P}(B|A)\mathcal{P}(A) \quad (2.2)$$

to evaluate  $\mathcal{P}(\vec{y}|\vec{N})$  as

$$\mathcal{P}\left(\underbrace{\vec{y}}_B \middle| \underbrace{\vec{N}}_A\right) = \frac{\mathcal{P}(\vec{N}, \vec{y})}{\mathcal{P}(\vec{N})} \quad (2.3)$$

with the denominator here is recognized as the normalization of the PDF. The compound PDF  $\mathcal{P}(\vec{N}, \vec{y})$  can expanded using Bayes' theorem which states

$$\mathcal{P}(A|B)\mathcal{P}(B) = \mathcal{P}(B|A)\mathcal{P}(A), \quad (2.4)$$

and combined with ( 2.2) yielding

$$\mathcal{P}\left(\underbrace{\vec{N}}_A, \underbrace{\vec{y}}_B\right) = \mathcal{P}(\vec{N}|\vec{y}) \times \mathcal{P}(\vec{y}), \quad (2.5)$$

where the PDFs to the left and right of the  $\times$  operator are recognized as the likelihoods and priors, respectively. Combining resulting in ( 2.3) and ( 2.5) reproduces the original expression of ( 2.1).

## 2.1 BANFF Fit Test Statistic

For the BANFF fit, one considers the problem of trying to maximize the agreement between measured and predicted data histograms. This is equivalent to maximizing a binned likelihood function  $\mathcal{L}$  of the data given a set of parameters in the likelihood function  $\mathcal{L}$  that predict the measured rate. The use of likelihood functions in fits to histogram is explained further in reference [16] and the PDG review on Statistics. By invoking Wilks' theorem, also known as the likelihood ratio theorem, the likelihood maximization procedure is converted into a minimization problem involving a test statistic denoted as a chi-squared. Below is an explanation of the BANFF test statistic,  $\Delta\chi^2$ , and its systematic model terms.

Consider many binned samples that select different charged current topologies. A convenient choice of observables for all the samples are the outgoing charged lepton  $l$  momentum

---

$P_l$  and angle  $\cos \theta_l$  as measured in ND280. Much of this is also documented in TN-220 [42] where additional details can be found. For each  $(P_l, \cos \theta_l)$  analysis bin  $i = 1, 2, \dots, M-1, M$ , the likelihood is given by

$$\mathcal{L}(\vec{N}^d | \vec{N}^p) = \left( \prod_{i=1}^M \left( \vec{N}_i^p \right)^{\vec{N}_i^d} \frac{e^{-\vec{N}_i^p}}{\vec{N}_i^p!} \right) \quad (2.6)$$

where  $\vec{N}_i^d$  is the number of observed data events in the  $i$ th bin and  $\vec{N}_i^p$  is the number of predicted events as a function of nuisance parameters in the  $i$ th bin. One recognizes the likelihood function in ( 2.6) as a product of Poisson distributions, since this is counting data measured in  $M$  analysis bins. The sets of dependent nuisance parameters, also sometimes called systematics, that affect the predicted event rate are

- cross section physics models, labeled as “xsec”,
- neutrino flux,
- detector biases and inefficiencies.

Given these three sets of systematics, the number of predicted CC events from any neutrino flavor  $\nu_l$  at ND280 is calculated using the general formula

$$N_{\nu_l} = \underbrace{\Phi_{\nu_l}}_{\text{Flux per area}} \left[ \sum_t \underbrace{\left( \sigma_{\nu_l}^t M^t \right)}_{\text{Effective area}} \right] \underbrace{\epsilon_{\nu_l}}_{\text{Efficiency}} , \quad (2.7)$$

where  $\Phi_{\nu_l}$  is the flux of  $l$  flavor neutrinos,  $\sigma_{\nu_l}^t$  is the cross section of the interaction for neutrino flavor  $l$  on target  $t$ ,  $M^t$  is the number of  $t$  targets, and  $\epsilon_{\nu_l}$  is the total efficiency to reconstruct and properly identify the event as  $\nu_l$ CC interactions. Since the cross section is a measure of interaction probability in units of area, multiplication of  $M_t$  represents the effective cross sectional area of material  $t$  in the detector. Each term in ( 2.7) is modeled carefully and the efficiency term is estimated using Monte Carlo (MC) simulations and control samples. The number of events in a given analysis bin is varied in the BANFF using flux, cross section,

---

detector efficiency weight functions. In the  $i$ th analysis bin, the number of events in that bin,  $N_i$ , is given by

$$N_i(\vec{b}, \vec{x}, \vec{d}) = w_i^{\text{POT}} (\vec{d})_i^{\text{Det}} \sum_{j=1}^{N_i^{\text{MC}}} \left[ \sum_{k=1}^{N^{\text{Flux}}} \left( \delta_{j,k}^{\text{Flux}} (\vec{b})_k^{\text{Flux}} \right) \prod_{l=1}^{N^{\text{xSyst}}} w_{j,l}((\vec{x})_l^{\text{xsec}}) \right]. \quad (2.8)$$

Here  $w_i^{\text{POT}}$  is the protons on target (POT) weight for analysis bin  $i$  which normalizes the MC statistics to expected data statistics. To account for the detector inefficiencies, the  $(\vec{d})_i^{\text{Det}}$  parameters are normalization parameters that vary the total number of predicted events in the  $i$ th bin. Each  $(\vec{d})_i^{\text{Det}}$  is determined prior to the fit by surveying over a large number of toy experiments with the detector systematics varied in each. The sum over  $j = 1, 2, \dots, N_i^{\text{MC}} - 1, N_i^{\text{MC}}$  considers the contribution of all MC events in the  $i$ th analysis bin. The  $(\vec{b})_k^{\text{Flux}}$  parameters, out of a total of  $N^{\text{Flux}}$ , are flux normalization systematics for each flux bin. Since the flux bins are categorized not only by neutrino energy, but also by flavor and horn current, the  $\delta_{j,k}^{\text{Flux}}$  term in the sum over  $k$  selects the correct flux bin. The parameters  $w_{j,l}$  are pre-calculated weights as a function for the  $l$ th cross section model,  $(\vec{x})_l^{\text{xsec}}$ , with a total of  $N^{\text{xSyst}}$  cross section model terms. Different  $t$  target materials have separate cross section parameters. Also the number of targets  $M_t$  can vary via detector systematics.

Using the likelihood ratio test theorem, a test statistic is defined as taking -2 times the natural logarithm of the ratio of predicted to observed likelihoods

$$\begin{aligned} \Delta\chi_{\text{LLR}}^2 &= -2 \log \frac{\mathcal{L}(\vec{N}^d | \vec{N}^p)}{\mathcal{L}(\vec{N}^d | \vec{N}^d)} \\ &= 2 \sum_{i=1}^M \left[ \vec{N}_i^p - \vec{N}_i^d + \vec{N}_i^d \log \left( \frac{\vec{N}_i^d}{\vec{N}_i^p} \right) \right] \end{aligned} \quad (2.9)$$

where this test statistic  $\Delta\chi_{\text{LLR}}^2$  obeys a true chi-squared distribution for asymptotically large statistics and the likelihood functions are of the form ( 2.6). The denominator in ( 2.9) is the MC predicted probability which assumes the best maximum likelihood estimate is the number

of observed events. Penalty terms from the cross section, flux, and detector systematics are included in order to force the results to be consistent with systematic uncertainties. The new test statistic for all of ND280,  $\Delta\chi^2_{\text{ND280}}$ , is given by

$$\begin{aligned}\Delta\chi^2_{\text{ND280}} &= \Delta\chi^2_{\text{LLR}} + \Delta\chi^2_{\text{xsec}} + \Delta\chi^2_{\text{Flux}} + \Delta\chi^2_{\text{Det}} \\ &= \Delta\chi^2_{\text{LLR}} - 2 \left( \underbrace{\log \pi(\vec{x})}_{\text{xsec}} + \underbrace{\log \pi(\vec{b})}_{\text{Flux}} + \underbrace{\log \pi(\vec{d})}_{\text{Det}} \right),\end{aligned}\quad (2.10)$$

where each of the PDFs  $\pi(\vec{y} = \{\vec{x}, \vec{b}, \vec{d}\})$  are assumed multivariate normal distributions

$$\pi(\vec{y}) = C_y e^{(-\frac{1}{2}(\Delta\vec{y})^T \cdot V_y^{-1} \cdot \Delta\vec{y})}, \quad (2.11)$$

$\Delta\vec{y}$  is a  $d$  dimensional vector of the difference between the current/explored and nominal set of vector parameters  $\vec{y}$ ,  $T$  corresponds to the transpose operator, and the normalization is given by

$$C_y = ((2\pi)^{k_y} \det(V_y))^{-\frac{1}{2}} \quad (2.12)$$

with  $V_y$  being the covariance matrix for a vector  $\vec{y}$  with  $k_y$  rows. The expanded form of the test statistic  $\Delta\chi^2_{\text{ND280}}$  is given by

$$\begin{aligned}\Delta\chi^2_{\text{ND280}} &= 2 \sum_{i=1}^M \left[ \vec{N}_i^p(\Delta\vec{y}) - \vec{N}_i^d + \vec{N}_i^d \log \left( \frac{\vec{N}_i^d}{\vec{N}_i^p(\Delta\vec{y})} \right) \right] \\ &\quad + (\Delta\vec{x})^T \cdot (V_x^{-1}) \cdot (\Delta\vec{x}) + (\Delta\vec{b})^T \cdot (V_b^{-1}) \cdot (\Delta\vec{b}) + (\Delta\vec{d})^T \cdot (V_d^{-1}) \cdot (\Delta\vec{d})\end{aligned}\quad (2.13)$$

where the “ $\cdot$ ” is the matrix multiplication operator. It must be stated that the test statistic ( 2.13) purposefully *excludes normalization terms*. The specific parameterization of the penalty terms in ( 2.13) will be further discussed in Chapter 4.

The best fit parameters are those that minimizes the chi-squared statistic

---


$$\Delta\hat{\chi}_{\text{ND}280}^2 = \underset{\Delta\vec{y} \in \mathbb{R}^d}{\operatorname{argmin}} \left\{ \Delta\chi_{\text{LLR}}^2(\vec{N}^d, \vec{N}^p) + \Delta\chi_{\text{Penalty}}^2(\Delta\vec{y}) \right\}. \quad (2.14)$$

Once the global minimum is found, the postfit covariance matrix  $V$  needs to be calculated. In a one-dimensional fit with best fit parameter  $\hat{y}$ , the standard error on  $y$  ( $\sigma_y$ ) would be calculated when the difference between the quantity

$$\frac{(y - \hat{y})^2}{\sigma_y^2}$$

changes by one (1), assuming  $y$  is normally distributed. This calculation needs to generalized to account for multidimensional covariance between many parameters. Consider taking small steps  $\Delta\vec{y}$  starting at the maximum likelihood estimate  $\hat{y}$  (zero gradient), the change in the test statistic is given approximately by a Taylor series

$$\begin{aligned} \Delta\chi^2(\hat{y} + \Delta\vec{y}) &\approx \frac{\Delta\chi^2(\hat{y})}{0!} + \frac{\nabla(\Delta\chi^2)|_{\vec{y}=\hat{y}}^T \cdot \Delta\vec{y}}{1!} + \frac{(\Delta\vec{y})^T \cdot \nabla[\nabla(\Delta\chi^2)|_{\vec{y}=\hat{y}}] \cdot \Delta\vec{y}}{2!} \\ &\approx \Delta\chi^2(\hat{y}) + \frac{1}{2} (\Delta\vec{y})^T \cdot \mathcal{H} \cdot \Delta\vec{y}, \end{aligned} \quad (2.15)$$

where  $\mathcal{H}$  is recognized as a square matrix called the Hessian matrix

$$\mathcal{H}_{i,j} = \frac{\partial^2}{\partial y_i \partial y_j} (\Delta\chi^2) \Big|_{\vec{y}=\hat{y}}, \quad (2.16)$$

where  $y_i, y_j \in \vec{y}$ . Assuming that our test statistic is distributed according to a multivariate normal distribution like that of ( 2.11), we can compare terms and find that

$$-\mathcal{H} = V^{-1}, \quad (2.17)$$

or in other words the inverse of the negative Hessian matrix is the covariance matrix.

---

# Chapter 3

## The PØD Selections and Samples

This chapter describes the development of  $\nu_\mu$  and  $\bar{\nu}_\mu$  CC inclusive selections in both FHC and RHC beam configuration for PØD-based analyses. These selections are the continuation of previous works that developed  $\nu_\mu$  CC inclusive selections between the PØD and the TPC. The first such analysis was the  $\nu_\mu$  CC inclusive cross-section using the previous ND280 simulation and reconstruction software called Production 5 [29]. That analysis relied on each sub-detector's reconstruction software and developed a track matching algorithm since the ND280 “Global” reconstruction matching was not available in that software production. Another cross section analysis measuring the cross section ratio of  $\bar{\nu}_\mu/\nu_\mu$  also used this “pre-Global” technique with the modern T2K Production 6 software [6]. As the inter-detector matching reconstruction became available in Global, two cross section analyzes,  $\nu_\mu$  CC  $0\pi$  [7] and  $\bar{\nu}_\mu$  CC  $0\pi$  [9, 20], were developed that also used the CC inclusive selection as pre-selection cuts. These pre-selection cuts are well validated and have published results as shown in Figure 3.1 on page 61. The selections described in this thesis also employ the same pre-selection cuts with the latest stable Global reconstruction software, Production 6.

This paragraph is a layout of the topics in the chapter. The first topic is the event reconstruction using the “Global” reconstruction software. Next is the pre-selection cut flow. With the pre-selection cuts established, each of the three CC inclusive selection’s cut

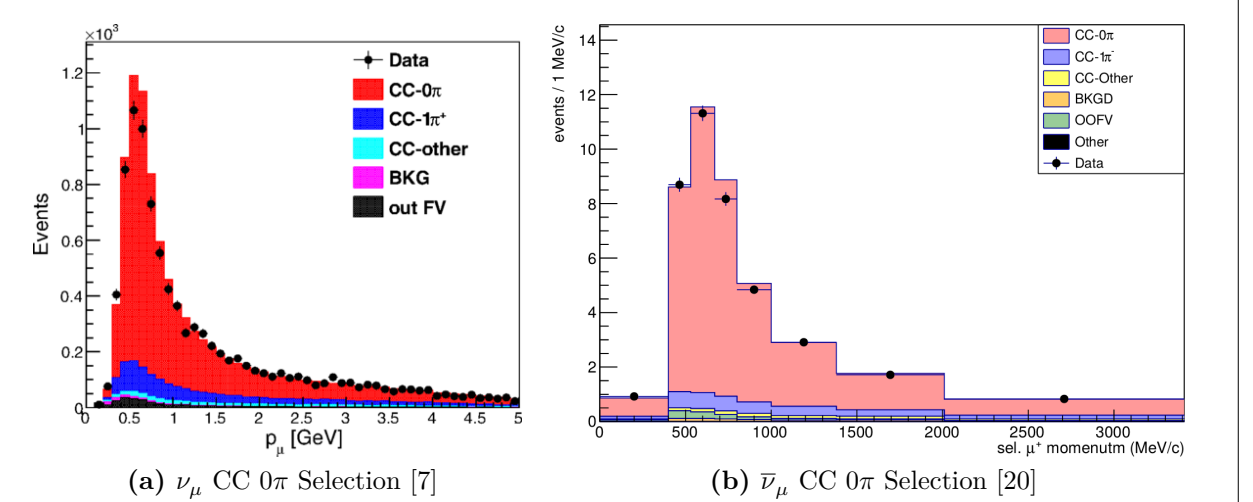


**Figure 3.1:** Data and MC distributions of the PØD water-in  $\nu_\mu$  and  $\bar{\nu}_\mu$  CC  $0\pi$  signal selections. They importantly share the same pre-selection cuts as this analysis. The plots have been normalized to data POT and are sorted into various truth topologies.

flow is described. Concluding this section is a discussion of the three samples in the following order:  $\nu_\mu$  in FHC mode,  $\bar{\nu}_\mu$  in RHC, and  $\nu_\mu$  background in RHC.

### 3.1 Global Reconstruction

The task of the Global reconstruction is to combine all the ND280 information into a combined reconstructed object. It was originally designed to analyze “CCQE-like” events in the Tracker, FGD+TPC, region and has been extended to operate with all of ND280.

The Global reconstruction is a software package that attempts to recognize patterns in data events to form tracks and find their common origin, or vertices, for those tracks. Particle shower reconstruction in Global will not be discussed in this thesis since no shower objects are considered. Each sub-detector reconstruction is run separately as the seed to Global’s track matching algorithms. This includes the PØD’s track-finding algorithms, which defines a PØD track as a sequence of nodes each at a single bar layer. To facilitate inter-detector matching, Global attempts to re-fit the PØD track using a Kalman filter [73]. The re-fit procedure also corrects for particle energy loss as a function of length ( $dT/dx$ ) and multiple scattering processes. A PØD vertex, which is the reconstructed location of the neutrino

---

interaction, is then associated with the re-fit track using another Kalman filter algorithm. Matching tracks between the PØD and the TPC is done automatically in the ND280 Global fit.

## 3.2 PØD Selection Cuts

The selection of CC inclusive events use a series of cuts to select the primary lepton. Prior to any cuts and after the reconstruction, corrections are applied first to both data and MC events to correct for well known residual differences between them. This includes the correcting the particle  $dT/dx$  in the TPC. The pre-selection cuts (“precuts”) are then applied to extract events that start in the PØD fiducial volume (FV). A minimum ionizing particle (MIP) is more likely to reach TPC1 from the PØD FV since the PØD is constructed out of heavy materials especially in the CECal. So the main track each selection is designed to select a muon.

This following sections will describe the precuts common to all CC inclusive selections and the branching of different cuts, after the precuts, to select the main track.

### 3.2.1 Precuts

The precuts were initially developed to select  $\nu_\mu$  CC inclusive to select events using the PØD and TPC sub-detector reconstruction softwares separately [6, 29]. They were then used with the Global reconstruction software for the  $\nu_\mu$  CC- $0\pi$  selection in the FHC beam configuration [7]. The description and sequence of the precuts is described below.

The following precuts are checked on the collected data from each Trip-T integration cycle as follows:

1. The event has a “good” data quality flag.
  - An event is rejected if any sub-detector or electronics in ND280 reported as “bad” during that bunch.

2. There is at least one (1) track reconstructed in TPC1.

- There are no restrictions on the number of tracks fully contained in the PØD or exiting into other sub-detectors.

3. The track in the TPC must have more than 18 nodes.

- The TPC reconstruction gathers vertical and horizontal hits into clusters of hits. The charge distribution of the cluster is used to get a vertical (horizontal) position that is more accurate than the individual readout pads. A node is constructed out of each cluster with associated track state information. The set of nodes are used to fit a helix shaped track.

4. The reconstructed vertex is within the PØD water target (WT) FV.

- The PØD FV is defined to include as much as the WT regions as possible. Its X and Y borders are 25 cm away from the PØDule edges while its Z borders intersect the last and first half downstream PØDule in the USECal and CECal, respectively. The enumerated volume edges are shown in Table 3.1 on page 64. This volume, while used for track-based analyzes in the past, was optimized for  $\pi^0$  and  $\nu_e$  analyses.

5. All tracks that enter the TPC pass the veto cut

- An event is rejected if any PØD track enters the TPC from outside the “corridor” volume. This cut was designed to eliminate broken tracks between the PØD and TPC1 the pre-Global separate sub-detector reconstruction was used [21]. In practice, this cut ensures that Global tracks entering the TPC are away from its X and Y edges. The corridor definition is the same as defined in the pre-published  $\bar{\nu}_\mu/\nu_\mu$  cross section ratio analysis [22] and shown in Table 3.1 on page 64.

PØD WT FV			Corridor Volume		
-836	< X <	764	-988	< X <	910
-871	< Y <	869	-1020	< Y <	1010
-2969	< Z <	-1264	-3139	< Z <	-900

**Table 3.1:** The PØD WT FV (left) and veto corridor volume (right) in the ND280 coordinate system. The corridor spans from the 5th (8th) to 40th (80th) PØDule (scintillator layer). All the units are given in millimeters.

After passing all the precuts, a single, global track, which is observed in TPC1, is assigned as the lepton candidate or “main track” of a selection.

The momentum of the main track,  $P$ , is sum of its momentum in the TPC,  $P_{\text{TPC}}$ , with the estimate momentum lost in the PØD,  $\Delta P_{\text{PØD}}$

$$P = P_{\text{TPC}} + \Delta P_{\text{PØD}}. \quad (3.1)$$

Momentum lost in the PØD is estimated by first summing the total energy loss,  $\Delta T$ , along the track path  $\mathcal{C}$

$$\Delta T = \int_{\mathcal{C}} \left( \frac{dT}{dx} \right) dx. \quad (3.2)$$

Using the chain rule, we can convert the energy loss function,  $dT/dx$ , into momentum loss

$$\begin{aligned} \frac{dT}{dx} &= \left( \frac{dT}{dP} \right) \left( \frac{dP}{dx} \right) \\ &= \left( \frac{Pc^2}{E} \right) \left( \frac{dP}{dx} \right) \\ &= \beta c \left( \frac{dP}{dx} \right), \end{aligned} \quad (3.3)$$

where  $\beta$  is the changing particle velocity as a ratio of the speed of light  $c$ . The fundamental theorem of Calculus permits us to write the energy loss as a momentum loss along the track’s

path  $\mathcal{C}$  as

$$\Delta P_{\text{P}\bar{\text{O}}\text{D}} = \int_{\mathcal{C}} \left( \frac{dP}{dx} \right) dx = \frac{1}{c} \int_{\mathcal{C}} \left[ \left( \frac{dT}{dx} \right) \frac{1}{\beta(x)} \right] dx. \quad (3.4)$$

Since the reconstructed track's path  $\mathcal{C}$  is not infinitesimally precise due to inherent detector resolution, we must replace the integral with a sum and differential  $dx \rightarrow \Delta x$ . We then arrive at the expression of the momentum loss estimate in the PØD as

$$P = P_{\text{TPC}} + \frac{1}{c} \sum_t \left[ \left( \frac{dT}{dx} \right) \left( \frac{\Delta x}{\beta(x)} \right) \right]_t. \quad (3.5)$$

For most tracks entering the TPC, they will be highly relativistic in the PØD ( $\beta \approx 1$ ), and (3.5) simplifies to

$$P = P_{\text{TPC}} + \frac{1}{c} \sum_t \left[ \left( \frac{dT}{dx} \right) \Delta x \right]_t \quad (3.6)$$

The next sections describe the selection cuts, first in FHC mode and then RHC mode.

### 3.2.2 The $\nu_\mu$ CC Inclusive in FHC Cut

- The highest momentum negatively charged track (HMNT) is the lepton candidate

As discussed in Section section 3.2.1 on page 62, this selection is the basis for the PØD  $\nu_\mu$  CC-0 $\pi$  analysis [7]. In FHC mode, the vast majority of neutrino interactions are  $\nu_\mu$ CC events producing an outgoing, negatively charged muon. So if there is no negatively charged track in the TPC, the event is rejected.

### 3.2.3 The $\bar{\nu}_\mu$ CC Inclusive in RHC Cuts

- The highest momentum positively charged track (HMPT) is the lepton candidate
- The HMPT must be the highest momentum track (HMT)

In RHC, the majority of neutrinos in the beam is  $\bar{\nu}_\mu$  since the horn focuses negatively charged pions. To select  $\bar{\nu}_\mu$  CC interaction events, the lepton candidate is the HMPT in the TPC.

---

The event is rejected if there is no positively charged track. However, since the RHC mode beam is not as  $\bar{\nu}_\mu$  pure as the FHC beam is for  $\nu_\mu$ , another cut was added to reduce this effect.

Since RHC neutrino beam can be described as a  $\bar{\nu}_\mu$ -enhanced beam, the HMPT must also be the HMT due to the significant “wrong-sign”  $\nu_\mu$  background. This effect is two fold due to the nature of the neutrino source and the cross section between neutrinos and antineutrinos. Firstly the neutrino flux is larger in RHC mode due to neutrino production at the target. The source of neutrinos are from mainly positively charged pions and kaons decays produced proton collisions on a graphite target. This method is more likely to produce positively charged pions in the target than negatively charged one. While the horns are designed to select the negatively charged pions in RHC mode, the excess amount of positively charged pions will penetrate this filter. Therefore there are many more  $\pi^+ \rightarrow \mu^+ + \nu_\mu$  decays in RHC compared to FHC mode. Secondly, antineutrino interactions on matter are suppressed by  $\sim 1/3$  compared to neutrinos due to helicity considerations as explained in Section 1.1.1.

### 3.2.4 The $\nu_\mu$ Background CC Inclusive in RHC Cuts

- The highest momentum negative track (HMNT) is the lepton candidate
- The HMNT must be the highest momentum track (HMT)

As discussed in section 3.2.3 on the preceding page, the RHC neutrino beam has a significant wrong-sign  $\nu_\mu$  background. The selection of the HMNT is designed to select the negatively charged muons. To prevent selecting the antineutrino events, the HMNT must also be the HMT. The event is rejected if there is no negatively charged track. If there are both positively and negatively charged tracks, the HMT cut discriminates if the event originates from a  $\nu_\mu$  or  $\bar{\nu}_\mu$ .

Run period	Horn current [kA]	PØD status	Data POT ( $\times 10^{20}$ )	MC POT ( $\times 10^{20}$ )
2	+250	Water	0.433934	12.0341
		Air	0.359149	9.23937
3b	+205		0.217273	4.47864
3c	+250		1.36447	26.3227
4			1.78271	34.996
		Water	1.64277	34.9712
5c	-250		0.43468	22.7766
6b		Air	1.28838	14.174
6c			0.505895	5.27562
6d			0.775302	6.884
6e			0.847902	8.59439
7b		Water	2.43682	33.7046
8	+250		1.58053	26.4664
		Air	4.14897	36.0694
Sand	+250		-	11.1988
Sand	-250		-	12.9201
2, 3b, 3c, 4, 8		FHC	Air	7.872757
2, 4, 8			Water	3.656589
6b, 6c, 6d, 6e		RHC	Air	3.382490
5c, 7b			Water	2.852340
				54.53

**Table 3.2:** T2K MC and data POT divided by run periods. The bottom four rows are the aggregated periods grouped by horn current and PØD status which is how the data analysis is performed.

### 3.3 Selection Kinematics

This section examines the kinematics for each of selections while differentiating between water-in and water-out mode. The selection cuts were implemented in Psyche which is the software interface that BANFF uses to select events. The data sets used in this analysis are runs 2-8 in both PØD water-in and water-out (air) modes as shown in Table 3.2 on page 67. There will be no data events shown to prevent any potential biases that exist between the data and MC. Simulated events will be broken down into various true categories to understand selection kinematics, efficiencies, and purities.

True interactions for these selections are generally divided into four interactions classes:

- neutrino-induced CCQE ( $\nu$  CCQE):
  - Only NEUT generated neutrino-induced CCQE event at the interaction vertex
- neutrino-induced non-CCQE ( $\nu$  non-CCQE),
  - Any NEUT generated neutrino-induced CC and NC event *except* neutrino-induced CCQE at the interaction vertex
- antineutrino-induced CCQE ( $\bar{\nu}$  CCQE)
  - Only NEUT generated antineutrino-induced CCQE event at the interaction vertex
- antineutrino-induced non-CCQE ( $\bar{\nu}$  non-CCQE)
  - Any NEUT generated antineutrino-induced CC and NC event *except* antineutrino-induced CCQE at the interaction vertex

An enlarged legend of these four interaction classes used in this analysis is shown in Figure 3.2 on page 69. Out of fiducial volume (OOFV) events refer to neutrino and antineutrino interactions occurring in ND280, but not in the PØD water target (WT) fiducial volume (FV). Sand muons, similar to OOFV events, are any neutrino/antineutrino-induced interaction truly occurring in the sand surrounding the ND280 pit.

The non-CCQE category can be further divided among the dominant T2K CC and all NC interactions modes as enumerated in Table 3.3 on page 69 and Table 3.4 on page 70. For neutrino-based selections, the legend shown in Figure 3.4 on page 71 is also used to describe the neutrino-induced interaction purity of the selection. Similarly for antineutrino-based selections, the legend shown in Figure 3.5 on page 71 is used for the same purpose.

The true particle matched with the main track is also analyzed here as shown in Figure 3.3 on page 70. The ND280 MC uses the GEANT4 software toolkit [13] to simulate the passage of particles through matter. A GEANT4 particle is assigned to a reconstructed track if it contributed the most to the track's reconstructed hits. True particles include protons (p)

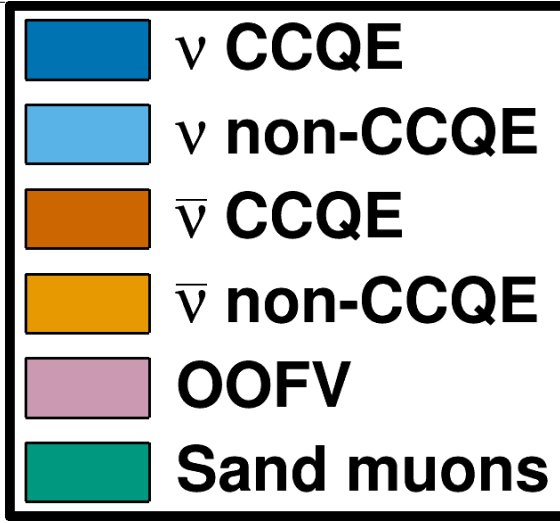


**Figure 3.2:** NEUT CCQE and non-CCQE interactions legend. The enumerated NEUT codes are given in Figure 3.4 on page 71 and Figure 3.5 on page 71.

Category	NEUT Codes
$\nu$ CCQE	1
$\nu$ 2p2h	2
$\nu$ CC-1 $\pi$	11 → 16
$\nu$ non-CCQE	$\nu$ CC-N $\pi$ 21 $\nu$ CC-DIS      26 $\nu$ CC-Other    17, 22, 23 $\nu$ NC          31 → 100
$\bar{\nu}$	-1 → -100
OOFV	-100 → 100
Sand muons	-100 → 100

**Table 3.3:** The expanded  $\nu$  NEUT reactions table as shown in Figure 3.4 on page 71. An arrow indicates a sequence of integer steps from left to right of the arrow.

Category	NEUT Codes
$\bar{\nu}$ CCQE	-1
$\bar{\nu}$ 2p2h	-2
$\bar{\nu}$ CC-1 $\pi$	-11 → -16
$\bar{\nu}$ non-CCQE	$\bar{\nu}$ CC-N $\pi$ $\bar{\nu}$ CC-DIS $\bar{\nu}$ CC-Other $\bar{\nu}$ NC
$\bar{\nu}$ CC-N $\pi$	-21
$\bar{\nu}$ CC-DIS	-26
$\bar{\nu}$ CC-Other	-17, -22, -23
$\bar{\nu}$ NC	-31 → -100
$\nu$	1 → 100
OOFV	-100 → 100
Sand muons	-100 → 100

**Table 3.4:** The expanded  $\bar{\nu}$  NEUT reactions table as shown in Figure 3.5 on page 71.

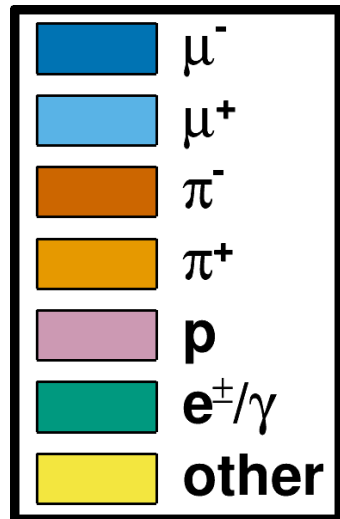


**Figure 3.3:** True particle selected legend

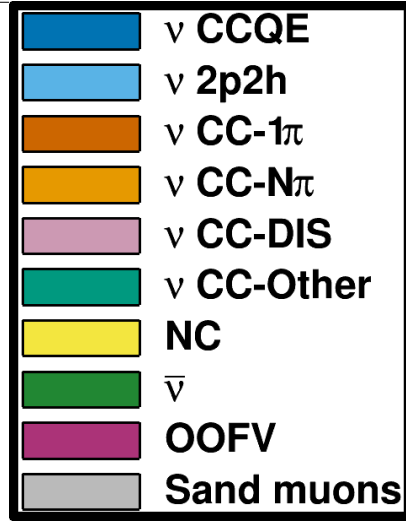


**Figure 3.4:** The NEUT neutrino interaction legend used in this analysis. The labels are enumerated in Table 3.3 on page 69.

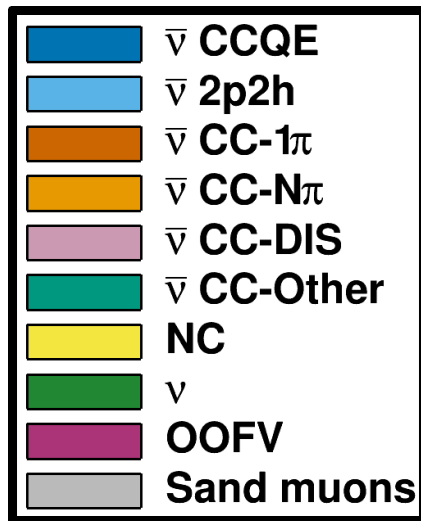


**Figure 3.5:** NEUT antineutrino interaction legend used in this analysis. The labels are enumerated in Table 3.4 on page 70.

---

and both negatively and positively charged muons ( $\mu^\pm$ ), pions ( $\pi^\pm$ ), and electrons/positrons ( $e^\pm$ ). In addition, any electron and positron generated from pair production are grouped together as “ $e^\pm/\gamma$ ”. Particles that do not match any of these categories is labeled as “other”.

### 3.3.1 $\nu_\mu$ in FHC CC 1-Track

This selection provides the CCQE-like samples in FHC mode. Figure 3.6 on page 73 and Figure 3.7 on page 74 displays the momentum and angular distributions that are inputs to BANFF. Comparing between water-in and water-out modes, we see the reconstructed kinematics are nearly identical. In the majority of cases, the lepton candidate is the true muon, making this a very pure  $\nu_\mu$  sample. We also see that there are non-CCQE events which will be better understood in the coming paragraphs. Following this paragraph and the following sections, only the PØD water-in mode kinematics, i.e.  $p$  and  $\cos\theta$ , will be shown.

The target nuclei between water-in and water-out modes is slightly different as seen in Figure 3.8 on page 75. This is expected given that there is atmosphere instead of water in the bags and the simulated neutrino-nucleus scattering target is either an oxygen or hydrogen nucleus. After carbon and oxygen as the most likely targets, copper in the brass layers contribute a significant fraction of events. The events on lead are true OOFV and primarily occur in the last PØDule. Due to a software bug in the MC, coherent events on hydrogen were incorrectly categorized and have their own category.

The underlying true kinematics of the interactions are shown in Figure 3.10 on page 76 which are of theoretical importance in the cross section and flux models. Using Figure 1.5 on page 13 as reference, the true neutrino energy  $E_\nu = k_0$  and 4-momentum transfer  $Q^2 = -q^2$ . An interesting CCQE-like topology in this selection are 2p2h events. Interaction model uncertainties for 2p2h are quite large in T2K and are included the BANFF fit. Therefore these events could help reduce the 2p2h model uncertainties.

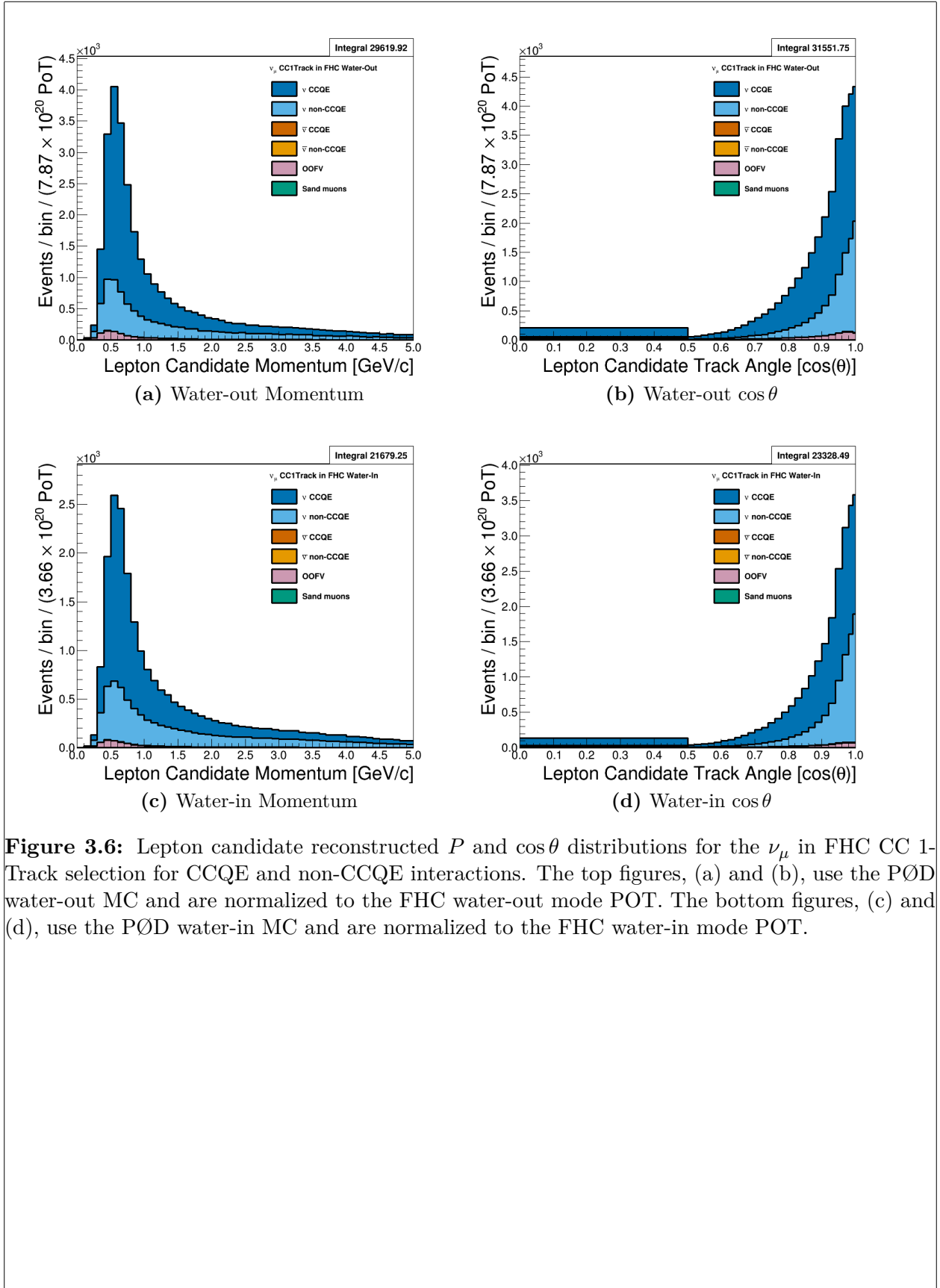


**Figure 3.6:** Lepton candidate reconstructed  $P$  and  $\cos\theta$  distributions for the  $\nu_{\mu}$  in FHC CC 1-Track selection for CCQE and non-CCQE interactions. The top figures, (a) and (b), use the PØD water-out MC and are normalized to the FHC water-out mode POT. The bottom figures, (c) and (d), use the PØD water-in MC and are normalized to the FHC water-in mode POT.

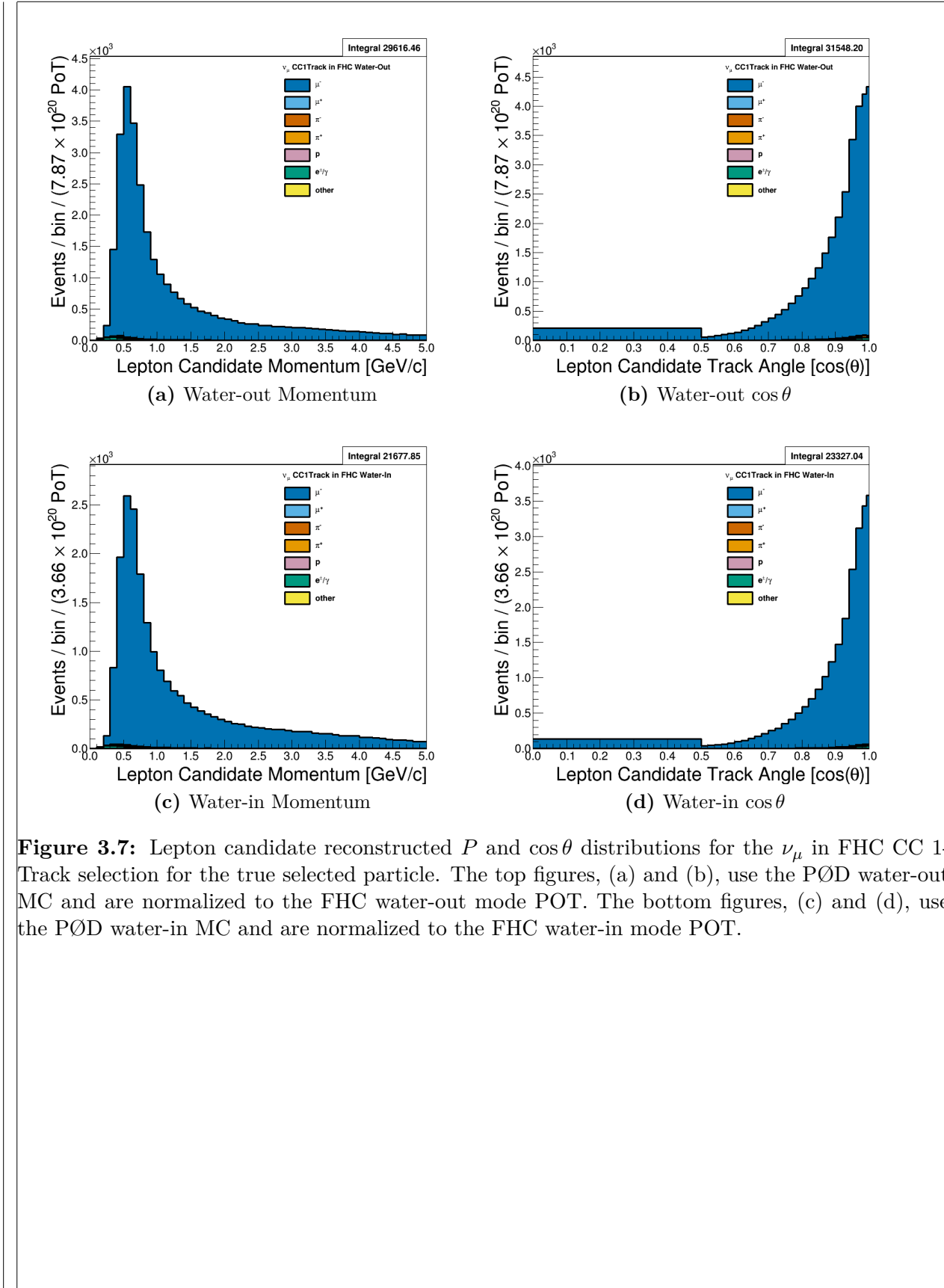


**Figure 3.7:** Lepton candidate reconstructed  $P$  and  $\cos\theta$  distributions for the  $\nu_\mu$  in FHC CC 1-Track selection for the true selected particle. The top figures, (a) and (b), use the PØD water-out MC and are normalized to the FHC water-out mode POT. The bottom figures, (c) and (d), use the PØD water-in MC and are normalized to the FHC water-in mode POT.

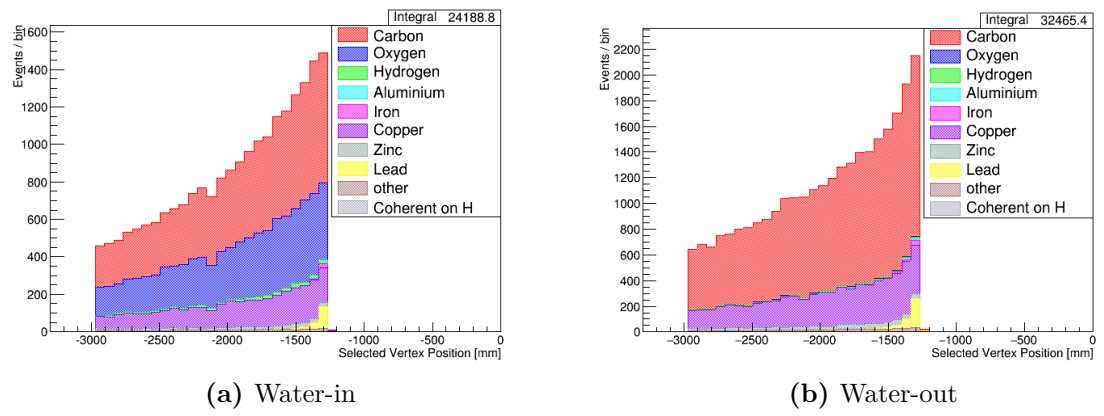


**Figure 3.8:** Vertex Z position of the  $\nu_\mu$  in FHC CC 1-Track selection broken down by true target nucleus. The number of events increases with increasing Z since the probability of an interaction increases as the neutrino crosses more media in the PØD.

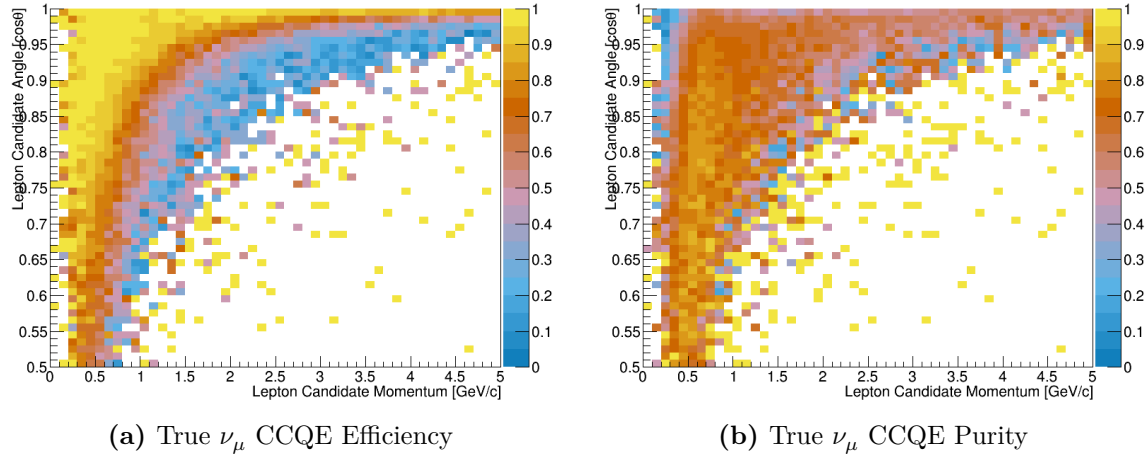


**Figure 3.9:** The efficiency and purity in reconstructed kinematics of  $\nu_\mu$  CCQE interactions in the  $\nu_\mu$  in FHC CC 1-Track selection. True events are defined as correctly matched  $\mu^-$  tracks from  $\nu_\mu$ -induced CCQE interactions at the vertex .

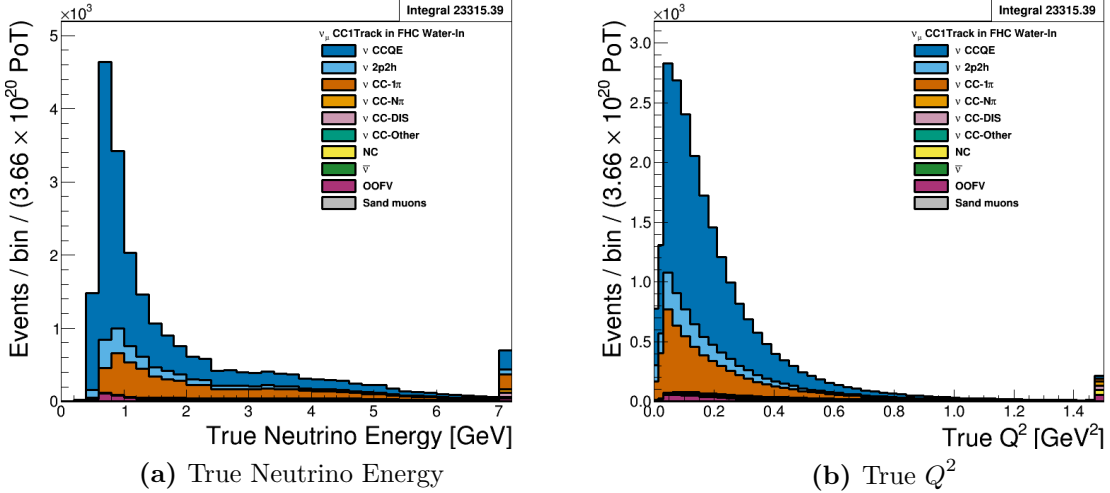


**Figure 3.10:** The  $\nu_\mu$  in FHC CC 1-Track true kinematics broken down by true NEUT interaction modes. Water-in mode is displayed here only with the last bin shown is used as overflow. The figures use the PØD water-in MC and are normalized to the FHC water-in mode POT.

This selection contains a modest fraction of non-CCQE interactions. The largest contamination is  $1\pi$  interactions, which can happen primarily for a couple of reasons. Firstly, when the final state pion is produced, it is subject to final state interactions (FSI) where a pion can be absorbed or scattered in the nucleus. Secondly, and more importantly, a pion might not be reconstructed as a track in the PØD if its energy is below reconstruction threshold. Together, the large  $1\pi$  background affects the CC- $0\pi$  and CC- $1\pi$  model parameters in the BANFF fit.

We can examine the efficiencies and purities differentially for true  $\nu_\mu$  CCQE interactions in Figure 3.9 on page 75. The efficiency,  $\epsilon$ , and purity,  $\rho$ , are defined as

$$\epsilon = \frac{N_{\text{Selected}}^{\text{True}}}{N^{\text{True}}} \quad \rho = \frac{N_{\text{Selected}}^{\text{True}}}{N_{\text{Selected}}}, \quad (3.7)$$

where  $N_{\text{Selected}}^{\text{True}}$  is the number of true, selected events,  $N^{\text{True}}$  is the number of true events, and  $N_{\text{Selected}}$  is the number of selected events. They demonstrate that the purity is highest near 0.5 GeV/c with the efficiency highly dependent on the track angle.

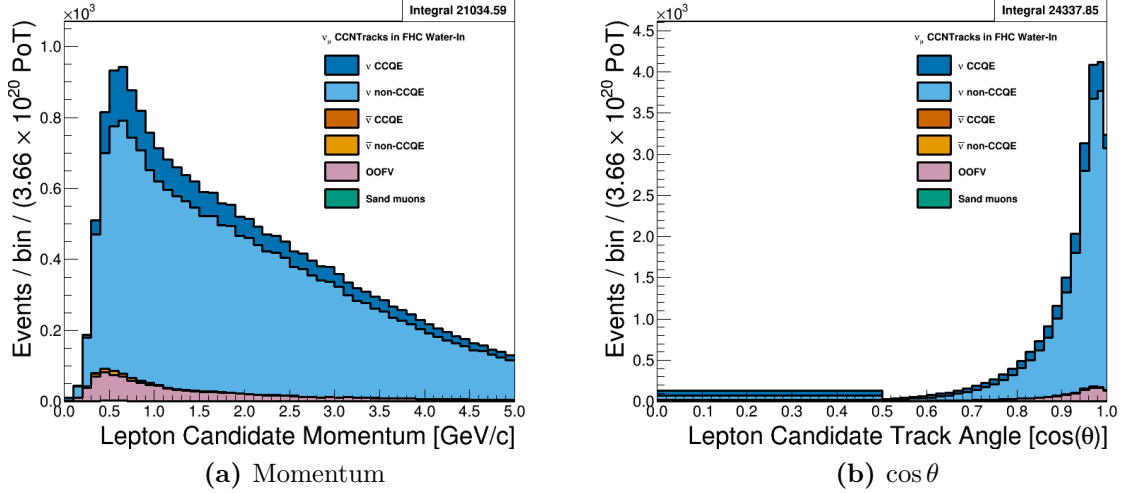
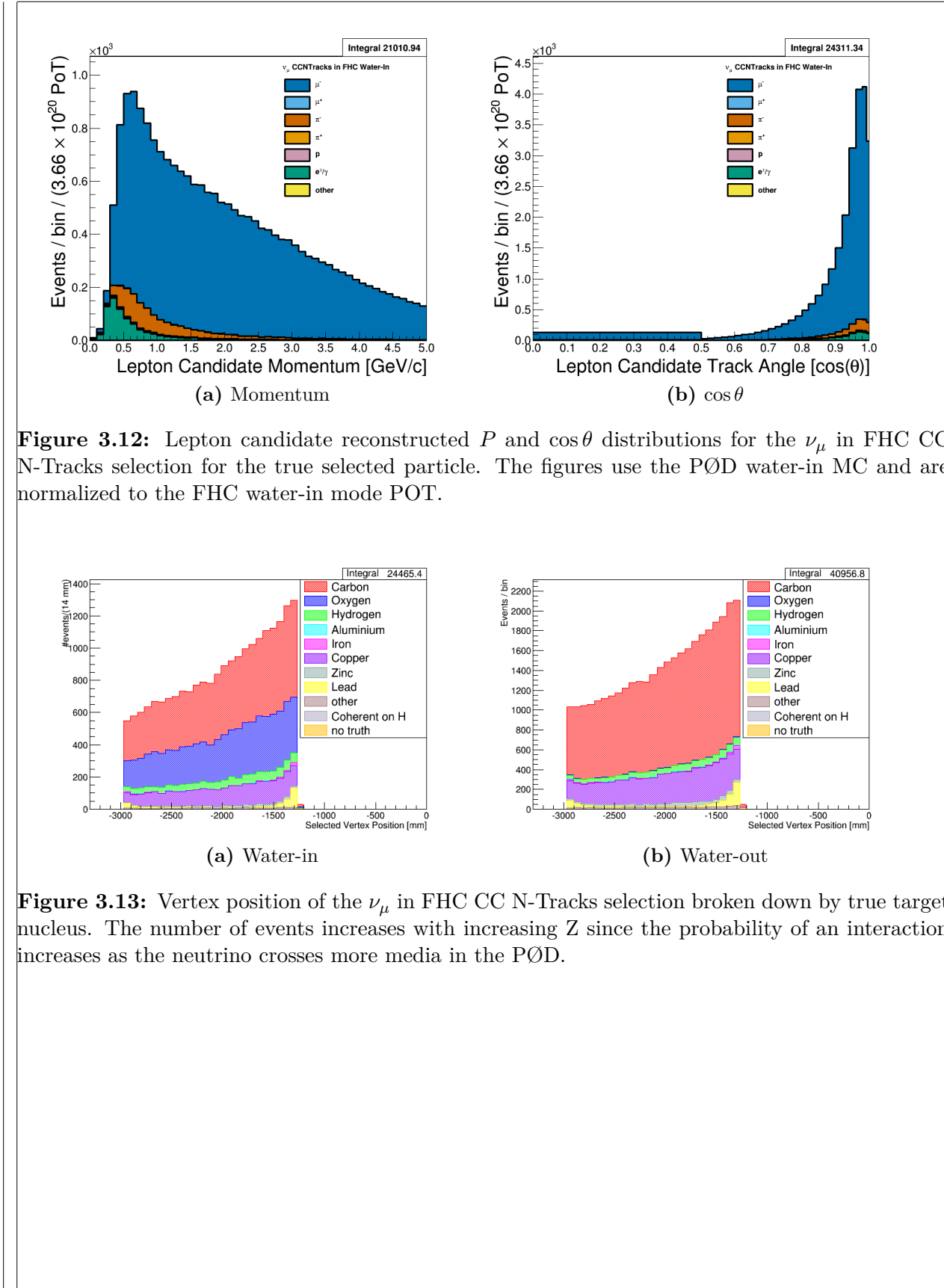


**Figure 3.11:** Lepton candidate reconstructed  $P$  and  $\cos\theta$  distributions for the  $\nu_\mu$  in FHC CC N-Tracks selection for CCQE and non-CCQE interactions. The figures use the PØD water-in MC and are normalized to the FHC water-in mode POT.

### 3.3.2 $\nu_\mu$ in FHC CC N-Tracks

This selection provides non-CCQE-like samples in FHC mode inputs to BANFF. The reconstructed momentum and angular distributions are shown in Figure 3.11 on page 77 and Figure 3.12 on page 78. Since this selection is not optimized for any particular CC topology, there are a variety of interactions modes present including  $1\pi$ , multiple pion ( $N\pi$ ) and deep inelastic scattering (DIS). There are a number of mis-identified lepton candidates in the form of electrons and pions. There is a relatively larger OOFV contamination compared with the 1-Track selection with some events originating in the USECal as seen in Figure 3.13 on page 78. Otherwise, the vertex position and target materials are quite similar between the 1-Track and N-Tracks selections.

We can examine the efficiencies and purities differentially for the selection in Figure 3.14 on page 79. The true signal here is any  $\nu_\mu$  CC interaction except  $\nu_\mu$  CCQE (CC non-QE) which the CC 1-Track selection is designed to select. The efficiency is high for the higher momenta and higher angle tracks suggesting this is a high  $Q^2$  selection. In addition, the purity is around ~70% in this region.



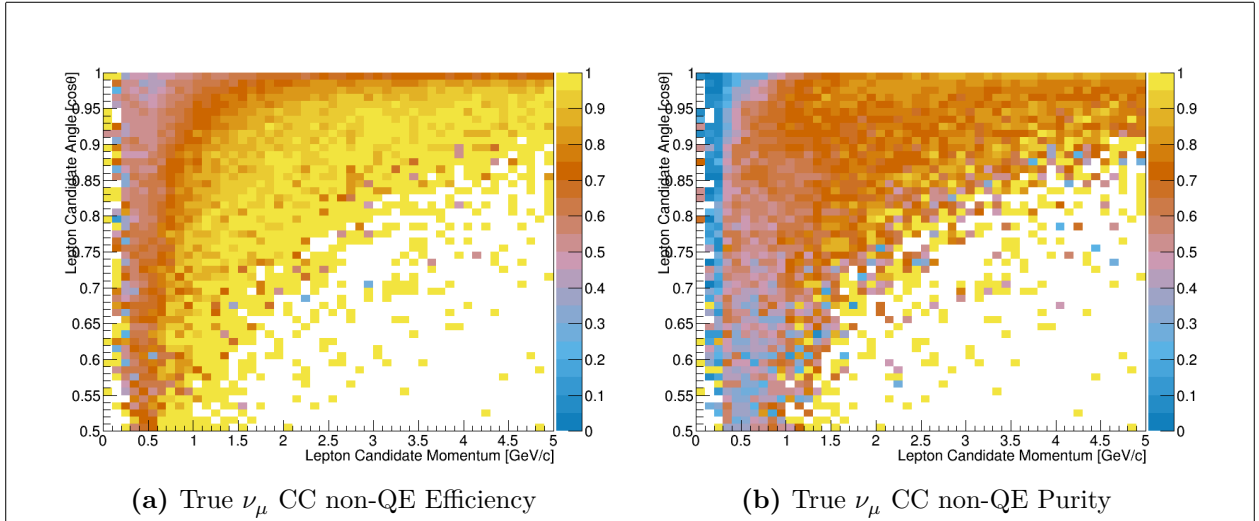


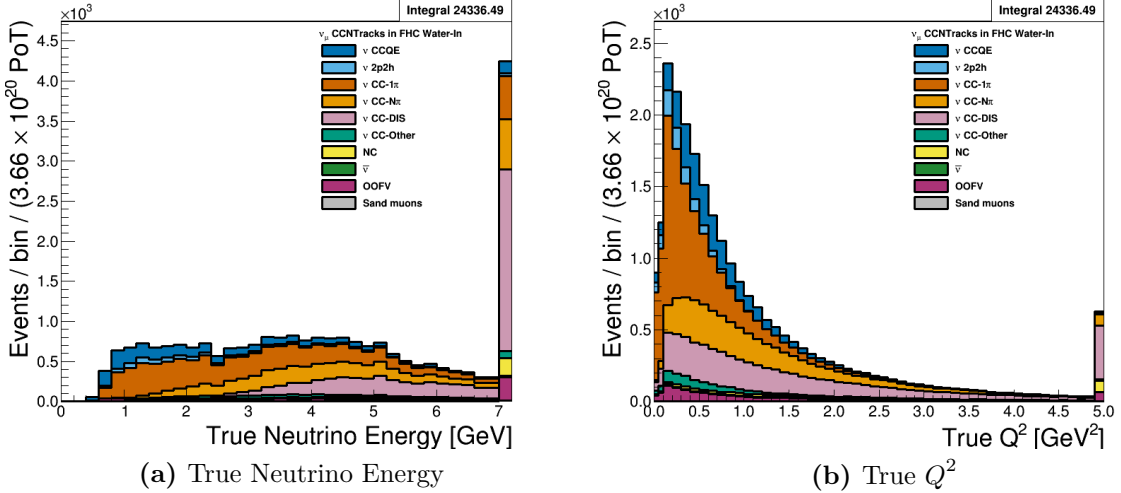
**Figure 3.14:** The efficiency and purity in reconstructed kinematics of  $\nu_\mu$  CC non-QE interactions in the  $\nu_\mu$  in FHC CC N-Tracks selection. True events are defined as correctly matched  $\mu^-$  tracks from  $\nu_\mu$ -induced CC non-QE interactions at the vertex.

The fundamental kinematics of the selection are shown in Figure 3.15 on page 80. The selection is relatively  $\nu_\mu$ -pure and captures the high energy tail of the neutrino flux. True kinematics that describe the  $1\pi$ ,  $N\pi$ , and DIS models are parameterized in  $Q^2$  and the hadronic system mass  $W$ . Using Figure 1.5 on page 13, we can define the invariant mass of hadronic system as

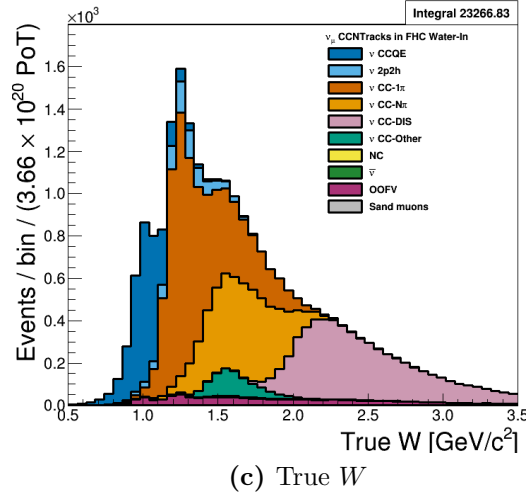
$$\begin{aligned} (Wc^2)^2 &= (p+q)^2 = p^2 + 2p \cdot q + q^2 \\ &= (M_N c^2)^2 + 2(M_N c^2)(k_0 - k'_0) - Q^2, \end{aligned} \tag{3.8}$$

where  $M_N$  is the mass of the struck nucleon and  $k_0/k'_0$  is the energy of the neutrino/outgoing lepton. A dominant mode in the selection are  $1\pi$  events from a  $\Delta$  resonance. A resonance is clearly seen in the  $W$  distribution in Figure 3.15 on page 80 which is the  $\Delta$  baryon which has a rest mass of  $1.232 \text{ GeV}/c^2$ . Higher order resonance states are present as well since there are no cuts to distinguish muons and pions from protons.

The origin of the mis-identified particles, in particular the pions, becomes more clear since this is a high  $Q^2$  selection. Multiple pion and DIS events can produce a negatively charged pion. For high  $Q^2$  interactions topologies, the energy transfer to the final hadronic



(a) True Neutrino Energy

(b) True  $Q^2$ (c) True  $W$ 

**Figure 3.15:** The  $\nu_\mu$  in FHC CC N-Tracks true kinematics broken down by true NEUT interaction modes. The last bin shown in (a) and (b) is used as overflow. The figures use the PØD water-in MC and are normalized to the FHC water-in mode POT.

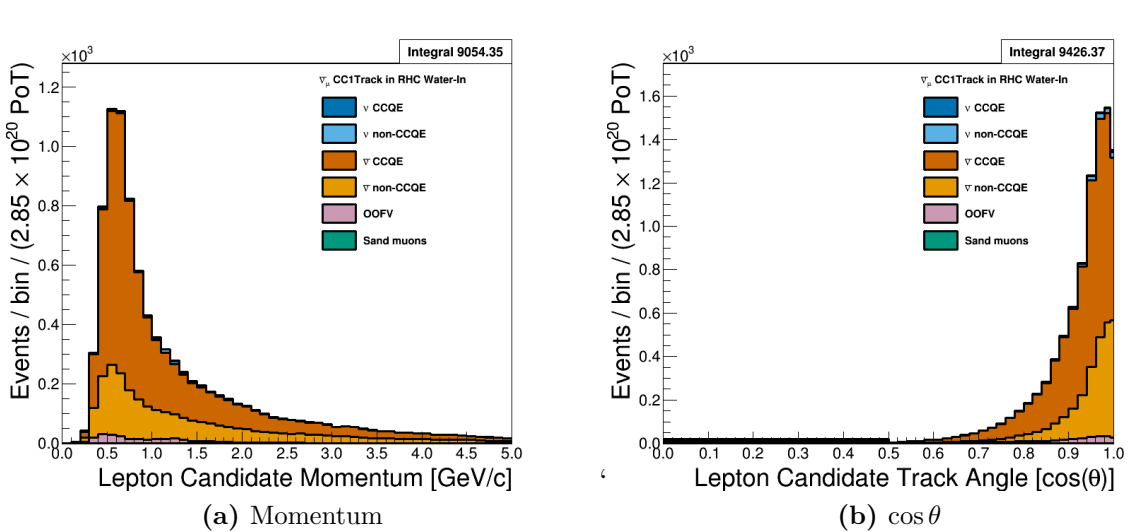


**Figure 3.16:** Lepton candidate reconstructed  $P$  and  $\cos\theta$  distributions for the  $\bar{\nu}_\mu$  in RHC CC 1-Track selection for CCQE and non-CCQE interactions. The figures use the PØD water-in MC and are normalized to the RHC water-in mode POT.

state can produce a higher energy pion than the true muon or the muon does not enter the TPC.

### 3.3.3 $\bar{\nu}_\mu$ in RHC CC 1-Track

This selection provides the  $\bar{\nu}_\mu$  CCQE-like samples in RHC mode that are inputs to BANFF. In Figure 3.16 on page 81 and Figure 3.17 on page 82 display the momentum and angular distributions for this selection. The selection is  $\bar{\nu}_\mu$ -pure with the selected lepton candidate being positively charged muons. There is a large OOFV background from proton tracks. They are high momentum ( $> 1$  GeV/c) tracks which, at these energies, are become minimum ionizing and can reach into the TPC.

We can examine the efficiencies and purities differentially for the selection in Figure 3.18 on page 82. The two distributions are very similar to the  $\nu_\mu$  in FHC CC 1-Track efficiencies and purities, with the efficiency being relatively high (90%) for high statistics regions.

The underlying true kinematics,  $E_\nu$  and  $Q^2$ , of the interactions are shown in Figure 3.19 on page 83. We see a similar true reaction composition to the  $\nu_\mu$  in FHC selection in

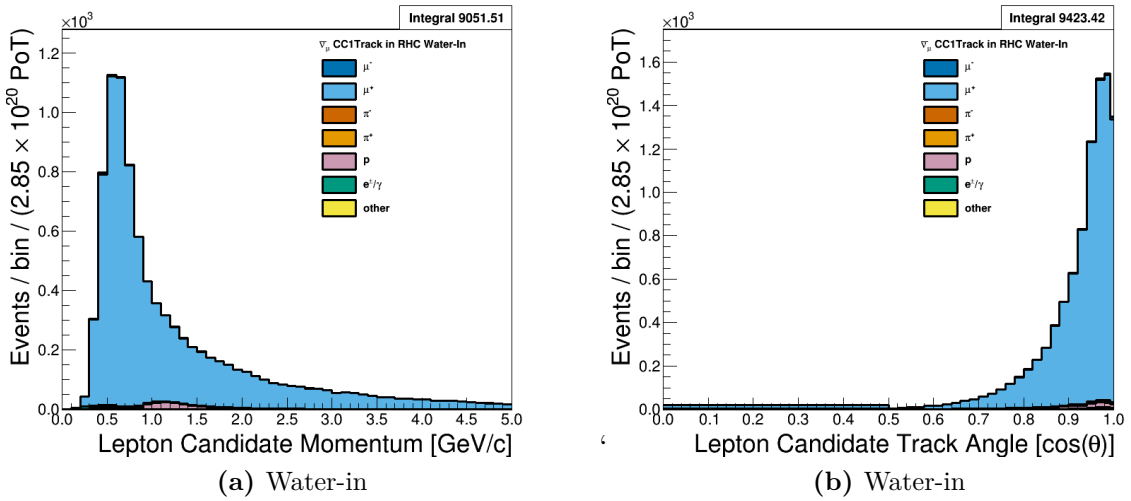


**Figure 3.17:** Lepton candidate reconstructed  $P$  and  $\cos\theta$  distributions for the  $\bar{\nu}_\mu$  in RHC CC 1-Track selection for the true selected particle. The figures use the PØD water-in MC and are normalized to the RHC water-in mode POT.

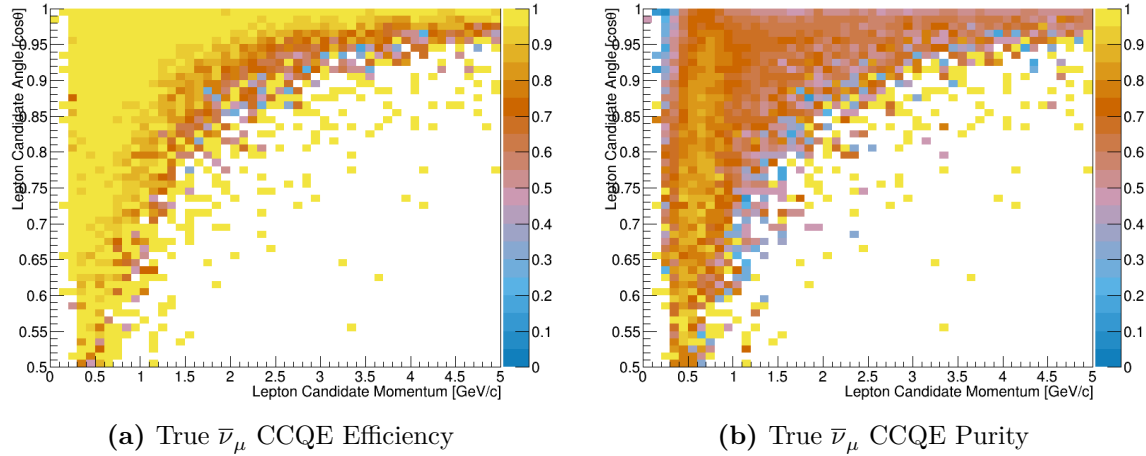


**Figure 3.18:** The efficiency and purity in reconstructed kinematics of  $\bar{\nu}_\mu$  CCQE interactions in the  $\bar{\nu}_\mu$  in RHC CC 1-Track selection. The true events are  $\bar{\nu}_\mu$  CCQE at the vertex and the selected lepton candidate is the true  $\mu^+$ .

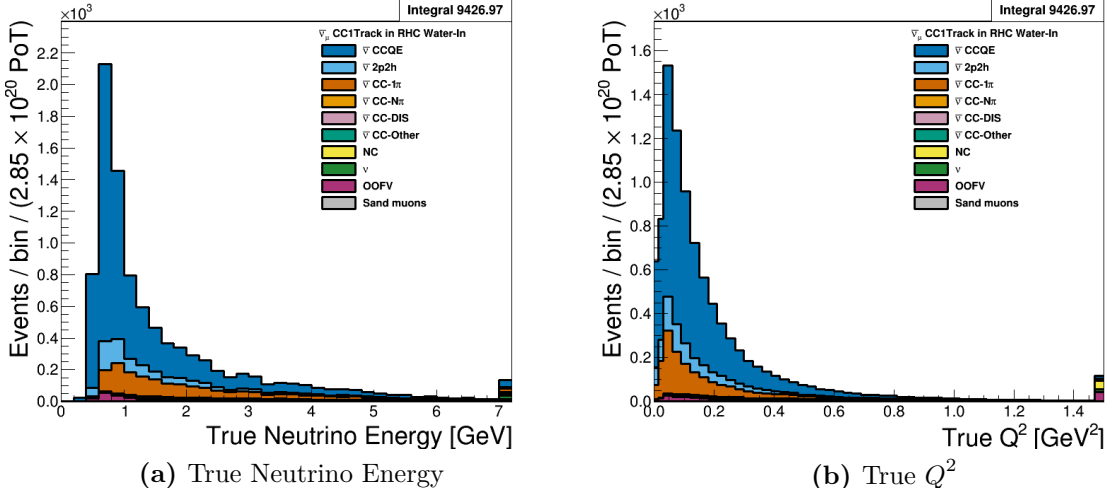


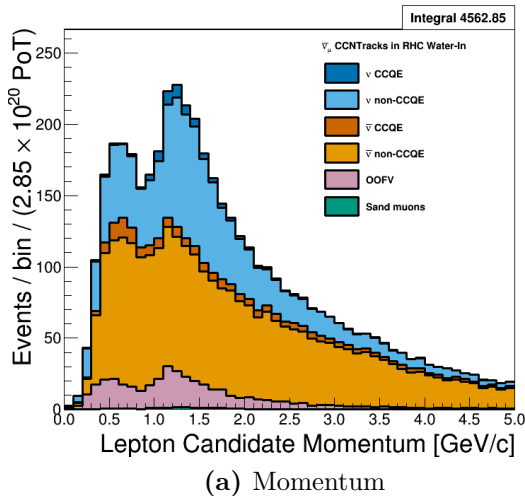
**Figure 3.19:** The  $\bar{\nu}_\mu$  in RHC CC 1-Track true kinematics broken down by true NEUT interaction modes. Water-in mode is displayed here only with the last bin shown is used as overflow. The figures use the PØD water-in MC and are normalized to the RHC water-in mode POT.

Section 3.3.1. Most reactions are true CCQE with a mixture of 2p2h and  $1\pi$  events. As previously seen in Section 3.3.1, the significant  $1\pi$  contamination may reduce the sensitivity both CC- $0\pi$  and CC- $1\pi$  model parameters in the BANFF fit.

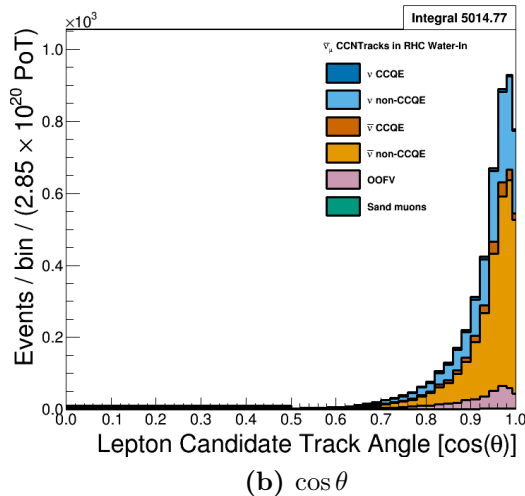
### 3.3.4 $\bar{\nu}_\mu$ in RHC CC N-Tracks

This selection provides the  $\bar{\nu}_\mu$  non-CCQE-like samples in RHC mode. Figure 3.20 on page 84 and Figure 3.21 on page 84 display the momentum and angular distributions that are inputs to BANFF. The most striking feature of this selection is the the number of mis-identified events. In particular protons are selected as the HMPT when they become minimum ionizing particles, which is about 1.3 GeV/c. At these energies protons can escape the PØD into the TPC since it deposits less energy per unit length. In addition, the intrinsic  $\nu_\mu$  background contribution is comparable to the desired  $\bar{\nu}_\mu$  flavor. These two features should be addressed to increase the utility of the selection for the next iteration of the analysis.

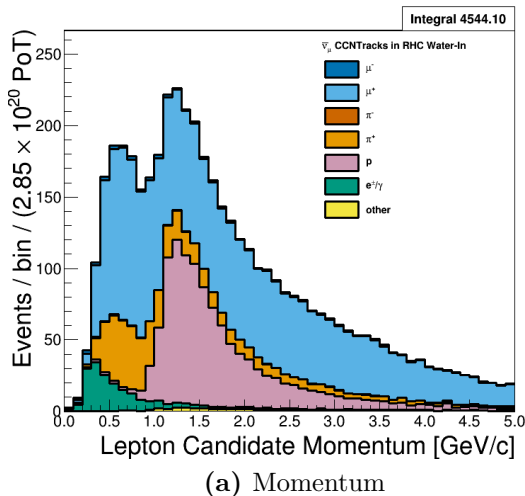
We can examine the efficiencies and purities differentially for the selection in Figure 3.14 on page 79. The true signal here is any  $\bar{\nu}_\mu$  CC interaction except  $\bar{\nu}_\mu$  CCQE which the CC



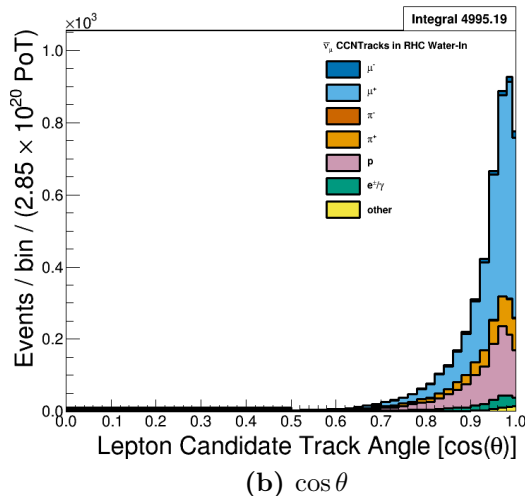
(a) Momentum



(b)  $\cos \theta$



(a) Momentum



(b)  $\cos \theta$

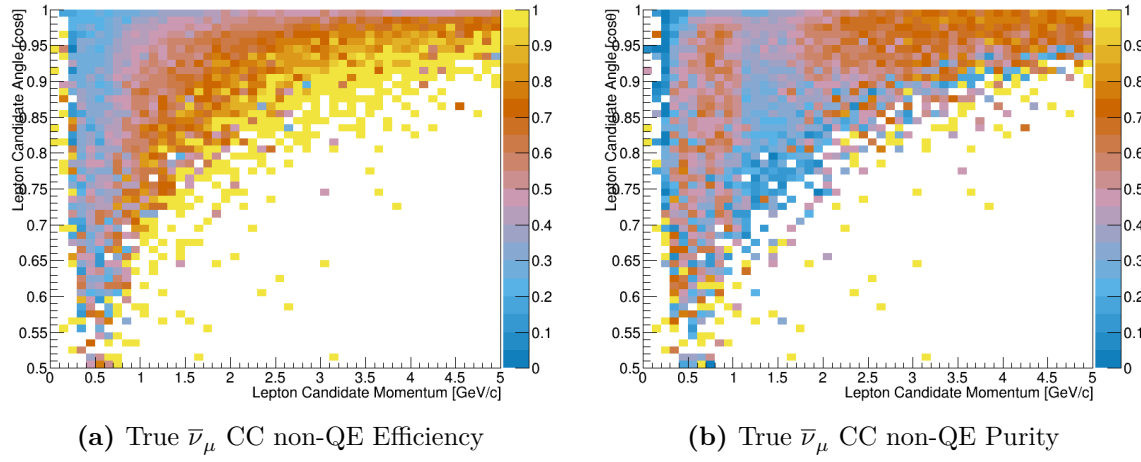


**Figure 3.22:** The efficiency and purity in reconstructed kinematics of  $\bar{\nu}_\mu$  CC non-QE interactions in the  $\bar{\nu}_\mu$  in RHC CC N-Track selections. The true events are any  $\bar{\nu}_\mu$  CC interaction except  $\bar{\nu}_\mu$  CCQE at the vertex and the selected lepton candidate is the true  $\mu^+$ .

1-Track is designed to select. As seen before, both the efficiency and purity are low where statistics are high.

The underlying true kinematics,  $E_\nu$ ,  $Q^2$ , and  $W$ , of the interactions are shown in Figure 3.23 on page 86. Here we see in better detail the origin of the  $\nu_\mu$  contamination. As a function of increasing energy, the  $\bar{\nu}_\mu$  content is decreasing while the relative  $\nu_\mu$  contribution is increasing. The  $\nu_\mu$  events also have a high  $Q^2$  content which explains the significant number of misidentified proton main track events. For the hadronic final states, the shape of the  $\bar{\nu}_\mu$ -induced resonances is similar to what we saw in Figure 3.15 on page 80. Interestingly, the  $\nu_\mu$  background hadronic mass distribution does not peak in any one region.

### 3.3.5 $\nu_\mu$ Background in RHC CC 1-Track

This selection provides the  $\nu_\mu$  in RHC, also called wrong-sign background, CCQE-like samples. Figure 3.24 on page 87 and Figure 3.25 on page 88 display the momentum and angular distributions that are inputs to BANFF. We can see this is a relatively low-angle, forward going selection compared to previous selections. Importantly the selection is  $\nu_\mu$ -pure

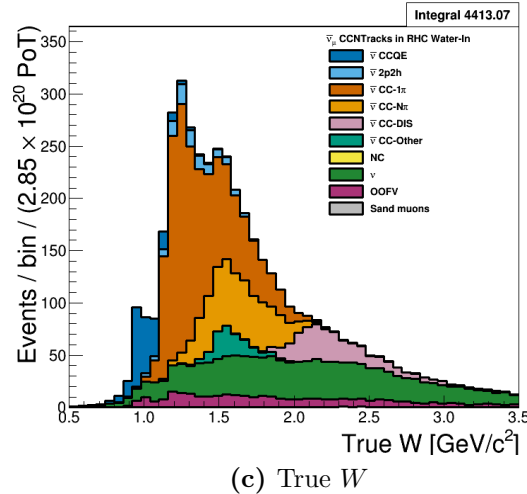
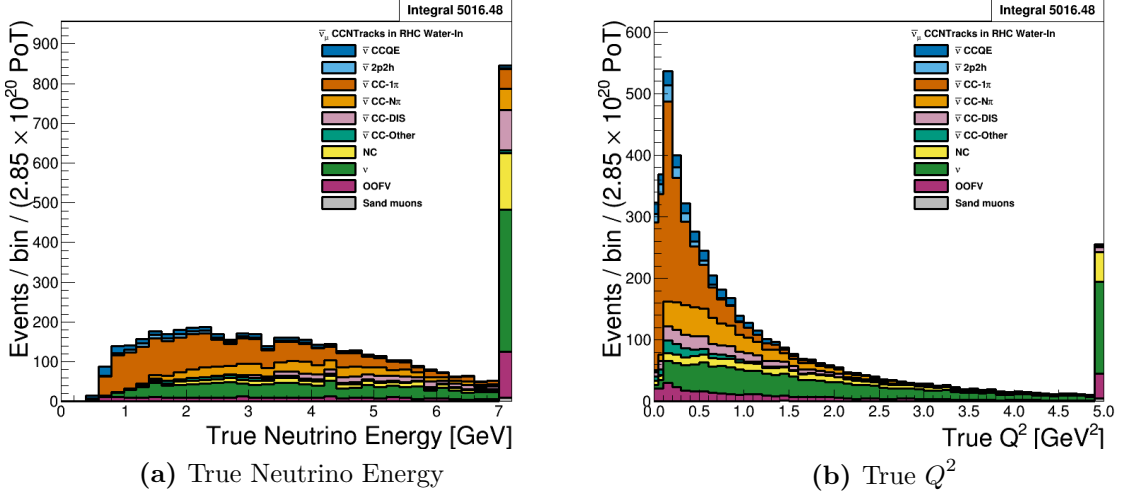


**Figure 3.23:** The  $\bar{\nu}_\mu$  in RHC CC N-Tracks true kinematics broken down by true NEUT interaction modes. The last bin shown in (a) and (b) is used as overflow. The figures use the PØD water-in MC and are normalized to the RHC water-in mode POT.

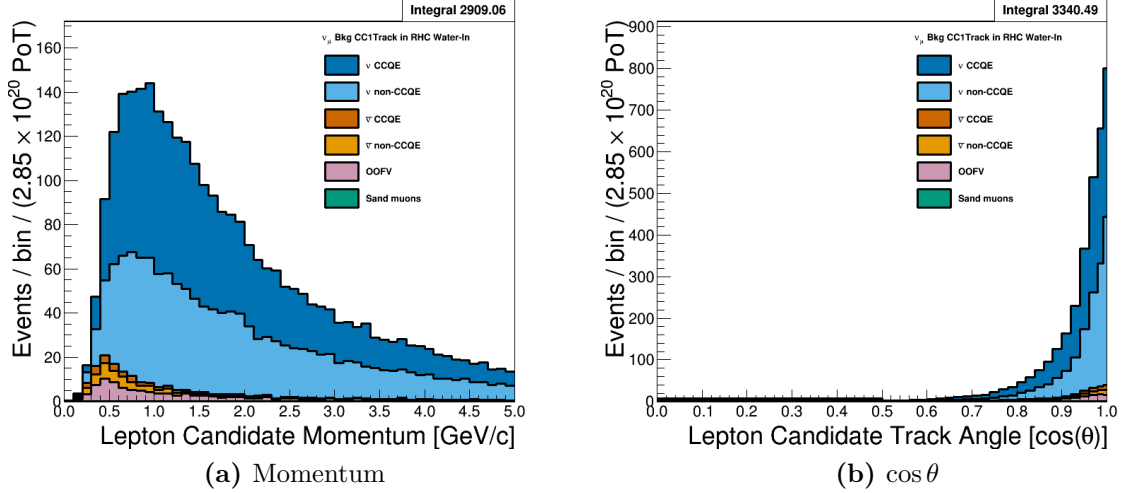


**Figure 3.24:** Lepton candidate reconstructed  $P$  and  $\cos\theta$  distributions for the  $\nu_\mu$  in RHC CC 1-Track selection for CCQE and non-CCQE interactions. The figures use the PØD water-in MC and are normalized to the RHC water-in mode POT.

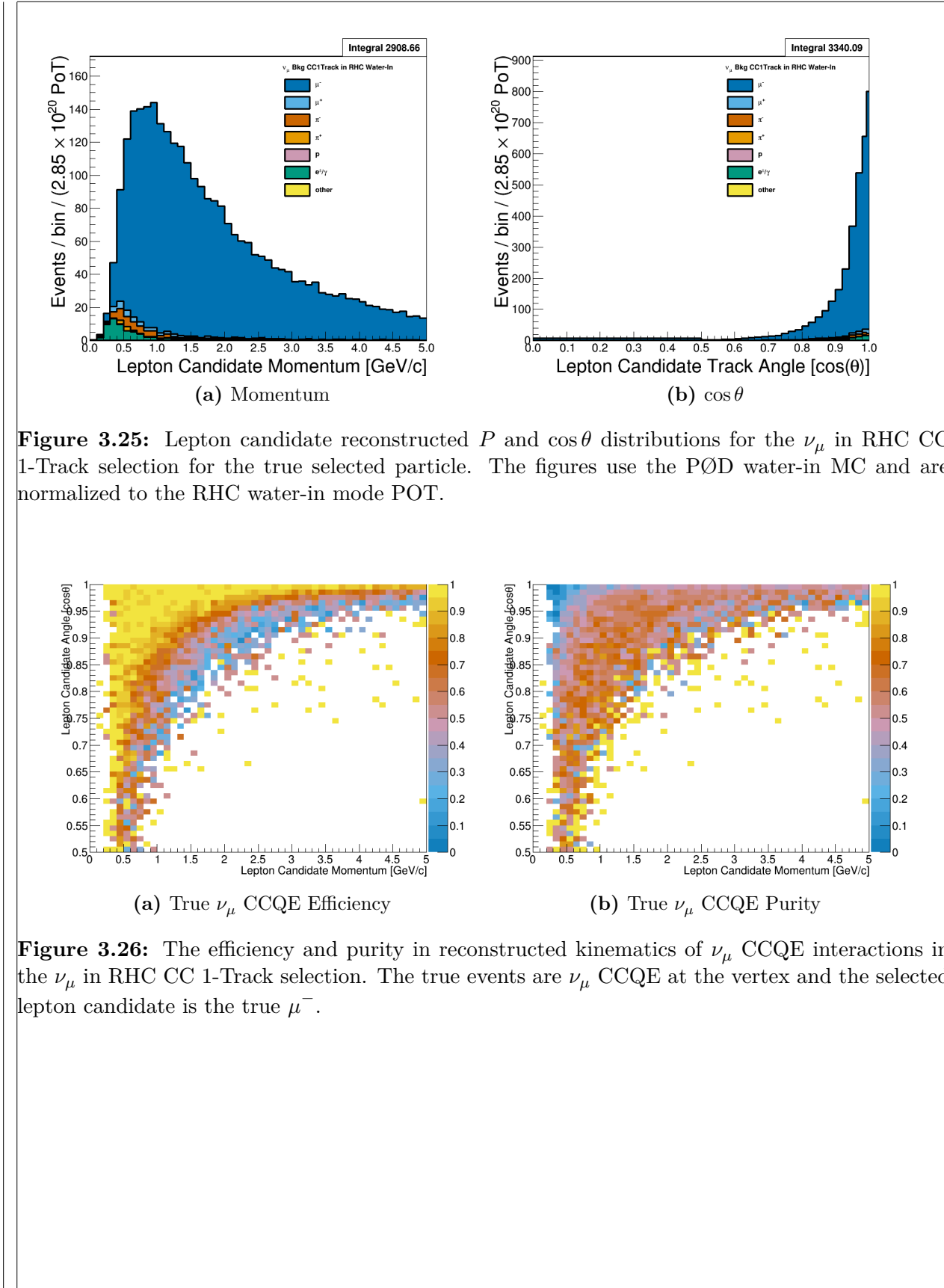
which should help constrain the wrong-sign background in BANFF. However, the CCQE purity is modest given number of correctly identified lepton candidates.

We can examine the efficiencies and purities differentially for the selection in Figure 3.26 on page 88. The efficiency is similar to the  $\nu_\mu$  in FHC CC 1-Track efficiency. As for the purity, it is roughly 70% in a banded region between low momenta, low angle and high momenta, high angle tracks.

The underlying true kinematics,  $E_\nu$  and  $Q^2$ , of the selection are shown in Figure 3.27 on page 89. Due to the flux of the wrong-sign background, the neutrino energy is not sharply peaked at 0.6 GeV. This explains the significant non-CCQE event contamination in the form of 2p2h and 1π interactions.

### 3.3.6 $\nu_\mu$ Background in RHC CC N-Tracks

This selection provides the  $\nu_\mu$  background non-CCQE-like samples in RHC mode. Figure 3.28 on page 90 and Figure 3.29 on page 90 show the momentum and angular distributions that are inputs to BANFF. We can see the selection is relatively  $\nu_\mu$ -pure with a



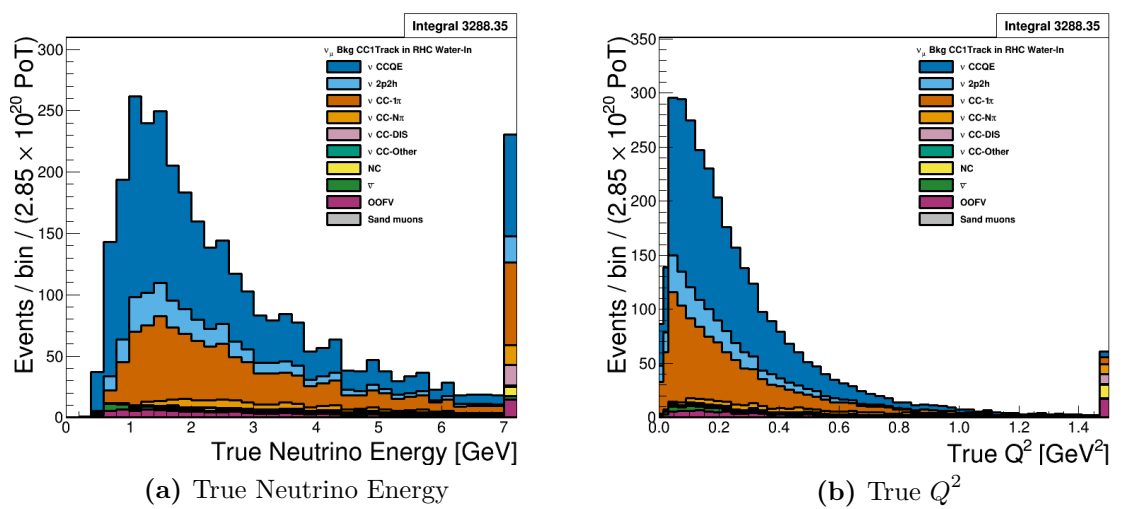


**Figure 3.27:** The  $\nu_\mu$  in RHC CC 1-Track true kinematics broken down by true NEUT interaction modes. Water-in mode is displayed here only with the last bin shown is used as overflow. The figures use the PØD water-in MC and are normalized to the RHC water-in mode POT.

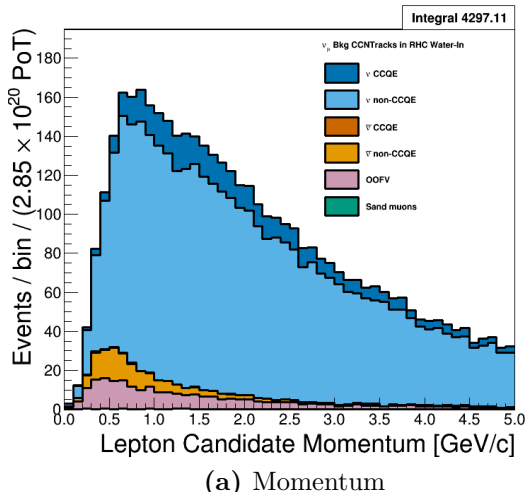
significant mis-identified track rate. Interestingly, the misidentified pion main tracks have a high momentum tail.

We can examine the  $\nu_\mu$  CC non-QE efficiency and purity of the selection in Figure 3.30 on page 91. There is a reduction in the purity below 1.5 GeV/c due to the the  $\bar{\nu}_\mu$  selections occupying the same phase space. Fortunately, the efficiency and purity are relatively high above 1.5 GeV/c.

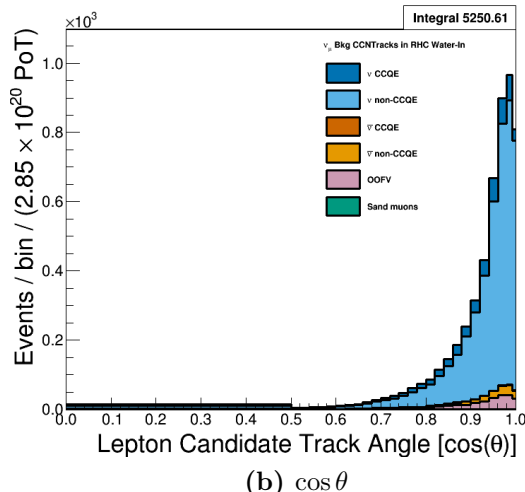
The underlying true kinematics,  $E_\nu$ ,  $Q^2$ , and  $W$ , of the interactions are shown in Figure 3.31 on page 92. As we have seen before with the CC N-Tracks samples, these are high  $E_\nu$  events with large  $Q^2$  exchanges. The invariant hadronic system displays the previously seen resonances, with the largest still being from the  $\Delta$  baryon.

### 3.4 Summary of Selections

We have examined that the selection procedures described above produces some reasonably pure CCQE samples using the 1-Track cut. By inverting that cut, we obtain some handles on other topologies like CC  $1\pi$  and high  $Q^2$  CCDIS events. Importantly is the abil-

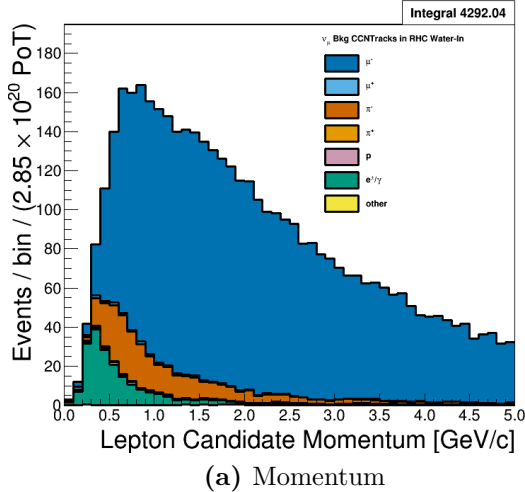


(a) Momentum

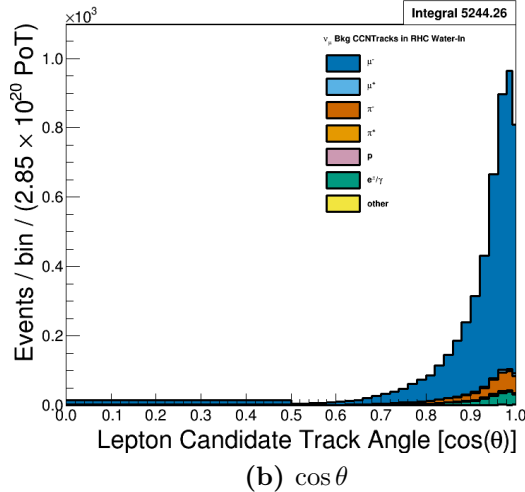


(b)  $\cos \theta$

**Figure 3.28:** Lepton candidate reconstructed  $P$  and  $\cos\theta$  distributions for the  $\nu_\mu$  in RHC CC N-Tracks selection for CCQE and non-CCQE interactions. The figures use the PØD water-in MC and are normalized to the RHC water-in mode POT.

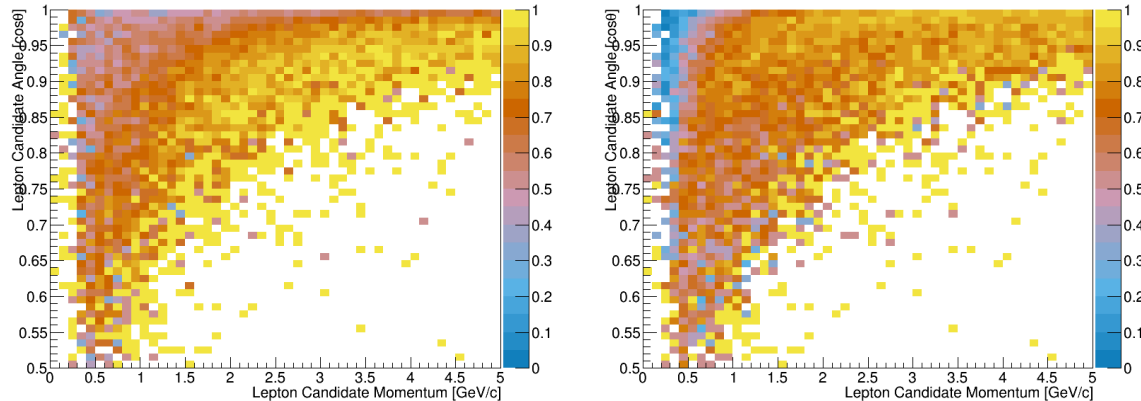


### (a) Momentum



(b)  $\cos \theta$

**Figure 3.29:** Lepton candidate reconstructed  $P$  and  $\cos\theta$  distributions for the  $\nu_\mu$  in RHC CC N-Tracks selection for the true selected particle. The figures use the PØD water-in MC and are normalized to the RHC water-in mode POT.

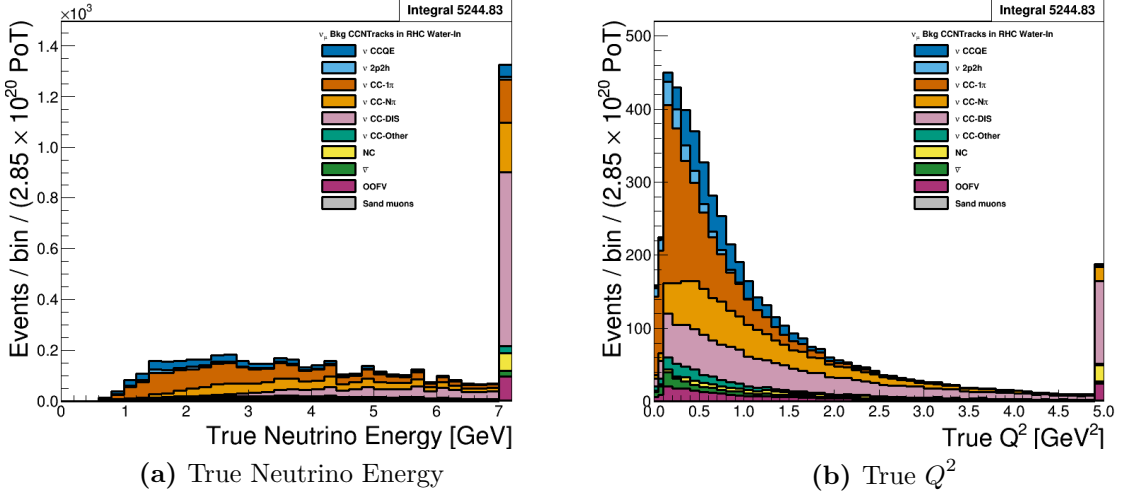


(a) True  $\nu_\mu$  CC non-QE Efficiency

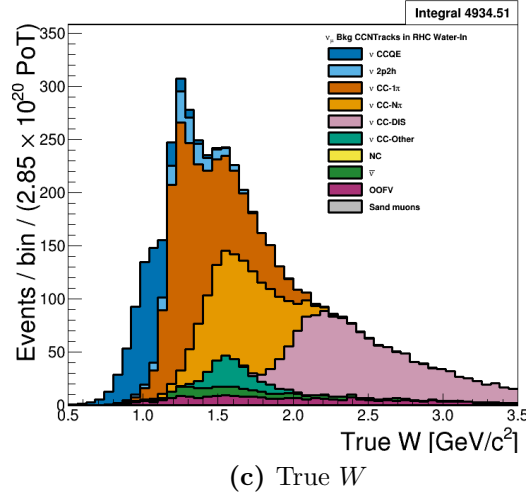
(b) True  $\nu_\mu$  CC non-QE Purity

**Figure 3.30:** The efficiency and purity in reconstructed kinematics of  $\bar{\nu}_\mu$  CC non-QE interactions in the  $\nu_\mu$  in RHC CC N-Tracks selection. The true events are any  $\nu_\mu$  CC interaction except  $\nu_\mu$  CCQE at the vertex and the selected lepton candidate is the true  $\mu^-$ .

ity to constrain the correct sign  $\nu_\mu$  and wrong sign backgrounds in RHC. We can now move forward to the next chapter to examine the systematic uncertainties present in the analysis.



(a) True Neutrino Energy

(b) True  $Q^2$ (c) True  $W$ 

**Figure 3.31:** The  $\nu_\mu$  in RHC CC N-Tracks true kinematics broken down by true NEUT interaction modes. The last bin shown in (a) and (b) is used as overflow. The figures use the PØD water-in MC and are normalized to the RHC water-in mode POT.

---

# Chapter 4

## The PØD-Only in BANFF Parameterization

In addition to the likelihood ratio maximization, the BANFF fit includes three sources of systematic uncertainties: neutrino flux, cross section model, and detector inefficiencies. This chapter explores the fit binning and penalty terms in the test statistic in this analysis. The sources of systematic uncertainties, also referred to just as systematics, will be defined in order to understand their effect on any analysis.

This chapter is presented in the following order. The first section explores the method to define fit bins in the likelihood ratio. The second section is divided into three subsections to define the parameterization of each penalty term in the test statistic. The penalty terms discussed in order are the neutrino flux model, the detector inefficiencies, and lastly the cross section model. These three terms directly affect the flux of neutrinos, efficiency of reconstruction, and the cross section for  $\nu_\alpha$  terms, respectively, in the expected rate equation given in ( 1.56).

---

## 4.1 Fit Binning

The PØD ND280 BANFF fit uses the samples described in Chapter 3. The bin edges used in the BANFF fit to evaluate the log-likelihood ratio term,  $\Delta\chi^2_{\text{LLR}}$ , are tabulated below. There are a total 988 fit bins with water-in and water-out modes sharing the same bin edges. The determination of the fit binning is discussed in the next subsection.

- $\nu_\mu$  in CC 1-Track fit bin edges:
  - $p$  [GeV/c]: 0, 0.3, 0.4, 0.5, 0.6, 0.7, 0.8, 1, 1.25, 1.5, 2, 3, 4, 5.5, 30
  - $\cos\theta$ : -1, 0.7, 0.8, 0.88, 0.94, 0.96, 0.975, 0.99, 1
- $\nu_\mu$  in FHC CC N-Tracks fit bin edges:
  - $p$  [GeV/c]: 0, 0.4, 0.5, 0.6, 0.7, 0.8, 1, 1.2, 1.5, 1.8, 2.2, 2.7, 3.5, 5, 10, 30
  - $\cos\theta$ : -1, 0.65, 0.77, 0.85, 0.9, 0.94, 0.97, 0.99, 1
- $\bar{\nu}_\mu$  in RHC CC 1-Track fit bin edges:
  - $p$  [GeV/c]: 0, 0.4, 0.5, 0.6, 0.7, 0.8, 1, 1.25, 1.5, 2, 3, 30
  - $\cos\theta$ : -1, 0.82, 0.87, 0.9, 0.93, 0.95, 0.97, 0.99, 1
- $\bar{\nu}_\mu$  in RHC CC N-Tracks fit bin edges:
  - $p$  [GeV/c]: 0, 0.5, 0.9, 1.25, 1.6, 2, 3, 8, 30
  - $\cos\theta$ : -1, 0.8, 0.89, 0.95, 0.97, 0.99, 1
- $\nu_\mu$  in RHC CC 1-Track fit bin edges:
  - $p$  [GeV/c]: 0, 0.4, 0.6, 0.8, 1.1, 2, 10
  - $\cos\theta$ : -1, 0.78, 0.84, 0.89, 0.92, 0.95, 0.97, 0.98, 0.99, 1
- $\nu_\mu$  in RHC CC N-Tracks bin edges:

- $p$  [GeV/c]: 0, 0.4, 0.6, 0.8, 1, 1.5, 2, 3, 10
- $\cos \theta$  : -1, 0.7, 0.8, 0.85, 0.9, 0.94, 0.965, 0.98, 0.99, 1

### 4.1.1 Fit Binning Determination

The fit binning is optimized to ensure at least 1 predicted Monte Carlo (MC) event in each bin when scaled to the collected data POT. The fit bins must also account for detector smearing effects. In order to mitigate smearing and event migration, the reconstructed kinematics were examined to their MC truth value using only correctly identified leptons in one-dimensional kinematic slices. Since the MC provides about  $10\times$  the data statistics, the statistical uncertainty for each bin should be negligible in high statistics regions. The kinematics are scanned across their full relevant spaces in order to understand the required width for a fit bin. The first fit bin is always defined starting from the kinematic maximum.

For the momentum bins, the momentum resolution is compared to MC truth. The momentum resolution is defined as

$$R(r, t) = \frac{r - t}{t},$$

where  $r$  is the reconstructed momentum and  $t$  is the true momentum. The momentum was scanned in finite bin widths with the mean and standard deviation of the resolution  $R$  extracted. The mean and standard deviation are used as a proxy for the true bias and resolution, respectively. In addition, a bootstrapping algorithm was employed to understand the accuracy of the sample estimates. Bootstrapping in this context is sampling over all relevant values of true momentum and randomly replacing the values. For each scanned bin, at least 1000 bootstrapping sampling with replacement was performed. In the case of large variances in the bootstrapping samples, additional 10000 sampling with replacement were performed. The results for analyzing the  $\nu_\mu$  in FHC CC 1-Track selection is shown in Figure 4.1 on page 96.

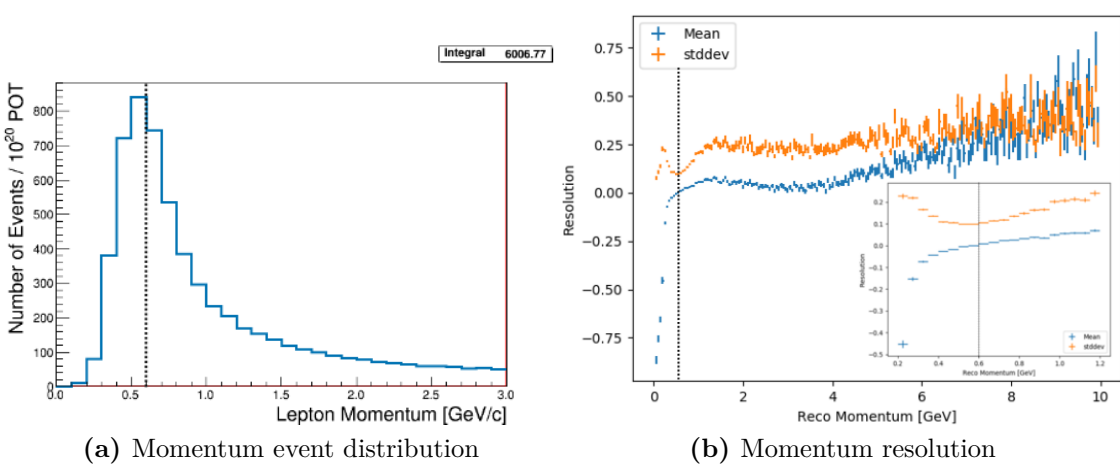


**Figure 4.1:** The momentum event distribution and uncertainty for  $\nu_\mu$  in FHC CC 1-Track events is shown above. Only correctly identified muons are shown. (a) The number of events is scaled to  $10^{20}$  POT which is the approximate scale for all the samples in this analysis. A dashed line indicates the maximum of the peak. (b) The resolution of the momentum measurement is shown for a wide region of momenta. In the inset is the resolution zoomed near the momentum distribution maximum. Like in (a), a dashed line shows the momentum maximum.

The angle fit bins are treated in an almost identical manner. While the fit bins and Physics are dictated in  $\cos\theta$  space, the detector smearing is a function  $\theta$ . In addition, since the angle can be nearly zero for the most forward-going tracks, the resolution was not used to characterize the angular uncertainties. Instead, the difference between the true and reconstructed angle were analyzed as shown in Figure 4.2 on page 97. The mean and standard deviation were studied as before to set the fit  $\cos\theta$  bin edges. Bootstrapping was again used to quantify the accuracy of the mean and standard deviation.

## 4.2 Penalty Terms and Systematic Uncertainties

This section expands on the definition of the penalty terms in the BANFF fit. The cross section and flux penalty terms in this analysis are identical to previous BANFF studies since the T2K experiment utilizes a set of canonical flux and cross section systematics that are shared between ND280 and SK. Also, those systematics are not altered in this analysis for the purpose of comparability between PØD-only and FGD-only best fit results. For the ND280

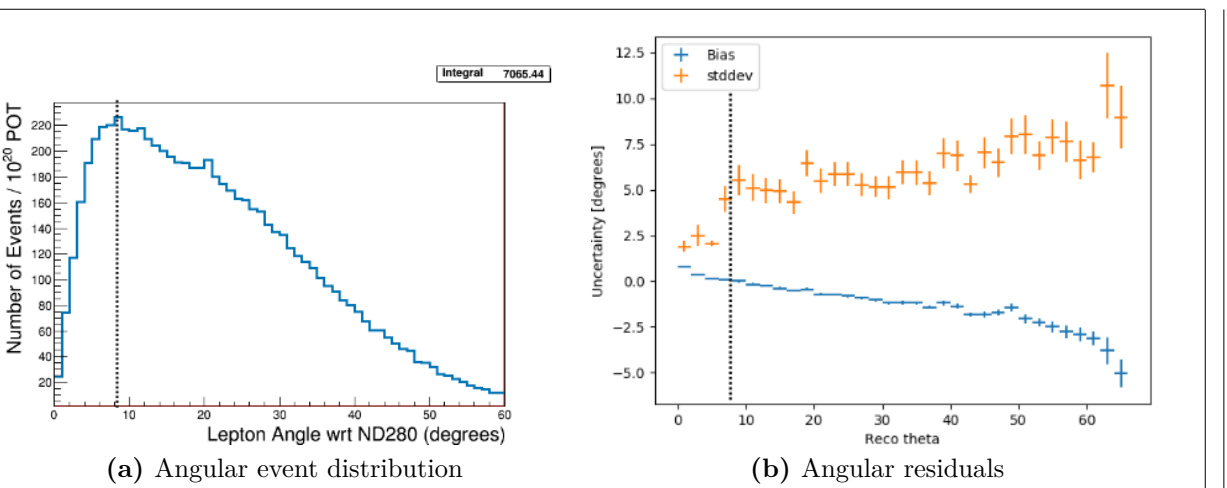


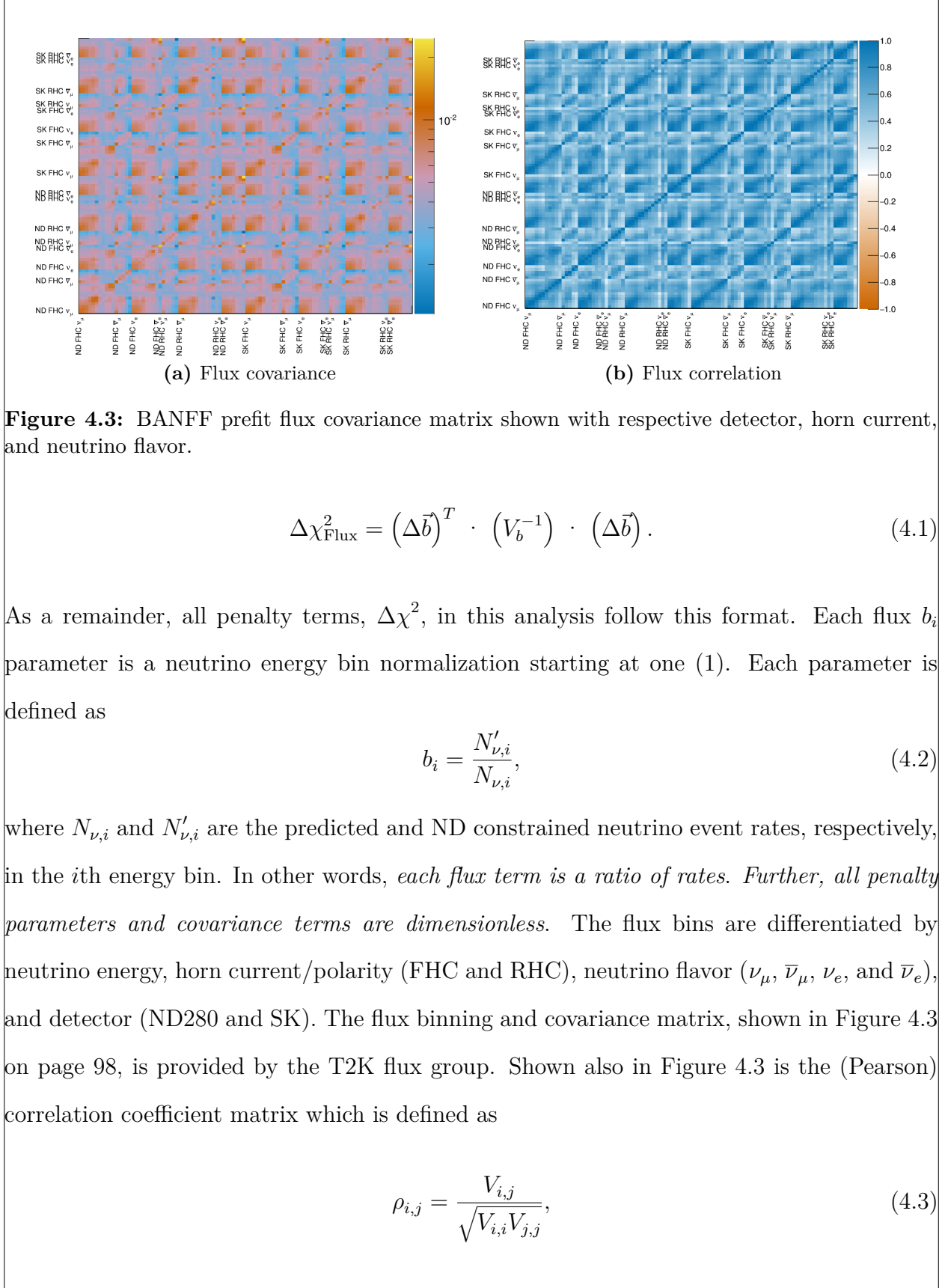
**Figure 4.2:** The angular event distribution and uncertainty for  $\nu_\mu$  in FHC CC 1-Track events is shown above. Only correctly identified muons are shown. (a) The number of events is scaled to  $10^{20}$  POT which is the approximate scale for all the samples in this analysis. A dashed line indicates the track angle distribution maximum of the peak. (b) The residual of the angular measurement is shown up to where there are sufficient statistics. Like in (a), a dashed line shows the distribution maximum.

detector systematics, many are shared between the PØD and TPC subdetectors. However, due to the different detector technologies, additional detector inefficiency systematics will be incorporated.

### 4.2.1 Flux Model

The T2K neutrino flux model is a description of the neutrino beam spectrum by run period and flavor. This model includes simulations of the beam interactions and subsequent hadron production at the target. The predicted hadron production rate, including inside and outside the target, is tuned to the results from the NA61/SHINE [10] replica target experiment and other hadron production experiments. The uncertainties in the unoscillated flux tuning are dominated on hadron production. Smaller effects on the unoscillated flux uncertainty include the proton beam profile, off-axis angle, horn current, and horn alignment. Further details about the flux model and uncertainties can be found in the following reference [4].

The flux penalty term in the BANFF fit is defined, as previously seen in Chapter 2, as



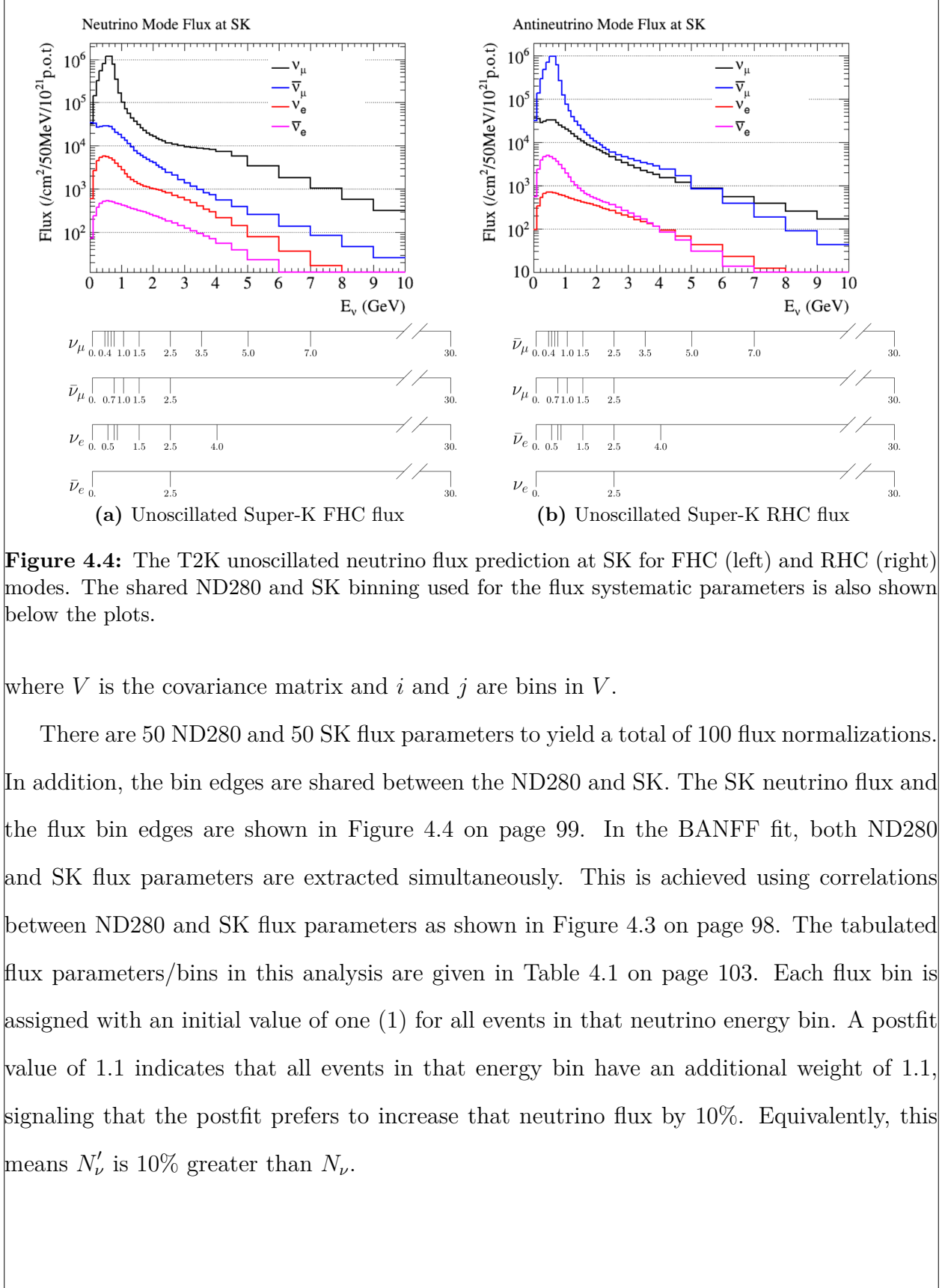


**Figure 4.4:** The T2K unoscillated neutrino flux prediction at SK for FHC (left) and RHC (right) modes. The shared ND280 and SK binning used for the flux systematic parameters is also shown below the plots.

where  $V$  is the covariance matrix and  $i$  and  $j$  are bins in  $V$ .

There are 50 ND280 and 50 SK flux parameters to yield a total of 100 flux normalizations. In addition, the bin edges are shared between the ND280 and SK. The SK neutrino flux and the flux bin edges are shown in Figure 4.4 on page 99. In the BANFF fit, both ND280 and SK flux parameters are extracted simultaneously. This is achieved using correlations between ND280 and SK flux parameters as shown in Figure 4.3 on page 98. The tabulated flux parameters/bins in this analysis are given in Table 4.1 on page 103. Each flux bin is assigned with an initial value of one (1) for all events in that neutrino energy bin. A postfit value of 1.1 indicates that all events in that energy bin have an additional weight of 1.1, signaling that the postfit prefers to increase that neutrino flux by 10%. Equivalently, this means  $N'_\nu$  is 10% greater than  $N_\nu$ .

**Table 4.1:** Flux binning and uncertainties used in the BANFF fit.

Fit index	Beam mode	Bin edges [GeV]	Prefit
0	ND280 $\nu_\mu$ FHC	0.0 - 0.4	$1 \pm 0.100909$
1		0.4 - 0.5	$1 \pm 0.099431$
2		0.5 - 0.6	$1 \pm 0.092025$
3		0.6 - 0.7	$1 \pm 0.085239$
4		0.7 - 1.0	$1 \pm 0.105356$
5		1.0 - 1.5	$1 \pm 0.104375$
6		1.5 - 2.5	$1 \pm 0.073612$
7		2.5 - 3.5	$1 \pm 0.068993$
8		3.5 - 5.0	$1 \pm 0.082334$
9		5.0 - 7.0	$1 \pm 0.097308$
10		7.0 - 30	$1 \pm 0.114706$
11	ND280 $\bar{\nu}_\mu$ FHC	0.0 - 0.7	$1 \pm 0.103804$
12		0.7 - 1.0	$1 \pm 0.084158$
13		1.0 - 1.5	$1 \pm 0.081349$
14		1.5 - 2.5	$1 \pm 0.085208$
15		2.5 - 30	$1 \pm 0.087735$
16	ND280 $\nu_e$ FHC	0.0 - 0.5	$1 \pm 0.091336$
17		0.5 - 0.7	$1 \pm 0.089699$
18		0.7 - 0.8	$1 \pm 0.084648$
19		0.8 - 1.5	$1 \pm 0.079722$
20		1.5 - 2.5	$1 \pm 0.079766$
21		2.5 - 4.0	$1 \pm 0.081399$
22		4.0 - 30	$1 \pm 0.095795$
23	ND280 $\bar{\nu}_e$ FHC	0.0 - 2.5	$1 \pm 0.072069$
24		2.5 - 30	$1 \pm 0.142921$

**Table 4.1:** Flux binning and uncertainties used in the BANFF fit.

Fit index	Beam mode	Bin edges [GeV]	Prefit
25	ND280 $\nu_\mu$ RHC	0.0 - 0.7	$1 \pm 0.094066$
26		0.7 - 1.0	$1 \pm 0.079866$
27		1.0 - 1.5	$1 \pm 0.080948$
28		1.5 - 2.5	$1 \pm 0.083251$
29		2.5 - 30	$1 \pm 0.082653$
30	ND280 $\bar{\nu}_\mu$ RHC	0.0 - 0.4	$1 \pm 0.107277$
31		0.4 - 0.5	$1 \pm 0.098851$
32		0.5 - 0.6	$1 \pm 0.089710$
33		0.6 - 0.7	$1 \pm 0.084692$
34		0.7 - 1.0	$1 \pm 0.106871$
35		1.0 - 1.5	$1 \pm 0.098711$
36		1.5 - 2.5	$1 \pm 0.073350$
37		2.5 - 3.5	$1 \pm 0.070520$
38		3.5 - 5.0	$1 \pm 0.092905$
39		5.0 - 7.0	$1 \pm 0.089083$
40		7.0 - 30	$1 \pm 0.134911$
41	ND280 $\nu_e$ RHC	0.0 - 2.5	$1 \pm 0.066214$
42		2.5 - 30	$1 \pm 0.086977$
43	ND280 $\bar{\nu}_e$ RHC	0.0 - 0.5	$1 \pm 0.095575$
44		0.5 - 0.7	$1 \pm 0.089033$
45		0.7 - 0.8	$1 \pm 0.088406$
46		0.8 - 1.5	$1 \pm 0.081472$
47		1.5 - 2.5	$1 \pm 0.078353$
48		2.5 - 4.0	$1 \pm 0.089427$
49		4.0 - 30	$1 \pm 0.156972$

**Table 4.1:** Flux binning and uncertainties used in the BANFF fit.

Fit index	Beam mode	Bin edges [GeV]	Prefit
50	Super-K $\nu_\mu$ FHC	0.0 - 0.4	$1 \pm 0.102555$
51		0.4 - 0.5	$1 \pm 0.101771$
52		0.5 - 0.6	$1 \pm 0.092573$
53		0.6 - 0.7	$1 \pm 0.084265$
54		0.7 - 1.0	$1 \pm 0.102271$
55		1.0 - 1.5	$1 \pm 0.084528$
56		1.5 - 2.5	$1 \pm 0.066909$
57		2.5 - 3.5	$1 \pm 0.072355$
58		3.5 - 5.0	$1 \pm 0.085299$
59		5.0 - 7.0	$1 \pm 0.096725$
60		7.0 - 30	$1 \pm 0.114112$
61	Super-K $\bar{\nu}_\mu$ FHC	0.0 - 0.7	$1 \pm 0.103129$
62		0.7 - 1.0	$1 \pm 0.078327$
63		1.0 - 1.5	$1 \pm 0.082367$
64		1.5 - 2.5	$1 \pm 0.082121$
65		2.5 - 30	$1 \pm 0.085123$
66	Super-K $\nu_e$ FHC	0.0 - 0.5	$1 \pm 0.090918$
67		0.5 - 0.7	$1 \pm 0.087065$
68		0.7 - 0.8	$1 \pm 0.082527$
69		0.8 - 1.5	$1 \pm 0.076514$
70		1.5 - 2.5	$1 \pm 0.075773$
71		2.5 - 4.0	$1 \pm 0.082078$
72		4.0 - 30	$1 \pm 0.092882$
73	Super-K $\bar{\nu}_e$ FHC	0.0 - 2.5	$1 \pm 0.071921$
74		2.5 - 30	$1 \pm 0.128982$

**Table 4.1:** Flux binning and uncertainties used in the BANFF fit.

Fit index	Beam mode	Bin edges [GeV]	Prefit
75	Super-K $\nu_\mu$ RHC	0.0 - 0.7	$1 \pm 0.093954$
76		0.7 - 1.0	$1 \pm 0.076369$
77		1.0 - 1.5	$1 \pm 0.074900$
78		1.5 - 2.5	$1 \pm 0.078108$
79		2.5 - 30	$1 \pm 0.077505$
80	Super-K $\bar{\nu}_\mu$ RHC	0.0 - 0.4	$1 \pm 0.108593$
81		0.4 - 0.5	$1 \pm 0.101912$
82		0.5 - 0.6	$1 \pm 0.092787$
83		0.6 - 0.7	$1 \pm 0.082669$
84		0.7 - 1.0	$1 \pm 0.102090$
85		1.0 - 1.5	$1 \pm 0.087732$
86		1.5 - 2.5	$1 \pm 0.068117$
87		2.5 - 3.5	$1 \pm 0.069902$
88		3.5 - 5.0	$1 \pm 0.091711$
89		5.0 - 7.0	$1 \pm 0.084736$
90		7.0 - 30	$1 \pm 0.115488$
91	Super-K $\nu_e$ RHC	0.0 - 2.5	$1 \pm 0.066204$
92		2.5 - 30	$1 \pm 0.082645$
93	Super-K $\bar{\nu}_e$ RHC	0.0 - 0.5	$1 \pm 0.095453$
94		0.5 - 0.7	$1 \pm 0.088889$
95		0.7 - 0.8	$1 \pm 0.085644$
96		0.8 - 1.5	$1 \pm 0.078536$
97		1.5 - 2.5	$1 \pm 0.075246$
98		2.5 - 4.0	$1 \pm 0.086384$
99		4.0 - 30	$1 \pm 0.152507$

### 4.2.2 Detector Inefficiencies Model

In the BANFF fit, bin normalization parameters are used to evaluate the detector inefficiency penalty term,  $\Delta\chi^2_{\text{Det}}$ . Varying fit bins without constraint is nonphysical due to known detector inefficiencies and their systematic uncertainties. Since improperly modeled inefficiencies can cause events to migrate from bin-to-bin, numerous fake “toy experiments” are performed to evaluate the systematic uncertainties in detector inefficiencies. When all toy experiments are analyzed together, correlated variations among fit bins become apparent. These correlations provide the constraints on freely changing bin normalizations. We will see the result of running such toy experiment variations in the coming pages. Hitherto in this thesis, detector inefficiency uncertainties will be referred to as detector systematics.

All the detector systematics are evaluated either as observable variations or weights as given in given in Table 4.2 on page 105. An observable variation affects the physical observables of selected events like the calculated energy loss of a track in the PØD. A weight is a multiplicative factor that alters the normalization of a single event in a bin. There are detector systematics that affect the PØD-only, TPC-only, or both. So a description of the systematic treatments is discussed in the next section. The new PØD-only systematics in BANFF will then be explained later. Details on the TPC-only systematics implementations are discussed in the following reference [4].

## Systematic Treatments

There are two types of systematic treatments in the BANFF analysis: observable variations and weights. Each rely on the method of throwing a random number,  $x$ , to evaluate the systematic.

Efficiency-like systematics are treated as weights to the MC predictions in order to evaluate the uncertainty the systematic has on an analysis. They are based on studies comparing

Systematic effect	Affected Detector	Treatment
TPC cluster eff.	TPC	efficiency
TPC tracking eff.	TPC	efficiency
TPC charge misassignment	TPC	efficiency
TPC momentum resol.	TPC	observable variation
TPC momentum scale	TPC	observable variation
B field distortion	TPC	observable variation
Pion secondary interactions	All	efficiency
Proton secondary interactions	All	efficiency
TPC Particle ID	TPC	observable variation
TPC track quality eff.	TPC	efficiency
<hr/>		
PØD energy loss scale	PØD	observable variation
PØD energy loss resol.	PØD	observable variation
PØD mass	PØD	(see text)
PØD-TPC matching eff.	PØD+TPC	(see text)

**Table 4.2:** List of detector systematic effects and the way each one is treated within the simulated samples to propagate the uncertainty. The systematics listed above the horizontal line are discussed in the following reference [4]. The PØD mass and track matching systematics were not available in the BANFF framework and treated as uncorrelated additions to the total covariance matrix.

data and MC predictions in control samples (CS). A CS is designed to provide a reliable measurement with minimal influence from other dependent and independent factors. An example of a well established CS is a collection of single, isolated cosmic ray (muon) tracks to measure the energy loss in a detector. In general, a CS may have different properties than the analysis sample like event topology. In particular the cosmic ray CS cannot account for efficiency effects if other tracks present. Therefore a model extrapolation is needed to map the CS to the analysis sample. The model used in BANFF is that the efficiency of the data and MC is the same in both analysis sample and CS

$$\epsilon_{\text{Data}}(o) = \left( \frac{\epsilon_{\text{Data}}(o)}{\epsilon_{\text{MC}}(o)} \right)_{\text{CS}} \epsilon_{\text{MC}}(o), \quad (4.4)$$

where  $\epsilon_{\text{MC}}/\epsilon_{\text{Data}}$  denotes the mean efficiency of the MC/data as a function of some observable  $o$ . We need to update this model to account for statistical uncertainties in the CS. The updated model, with  $o$  dependence assumed, is now

$$\epsilon'_{\text{Data}} = \left( \frac{\epsilon_{\text{Data}} + x_{\text{Data}} \cdot \sigma_{\epsilon_{\text{Data}}}}{\epsilon_{\text{MC}} + x_{\text{MC}} \cdot \sigma_{\epsilon_{\text{MC}}}} \right)_{\text{CS}} \epsilon_{\text{MC}} \quad (4.5)$$

where  $\sigma_{\epsilon_{\text{MC}}} / \sigma_{\epsilon_{\text{Data}}}$  is the standard deviation of the efficiency of the MC/Data and  $x_{\text{Data}}$  and  $x_{\text{MC}}$  are different, random normally distributed numbers from  $\mathcal{N}(\mu = 0, \sigma^2 = 1)$ . The selection is rerun on the event and a weight is derived depending if the event is selected,  $w_{\text{eff}}$ , or not selected,  $w_{\text{ineff}}$ . These weights are given below

$$w_{\text{eff}} = \frac{\epsilon'_{\text{Data}}}{\epsilon_{\text{MC}}} \quad (4.6)$$

$$w_{\text{ineff}} = \frac{1 - \epsilon'_{\text{Data}}}{1 - \epsilon_{\text{MC}}}.$$

Observable variation systematics are evaluated as alterations to physically measured quantities like momentum and energy. The systematic can be evaluated in two different ways:

- If the reconstructed observable,  $o_{\text{reco}}$ , has a known true value,  $o_{\text{true}}$ , then the difference between those two is used as scaling. The varied observable is given by

$$o' = o_{\text{true}} + (o_{\text{reco}} - o_{\text{true}})(s + x\sigma_s), \quad (4.7)$$

where  $s$  is the mean scaling parameter to match the true value,  $\sigma_s$  is the uncertainty on  $s$ , and  $x$  is a random number from  $\mathcal{N}(\mu = 0, \sigma^2 = 1)$ . The mean scaling parameter and its uncertainty are determined from the standard deviations observed in the data and MC by

$$s = \frac{\delta^{\text{data}}}{\delta^{\text{MC}}} \quad \sigma_s = s \left| \frac{\sigma_{\delta^{\text{data}}}}{\delta^{\text{data}}} - \frac{\sigma_{\delta^{\text{MC}}}}{\delta^{\text{MC}}} \right|. \quad (4.8)$$

- If the MC reconstructed observable is corrected to match the mean from some CS reconstructed observable. The varied observable in this case is given by

$$o' = o_{\text{Nom}} + \Delta o + x\sigma_{\Delta o}, \quad (4.9)$$

---

where  $o'$  is the varied observable value,  $o_{\text{Nom}}$  is the nominal MC value,  $\Delta o$  is the average correction to the observable,  $\sigma_{\Delta o}$  is the uncertainty on the correction, and  $x$  is a random, normal number from  $\mathcal{N}(\mu = 0, \sigma^2 = 1)$ . Special cases exist for this treatment and are further discussed in the following thesis [75].

In both cases, the selection cuts are rerun on the event determining if it has changed samples.

Now that we understand how the systematics affect our observables and by using toy experiments to evaluate the systematics, we can now begin to understand how the detector systematic penalty term  $\Delta\chi^2_{\text{Det}}$  is modeled in the BANFF fit.

### Bin Normalizations And Covariance

As stated before, the bin normalization penalty parameters are restrictions on freely varying fit bins. To determine how correlated different fit bins are, many toy experiments are performed which vary the observables  $(p, \cos \theta)$ . The bin normalization parameter for the  $i$ th bin, or  $d_i$ , is defined as

$$d_i = \frac{\langle N_i \rangle_{\text{toys}}}{N_i}, \quad (4.10)$$

where  $N_i$  predicted number of events in fit bin  $i$  and  $\langle N_i \rangle_{\text{toys}}$  is the average number of events in fit bin  $i$  evaluated over all toy experiments (toys). The predicted event rate for bin  $i$  is given by

$$N_i = \sum_k^{N_{\text{MC}}} \delta_{i,k}^{\text{bin}} w_k, \quad (4.11)$$

where  $N_{\text{MC}}$  being the number of unweighted MC events,  $\delta_{i,k}^{\text{bin}}$  determines if the  $k$ th event goes into analysis bin  $i$  as a function of  $(p, \cos \theta)$ , and  $w_k$  being the product of all the weights applied to the  $k$ th event. The weights used in ( 4.11) are

$$w_k = w_k^{\text{POT}} \times w_k^{\text{Flux}} \times w_k^{\text{xsec}} \times w_k^{\text{Det}}, \quad (4.12)$$

(see ( 2.8) for all possible weights). The average number of events in fit bin  $i$  over all toys is given by

$$\begin{aligned}\langle N_i \rangle_{\text{toys}} &= \frac{1}{N_{\text{toys}}} \sum_{t=1}^{N_{\text{toys}}} (N_i)_t \\ &= \frac{1}{N_{\text{toys}}} \sum_{t=1}^{N_{\text{toys}}} \left( \sum_k^{N_{\text{MC}}} [\delta_{i,k}^{\text{bin}} w_k] \right)_t,\end{aligned}\quad (4.13)$$

where now each MC event has a toy variation out of  $N_{\text{toys}}$  total toys. For every single event in a toy experiment  $t$ , the selections cuts must be reapplied to determine if the event has changed analysis bins since the toy alters the event observables like the number of tracks or

$$(p, \cos \theta) \xrightarrow{\text{toy}} (p', \cos \theta'),$$

where  $p \neq p'$  and  $\theta \neq \theta'$  and if the event is reconstructed at all. We therefore average the results of the toys to smooth out variations among all toy experiments.

As stated before, all the penalty parameters are dimensionless and the detector systematics covariance matrix must be constructed carefully. The bin-to-bin event rate covariance,  $V_{i,j}^{\text{Cov}}$ , between bins  $i$  and  $j$  is

$$V_{i,j}^{\text{Cov}} = \frac{1}{N_{\text{toys}}} \sum_{t=1}^{N_{\text{toys}}} ((N_i)_t - \langle N_i \rangle_{\text{toys}}) \left( (N_j)_t - \langle N_j \rangle_{\text{toys}} \right), \quad (4.14)$$

where  $(N_i)_t$  is defined in ( 4.13). We also need to account for statistical uncertainties in the fit bins, and so let us define  $V_{i,j}^{\text{Stat}}$  as

$$V_{i,j}^{\text{Stat}} = \delta_{i,j} \sum_k^{N_{\text{MC}}} \delta_{i,k}^{\text{bin}} w_k^2, \quad (4.15)$$

where  $\delta_{i,j}$  is the Kronecker delta function. In order to use both  $V_{i,j}^{\text{Cov}}$  and  $V_{i,j}^{\text{Stat}}$  uncertainties, the total detector covariance matrix,  $V_{i,j}^{\text{Det}}$ , in the BANFF fit is defined as

$$V_{i,j}^{\text{Det}} = \left[ \frac{1}{N_i} \right] \left[ \frac{1}{N_j} \right] (V_{i,j}^{\text{Cov}} + V_{i,j}^{\text{Stat}}), \quad (4.16)$$

---

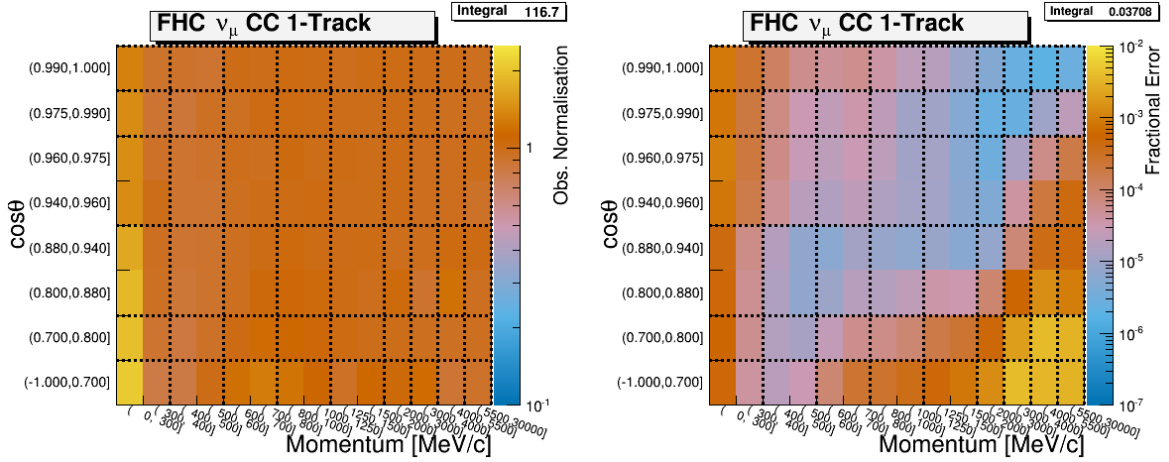
which is indeed dimensionless since we divided out the predicted event rate in bins  $i$  and  $j$ .

## Bin Normalization Edges

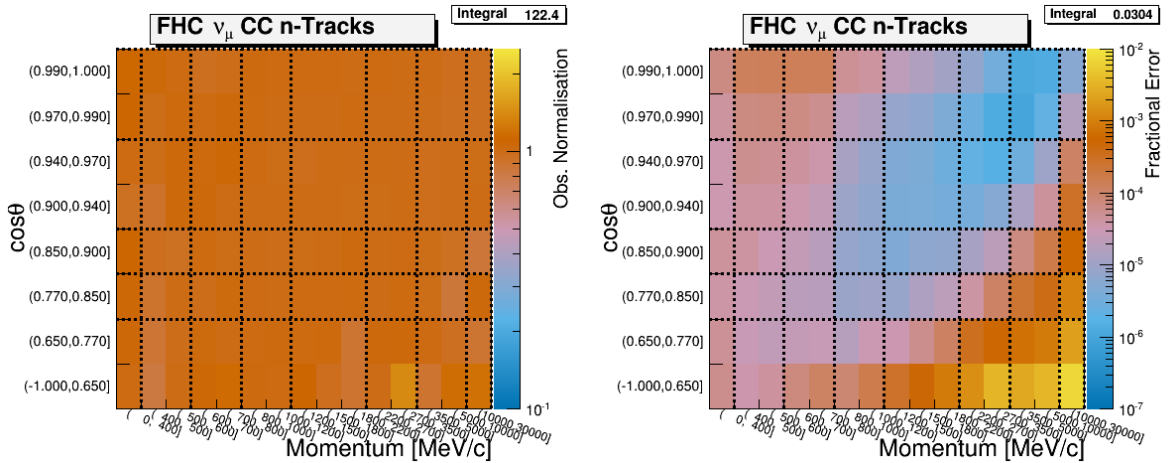
While there could be one observable normalization for each analysis bin, a single normalization can be assigned to multiple analysis bins. The purpose is to reduce the number of fit parameters since the time to fit increases non-linearly with the number of fit parameters and events. Previously, the observable normalization edges were determined by combining fit bins with “similar” covariance. This method proved problematic since the fit bins with relatively higher statistics were shared with the same observable normalization parameter. This left the remaining low statistics regions of  $(p, \cos \theta)$  phase space more susceptible to systematic variations in the toy experiments.

A new procedure was developed to improve the shortcomings of old procedure which requires careful consideration of the statistical uncertainties and variations between observable normalization prefit values. This procedure can be imagined as lowering the number of contours in a topographic map while considering external constraints from other sensing data. To start, initialize all the observable normalization bin edges to be the same as the fit bin edges. All steps after this are performed iteratively. Starting from the observable normalization bin with the highest statistics, consider merging it with all immediate adjacent bins. If the individual fractional errors differ significantly before the merge, do not merge them. In this analysis, a factor of 10 in fractional uncertainty was chosen to describe the similarity between bins. Additionally if the two unmerged bin normalizations differ by more than 10%, perform the bin merging. This step serves to smooth out the observable normalization prefit space.

While the problem of a few observable normalization parameters having the majority of statistics is still present, fluctuations between adjacent observable normalization parameters is iteratively minimized. The detector systematic that had the largest effect on the observable normalization prediction was the PØD energy loss resolution. With it, the event rate in each



(a)  $\nu_\mu$  in FHC CC 1-Track



(b)  $\nu_\mu$  in FHC CC N-Tracks

**Figure 4.5:** Bin normalization edges for the  $\nu_\mu$  in FHC selections. There are two plots shown for each sub-figure. The left and right plots show the bin normalization and the bin statistical fractional error, respectively, if each fit bin had a single bin normalization. The dashed lines indicate the edges of the bin normalization parameters finalized for this analysis.

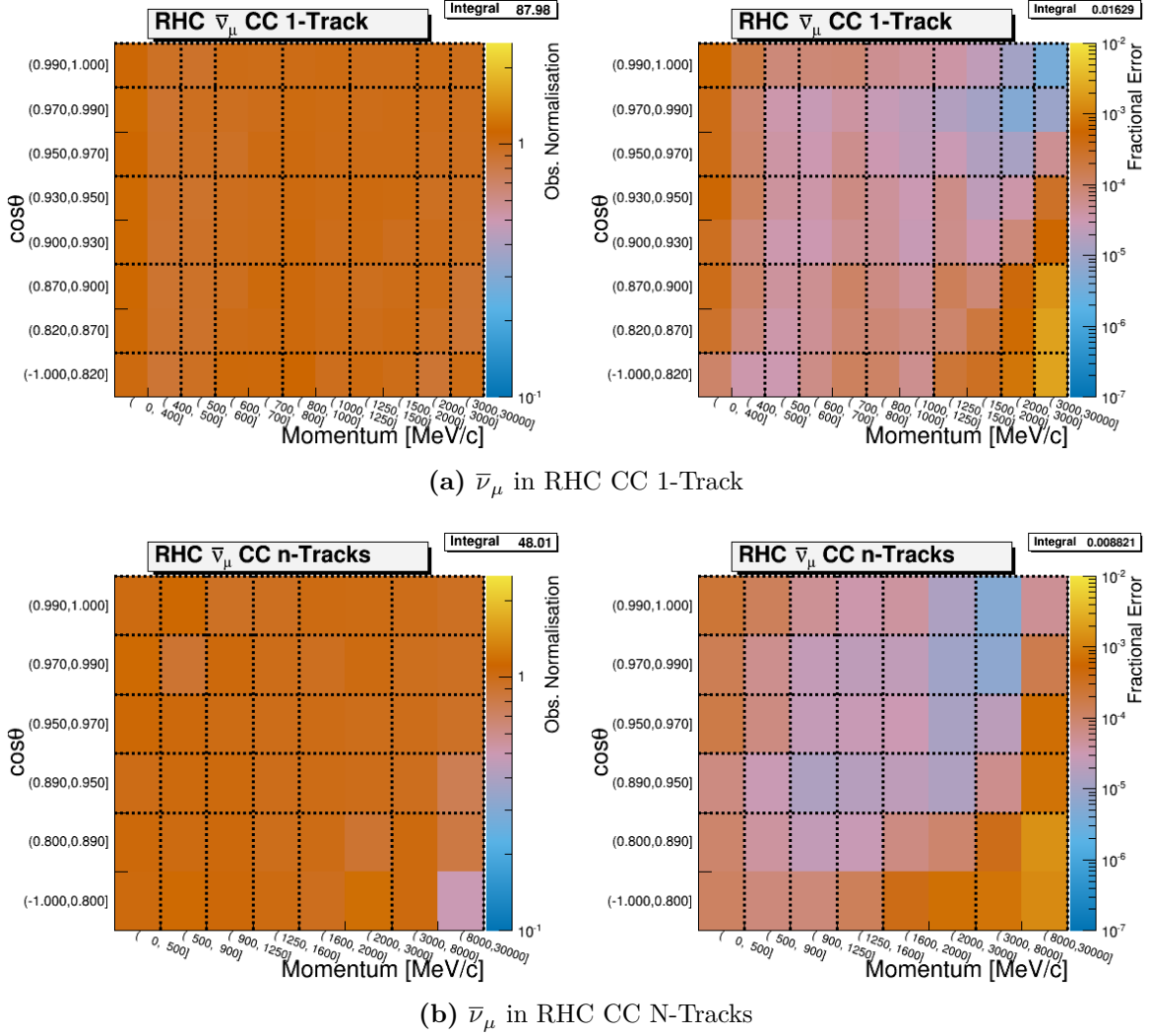


**Figure 4.6:** Bin normalization edges for the  $\bar{\nu}_\mu$  in RHC selections. There are two plots shown for each sub-figure. The left and right plots show the bin normalization and the bin statistical fractional error, respectively, if each fit bin had a single bin normalization. The dashed lines indicate the edges of the bin normalization parameters finalized for this analysis.

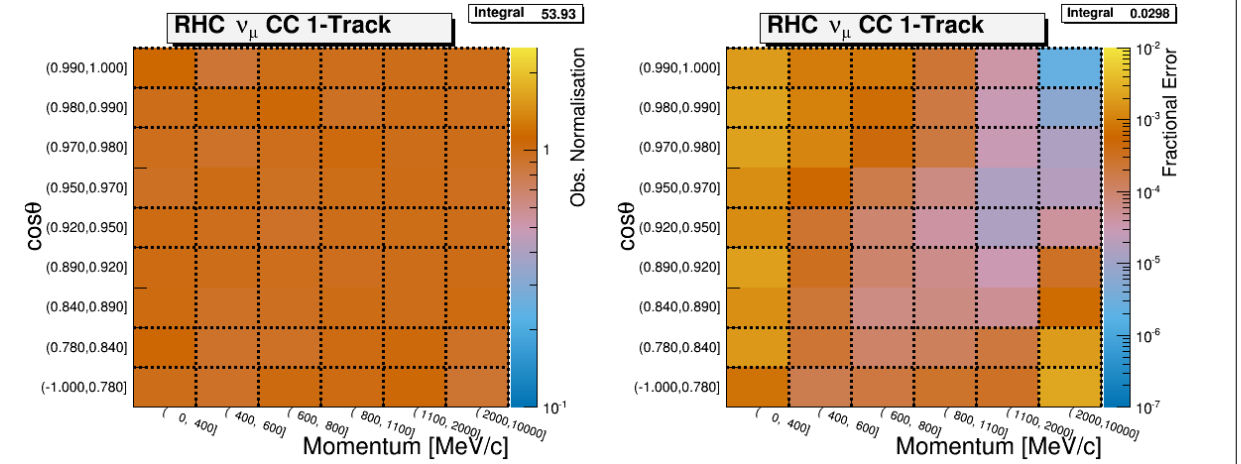
---

observable normalization bin varied non-normally. This effect can be seen in Figure 4.8 on page 115.

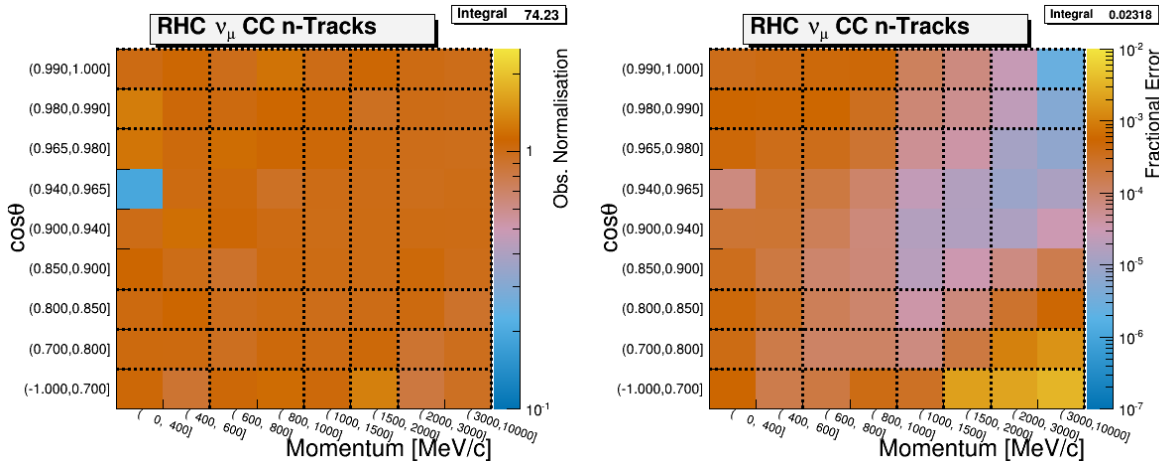
A considerable drawback to designing normalizations in this way of varying detector systematics in toy experiments is that not all detector systematics affect the observables ( $p, \cos \theta$ ) in the same way. There are non-symmetric systematics and are especially non-normal in their effects. Therefore, the covariance matrix from ( 4.16) is not an exact representation of the detector systematics. To demonstrate this, results of varied number of events are shown in Figure 4.8 on page 115 with all the varied toy experiment results are provided in ??.

We can also understand the effects the PØD energy loss resolution (ELossRes) correction and systematic on the bin normalizations, which was identified in the  $\nu_\mu$  CC-0 $\pi$  analysis as the leading uncertainty in the detector systematics. In Figure 4.8 on page 115, an additional red curve is shown in each sub-figure to represent disabling the PØD ELossRes correction and systematic variation in the toy experiments. We see this systematic broadens the number of possible events in a normalization bin and its correction shifts the bin mean. This is expected since one or more particles originating from a neutrino interaction in the water could remove reconstructed tracks from the event when varying the systematic.

Observed in most observable normalization bins is that the disabled ELossRes variation distribution is below the nominal MC expectation. However, there are in the 1-Track samples, as shown in Figure 4.8 on page 115, that the shape location is above the expectation. This behavior was unexpected prior to running the toy experiment variations. A relationship between the shape location and selection purity as a function of ( $p, \cos \theta$ ) was discovered. In high purity ( $p, \cos \theta$ )-regions of the 1-Track samples, the shape location of the disabled ELossRes variations was below the nominal MC expectation. When the purity was lower, however, the shape location was above it. This effect is likely due to events migrating into the N-Tracks samples. With the ELossRes variation disabled, events in the 1-Track samples



(a)  $\nu_\mu$  in RHC CC 1-Track



(b)  $\nu_\mu$  in RHC CC N-Tracks

**Figure 4.7:** Bin normalization edges for the  $\nu_\mu$  in RHC selections. There are two plots shown for each sub-figure. The left and right plots show the bin normalization and the bin statistical fractional error, respectively, if each fit bin had a single bin normalization. The dashed lines indicate the edges of the bin normalization parameters finalized for this analysis.

---

with low purity, which are also more likely to have multiple reconstructed tracks, are not being migrated into the N-Track samples.

The finalized observable normalization bins are listed below and shown visually in Figures 4.5 to 4.7. Their respective fit index and prefit values are tabulated in Appendix ??.

- $\nu_\mu$  in FHC CC 1-Track bin normalization edges:
  - $p$  [GeV/c]: 0, 0.4, 0.6, 0.8, 1.25, 2, 3, 4, 5.5, 30
  - $\cos \theta$ : -1, 0.7, 0.8, 0.94, 0.975, 0.99, 1
- $\nu_\mu$  in FHC CC N-Tracks bin normalization edges:
  - $p$  [GeV/c]: 0, 0.4, 0.6, 0.8, 1.2, 2.2, 3.5, 10, 30
  - $\cos \theta$  : -1, 0.77, 0.85, 0.9, 0.97, 1
- $\bar{\nu}_\mu$  in RHC CC 1-Track bin normalization edges:
  - $p$  [GeV/c]: 0, 0.5, 0.6, 0.8, 1.25, 2, 3, 30
  - $\cos \theta$  : -1, 0.82, 0.9, 0.95, 0.99, 1
- $\bar{\nu}_\mu$  in RHC CC N-Tracks bin normalization edges:
  - $p$  [GeV/c]: 0, 0.5, 0.9, 1.25, 1.6, 3, 30
  - $\cos \theta$  : -1, 0.89, 0.95, 0.97, 0.99, 1
- $\nu_\mu$  in RHC CC T-track bin normalization edges:
  - $p$  [GeV/c]: 0, 0.4, 0.6, 0.8, 1.1, 2, 10
  - $\cos \theta$  : -1, 0.78, 0.84, 0.92, 0.95, 0.98, 0.99, 1
- $\nu_\mu$  in RHC CC N-Tracks bin normalization edges:
  - $p$  [GeV/c]: 0, 0.6, 1, 1.5, 2, 10
  - $\cos \theta$  : -1, 0.7, 0.8, 0.85, 0.98, 0.99, 1

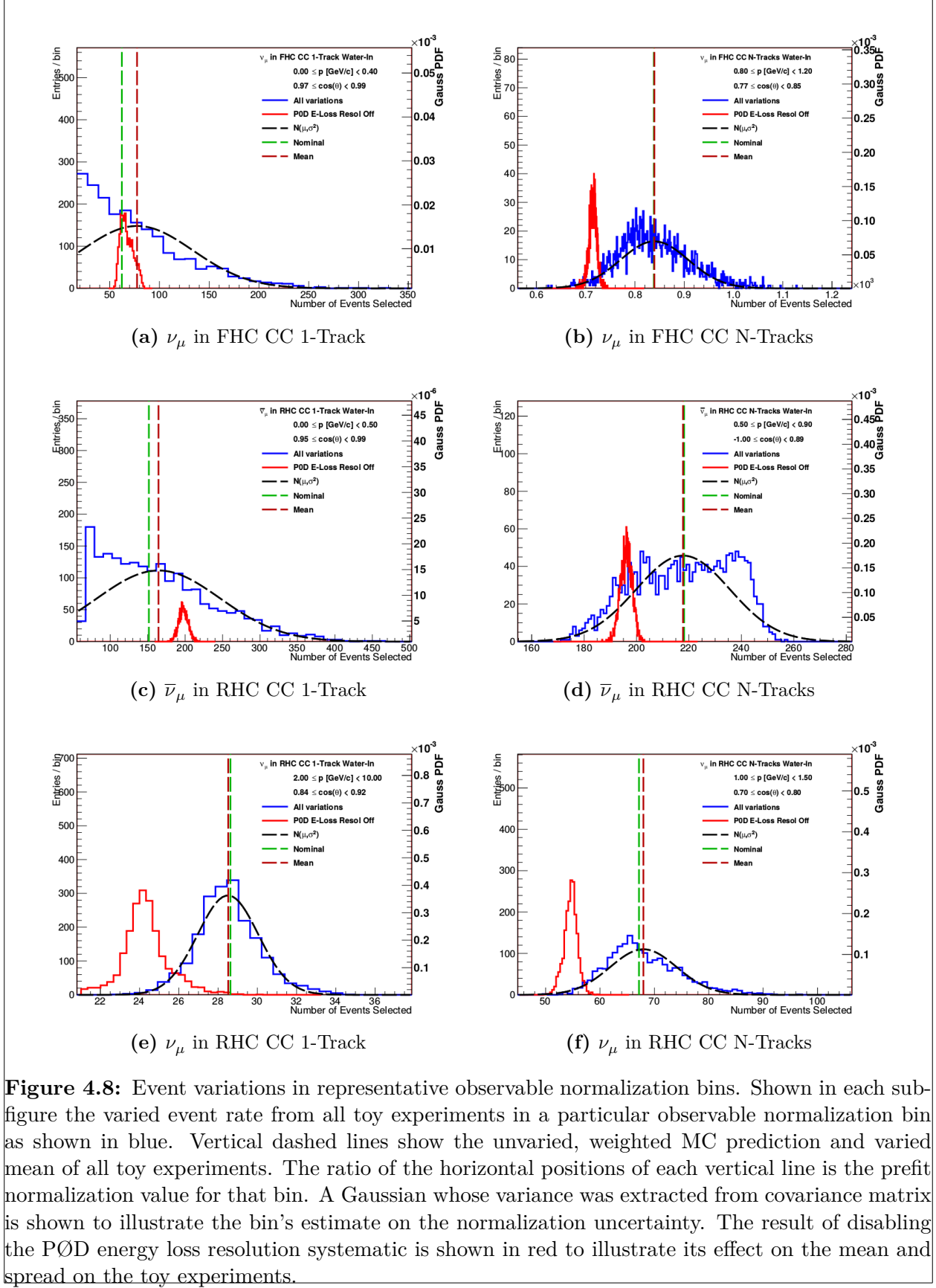


**Figure 4.8:** Event variations in representative observable normalization bins. Shown in each sub-figure the varied event rate from all toy experiments in a particular observable normalization bin as shown in blue. Vertical dashed lines show the unvaried, weighted MC prediction and varied mean of all toy experiments. The ratio of the horizontal positions of each vertical line is the prefit normalization value for that bin. A Gaussian whose variance was extracted from covariance matrix is shown to illustrate the bin's estimate on the normalization uncertainty. The result of disabling the PØD energy loss resolution systematic is shown in red to illustrate its effect on the mean and spread on the toy experiments.

---

## The PØD-Only Systematics

There are four new PØD-only systematics that are considered for this BANFF fit analysis as listed in Table 4.2 on page 105. All the new sources were initially analyzed in the PØD  $\nu_\mu$  CC-0 $\pi$  cross section analysis [7].

The energy loss scale and resolution affect the measured momentum in the PØD and are very significant sources of uncertainty. In the  $\nu_\mu$  CC-0 $\pi$  cross section analysis, the same selection as the  $\nu_\mu$  in FHC CC 1-Track selection, the scale and resolution contributed 1.3% and 6.7%, respectively, to the cross section uncertainty. Those large uncertainties are due to the inherent design of the PØD as a low resolution tracking detector. Slight variations in the track reconstruction can significantly alter the energy loss as measured in ( 3.5).

The remaining systematics, the PØD mass and the PØD-TPC matching efficiency, were not available to analyze in toy experiments variations. They were not implemented in the BANFF framework and unavailable to implement due to time constraints on the author. Instead, they were treated as additional uncorrelated systematics on each bin normalization uncertainty with the normalization value remaining fixed. The treatment of these two systematics will be discussed shortly.

The PØD mass uncertainty is a normalization systematic which affects the event rate. This is a challenging systematic for analyses of recent T2K data due to increasingly faulty sensors to measure the water content. The procedure to fill the water bags required filling them in unison to prevent uneven bulging. However, faulty sensors would provide poor quality data, hence bags were under and overfilled. This affect alters the expected event rate as a function of position.

Another problem with the mass uncertainty is due to bulging of the PØD. The PØD is mounted in each of its corners to the ND280 basket and has a physical air gap between it and the TPC. Since the upstream end of the PØD is physically against the ND280 support structure, this configuration permitted the downstream layers to expand from the middle into the air gap. Importantly, this left more water volume, and importantly more mass, in

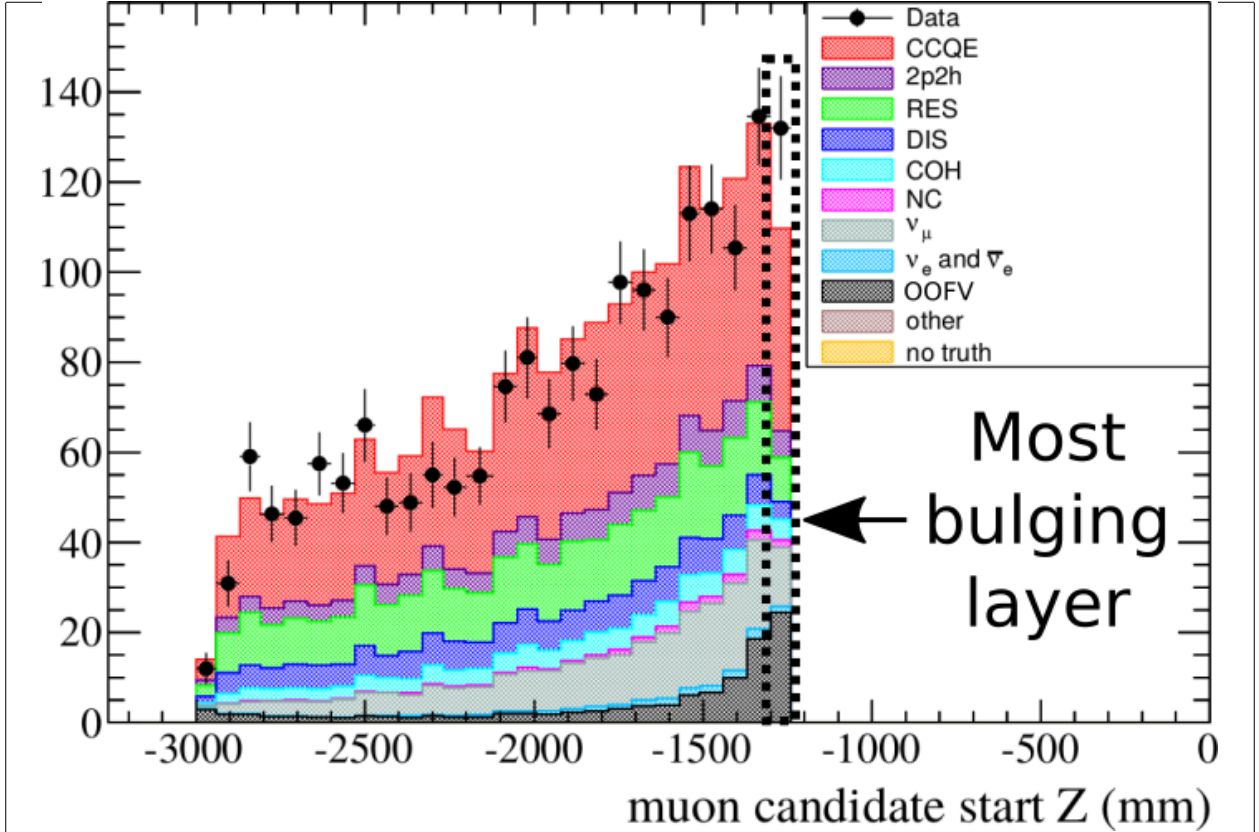


**Figure 4.9:** Vertex distribution showing evidence of bulging. In the  $\bar{\nu}_\mu/\nu_\mu$  cross section ratio analysis, a significant excess of events in the most downstream layer of the PØD (black, dashed line box) was observed. Initially thought to be OOFV events, the analyzers removed the most downstream and upstream layers in their analysis. This distribution was produced using the run 5, RHC period using selection precuts 1 through 4 and a having a positive track in the TPC. Each event is categorized by true interaction mode according to NEUT. This figure was altered for clarity from the following reference [22].

the most downstream water bags compared to the upstream bags. The effect of more mass in the PØD is evidenced in the vertex distribution as a function of the Z-position as shown in Figure 4.9 on page 117.

Prior PØD analyses have estimated the mass uncertainty using similar toy experiment techniques, but did not integrate them into the BANFF framework. In particular in the  $\nu_\mu$  in CC- $0\pi$  analysis [7], the PØD mass had an 1.5% systematic effect on the cross section. Since the PØD mass uncertainty estimate was determined using the same toy experiment variation method, *a conservative estimate of 2% on the mass uncertainty included in this*

---

*analysis.* So for the PØD mass systematic, let  $\tilde{\sigma}_{\text{Mass}} = 2\%$ , where the tilde ( $\tilde{\phantom{x}}$ ) refers to a fractional uncertainty. This will be used later.

The PØD and TPC matching efficiency is estimated to have a small systematic effect on the analysis. It was analyzed to have over a 99.8% data and MC efficiency in the single track  $\nu_\mu$  CC- $0\pi$  analysis and thus neglected. However, since this analysis includes multiple track selections, that matching efficiency is unknown. Also, it is hard to imagine a CS that could constrain it. The best handle is from the private T2K technical note on the  $\bar{\nu}_\mu/\nu_\mu$  cross section analysis [22] which estimated the uncertainty at less than 0.14% using its in-house matching algorithm. Since that was single bin measurement employing different matching algorithm, the uncertainty is not guaranteed to remain constant across  $(p, \cos \theta)$  bins. *A conservative estimate of 1% for the TPC matching efficiency was chosen in order to account for the inherent uncertainty in this systematic.* So for the matching efficiency systematic, let  $\tilde{\sigma}_{\text{Match}} = 1\%$ .

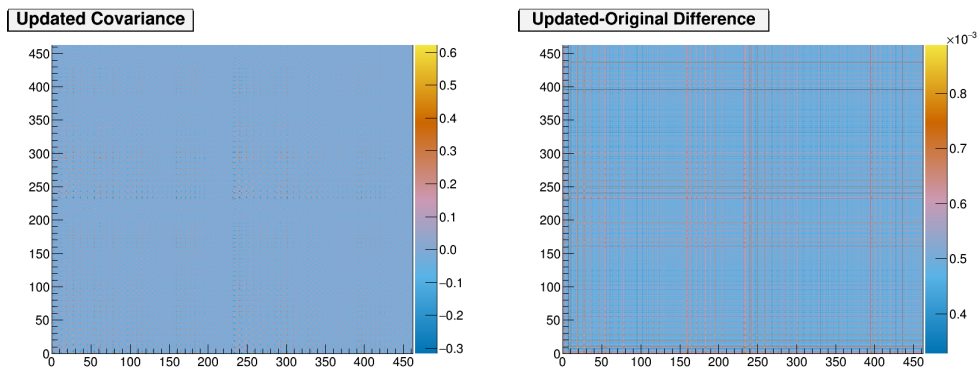
In order to propagate these two uncorrelated uncertainties, the detector covariance matrix given in ( 4.16) was converted into a fractional covariance matrix first. Let  $\tilde{V}_{i,j}^{\text{Det}}$  refer to the fractional covariance matrix, given explicitly as

$$\tilde{V}_{i,j}^{\text{Det}} = \frac{V_{i,j}^{\text{Det}}}{d_i d_j}, \quad (4.17)$$

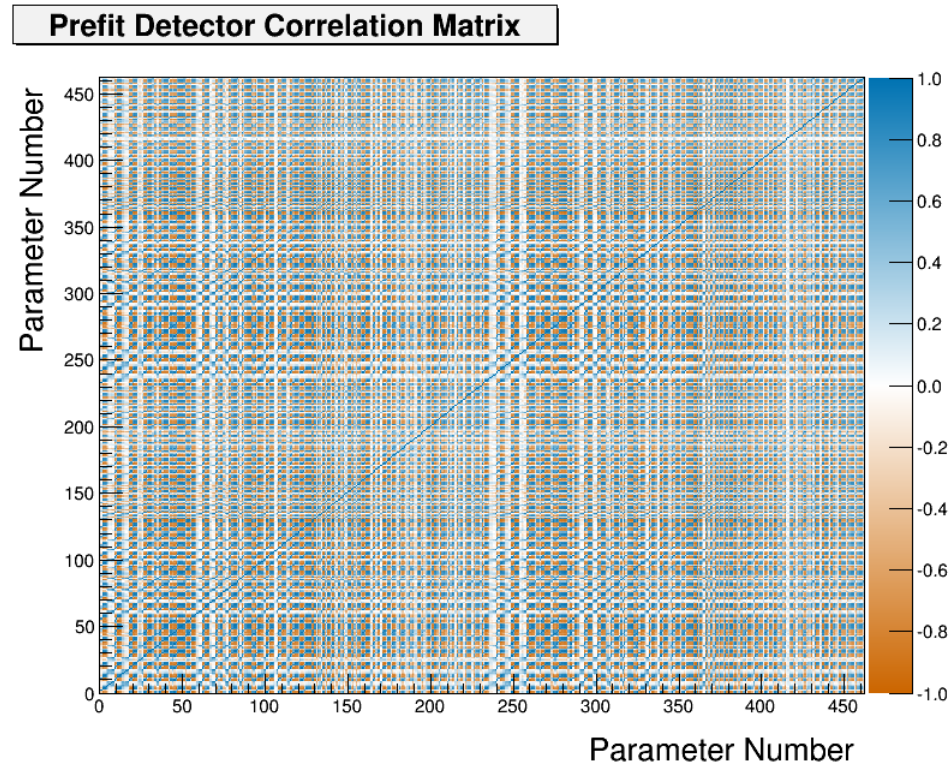
where we recognize  $\sqrt{\tilde{V}_{i,i}^{\text{Det}}}$  as the fractional uncertainty in the  $i$ th observable normalization parameter. The updated detector covariance matrix,  $\acute{V}_{i,j}^{\text{Det}}$ , which accounts for the PØD mass and TPC matching inefficiency systematics, is given by

$$\acute{V}_{i,j}^{\text{Det}} = \left( \tilde{V}_{i,j}^{\text{Det}} + \tilde{\sigma}_{\text{Mass}}^2 + \tilde{\sigma}_{\text{Match}}^2 \right) d_i d_j. \quad (4.18)$$

Together, the two additional sources of uncertainty increase each term in the covariance matrix by  $0.0005 d_i d_j$ , which increases each bin normalization error by about 2.23%. The updated covariance matrix used in this analysis is shown in Figure 4.10 on page 119.



(a) Updated detector covariance matrix   (b) Difference from original detector covariance matrix



(c) Updated detector correlation matrix

**Figure 4.10:** Updated detector covariance matrix (a), the difference from the original matrix (b), and updated correlation matrix (c). Note that the parameter numbers here are offset from their fit index value by 99.

### 4.2.3 Cross Section Model

There are a number of neutrino-nucleus model and other related systematics implemented in BANFF to account for the uncertainties in cross section measurements. They are frequently updated to account for new models and constraints from external data. The cross section models used in this analysis use the T2K 2017 parameterization, which is a canonical set of parameters shared among all analyses in T2K. A gross description of the cross section model is provided here with a full technical description of the parameterization is given in the following reference [8].

There are three types of cross section parameters: shape, normalization, and functional. A cross section shape parameter is defined as a fractional shift in the location of a certain feature in some parameter space. As a design choice, the shape location parameters all start with a prefit value of zero (0). A cross section normalization parameter,  $x_i^{\text{Norm}}$ , is defined as

$$x_i^{\text{Norm}} = \frac{p'}{p}, \quad (4.19)$$

where  $p$  and  $p'$  are NEUT nominal and ND constrained parameters, respectively. The prefit values for the normalization parameters are set to (1) unless the prefit is different from the nominal NEUT model. And finally functional parameters are normalization factors for basis functions in a particular parameter space. For example the parameters  $A$  and  $B$  are normalizations for the slope and intercept for a linear curve  $f(x) = Ax + B$ .

The next sections deal with the model parameterizations and systematic uncertainties in the NEUT version 5.3.3 [75] interaction library which is used in T2K MC and oscillation analysis.

#### CCQE and CC- $0\pi$

The cross section models with the largest impact on T2K's oscillation sensitivity are CCQE and CCQE-like interactions, collectively called CC- $0\pi$ . At energies near the  $\nu_e$  ap-

---

pearance maximum,  $E_\nu = 0.6$  GeV, the CCQE interaction is the largest contributor to the neutrino cross section as shown in Figure 1.30 on page 50. The nominal CCQE model in NEUT is a Spectral Function from Benhar and others [?]. An alternative CCQE model uses the Llewellyn-Smith model [49] with a dipole [24] axial form factor<sup>12</sup>, BBBA05 vector form factors [19] coupled to a Smith-Miniz Relativistic Fermi Gas [55, 69] (RFG). A CCQE-like excitation mode involves correlated nucleon pair scattering called “2 particle, 2 hole” [53] (2p2h)<sup>13</sup>. An additional nuclear model called “Random Phase Approximation” (RPA) [27] is used to modify single nucleon scattering by accounting for nucleon correlations inside the nucleus [54]. The default CC-0 $\pi$  model for T2K analyses is the combination of the Llewellyn-Smith+RFG model, 2p2h excitation, and RPA nuclear model. This combination was selected due to tension using the SF model to match with external data [75].

The selected CCQE model has three free parameters: the dipole axial form factor mass  $M_A^{\text{QE}}$  from the Llewellyn-Smith model, and two Fermi momentum parameters  $p_F$ , one for  $^{12}\text{C}$  and  $^{16}\text{O}$  that describe the momentum of nucleons on the surface of a RFG. In the past, these parameters have been shown to work as effective models in T2K when unconstrained. In this analysis, these three parameter are unconstrained. In other words, a flat prior is used for  $M_A^{\text{QE}}$ ,  $p_F^C$ , and  $p_F^O$ .

For the 2p2h excitation, there are a total of 5 parameters to describe the uncertainty in the model. Three are three normalization terms:  $\nu$  interaction on  $^{12}\text{C}$ ,  $\bar{\nu}$  interaction on  $^{12}\text{C}$ , and scaling for  $^{12}\text{C} \rightarrow ^{16}\text{O}$ . The remaining two systematic parameters in the 2p2h model are shape parameters, one for  $^{12}\text{C}$  and  $^{16}\text{O}$ , to describe the uncertainties in the contributing modes in 2p2h. These modes are called Meson Exchange Current (MEC) which involve a virtual meson exchange between the nucleons, nucleon-nucleon correlations (NN) which involves

---

<sup>12</sup>A form factor is a measure of scattering amplitude in the form of the Fourier transform of some charge distribution.

<sup>13</sup>The name 2p2h originates from Condensed Matter Physics which motivated the model. In solid state matter, a “hole” refers to the absence of an electron in a valence band. In the High Energy Physics context, 2p2h considers neighboring and interacting nucleon pairs (2p) scattering from an incoming  $\nu$ . The imparted energy on the pair excites them to higher energy states leaving two “hole” states (2h) behind.

virtual particle exchange, and the MEC-NN interference. A shape value of -1 determines 2p2h is completely due to MEC, 0 is the nominal MC 2p2h model, and +1 determines 2p2h is completely due to NN. Any value in between  $\pm 1$  include uses the interference term to absorb differences in the event rate. However, since no T2K nor external neutrino data can constrain the neutrino-induced 2p2h interaction, a flat prior is set for all 2p2h parameters.

The other nuclear interaction in the CC-0 $\pi$  model uses the Nieves RPA model [54] to describe nucleon correlations. The RPA model primarily alters the single nucleon cross section and has dependence on both  $E_\nu$  and  $Q^2$ . A functional weighting scheme only in  $Q^2$  was found to work well to mimic the inherent uncertainties in the Nieves RPA model. Using a third order polynomial in the Bernstein polynomial basis  $B_i^n$  [32]

$$B_i^n(x) = \binom{n}{i} x^i (1-x)^{n-i} \quad x \in [0, 1] \quad (4.20)$$

where

$$\binom{n}{i} = \frac{n!}{(n-i)! \times i!}. \quad (4.21)$$

with a high- $Q^2$  exponential tail, the “BeRPA” model functional weight is parameterized as

$$w_{\text{BeRPA}}(Q^2) = \begin{cases} A(1-x)^3 + 3B(1-x)^2x + 3p_1(1-x)x^2 + Dx^3 & Q^2 \leq U \\ 1 + p_2 \exp(-E[Q^2 - U]), & Q^2 > U \end{cases} \quad (4.22)$$

where  $x = Q^2/U$ ,  $A$ ,  $B$ ,  $D$ , and  $E$  are scale/normalization factors for the basis functions, and  $U$  signifies when the two functions intersect with  $p_1$  and  $p_2$  absorbing the continuity conditions

$$p_1 = D + \frac{UE(D-1)}{3}, \quad p_2 = D - 1. \quad (4.23)$$

The parameters  $A$ ,  $B$ ,  $D$ , and  $E$  are allowed to vary while  $U$  is fixed to prevent unwieldy correlations from appearing.

---

### CC- $1\pi$

Another important exclusive channel in NEUT are resonance states that produce a single pion or CC- $1\pi$ . The CC- $1\pi$  model is based on the Rein-Seghal model [59] with lepton mass corrections [17, 41] of neutrino-induced  $\Delta$  resonance decay [38–40]. There are three tunable parameters that describe the systematics in the CC- $1\pi$  model. They are resonant axial mass  $M_A^{\text{Res}}$ , the axial form factor normalization  $C_A^5$ , and the isospin= $1/2$  background. In particular,  $M_A^{\text{Res}}$  and  $C_A^5$  are strongly anticorrelated due to the parameterization of the form factor

$$f(Q^2) = C_A^5 \left( 1 + \frac{Q^2}{(M_A^{\text{Res}} c^2)^2} \right)^{-2}. \quad (4.24)$$

Again, this model is an effective model since the uncertainties were tuned to bubble chamber data from Brookhaven National Laboratory [47] and Argonne National Laboratory [58].

Harder to measure processes like coherent pion production are discussed next.

### Coherent Pion Production

Coherent scattering refers to scattering where the wavelength of the incoming particle is larger than the target. In the case of coherent neutrino-nucleus scattering, the neutrino's wavelength given by

$$\lambda = \frac{hc}{E_\nu}$$

is larger than the size of the nucleus. In the scattering, no quantum numbers are exchanged, but the nucleus experiences a momentum boost. In coherent pion production, the in-flight virtual boson is converted into a pion with that pion exchanging a Pomeron [5] with the nucleus. The coherent scattering model is described by Rein-Sehgal [60]. Lookup tables are used to scale the cross section to external data [75] and the Berger-Sehgal model [17]. Three tunable normalization parameters are used to describe the uncertainties in coherent production: CC on  $^{12}\text{C}$ , CC on  $^{16}\text{O}$ , and NC on all nuclei.

---

## CC DIS

The CC DIS process, which also includes multiple pion production, systematic is treated as a normalization with a relatively simple uncertainty,  $\tilde{\sigma}_{\text{CCDIS}}$ , of

$$\sigma_{\text{CCDIS}}(E_\nu) = \frac{0.4}{E_\nu \text{ [GeV]}}$$

where the fractional uncertainty at 4.0 GeV is  $\sim 10\%$  [75].

## NC Other

There is one free normalization parameter for the NC processes. The NC other parameter contains the normalization uncertainties in NC DIS, single kaon production, single  $\eta$ -meson production, and elastic processes with a conservative 30% fractional uncertainty [75].

## Final State Interactions (FSI)

Final state interactions [37] are effects that alter final state pions from neutrino-nucleus events before the pion exits the nucleus. The microscopic model in NEUT is a cascade implementation of the Salcedo-Oset model [64] which describes interactions in the nucleus as probabilities of position and momentum. The systematics are parameterized as scattering probabilities for different interaction processes tuned to world data [61]. These processes are divided into four classes: inelastic (INEL) scattering, pion absorption (ABS), pion production (PROD), and charge exchange (CEX). There are a total of six FSI shape parameters in the fit. The PROD and ABS classes are each single shape parameters. For the INEL and CEX classes, they divided into low (LO) and high (HI) energy regions where the transition occurs at  $p_\pi = 500$  MeV/c.

---

## Other Fixed Parameters

As mentioned in the CC- $0\pi$  model, the BeRPA  $U$  parameter is fixed to remove correlations with the other BeRPA scale parameters. However, there are four fixed normalization parameters in the BANFF fit since they correspond to Super-K only parameters. They are included in the fit in order to maintain consistency between the ND280 constraint and oscillation analysis parameterizations. In other words, they are spectators in the BANFF fit. These parameters are the CC  $\nu_e/\nu_\mu$  event rate ratio, CC  $\bar{\nu}_e/\bar{\nu}_\mu$  event rate ratio, NC  $1\gamma$  event rate, and NC other far event rate.

## Fit Parameters

There are a total of 31 cross section parameters in the BANFF fit, four of which are fixed. The fit parameters are listed in Table 4.3 on page 128 with the associated covariance matrix shown in Figure 4.11 on page 126. Following the definition of the flux and bin normalization parameters, cross section parameters are defined as fractional differences either in shape, scale, or normalization. If no prefit uncertainty is shown in Table 4.3 on page 128, and emphasized using red font, then the parameter had a flat prior assigned. A model parameter with an asterisk (\*) next to it is fixed in the fit. Abbreviations used in this table are “dim.-less” for dimensionless, “norm.” for normalization, “Near” for ND280, “Far” for Super-Kamiokande, and “bkg” for background. Parameters with physical units are shown in both dimensionless and dimensional values for comparison. Prefit values are relative to the NEUT nominal value.

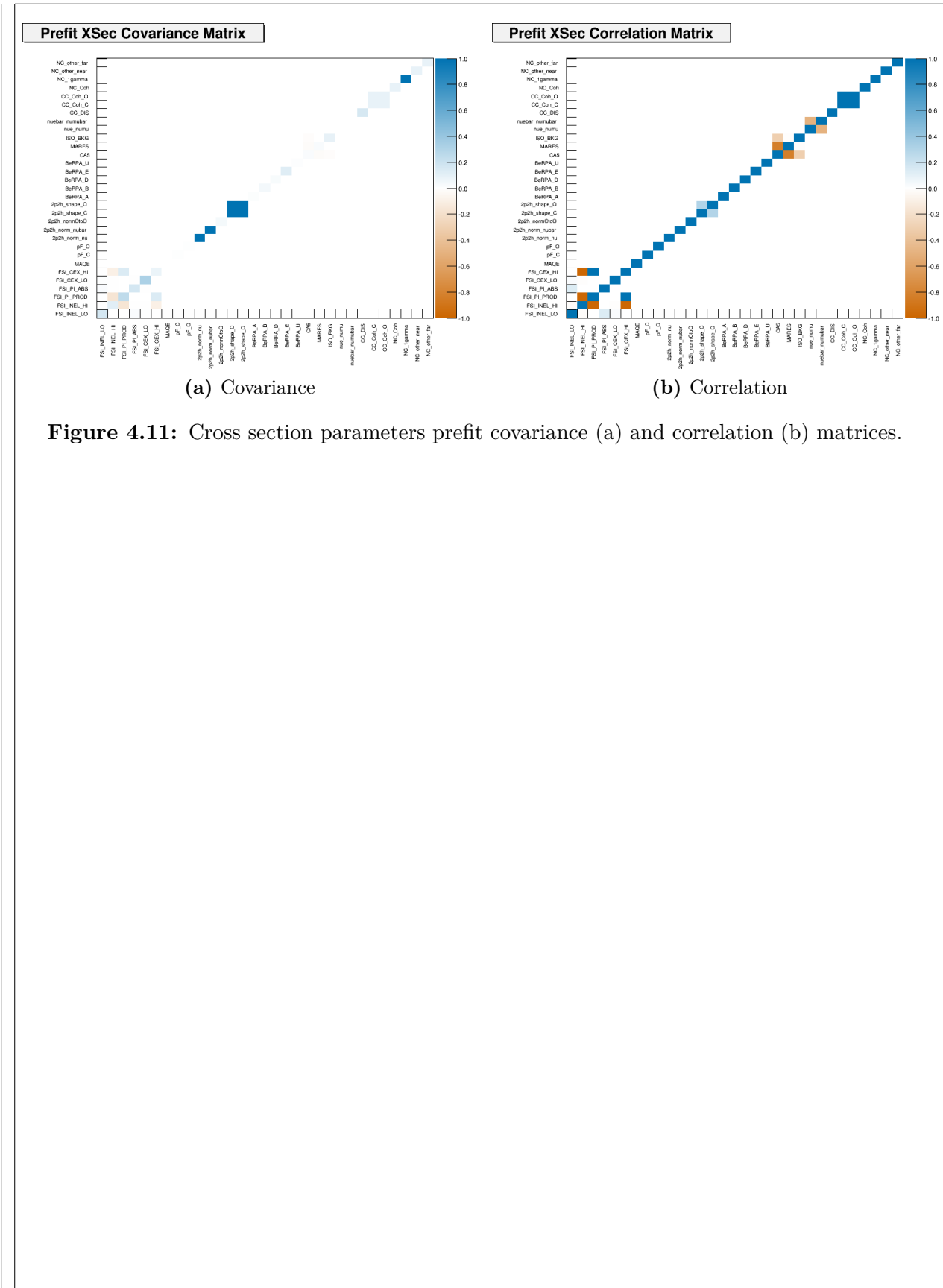


**Table 4.3:** Cross section model parameters in the fit. See the text for a full description.

Fit index	Topology	Model	Parameter	Prefit
562	FSI shape		Low energy INEL	$0 \pm 0.41$
563			High energy INEL	$0 \pm 0.34$
564			PROD	$0 \pm 0.41$
565			ABS	$0 \pm 0.5$
566			Low energy CEX	$0 \pm 0.57$
567			High energy CEX	$0 \pm 0.28$
568	CC-0 $\pi$	Llewellyn-Smith	$M_A^{\text{QE}}$ (dim.-less)	1
569			$M_A^{\text{QE}}$ ( $\text{GeV}/c^2$ )	1.20
570		RFG	$p_F^C$ (dim.-less)	1
571			$p_F^C$ ( $\text{MeV}/c$ )	217
572			$p_F^O$ (dim.-less)	1
573			$p_F^O$ ( $\text{MeV}/c$ )	225
574		Nieves 2p2h	$\nu$ norm. on $^{12}\text{C}$	1
575			$\bar{\nu}$ norm. on $^{12}\text{C}$	1
576			$^{12}\text{C}/^{16}\text{O}$ norm.	1
577			$^{16}\text{C}$ shape location	0
578			$^{12}\text{O}$ shape location	0
579	BeRPA nuclear model	(functional)	A scale	$0.59 \pm 0.118$
580			B scale	$1.05 \pm 0.21$
			D scale	$1.13 \pm 0.1695$
			E scale	$0.88 \pm 0.352$
			U scale*	$1.2 \pm 0.1$

**Table 4.3:** Cross section model parameters in the fit. See the text for a full description.

Fit index	Topology	Model	Parameter	Prefit
581	CC-1 $\pi$	Rein-Seghal resonant 1 $\pi$ prodction	$C_A^5$	$0.96 \pm 0.148$
582			$M_A^{\text{Res}} \text{ (dim.-less)}$	$1.1263 \pm 0.157$
			$M_A^{\text{Res}} \text{ (GeV/c}^2\text{)}$	$1.07 \pm 0.15$
583			I= $^{1/2}$ bkg. norm.	$0.74 \pm 0.307$
584	Other	Event rate at SK	CC- $\nu_e/\nu_\mu^*$	$1 \pm 0.0282$
585			CC- $\bar{\nu}_e/\bar{\nu}_\mu^*$	$1 \pm 0.0282$
586			CC-DIS shape location	$0 \pm 0.4$
587		Coherent pion production	CC norm. on $^{12}\text{C}$	$1 \pm 0.3$
588			CC norm. on $^{16}\text{O}$	$1 \pm 0.3$
589			NC norm.	$1 \pm 0.3$
590		Event rate	NC- $1\gamma^*$	$1 \pm 1$
591			NC Other Near	$1 \pm 0.3$
592			NC Other Far*	$1 \pm 0.3$

### 4.3 BANFF Fit Parameterization Summary

This chapter has described all the fit bins and systematic parameters that go into the BANFF fit. For the fit bins, they are used in the LLR term to model the best possible fit between data and MC without any constraints. However, since there are known systematic uncertainties in the flux, detector inefficiencies, and cross sections, we have described their parameterizations to force the fit work within those constraints. The flux model is constrained by T2K primary and secondary beamline data while the cross sections are con-

---

---

strained by external data. Finally, the detector systematics are determined via an ensemble of toy experiments based on well established control samples in the ND280.

Next chapter explores the set of validation studies to examine how the BANFF fit works.

---

# Chapter 5

## Fitter Validation

This chapter will present the checks, tests and validations of the BANFF fit using the MC as input. The first such test is using the weighted MC as the data, referred to as an Asimov data fit. The next are two validation tests using two different data sets that have altered event weights compared to the MC. These are referred to as "fake data" sets. One fake data set alters the flux prediction and is referred to as the "High Energy Neutrino Flux Variation" fake data set. The other is the "Single Pion Event Rate Variation" fake data set.

### 5.1 Asimov Data Fit

Asimov data refers replacing the ensemble of simulated data sets by a single representative one [28]. In this analysis, this involves fitting the MC data set to itself for the primary purpose of checking the closure of the fitting framework. The Asimov set is produced with the same models as is implemented in the fitter and has all parameters set to their prior central values as defined in Chapter 4. Instead of statistically sampling from the MC, which can insert statistical variations in the fit, the Asimov data set is created by scaling the set down to the full T2K POT with additional finer corrections like flux and cross section weights. The prefit correlation matrix is shown in Figure 5.1 on page 131.

---

---

### Prefit Correlation Matrix

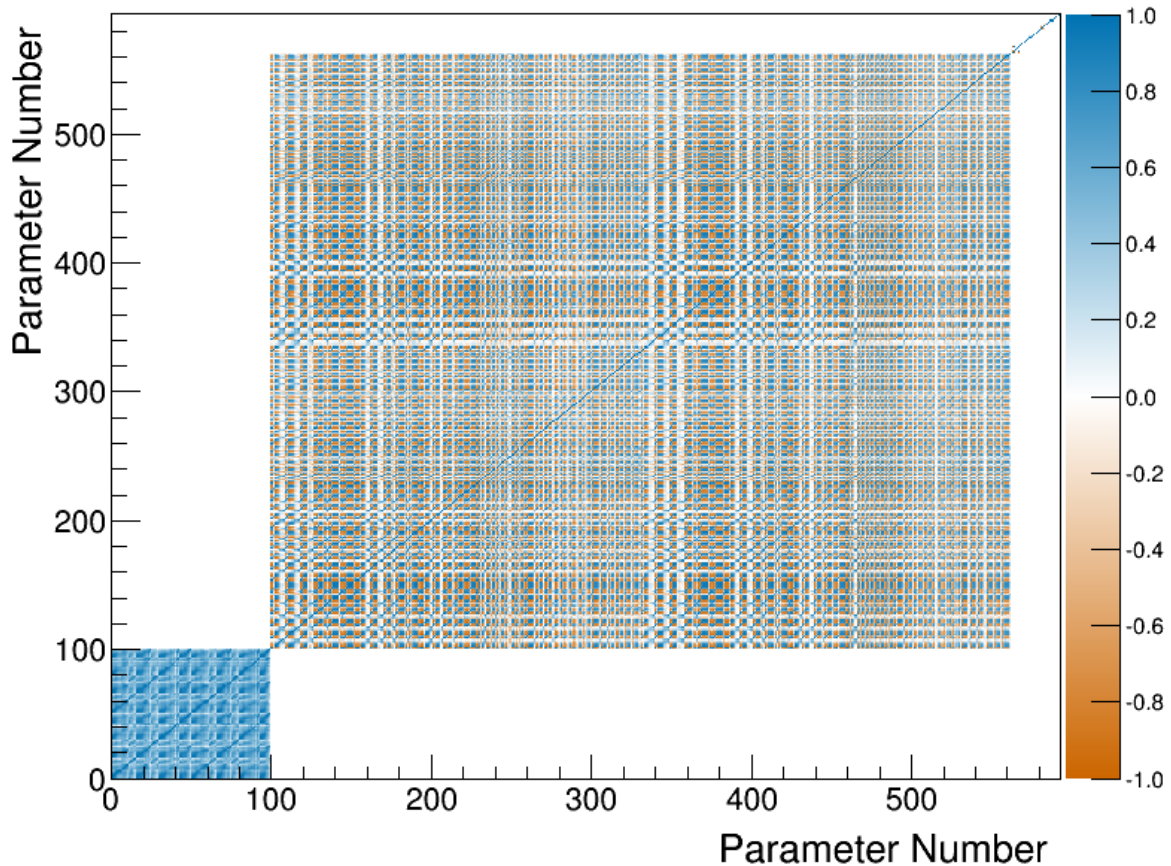


**Figure 5.1:** Complete prefit correlation matrix for the BANFF fit. The first 100 parameters are the flux bins. Between 100 and 561 are the bin normalization parameters. Finally 562 through 592 are the cross section parameters.

---

---

In addition to running an Asimov fit, other metrics were examined in the Asimov set. Shown first is a comparison of the event rates before and after applying weights to the MC. Next is an examination of the cross section weight functions. Finally is a set of scans of the test statistic space to ensure the sample and penalty terms are behaving as expected. Then the Asimov data set fit is explored.

### 5.1.1 Event Rate

Shown in Table 5.1 on page 133 is the event rates for the various samples for the Asimov fit. The data events column refers to real T2K data collected in the sample with the rest are MC events. There are a weights that correct differences between the data and MC. The POT weight normalizes the MC event rate to data rate. The other weights, which where discussed in Chapter 2, are the flux, cross section, and detector corrections. We see that applying the POT weight scales the MC event rate close to that of the data. The other weights are fine tuning corrections to the rate from known systematics like flux and cross sections. Application of all the weights is the prefit event rate and is collectively referred to as Asimov data set.

Sample name	Data events	Raw MC events	POT only	Application of weights			Prefit
				POT+Flux	POT+xsec	POT+Det	POT+flux+xsec+Det
$\nu_\mu$ 1-Trk Wtr	27151.00	526226.00	26270.98	28766.86	24222.45	26286.14	27327.94
$\nu_\mu$ N-Trks	31013.00	529538.00	26708.61	31464.27	26267.19	26708.74	31098.20
$\bar{\nu}_\mu$ RHC 1-Trk	8779.00	176007.00	9152.04	9365.78	8321.76	9161.91	8461.37
$\bar{\nu}_\mu$ RHC N-Trks	4613.00	93132.00	4876.93	5014.74	4652.01	4876.81	4802.12
$\nu_\mu$ RHC 1-Trk	3502.00	56861.00	2933.20	3182.20	2747.29	2938.29	3025.76
$\nu_\mu$ RHC N-Trks	5424.00	85599.00	4460.10	4988.89	4413.01	4464.45	4956.19
$\nu_\mu$ 1-Trk Air	23504.00	309373.00	23383.39	25319.17	21594.49	23402.63	23603.03
$\nu_\mu$ N-Trks	32736.00	371986.00	28495.10	33255.58	27822.42	28505.66	32302.08
$\bar{\nu}_\mu$ RHC 1-Trk	6681.00	75374.00	7374.13	7512.47	6732.25	7381.37	6767.79
$\bar{\nu}_\mu$ RHC N-Trks	4437.00	47951.00	4689.16	4820.43	4446.52	4690.57	4544.72
$\nu_\mu$ RHC 1-Trk	2324.00	20943.00	2049.01	2198.46	1916.33	2052.56	2067.12
$\nu_\mu$ RHC N-Trks	4801.00	42098.00	4119.63	4586.22	4050.71	4122.39	4567.72
Total	154965.00	2335088.00	144512.28	160475.06	137186.41	144591.53	153524.03

**Table 5.1:** Event rate table for Asimov set. The “Raw MC” column refers the number of events in the sample from the nominal MC prediction without any weights applied. From left to right, applications of weights are applied to understand their affect on the samples. The “POT only” column refers to applying the POT weight to all events. Columns with “POT+Flux”, “POT+xsec”, and “POT+Det” refer to applying the POT weight together with the flux, cross section, and detector weights, respectively. The “Prefit” column has the POT, flux, cross section, and detector (POT+Flux+xsec+Det) weights all multiplied together.

---

### 5.1.2 One Sigma Variation of Cross Section Parameters

To ensure the cross section spline weight functions were functioning properly, the samples were analyzed when the parameters were set to their  $\pm 1\sigma$  values. The results of the variations are shown in Appendix ??, which show the samples are indeed affected by the weight functions.

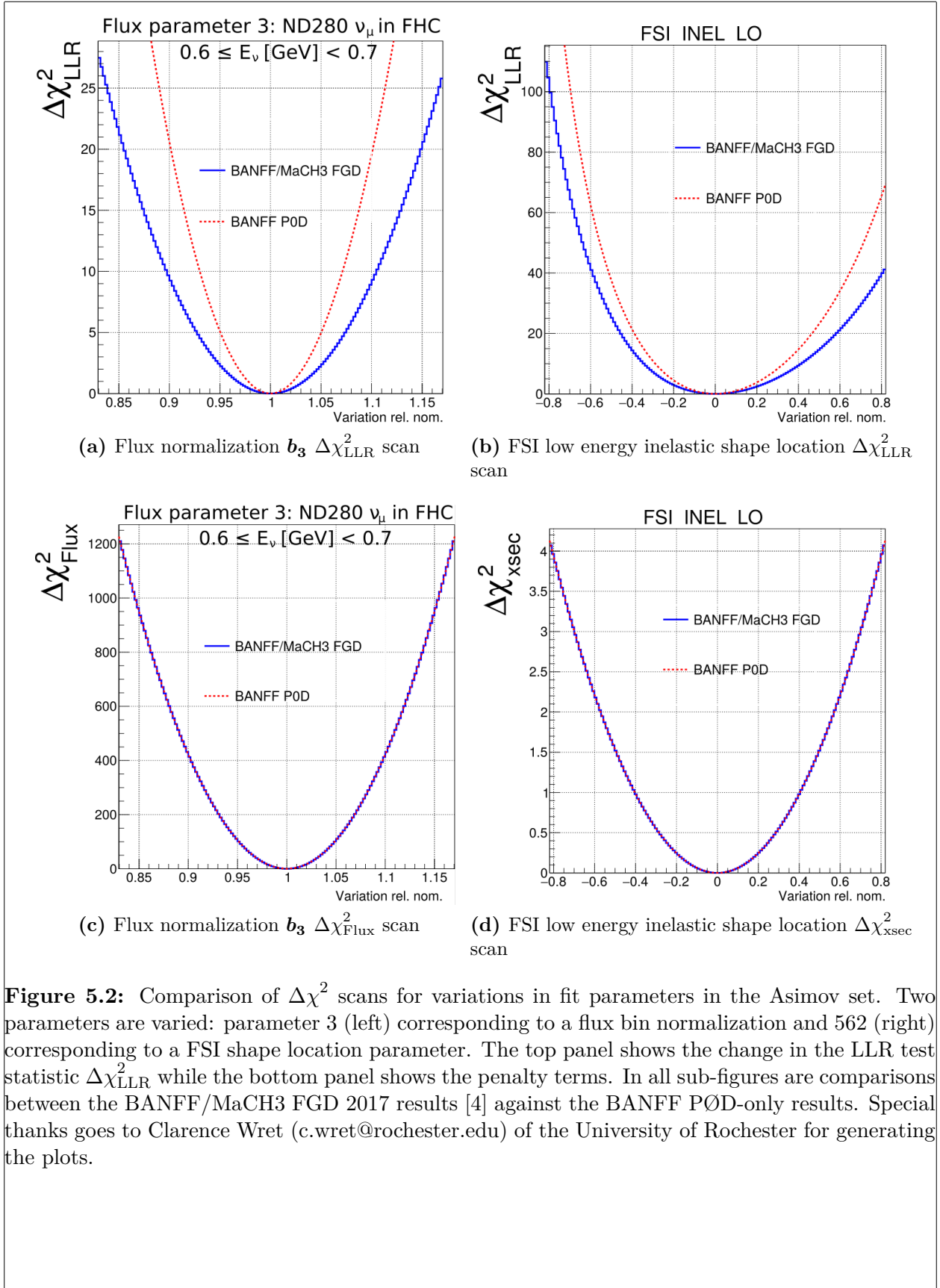
### 5.1.3 Log-Likelihood Scans

Log-likelihood scans of the sample and penalty terms were examined in the Asimov data set. The results of the scans are shown in Figure 5.2 on page 135 with comparisons between the PØD-only samples and FGD-only samples shown. It demonstrates that same penalties are applied between the PØD-only and FGD-only analyses. Also observed is that the PØD-only data has similar sensitivity and shape dependence on the flux parameters with that of the FGD-only data. The complete set of scans are shown in Appendix ?? and Appendix ??.

### 5.1.4 Fit Results

The postfit results of the Asimov data fit are shown in Figure 5.3 on page 136 to Figure 5.6 on page 139. In order to provide a unified graphical representation for all the parameters, the prefit and postfit cross section shape parameters are adjusted to be relative to one (1).

We see that the postfit parameters have uncertainties that are different compared to their prefit values. This is expected since correlations between the sub-matrices in the covariance matrix, which were assumed uncorrelated to start, have been calculated. The complete postfit correlation matrix is shown in Figure 5.7 on page 140 and the flux and cross section only correlation matrix is shown in Figure 5.8 on page 140. We observe significant anti-correlations between each of the sub-matrices which is predicted from ( 2.7) since any increase in one parameter weight forces a decrease in the others.



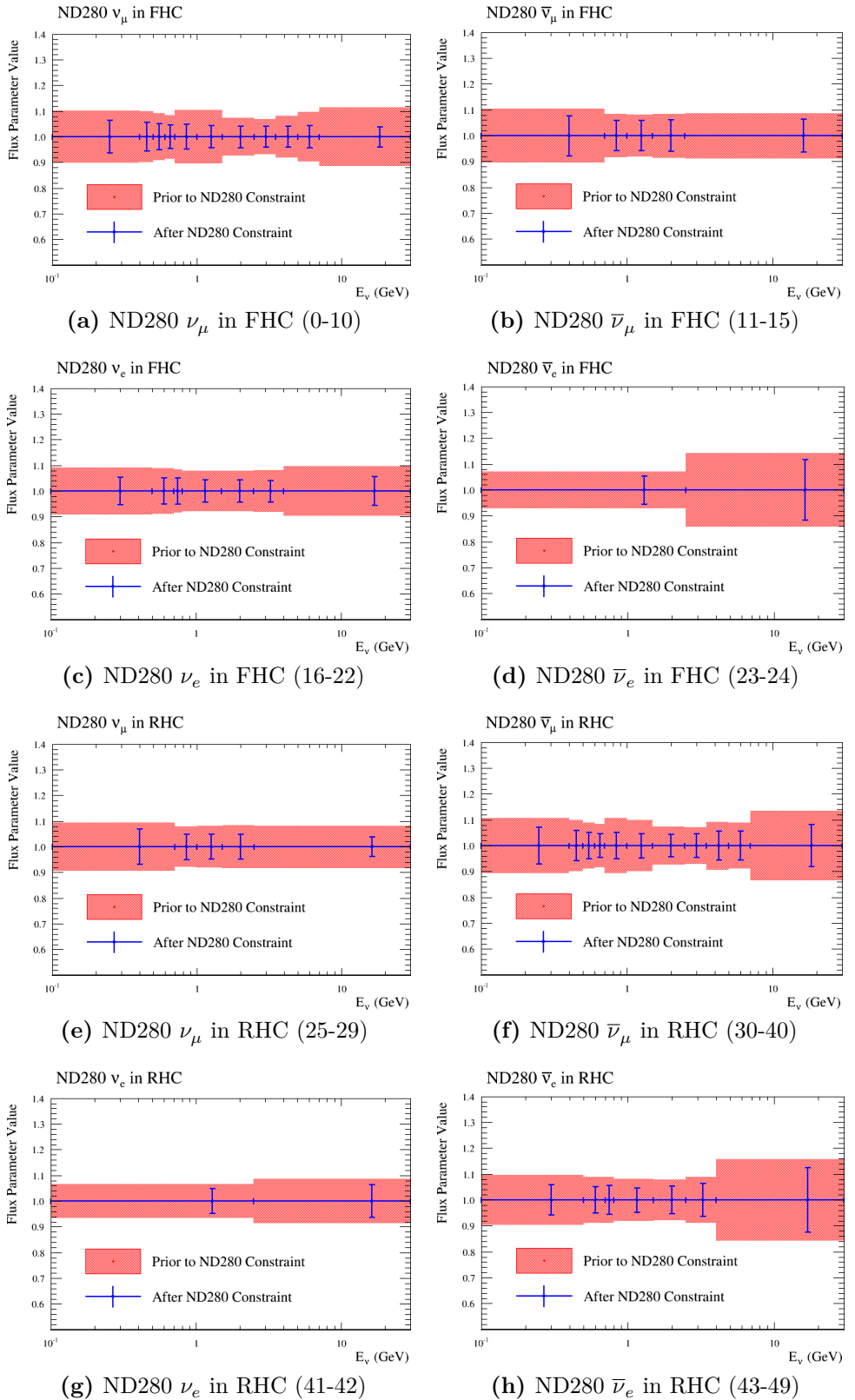


**Figure 5.3:** Asimov fit results for the Flux at ND280. The numbers in parentheses indicate the fit indices.

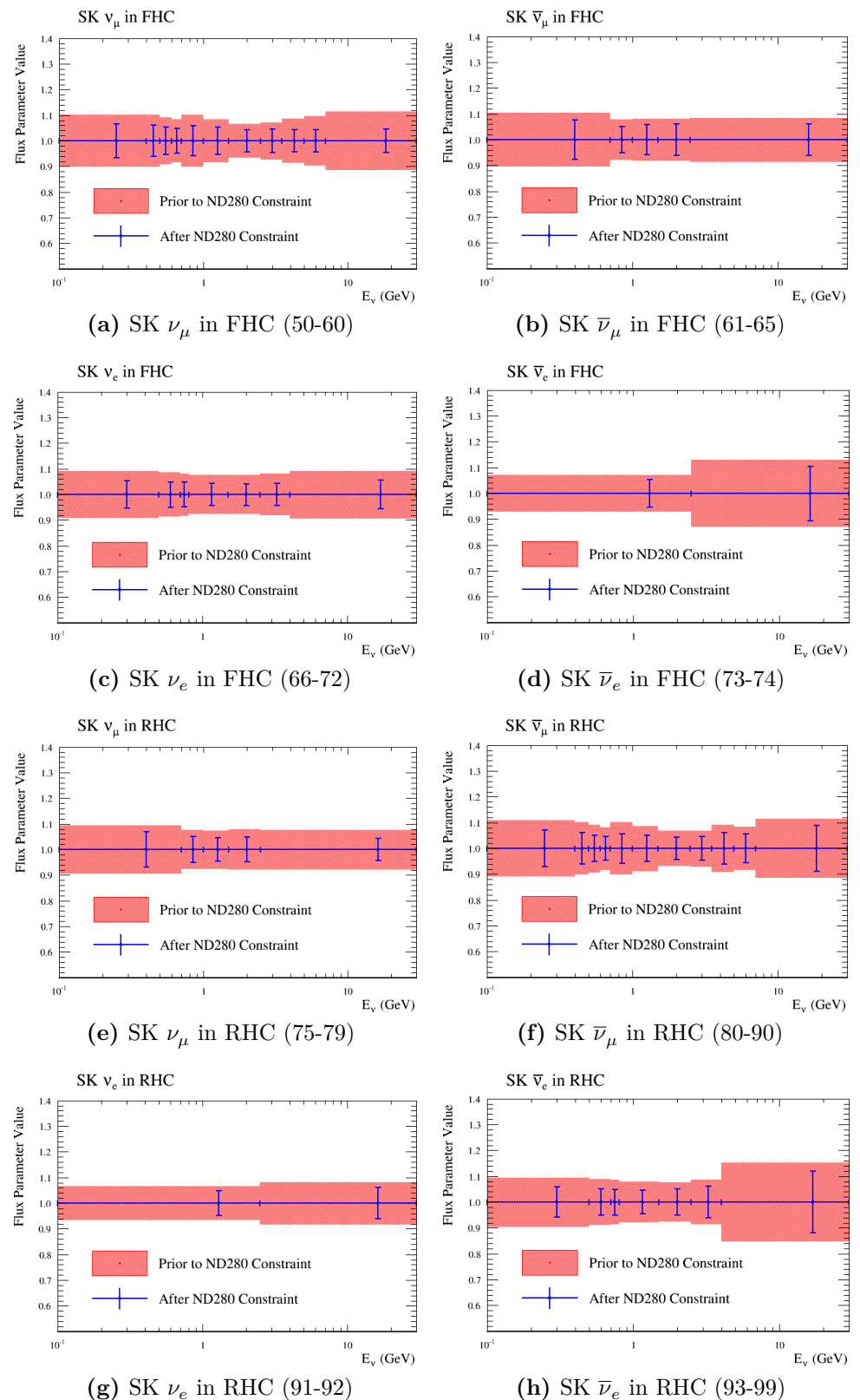


**Figure 5.4:** Asimov fit results for the Flux at Super-K. The numbers in parentheses indicate the fit indices .

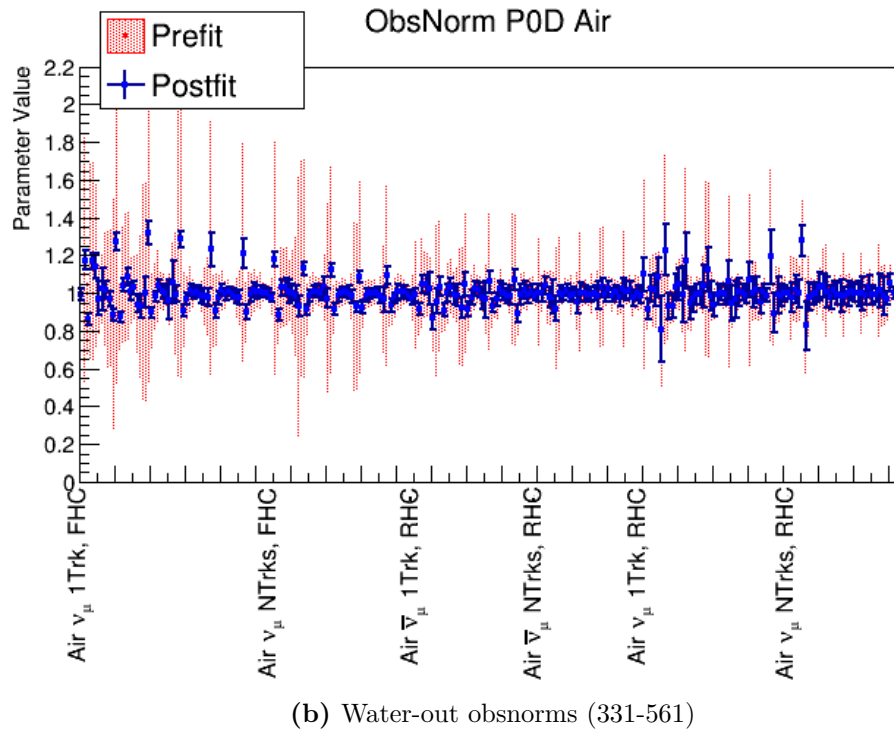
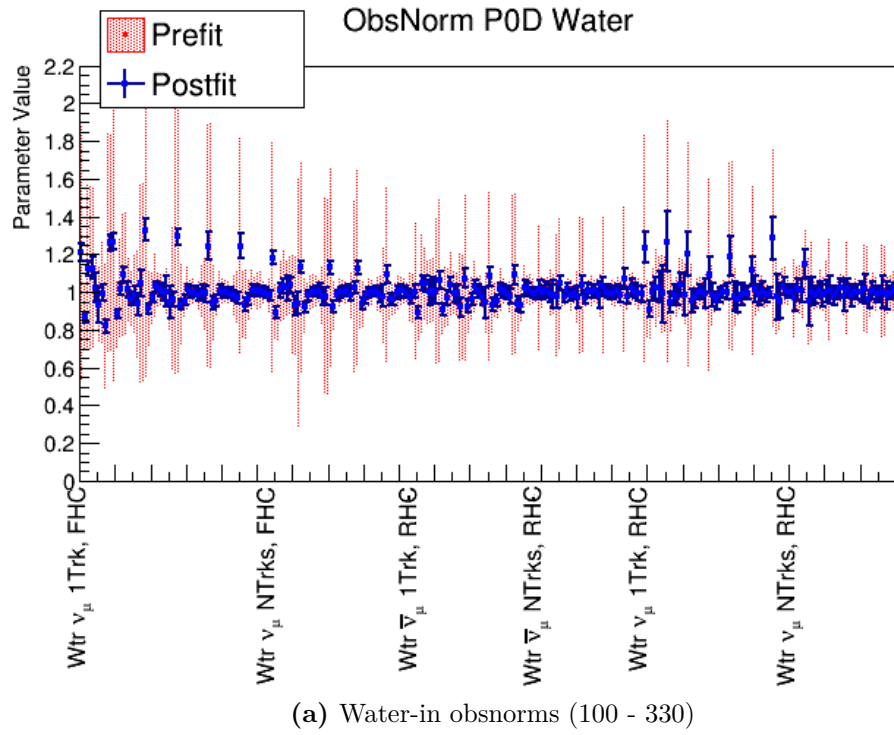
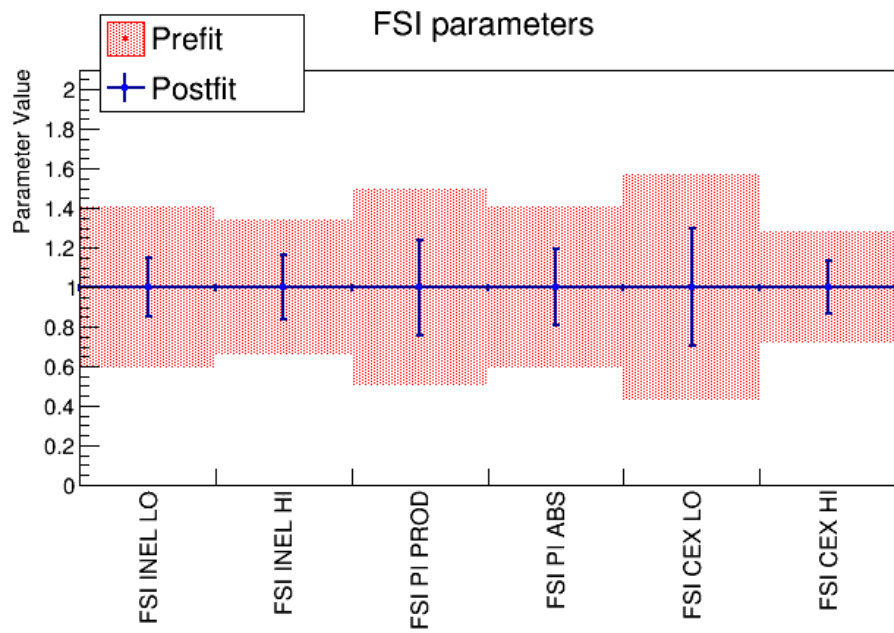
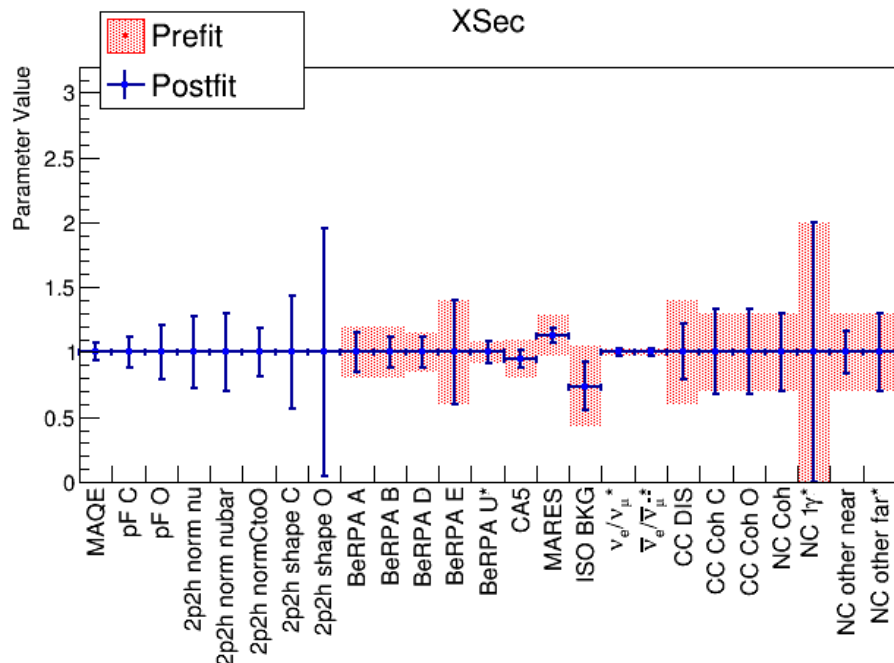


**Figure 5.5:** Asimov fit results for the obsnorm parameters. The numbers in parentheses indicate the fit indices. The large jumps in the bin normalization parameters is an artifact of the indexing choice with the indices increasing in increasing momentum in constant angular slices. Compare the changes in the bin normalizations in the  $\nu_\mu$  in FHC CC 1-Track in Figure 4.5 on page 110.



(a) FSI (562-567)



(b) Cross Section (568-592)

**Figure 5.6:** Asimov fit results for the FSI and cross section parameters. The numbers in parentheses indicate the fit indices. In order to provide a consistent presentation of parameter changes between prefit and postfit among all parameters, shape location and scale parameters are adjusted to prefits of one (1). In effect, the value and uncertainties for all parameters are fractional changes.

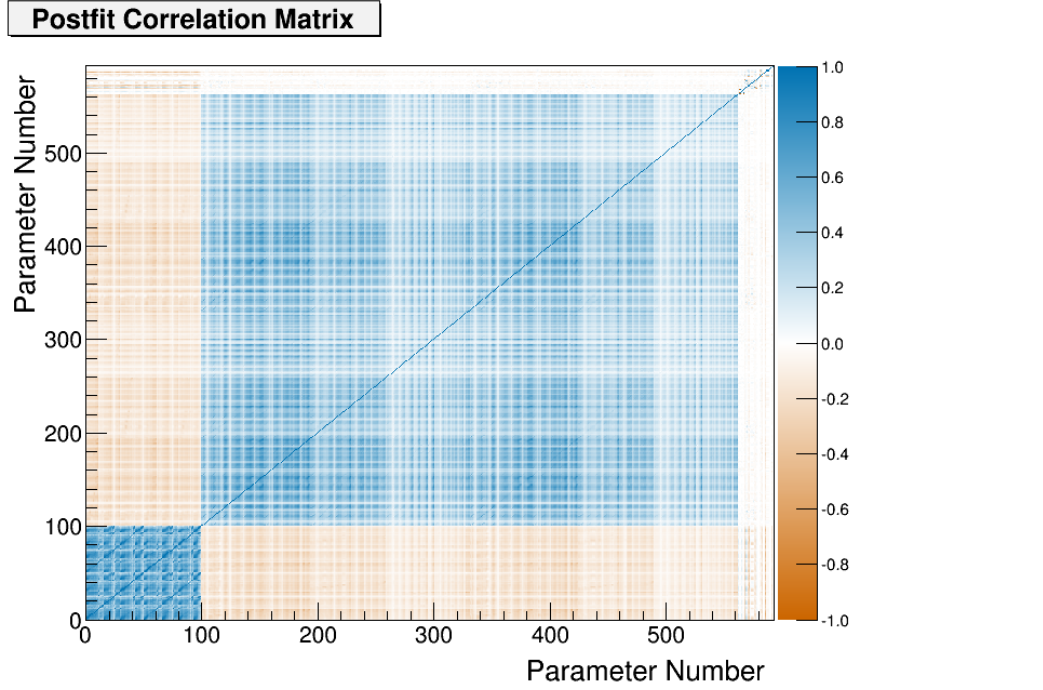


**Figure 5.7:** Complete postfit correlation matrix for the Asimov data fit.

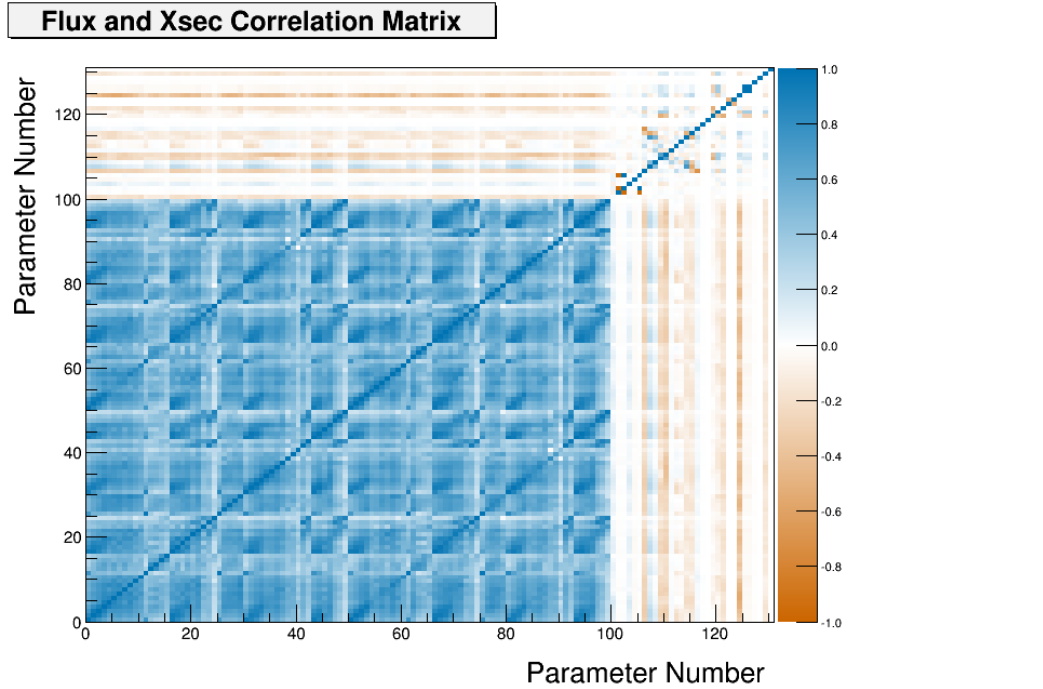


**Figure 5.8:** Flux and cross section postfit correlation matrix for the Asimov data fit. The parameters from 1-100 are the flux parameters and all parameters after are the cross section.

---

## 5.2 Fake Data

In this section, we examine the results of BANFF fits when given data sets with non-physical alterations. As stated earlier, these are called “fake data” sets since we are treating these as data in the fit, but they are in fact generated starting with the MC. These data sets initially start with the Asimov data set and have variations applied to it. Here we are only interested in the results of the flux and cross section parameters since they are the parameters that are propagated to the oscillation analysis. The first fake data set is a variation of the high energy  $\nu_\mu$  in FHC neutrino flux. The other test is a variation of the Single Pion Event Rate Variation.

While other fake data sets could be generated that are more or less similar to the Asimov data set, that is not the purpose of fitting to fake data sets. *The purpose of these tests is to show the fit can converge when provided with non-Asimov data sets and we can understand the results.* The fitting software MINUIT in the BANFF fit is known to not converge on a global minimum when using altered Asimov data. In particular, fitting FGD-only data generated from random and uncorrelated variations of all fit flux, cross section, and bin normalization parameters, 127 out of 500 fits ( $\sim 25\%$ ) reported fit convergence problems. So convergence is not assured in all situations, but is possible. The information it does provide is possible biases in the fit results for given systematic parameters. By demonstrating the BANFF fit converges with PØD-only fake data and we can sensibly understand the results, we establish that a credible PØD-only real data fit result is possible.

### 5.2.1 High Energy $\nu_\mu$ in FHC Flux Variation

This fake data set arbitrarily increases the  $\nu_\mu$  in FHC flux between 7 and 30 GeV by +25%. This variation was chosen since this energy range corresponds precisely to flux parameter  $b_{10}$  and it could affect all analysis bins. The input fake data in true neutrino energy is shown in Figure 5.9 on page 142.

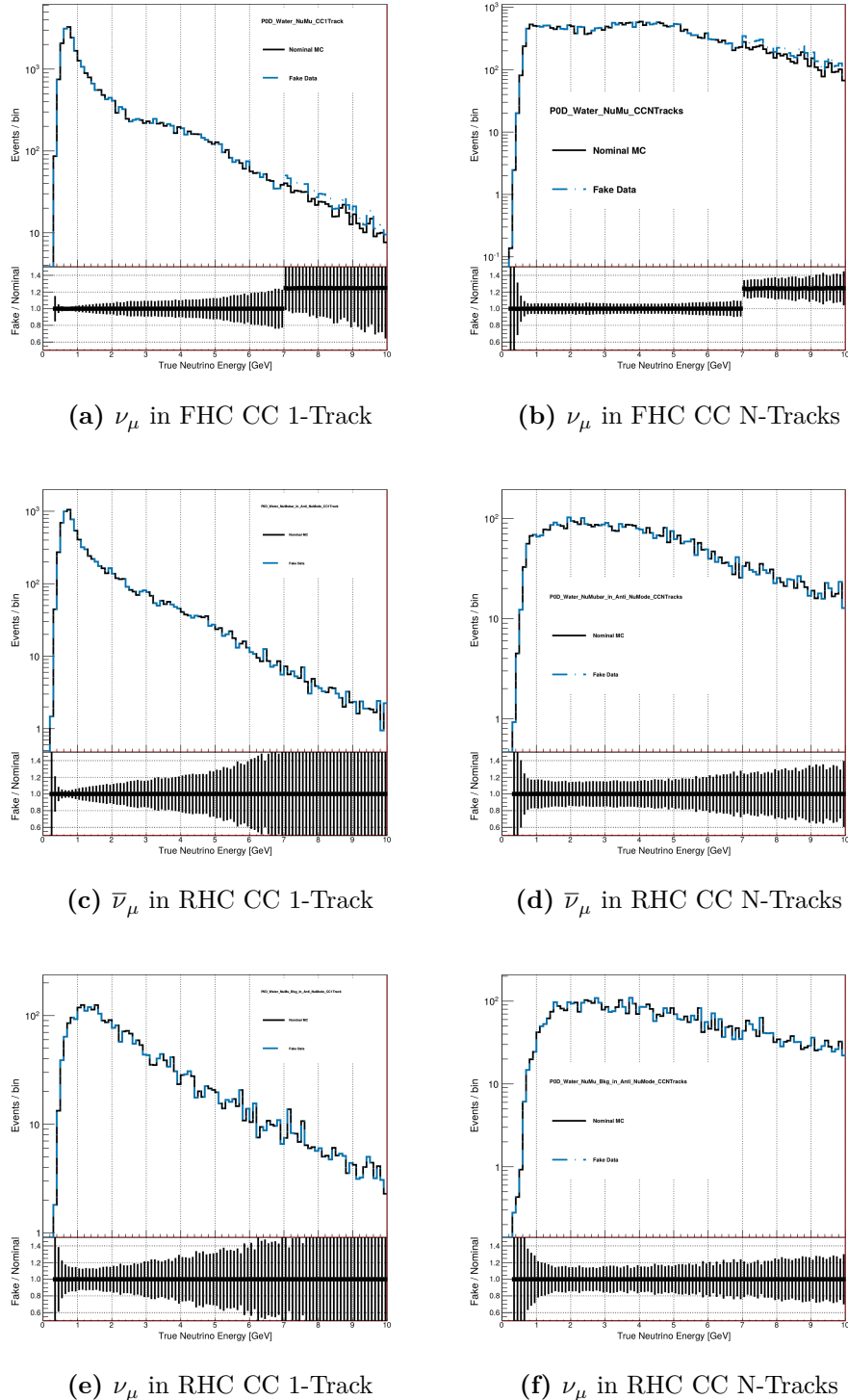


**Figure 5.9:** Neutrino flux before and after applying the +25% increase to  $\nu_\mu$  in FHC flux in the High Energy Neutrino Flux Variation data set. In the figures, “Nominal MC” refers to the Asimov prediction and “Fake Data” is the altered data set. A ratio of the fake data to nominal MC is shown below each histogram to show the variation was applied correctly. The flux of neutrinos, both  $\nu_\mu$  and  $\bar{\nu}_\mu$ , in RHC are not affected.

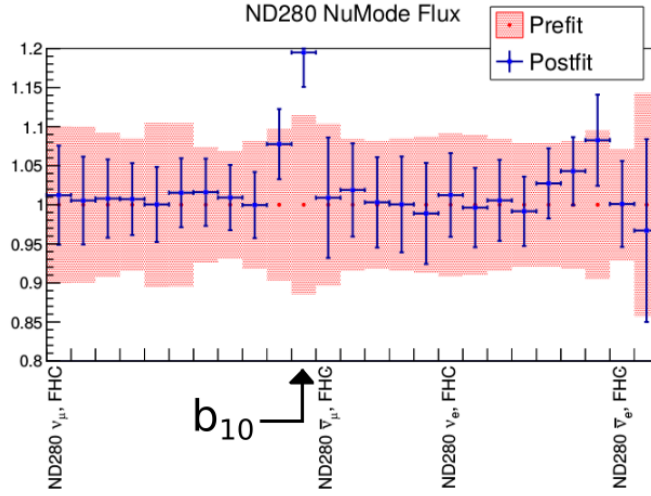
---

The postfit parameter plots are shown in Figure 5.10 on page 144. We see that the target flux parameter  $b_{10}$  has significantly increased from its prefit value by almost +20%. However, due to correlations in the flux covariance matrix, other flux parameters have changed. The BANFF fit prefers to increase the previous energy flux parameter and the high energy  $\nu_e$  flux parameters as well. While we saw that the flux and hence event rate was not changed in the RHC samples, the RHC flux parameters are also slightly affected. However, the RHC flux parameters are still well within prefit uncertainties. The statement is true for the cross section and FSI parameters. Therefore we can conclude that the fit prefers to resolve nonphysical changes large, singular changes with many correlated parameter variations.

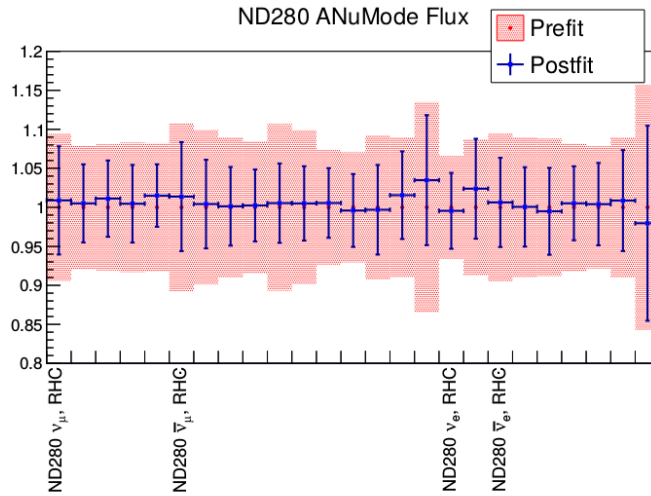
### 5.2.2 Single Pion Event Rate Variation

This fake data set arbitrarily increases the number of resonant single pion events by +25%. This was implemented by taking all true NEUT CC- $1\pi$  events, extracting the event weight, and increasing it by +25%. This is what is observed in the lepton candidate momentum distributions as shown in Figure 5.11 on page 145. According to the CC- $1\pi$  model, the event rate can be singly absorbed in  $C_A^5$ . However as seen in Appendix ??, increases in any CC- $1\pi$  parameter will increase the event rate. Additionally,  $C_A^5$  and  $M_A^{\text{Res}}$  are anticorrelated with one another meaning that these parameters will be forced to shift in opposite directions together. Given the postfit results from the previous fake data fit, we should expect to see more than just the CC- $1\pi$  parameters to vary.

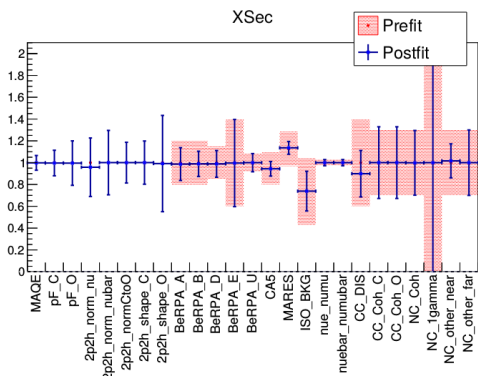
The postfit results for this fake data set are shown in Figure 5.12 on page 147. We observe that the CC- $1\pi$  parameter  $C_A^5$  increased by ~10%, but this is not enough to account for the input fake data shift. We also notice that due to anticorrelations,  $M_A^{\text{Res}}$  was decreased by about several percent. What the fit prefers is to increase the isospin= $1/2$  background, 2p2h normalization, and all the flux parameters. Like the first fake data set, we see that in the presence of nonphysical variations to the Physics, the fit prefers to spread out variations



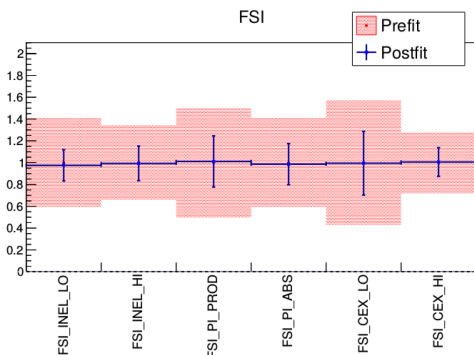
(a) ND280 FHC Flux



(b) ND280 RHC Flux



(c) Cross section parameters



(d) FSI parameters

**Figure 5.10:** Postfit parameters for the high energy  $\nu_\mu$  in FHC flux variation fake data fit. All the flux parameters in FHC are shown together and ordered sequentially from left to right. The same is true the RHC flux.

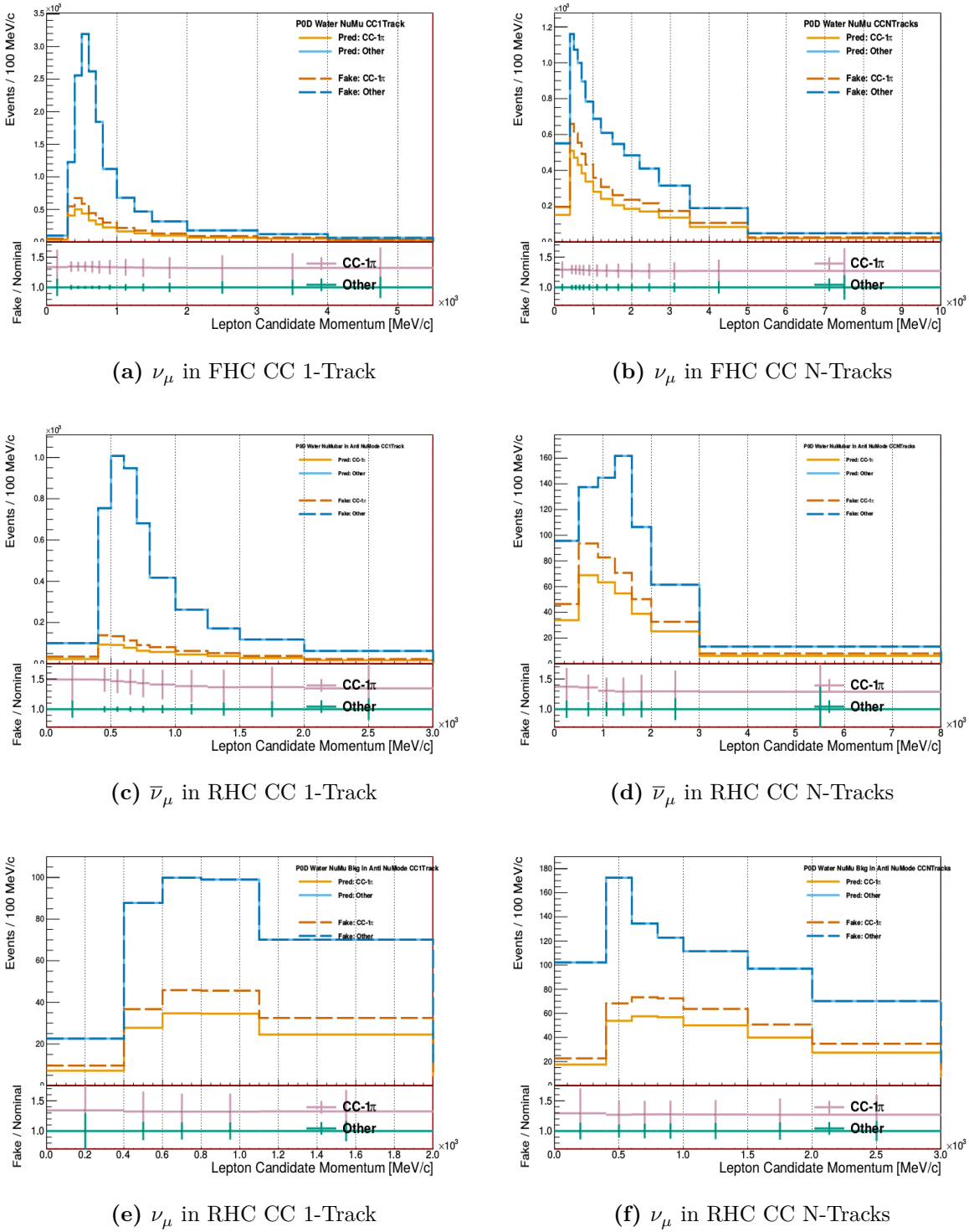


**Figure 5.11:** Lepton candidate momentum for the Single Pion Event Rate Variation fake data set. The nominal MC and fake data predictions are shown as solid and dashed lines, respectively. True CC- $\pi$  events are differentiated from all other interactions to illustrate the event scaling applied. A ratio plot of CC- $\pi$  events to all other interaction events shown beneath each main histogram.

---

among the other parameters. However, this time the variations are shared among flux and cross section parameters.

### 5.3 Validation Summary

We have validated the BANFF fit indeed works and tested its robustness in a variety of scenarios. We learned from the Asimov data set, which is the T2K nominal MC corrected to data POT with fine tuning corrections, in particular how the flux and cross section parameters affect the samples. In the fake data sets, we saw the effect of the penalty terms and how their correlations influence the fit. While more rigorous tests could establish where biases exist, these limitations are beyond the scope of this thesis. What has been established is that sensible fit results using the PØD selections are possible. We can now examine the PØD-only data and be assured the BANFF can fit can converge with PØD-only data.

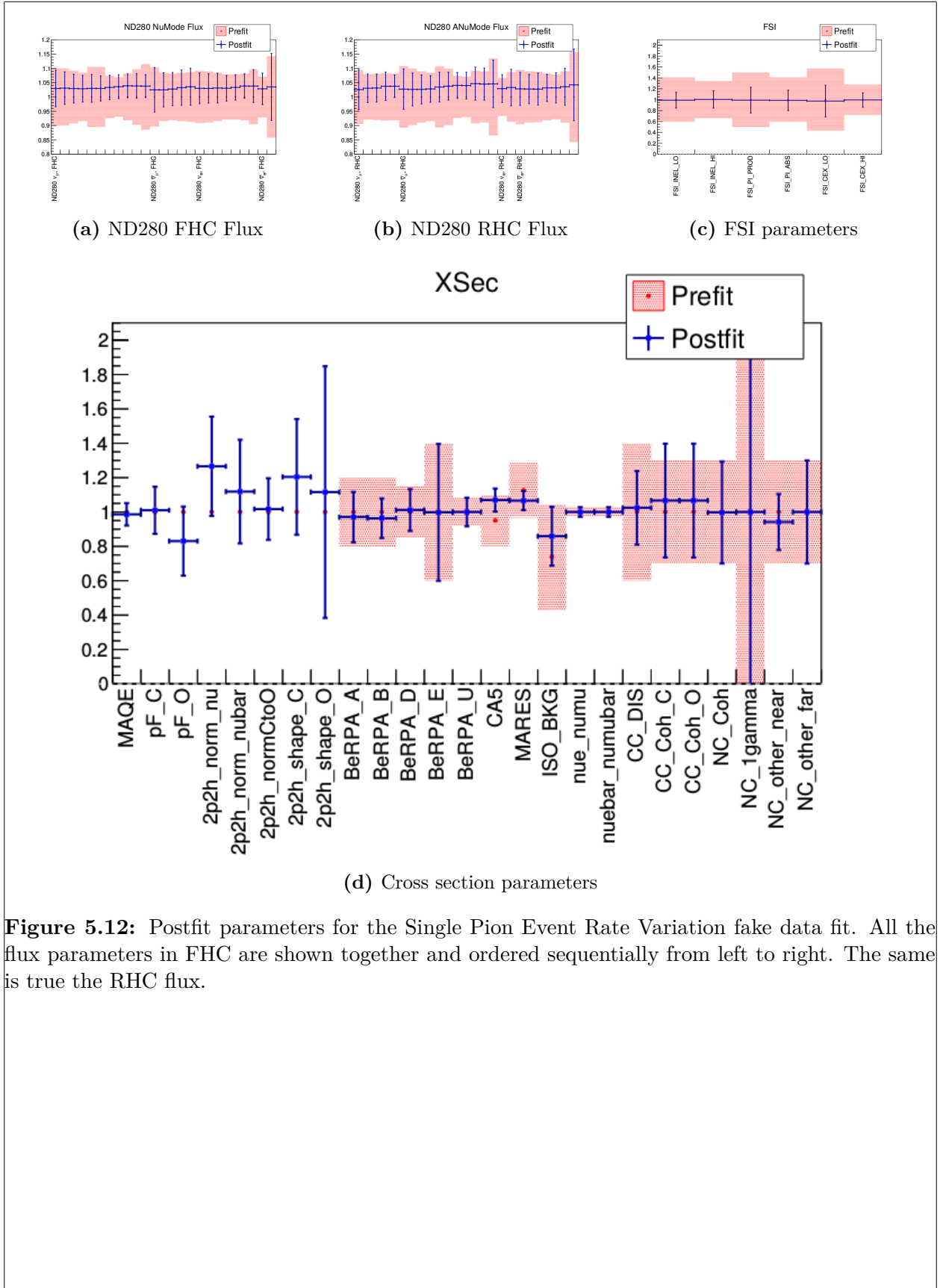


**Figure 5.12:** Postfit parameters for the Single Pion Event Rate Variation fake data fit. All the flux parameters in FHC are shown together and ordered sequentially from left to right. The same is true the RHC flux.

---

# Chapter 6

## Fitter Results

This chapter explores the results of performing the BANFF fit using the PØD-only samples. We have confirmed the fit machinery is working and the samples demonstrate sensitivity to flux and cross section parameters. The focus in this chapter is to examine the results of the PØD-only data fit and compare it against the FGD-only result.

The chapter will proceed in the following order. First the data will be examined since we have remained purposefully and mostly blind up to this state. Next the postfit results will be carefully examined and compared with that of the FGD-only fit. Finally, a hypothesis test will be performed to test the level of agreement between the two fits.

### 6.1 Prefit Sample Distributions

This section presents the first look at the data for the 12 samples according to the fit bins set in Chapter 4. The samples are categorized, as before seen, into four true interaction modes:  $\nu$  CCQE,  $\nu$  non-CCQE,  $\bar{\nu}$  CCQE, and  $\bar{\nu}$  non-CCQE. However, true fiducial volume (FV) and out of FV events are not differentiated in this case. The legend used to classify the data and prefit events is shown in Figure 6.1 on page 149. The prefit samples with the data shown are presented between Figure 6.2 on page 150 and Figure 6.13 on page 161. First

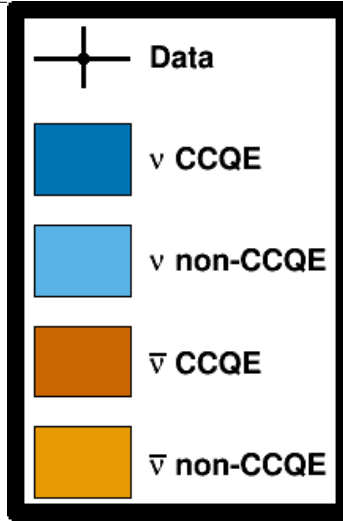


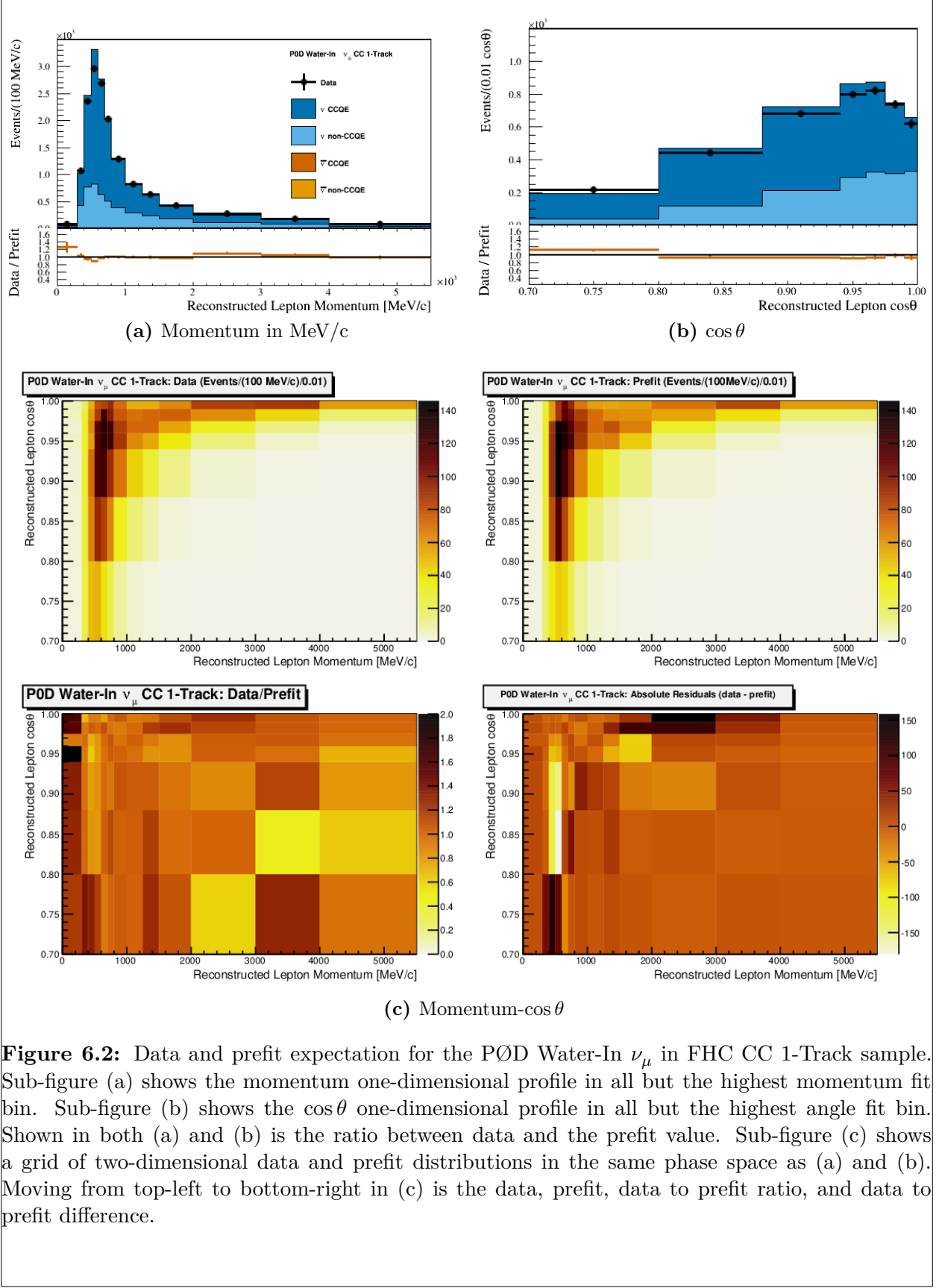
**Figure 6.1:** Data and prefit legend

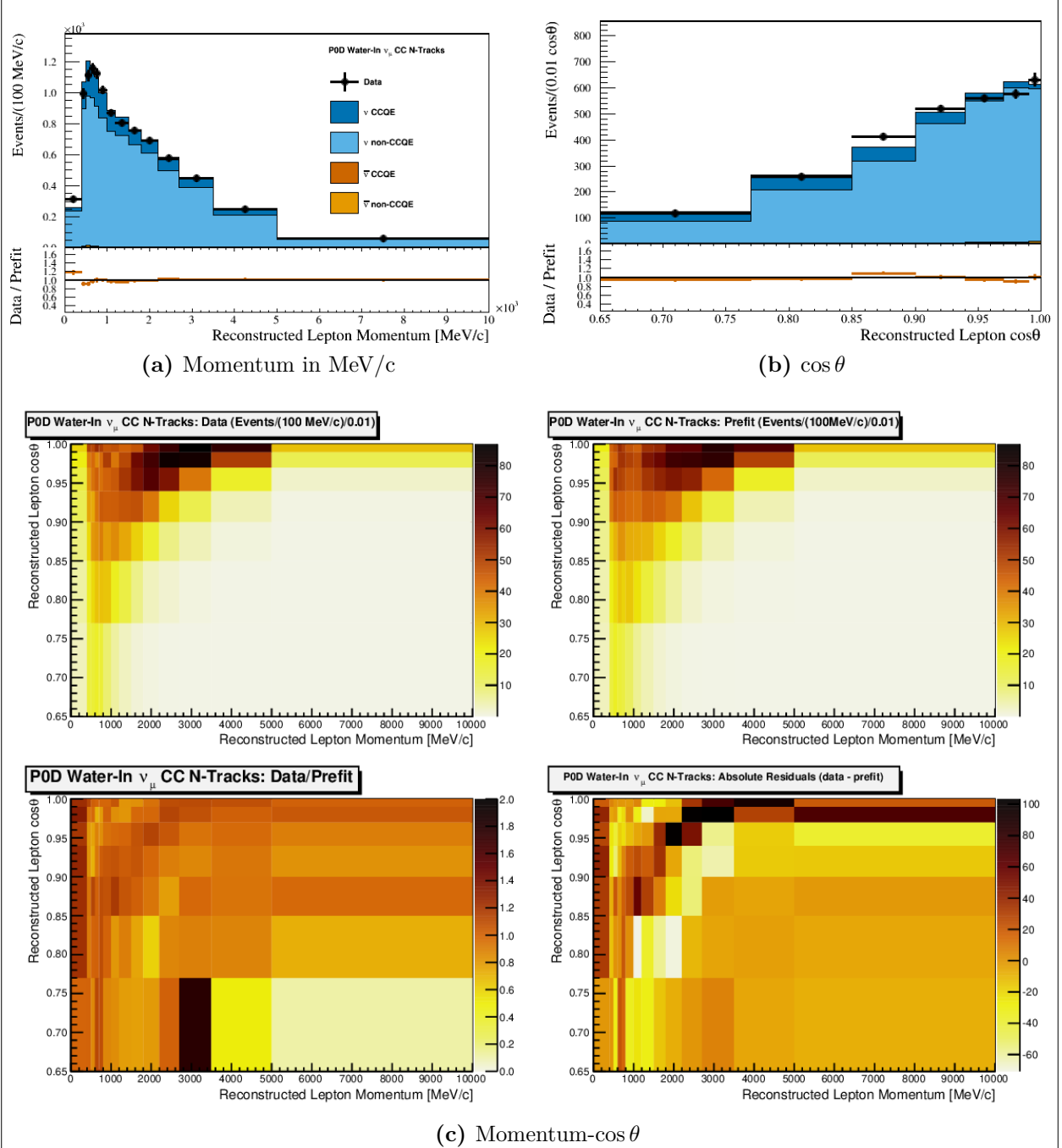
the water-in samples are displayed, and then the water-out samples are shown. As we saw before, the water-in and water-out samples are qualitatively the same.

In general, we notice good agreement between the data and prefit distributions. Their agreement is represented in one-dimensional profiles with the data to prefit ratio shown below the histograms. Evidence of the PØD bulging effect in the most downstream layers can be seen in all water-in samples. In particular, since there is more true mass in the most downstream layers, particles with lower momenta are more likely to enter the TPC than predicted by the MC using the as-built mass. Better agreement is observed in the water-out periods, but there is some initial tension in the samples.

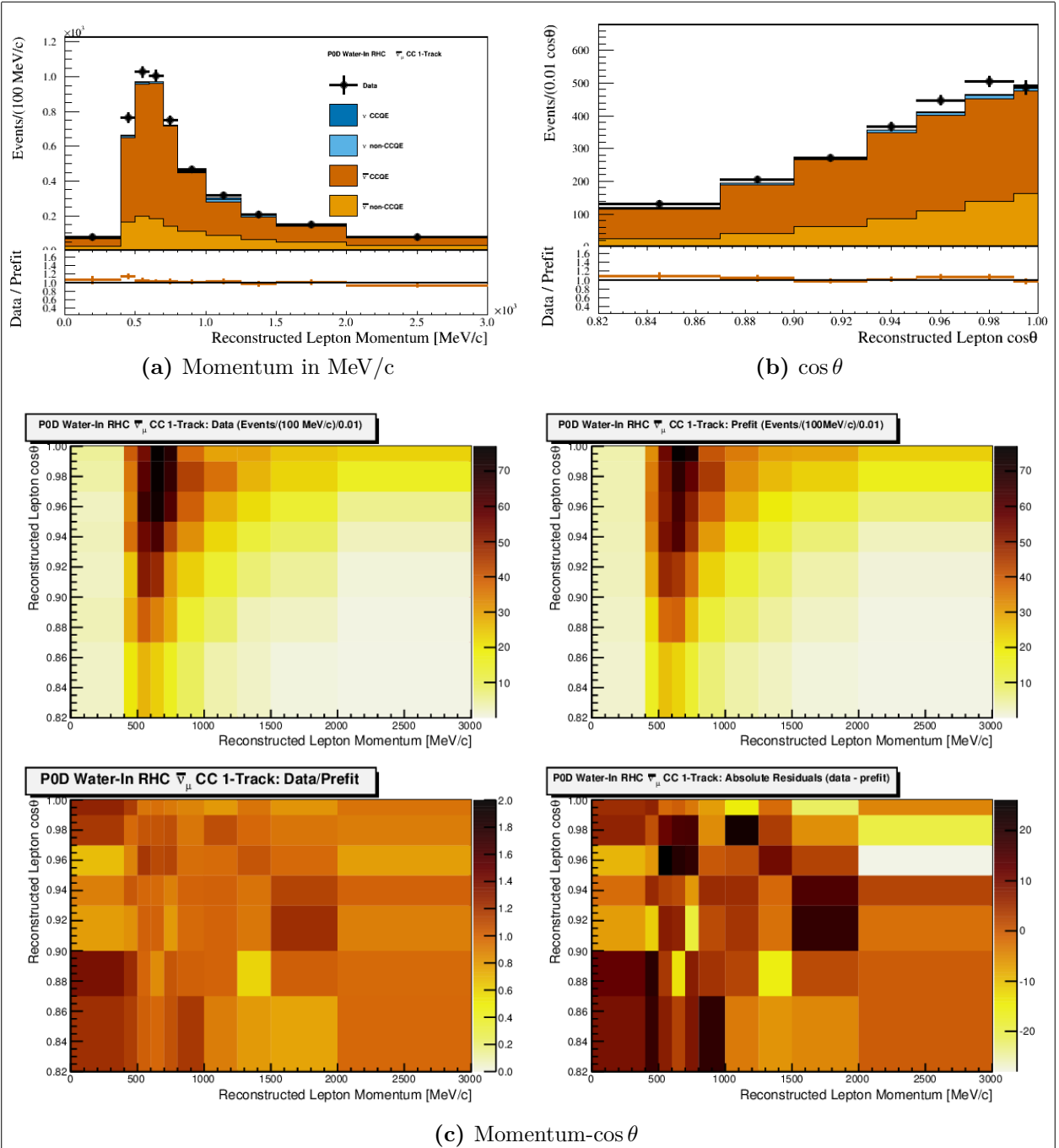
## 6.2 Postfit Results

The results of the PØD-only BANFF fit are presented here. MINUIT reported that it took between 149000 and 150000 iterations to find the  $\Delta\chi^2_{ND280}$  minimum with an additional 176000 iterations to calculate the Hessian matrix. The total time to load all the data and complete the Hessian calculation was 27.5 hours using OpenMP with 16 cores, which is not unreasonable in terms of large scale computational work. However, a significant fraction of

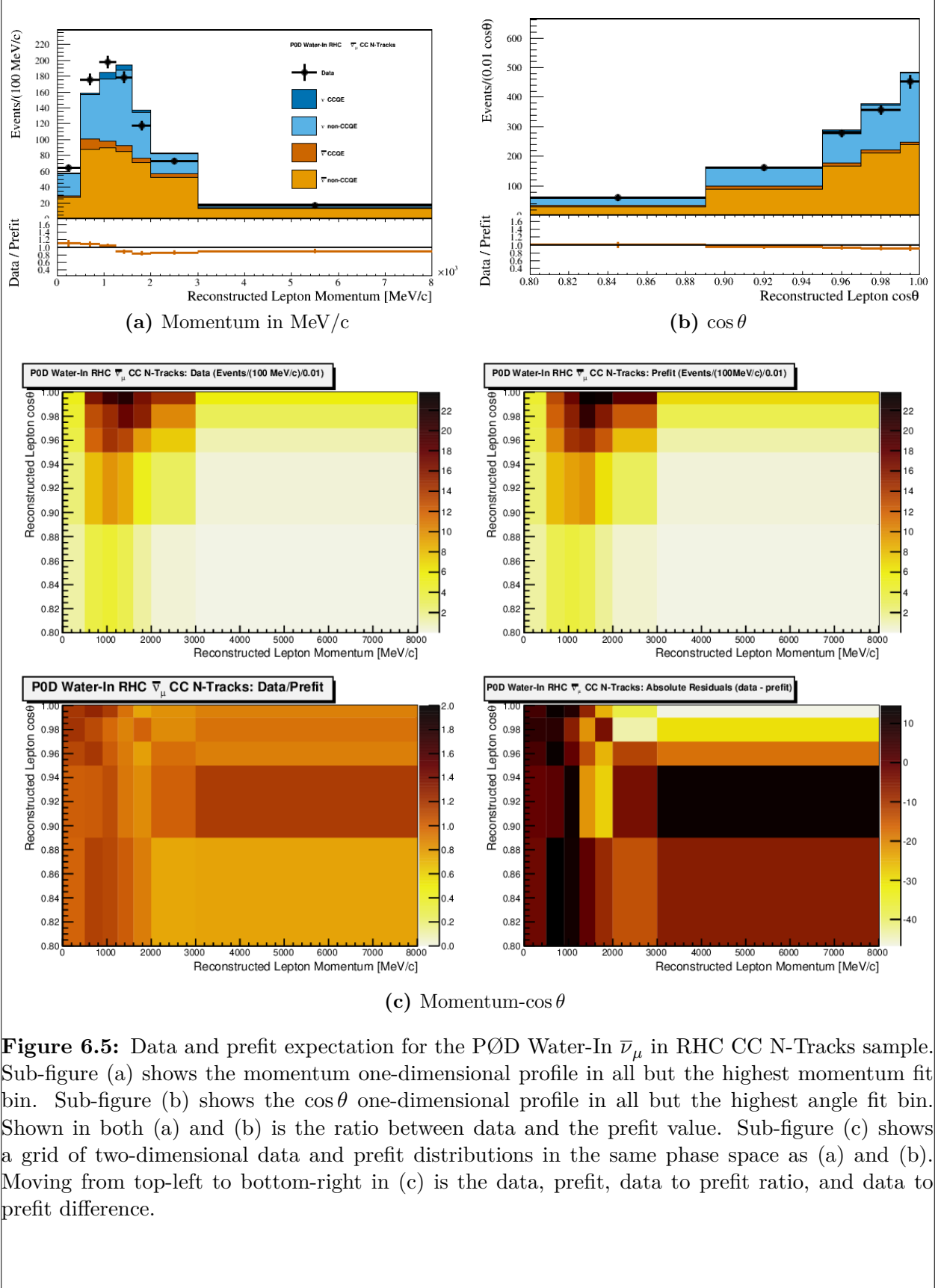


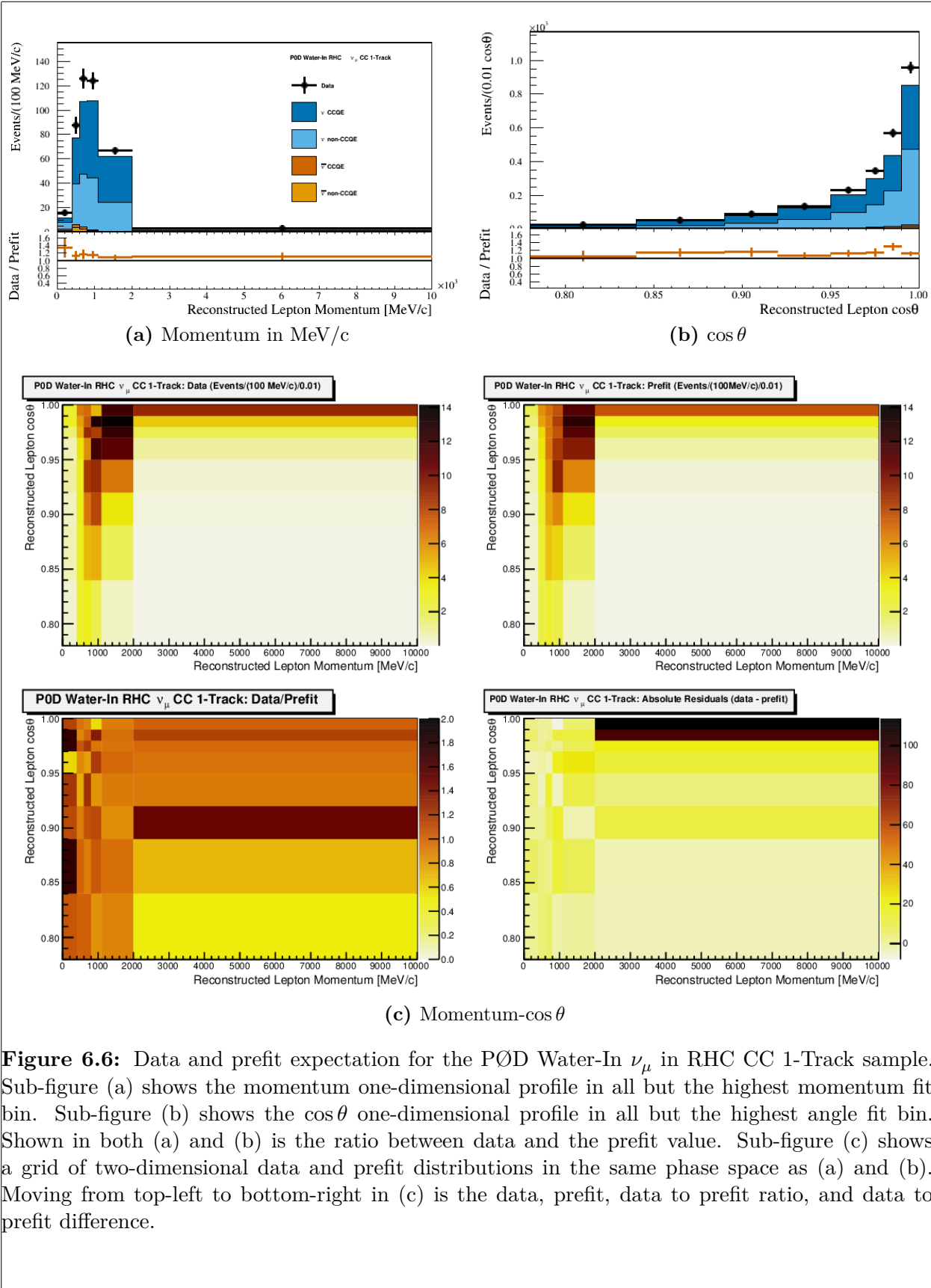


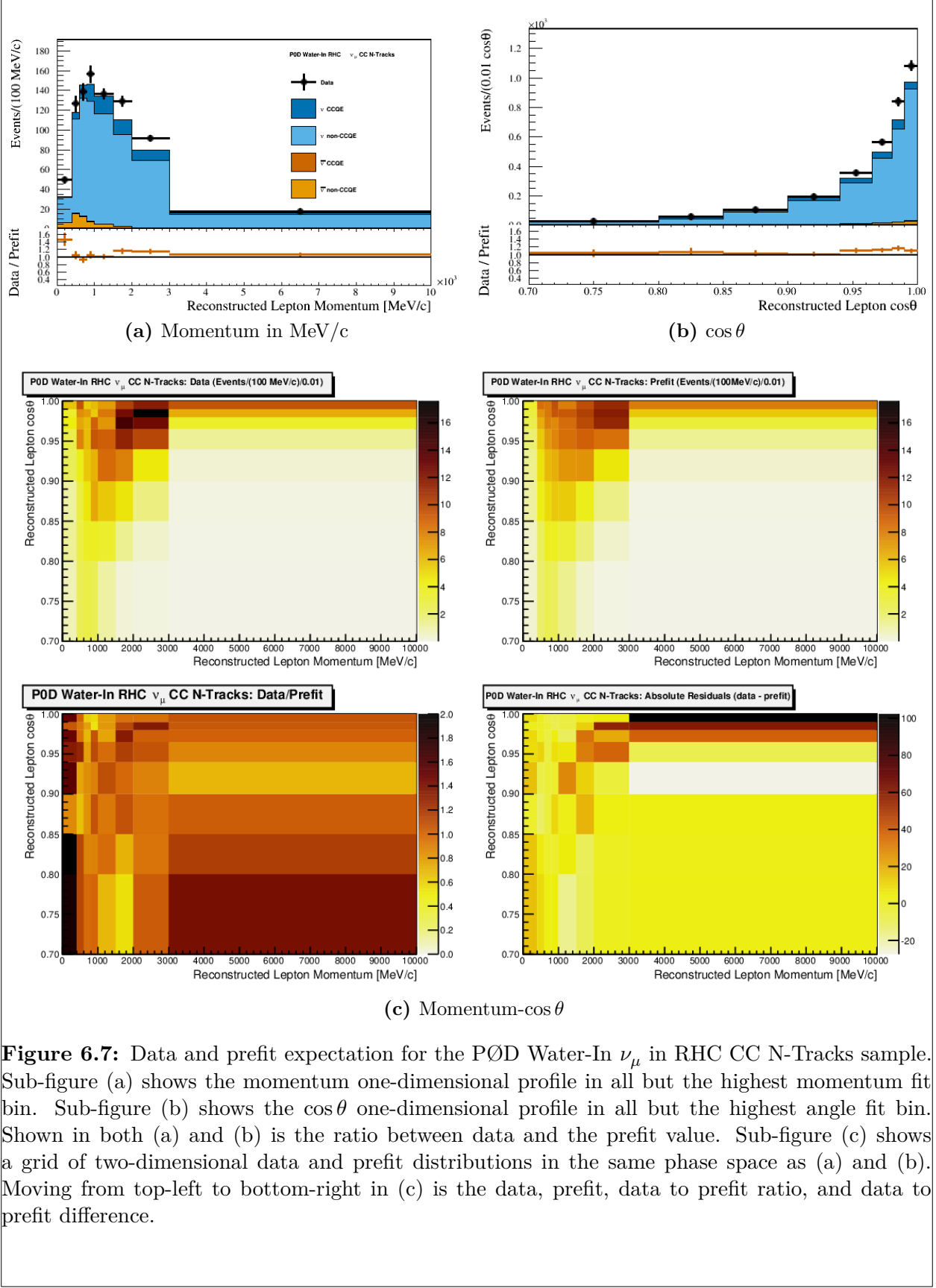
**Figure 6.3:** Data and prefit expectation for the PØD Water-In  $\nu_\mu$  in FHC CC N-Tracks sample. Sub-figure (a) shows the momentum one-dimensional profile in all but the highest momentum fit bin. Sub-figure (b) shows the  $\cos \theta$  one-dimensional profile in all but the highest angle fit bin. Shown in both (a) and (b) is the ratio between data and the prefit value. Sub-figure (c) shows a grid of two-dimensional data and prefit distributions in the same phase space as (a) and (b). Moving from top-left to bottom-right in (c) is the data, prefit, data to prefit ratio, and data to prefit difference.

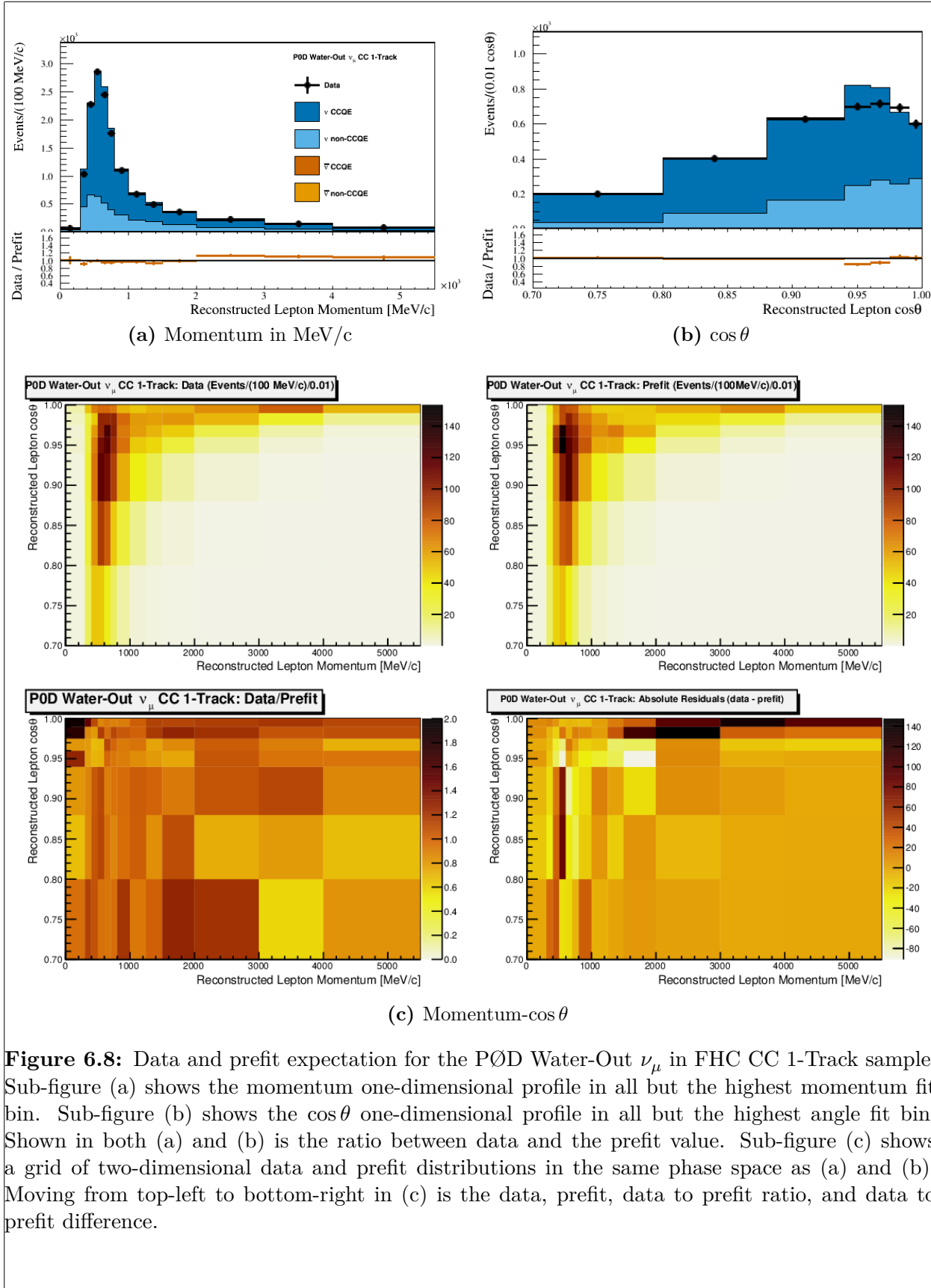


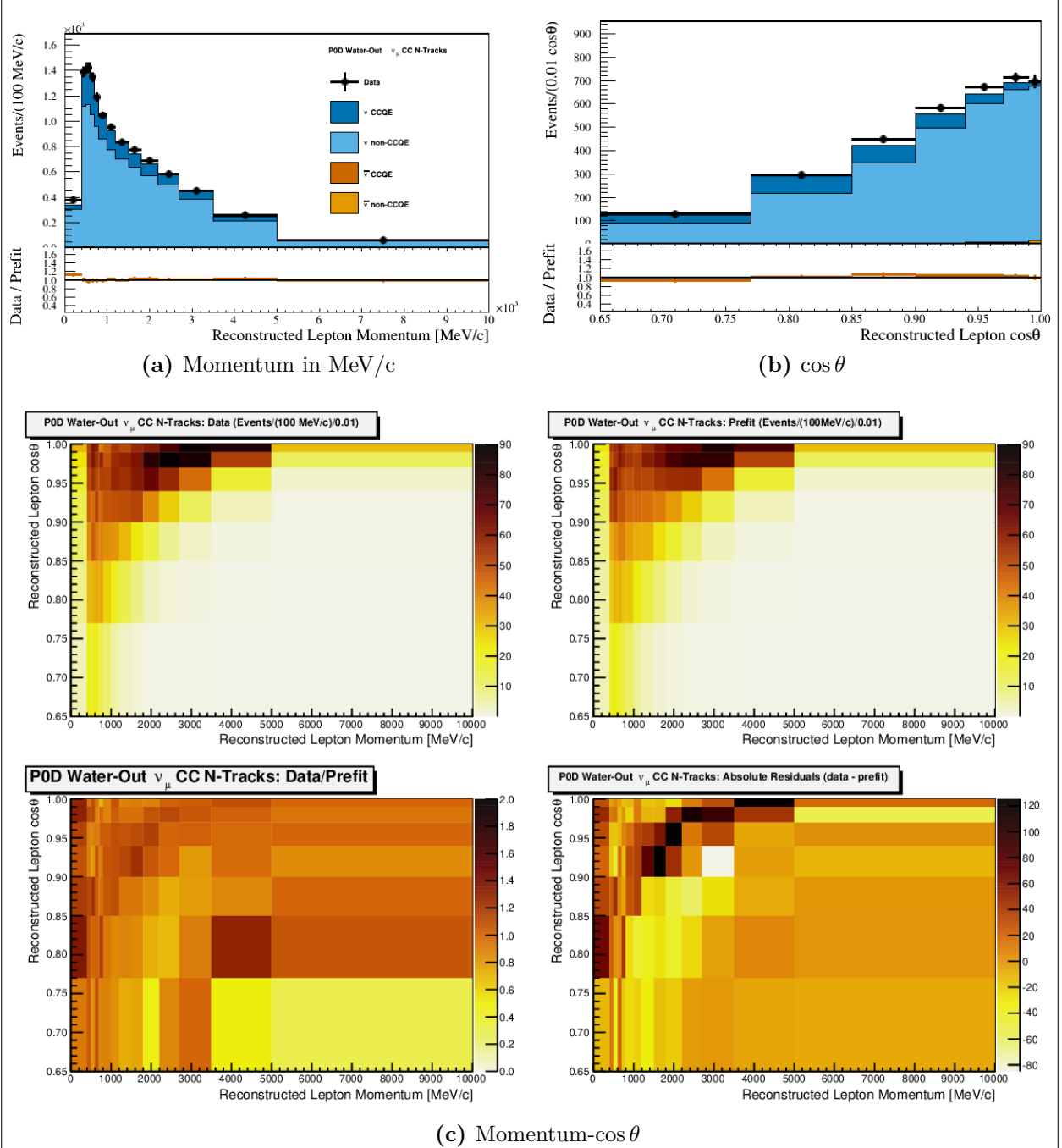
**Figure 6.4:** Data and prefit expectation for the PØD Water-In  $\bar{\nu}_\mu$  in RHC CC 1-Track sample. Sub-figure (a) shows the momentum one-dimensional profile in all but the highest momentum fit bin. Sub-figure (b) shows the  $\cos\theta$  one-dimensional profile in all but the highest angle fit bin. Shown in both (a) and (b) is the ratio between data and the prefit value. Sub-figure (c) shows a grid of two-dimensional data and prefit distributions in the same phase space as (a) and (b). Moving from top-left to bottom-right in (c) is the data, prefit, data to prefit ratio, and data to prefit difference.



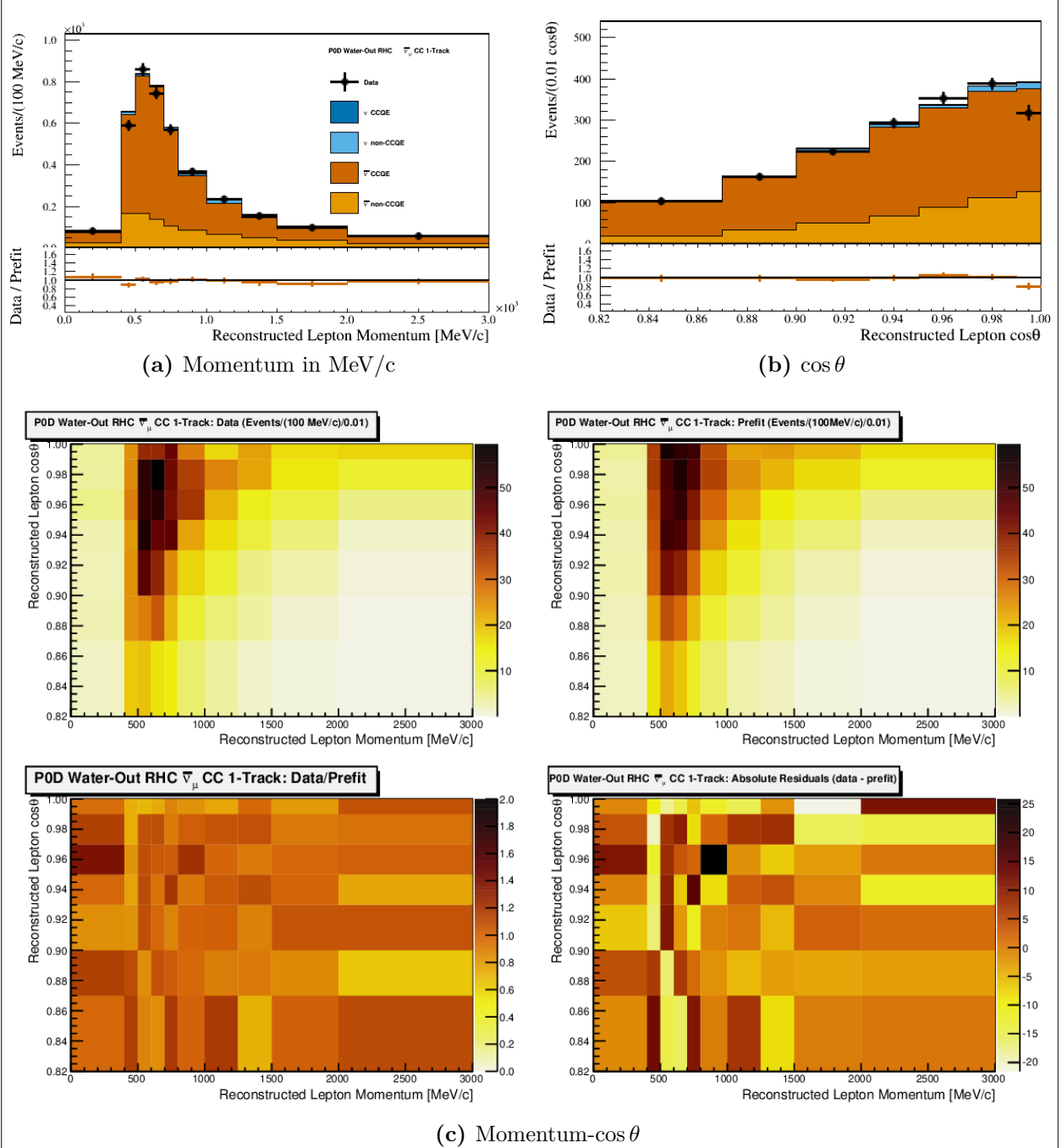




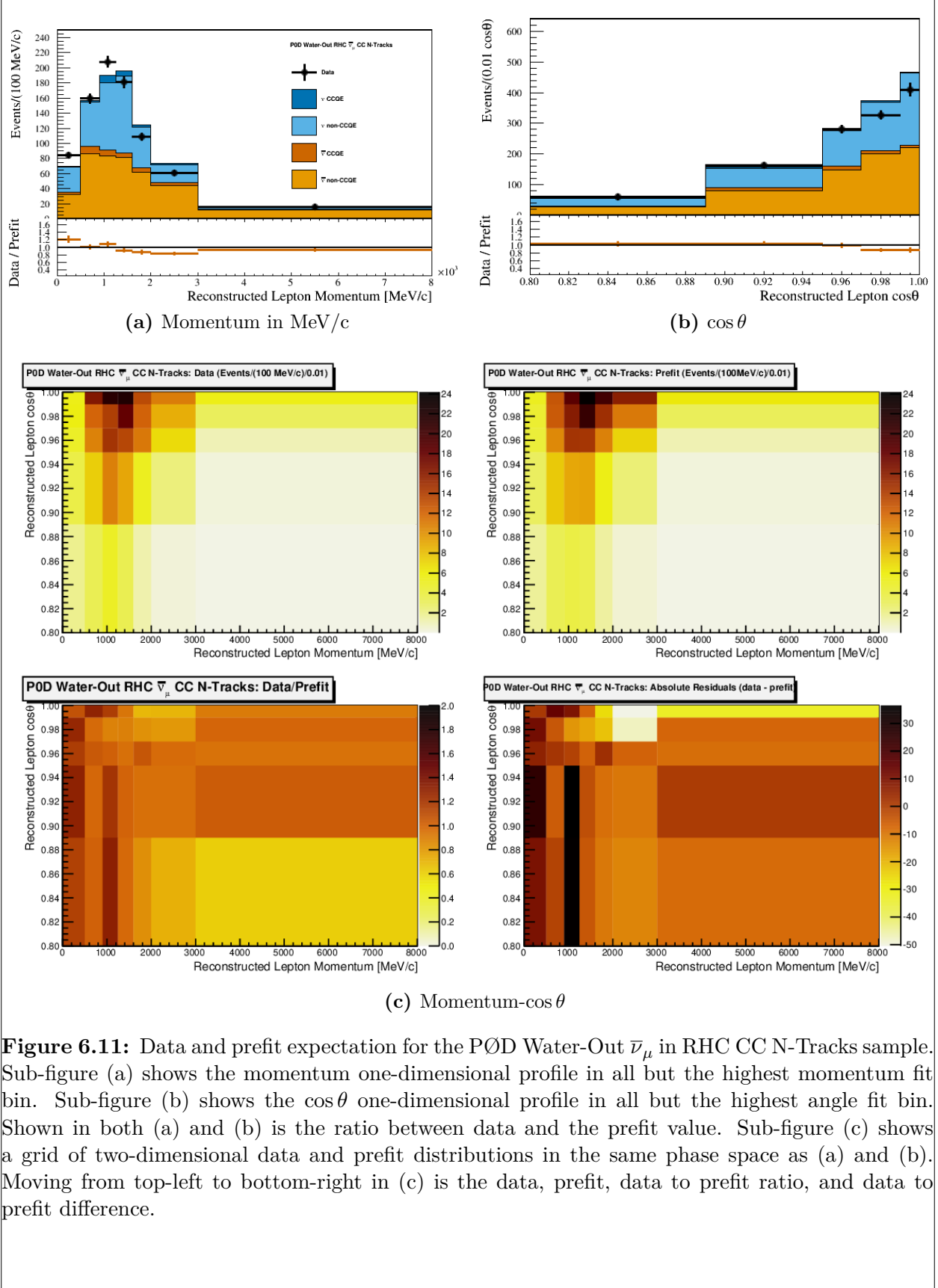




**Figure 6.9:** Data and prefit expectation for the PØD Water-Out  $\nu_\mu$  in FHC CC N-Tracks sample. Sub-figure (a) shows the momentum one-dimensional profile in all but the highest momentum fit bin. Sub-figure (b) shows the  $\cos \theta$  one-dimensional profile in all but the highest angle fit bin. Shown in both (a) and (b) is the ratio between data and the prefit value. Sub-figure (c) shows a grid of two-dimensional data and prefit distributions in the same phase space as (a) and (b). Moving from top-left to bottom-right in (c) is the data, prefit, data to prefit ratio, and data to prefit difference.



**Figure 6.10:** Data and prefit expectation for the PØD Water-Out  $\bar{\nu}_\mu$  in RHC CC 1-Track sample. Sub-figure (a) shows the momentum one-dimensional profile in all but the highest momentum fit bin. Sub-figure (b) shows the  $\cos \theta$  one-dimensional profile in all but the highest angle fit bin. Shown in both (a) and (b) is the ratio between data and the prefit value. Sub-figure (c) shows a grid of two-dimensional data and prefit distributions in the same phase space as (a) and (b). Moving from top-left to bottom-right in (c) is the data, prefit, data to prefit ratio, and data to prefit difference.



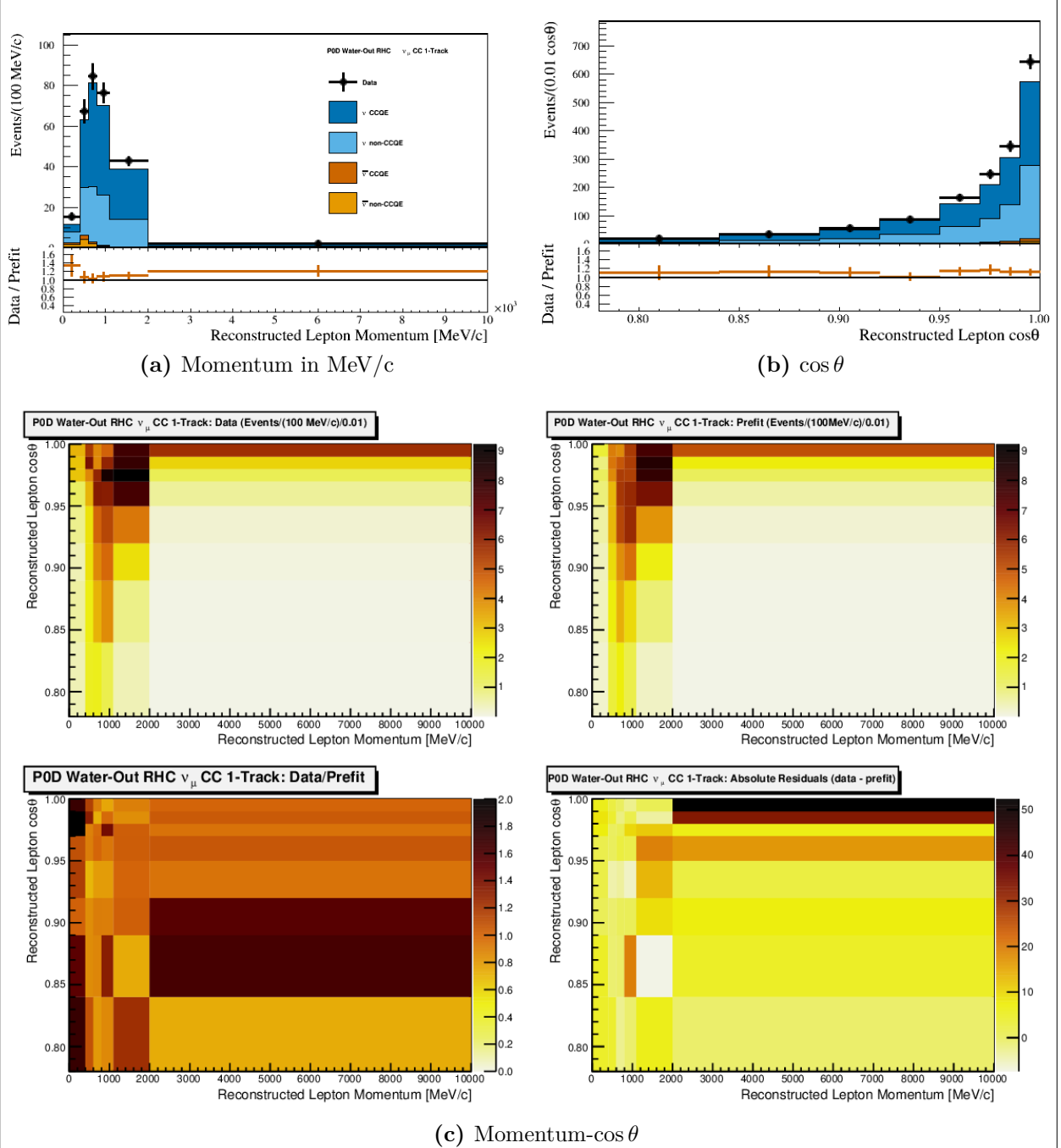


**Figure 6.12:** Data and prefit expectation for the PØD Water-Out  $\nu_\mu$  in RHC CC 1-Track sample. Sub-figure (a) shows the momentum one-dimensional profile in all but the highest momentum fit bin. Sub-figure (b) shows the  $\cos\theta$  one-dimensional profile in all but the highest angle fit bin. Shown in both (a) and (b) is the ratio between data and the prefit value. Sub-figure (c) shows a grid of two-dimensional data and prefit distributions in the same phase space as (a) and (b). Moving from top-left to bottom-right in (c) is the data, prefit, data to prefit ratio, and data to prefit difference.

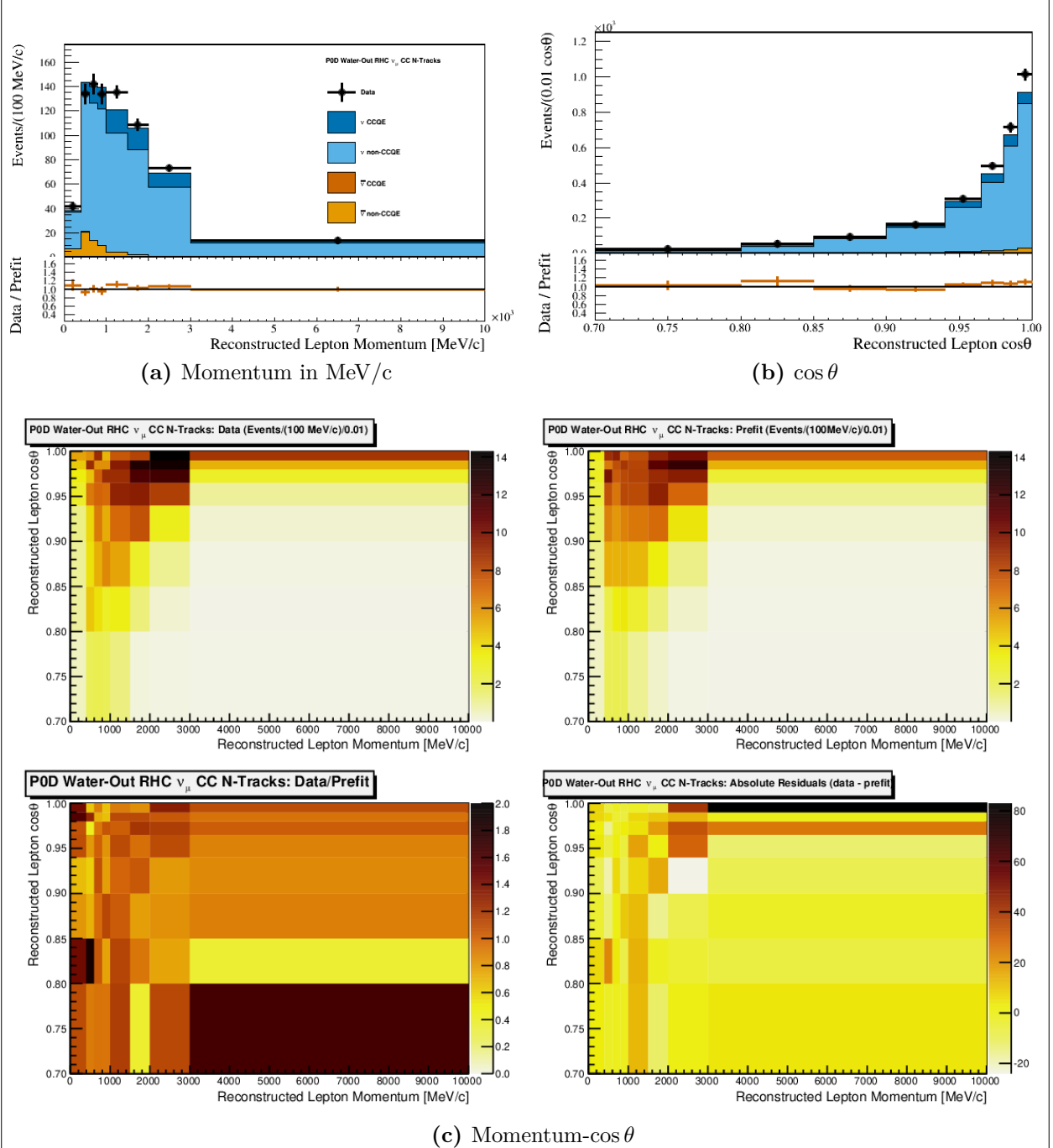


**Figure 6.13:** Data and prefit expectation for the PØD Water-Out  $\nu_\mu$  in RHC CC N-Tracks sample. Sub-figure (a) shows the momentum one-dimensional profile in all but the highest momentum fit bin. Sub-figure (b) shows the  $\cos\theta$  one-dimensional profile in all but the highest angle fit bin. Shown in both (a) and (b) is the ratio between data and the prefit value. Sub-figure (c) shows a grid of two-dimensional data and prefit distributions in the same phase space as (a) and (b). Moving from top-left to bottom-right in (c) is the data, prefit, data to prefit ratio, and data to prefit difference.

---

the time, about 6.2 hours hours, was spent loading the data and cross section splines into memory which consumed about 40 GB of RAM.

Specific topics on the postfit results are presented in the following order. First is an examination of the postfit samples in one-dimensional profiles and two-dimensional spaces. Next is a comparison of the parameter values among the prefit, PØD-only, and FGD-only results. And finally is a hypothesis test on the level of agreement between the PØD-only and FGD-only BANFF fit results.

### 6.2.1 Postfit Sample Distributions

Presented below are the 12 samples again, but with the postfit parameters applied to the fit bins. This ensures we have not altered the data and the data to tuned prediction (postfit) ratios have improved as a result of the fit. The samples are shown in Figure 6.14 on page 164 to Figure 6.25 on page 175 in the same order as presented in the previous section.

We see an improved agreement between the postfit prediction and the data. There still is tension, in particular, in the lowest momentum bins which could of been mitigated by having more bin normalization parameters. Between the water-in and water-out modes, disagreement between them is balanced since the flux affects them the same way. Given there still is tension in those lowest momentum bins, perhaps the water mass varied between T2K runs more than what could be accounted for using the static detector model in the BANFF fit.

To further explore this idea, a visual search was conducted of data to postfit ratio improvement in the water-in sample's lowest momentum bins with decreasing  $\cos \theta$ , or equivalently increasing angle. If this trend is observed, it could indicate the mass variability and additional bulging were problematic in the fit. The higher angle tracks are more likely to originate upstream of the most bulging layer due to geometric considerations. If better agreement is observed in higher angle bins compared to lower, more forward-going track bins, this would support the mass variability idea. There was a weak observed trend in the water-in samples

---

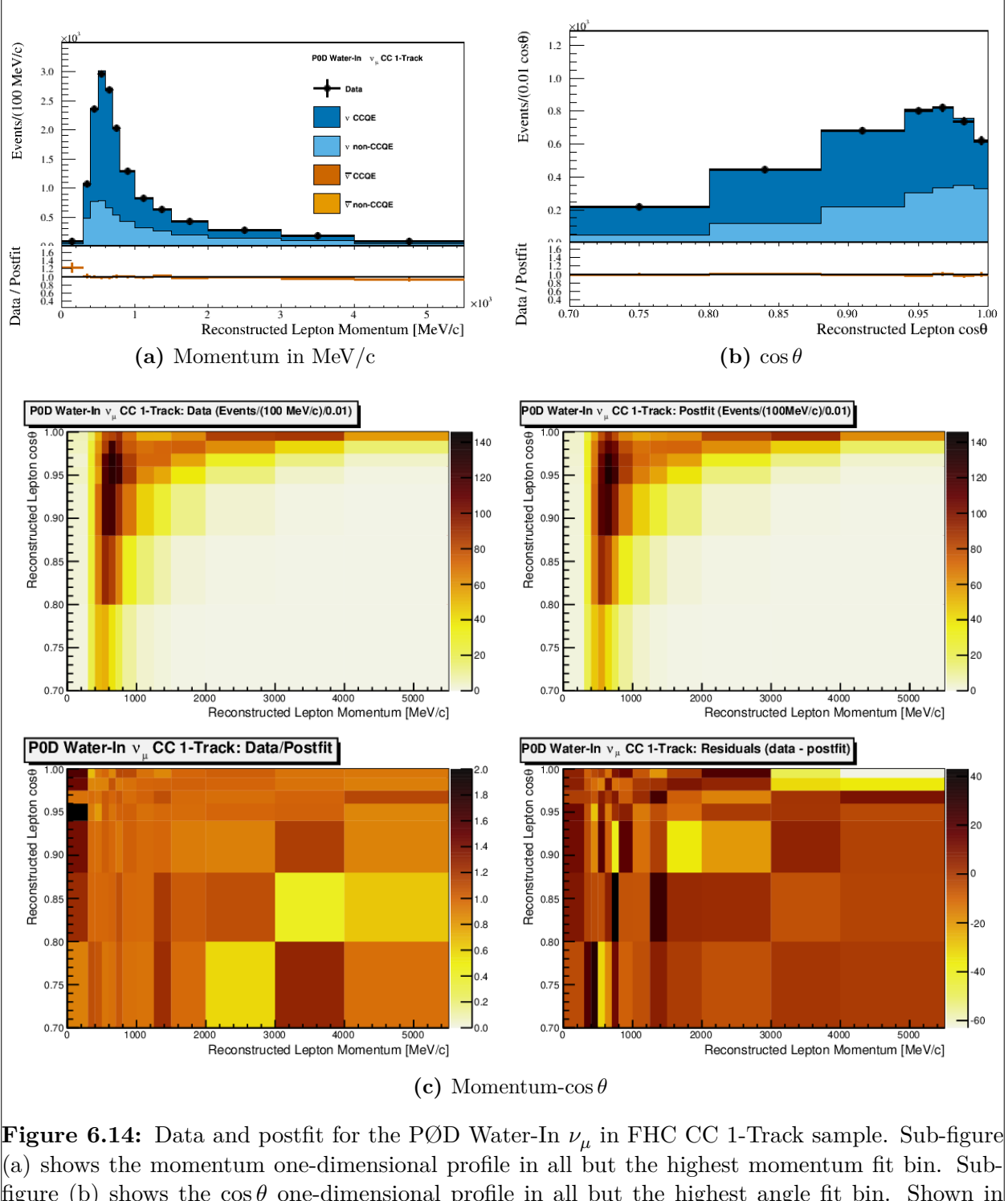
and such a weak one could be coincidental. Therefore, it is difficult to draw any conclusions at this stage about mass uncertainty contribution.

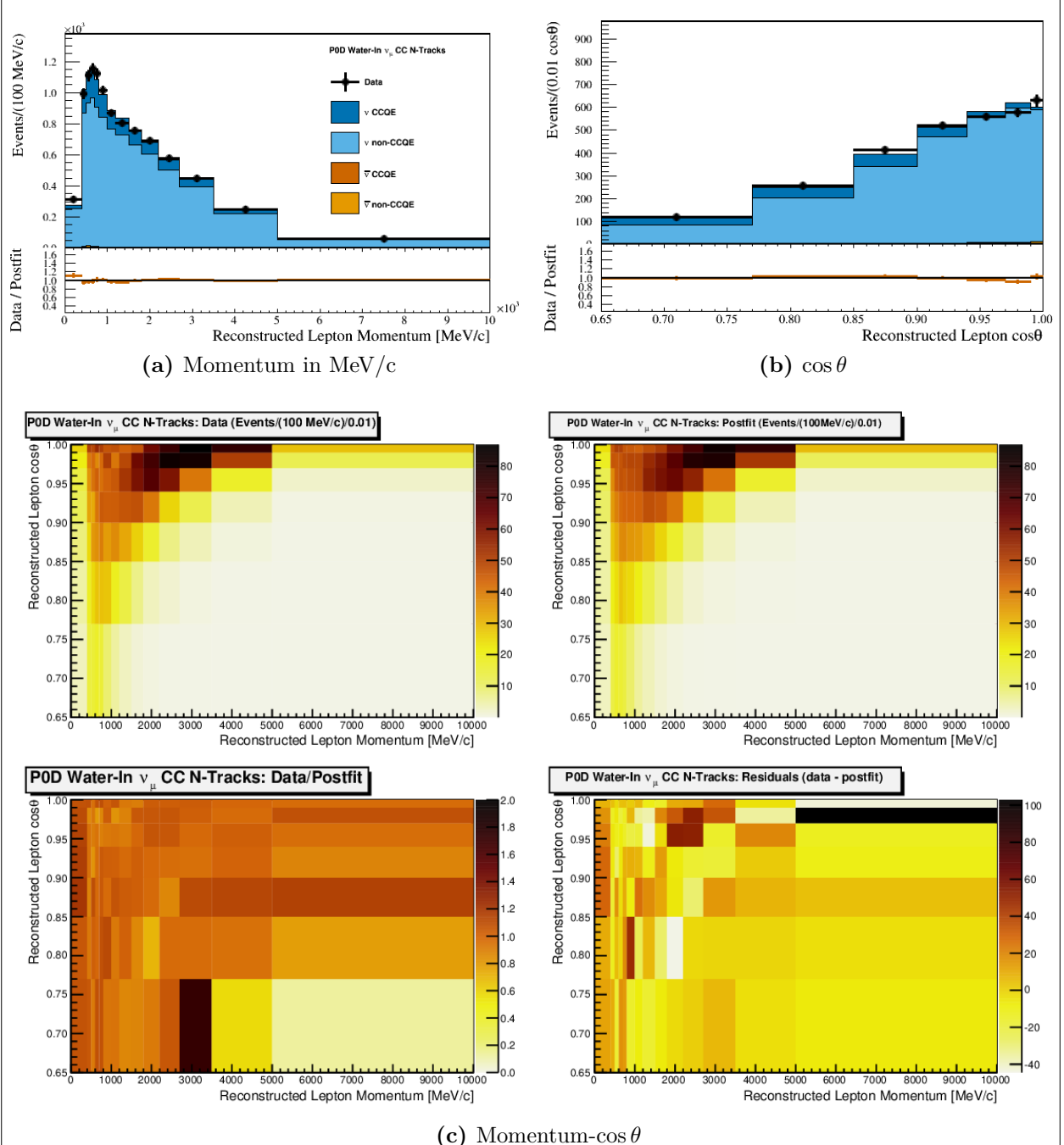
Now that we have examined the postfit samples and seen that the prediction has indeed changed, we can proceed to look at the parameter values.

### 6.2.2 Parameter Value and Correlation Comparisons

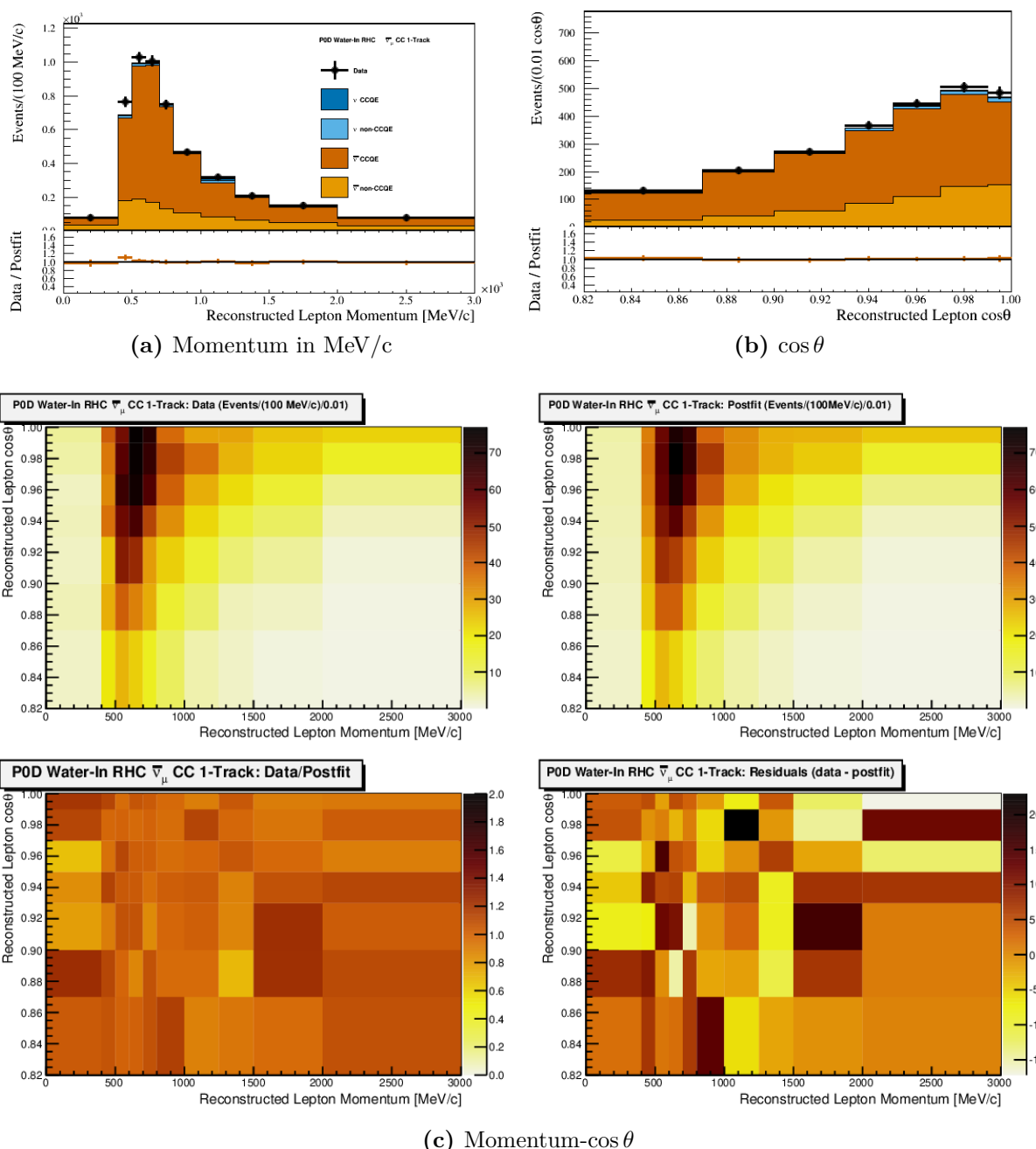
The postfit parameters from the PØD-only BANFF fit are shown in Figure 6.27 on page 180 through Figure 6.30 on page 183. A complete listing of the prefit and postfit values is given in Appendix ???. Additionally, a comparison is made between the PØD-only results with that of the FGD-only results. The legend used to compare between the PØD-only and FGD-only fits is shown in Figure 6.26 on page 176. It must be stated that while the PØD-only and FGD-only fits are using the same 2017 canonical cross section parameterization, the analyses had different POT exposures.

This PØD-only analysis fit uses runs 2 - 8 while the FGD-only fit uses runs 2 - 6. In order to understand how the two analyses compare to each other in terms of sensitivity to the flux, and carbon and oxygen cross section parameters, we can examine Table 6.1 on page 177. A proxy for the number of incident neutrinos to certain elements in the detector is the product of the fiducial mass and POT. While the PØD has much more mass, the water-in and water-out modes are mutually exclusive, resulting in a reduced aggregate POT exposure as compared to each static FGD. Also since the FGD2 has a larger water mass fraction compared to the PØD water-in mode, the amount of neutrino-oxygen interactions are very similar. The comparative advantage of the PØD-only data lies in the number of neutrino-carbon events, which is about 10 times greater than the FGD. This is all assuming the comparisons from Table 6.1 on page 177.

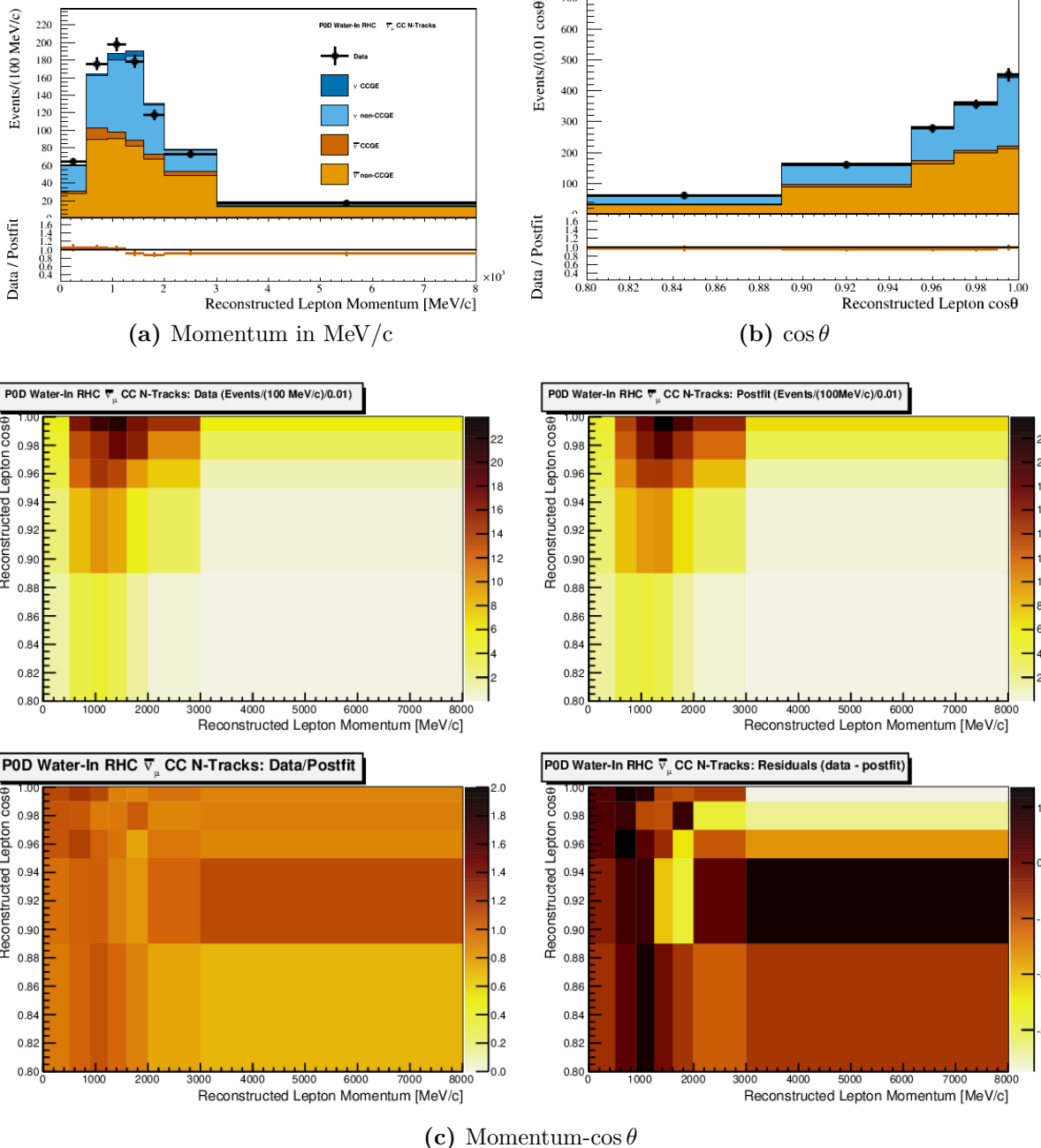




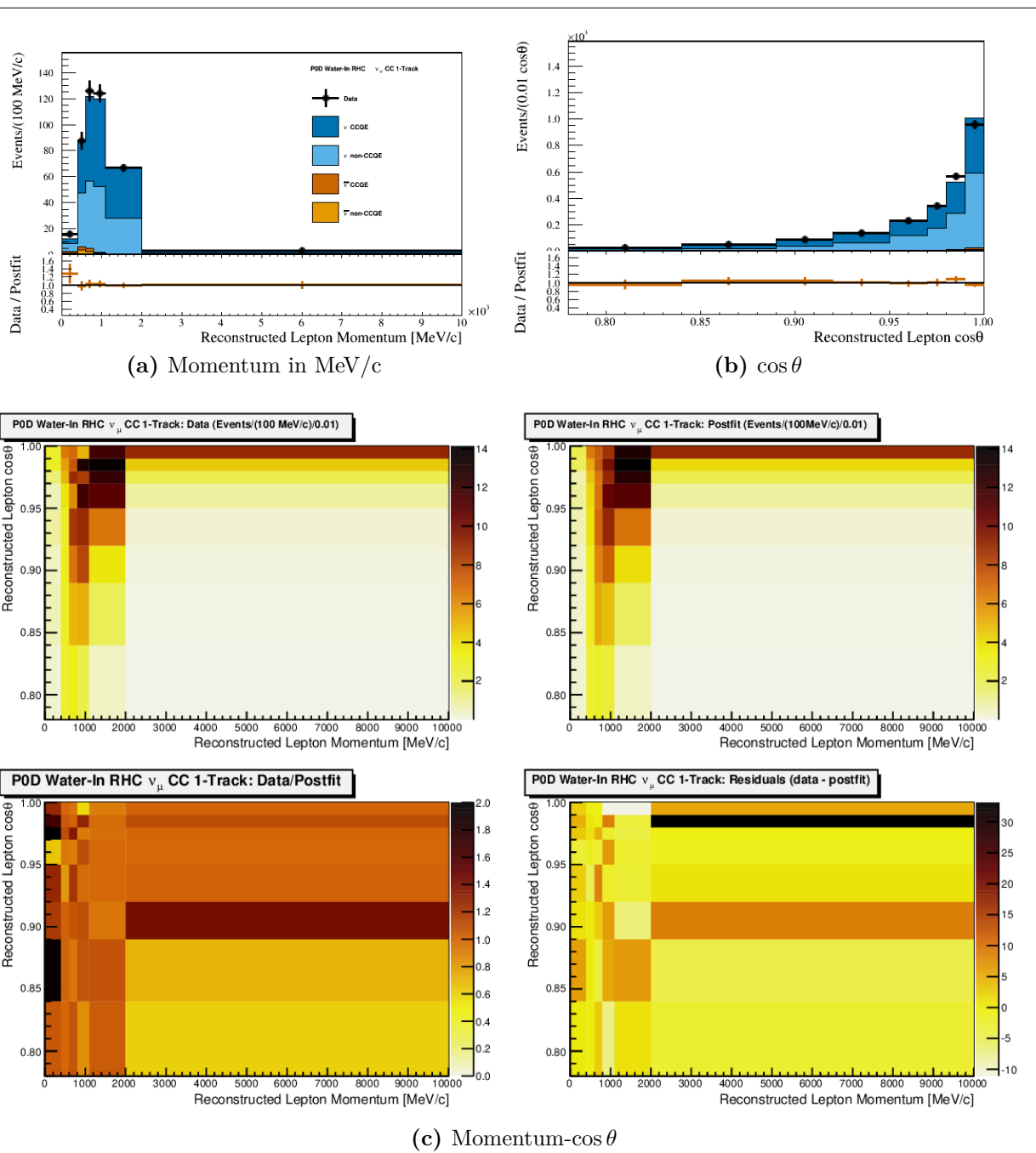
**Figure 6.15:** Data and postfit for the PØD Water-In  $\nu_\mu$  in FHC CC 1-Track sample. Sub-figure (a) shows the momentum one-dimensional profile in all but the highest momentum fit bin. Sub-figure (b) shows the  $\cos\theta$  one-dimensional profile in all but the highest angle fit bin. Shown in both (a) and (b) is the ratio between data and the postfit value. Sub-figure (c) shows a grid of two-dimensional data and postfit distributions in the same phase space as (a) and (b). Moving from top-left to bottom-right in (c) is the data, postfit, data to postfit ratio, and data to postfit difference.



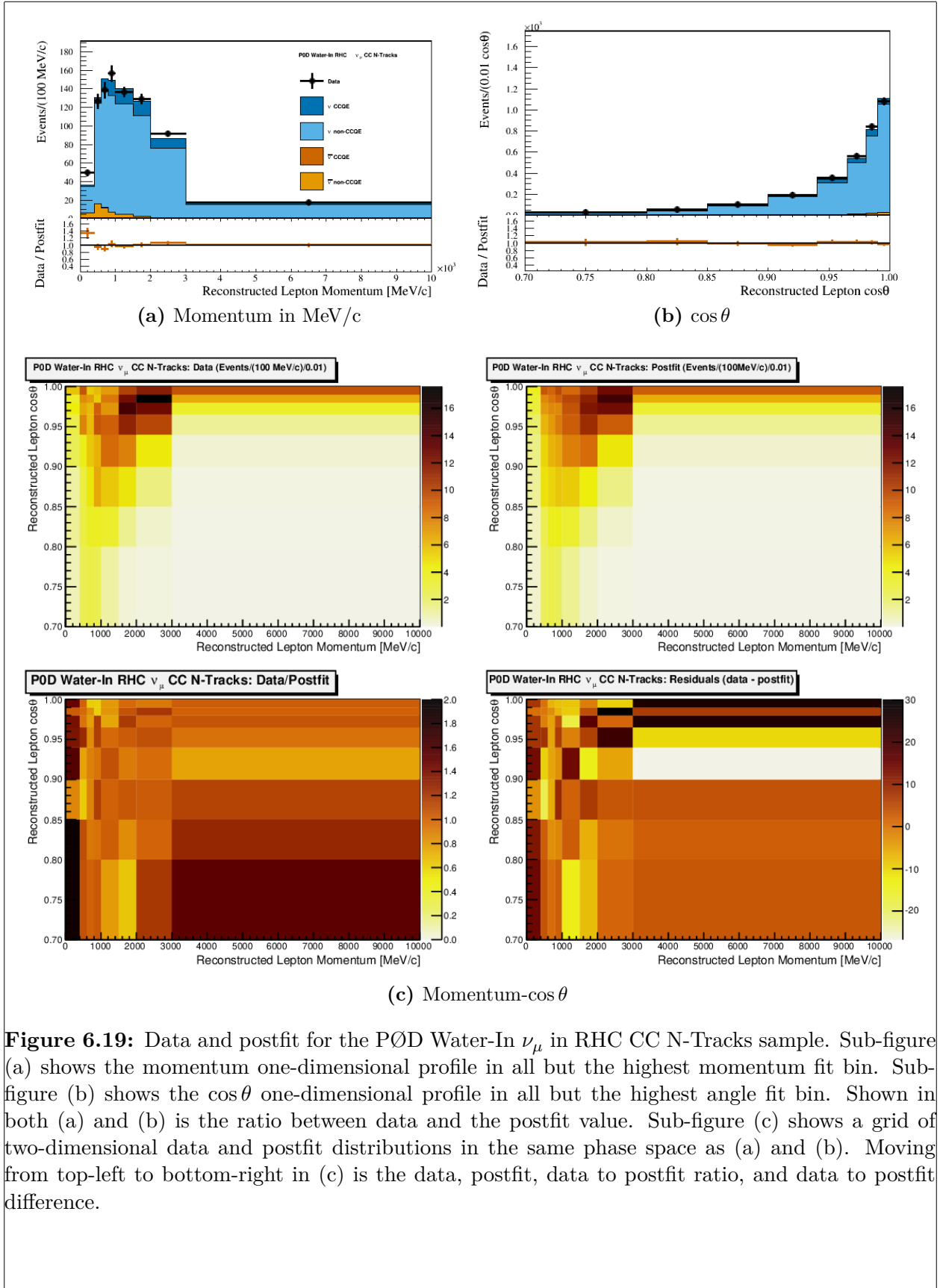
**Figure 6.16:** Data and postfit for the PØD Water-In  $\bar{\nu}_\mu$  in RHC CC 1-Track sample. Sub-figure (a) shows the momentum one-dimensional profile in all but the highest momentum fit bin. Sub-figure (b) shows the  $\cos\theta$  one-dimensional profile in all but the highest angle fit bin. Shown in both (a) and (b) is the ratio between data and the postfit value. Sub-figure (c) shows a grid of two-dimensional data and postfit distributions in the same phase space as (a) and (b). Moving from top-left to bottom-right in (c) is the data, postfit, data to postfit ratio, and data to postfit difference.

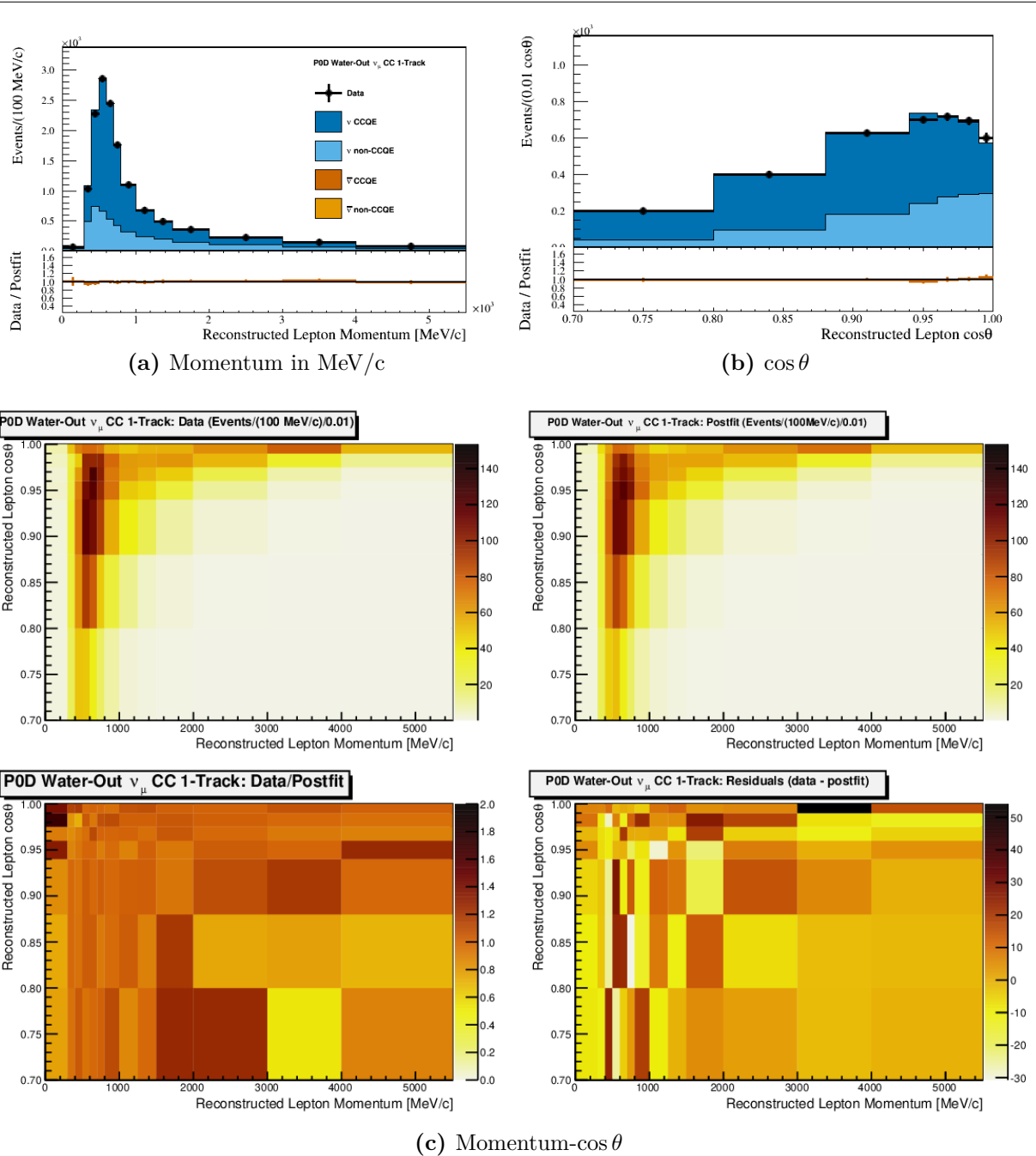


**Figure 6.17:** Data and postfit for the PØD Water-In  $\bar{\nu}_\mu$  in RHC CC N-Tracks sample. Sub-figure (a) shows the momentum one-dimensional profile in all but the highest momentum fit bin. Sub-figure (b) shows the  $\cos \theta$  one-dimensional profile in all but the highest angle fit bin. Shown in both (a) and (b) is the ratio between data and the postfit value. Sub-figure (c) shows a grid of two-dimensional data and postfit distributions in the same phase space as (a) and (b). Moving from top-left to bottom-right in (c) is the data, postfit, data to postfit ratio, and data to postfit difference.

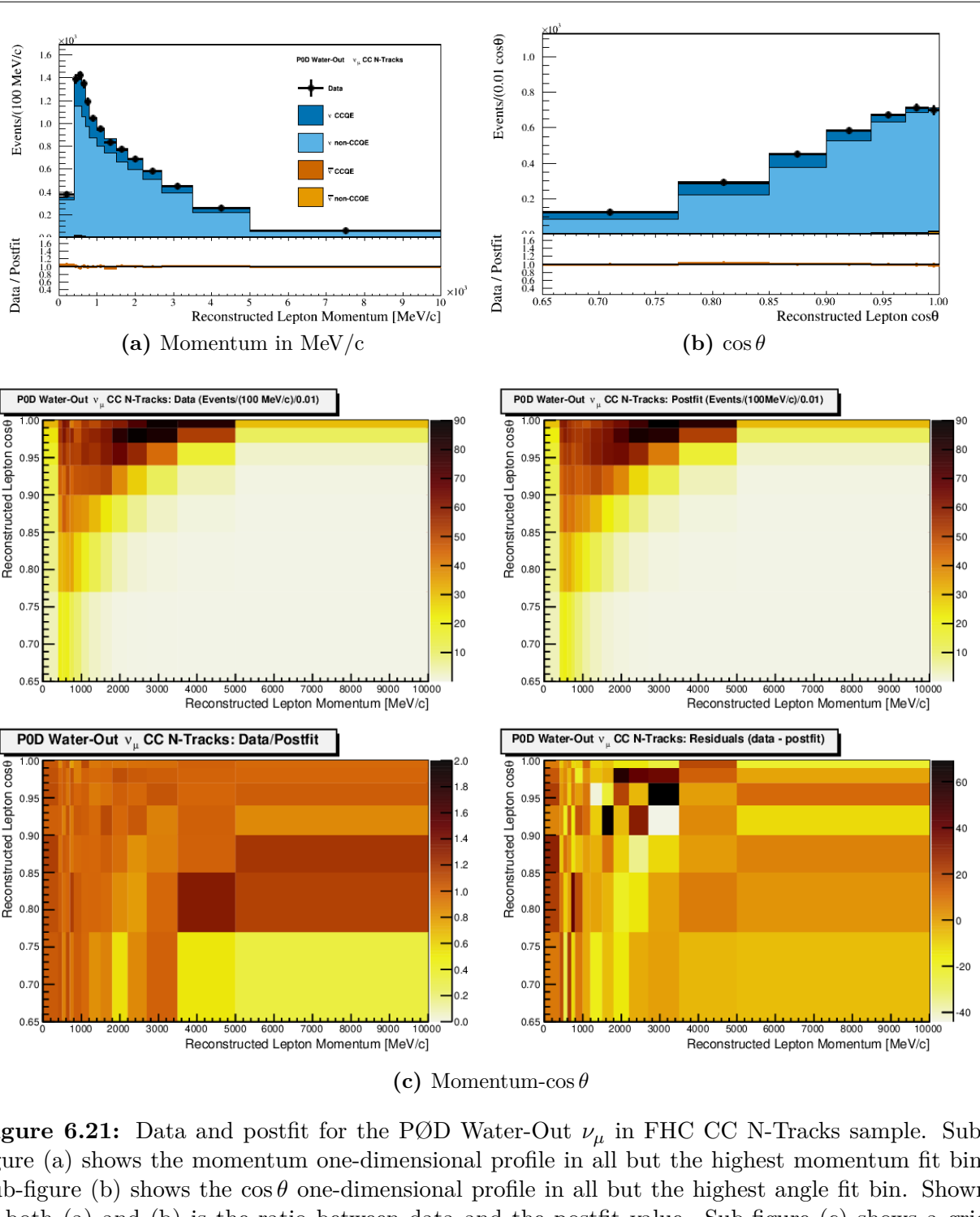


**Figure 6.18:** Data and postfit for the PØD Water-In  $\nu_\mu$  in RHC CC 1-Track sample. Sub-figure (a) shows the momentum one-dimensional profile in all but the highest momentum fit bin. Sub-figure (b) shows the  $\cos\theta$  one-dimensional profile in all but the highest angle fit bin. Shown in both (a) and (b) is the ratio between data and the postfit value. Sub-figure (c) shows a grid of two-dimensional data and postfit distributions in the same phase space as (a) and (b). Moving from top-left to bottom-right in (c) is the data, postfit, data to postfit ratio, and data to postfit difference.

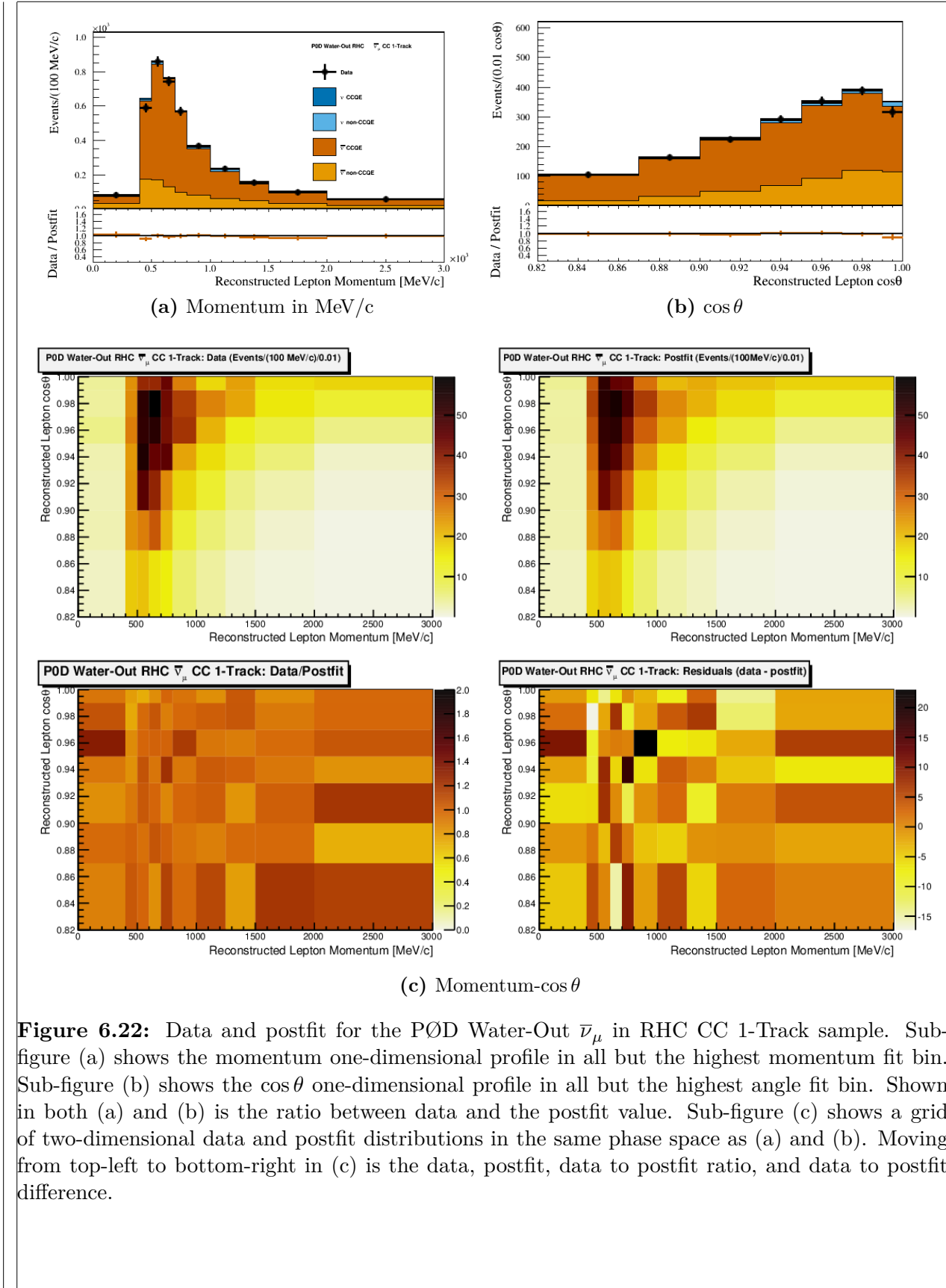




**Figure 6.20:** Data and postfit for the PØD Water-Out  $\nu_\mu$  in FHC CC 1-Track sample. Sub-figure (a) shows the momentum one-dimensional profile in all but the highest momentum fit bin. Sub-figure (b) shows the  $\cos\theta$  one-dimensional profile in all but the highest angle fit bin. Shown in both (a) and (b) is the ratio between data and the postfit value. Sub-figure (c) shows a grid of two-dimensional data and postfit distributions in the same phase space as (a) and (b). Moving from top-left to bottom-right in (c) is the data, postfit, data to postfit ratio, and data to postfit difference.



**Figure 6.21:** Data and postfit for the PØD Water-Out  $\nu_{\mu}$  in FHC CC N-Tracks sample. Sub-figure (a) shows the momentum one-dimensional profile in all but the highest momentum fit bin. Sub-figure (b) shows the  $\cos \theta$  one-dimensional profile in all but the highest angle fit bin. Shown in both (a) and (b) is the ratio between data and the postfit value. Sub-figure (c) shows a grid of two-dimensional data and postfit distributions in the same phase space as (a) and (b). Moving from top-left to bottom-right in (c) is the data, postfit, data to postfit ratio, and data to postfit difference.



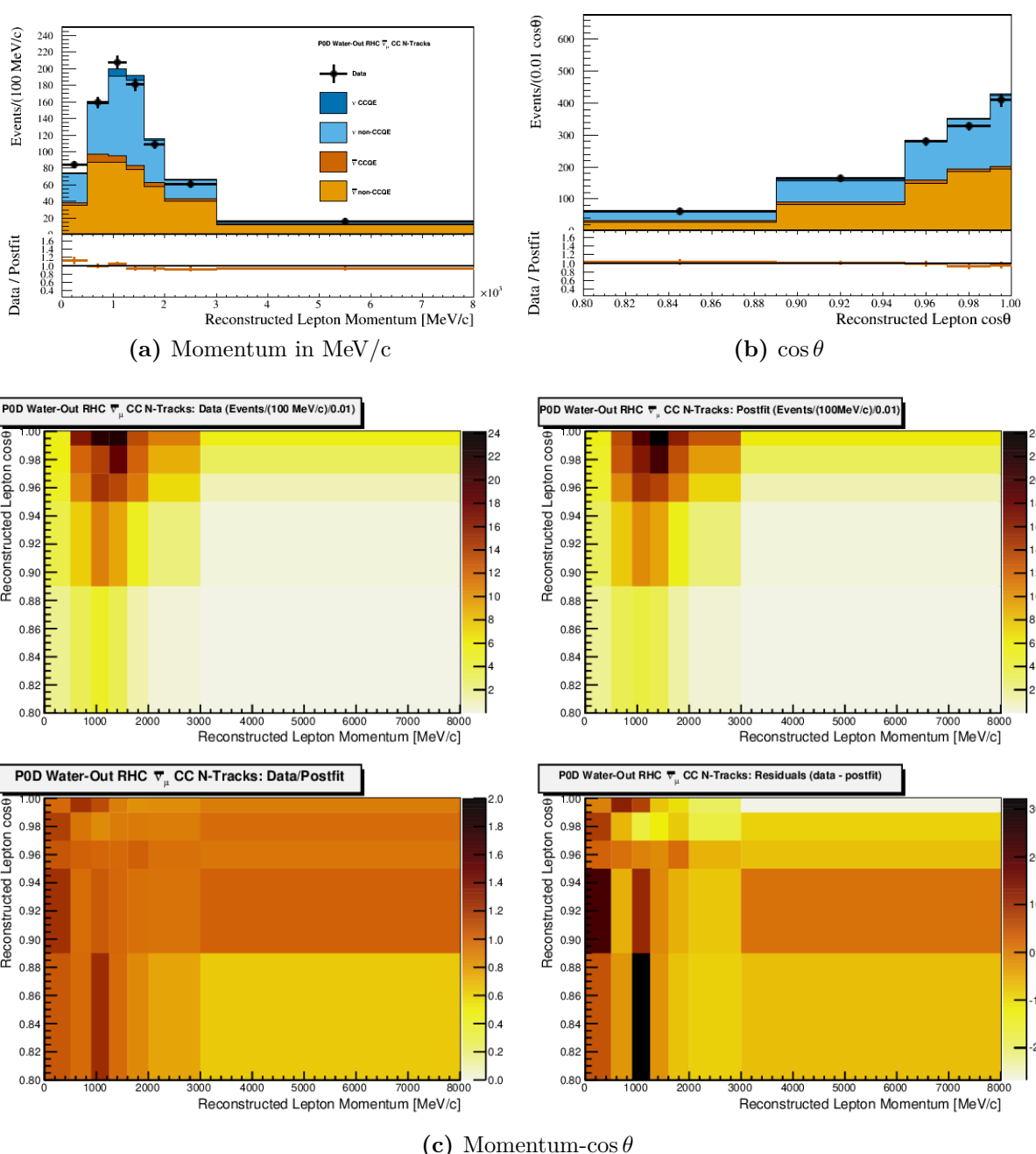


**Figure 6.23:** Data and postfit for the PØD Water-Out  $\bar{\nu}_\mu$  in RHC CC N-Tracks sample. Sub-figure (a) shows the momentum one-dimensional profile in all but the highest momentum fit bin. Sub-figure (b) shows the  $\cos \theta$  one-dimensional profile in all but the highest angle fit bin. Shown in both (a) and (b) is the ratio between data and the postfit value. Sub-figure (c) shows a grid of two-dimensional data and postfit distributions in the same phase space as (a) and (b). Moving from top-left to bottom-right in (c) is the data, postfit, data to postfit ratio, and data to postfit difference.

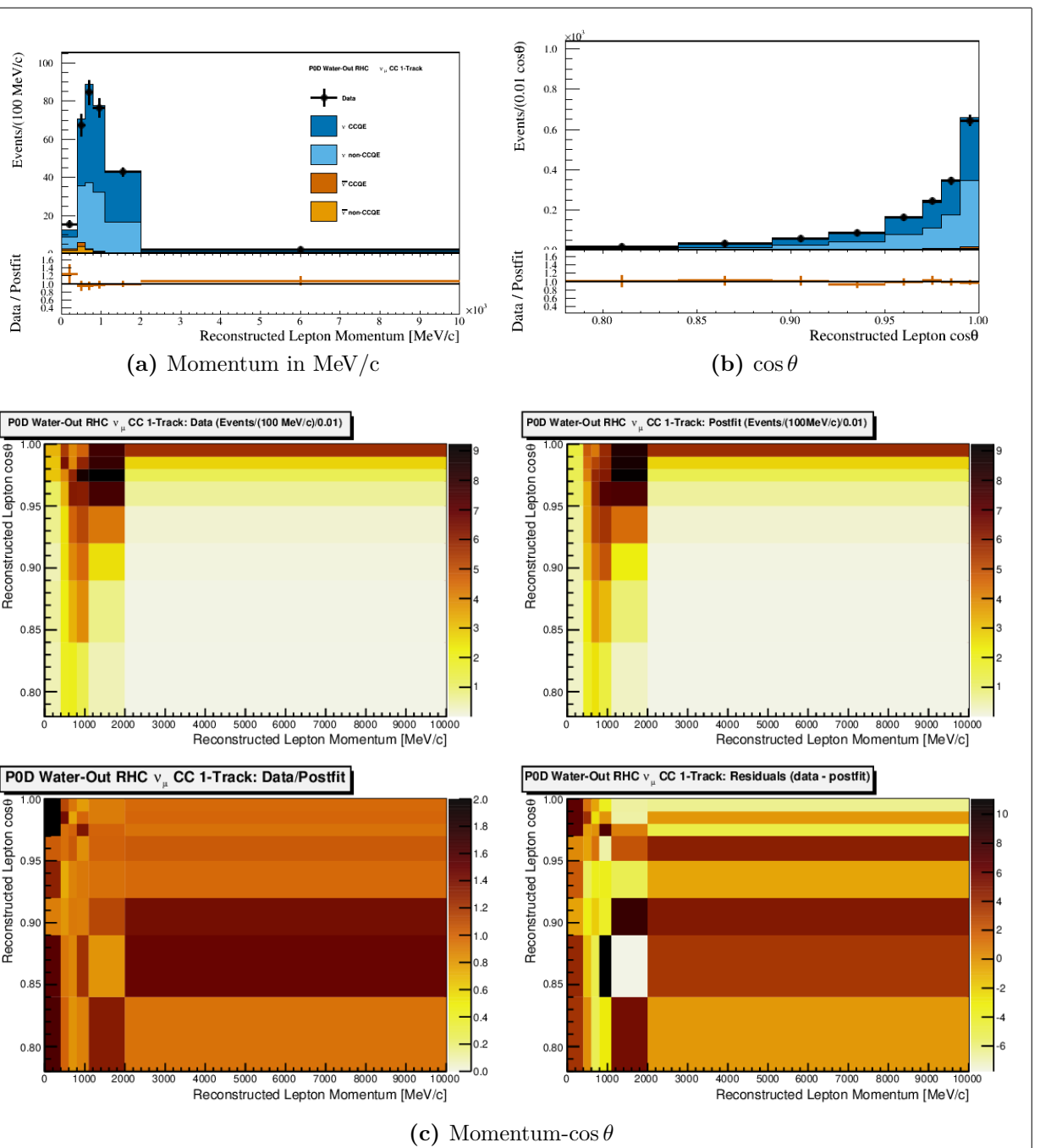


**Figure 6.24:** Data and postfit for the PØD Water-Out  $\nu_\mu$  in RHC CC 1-Track sample. Sub-figure (a) shows the momentum one-dimensional profile in all but the highest momentum fit bin. Sub-figure (b) shows the  $\cos \theta$  one-dimensional profile in all but the highest angle fit bin. Shown in both (a) and (b) is the ratio between data and the postfit value. Sub-figure (c) shows a grid of two-dimensional data and postfit distributions in the same phase space as (a) and (b). Moving from top-left to bottom-right in (c) is the data, postfit, data to postfit ratio, and data to postfit difference.

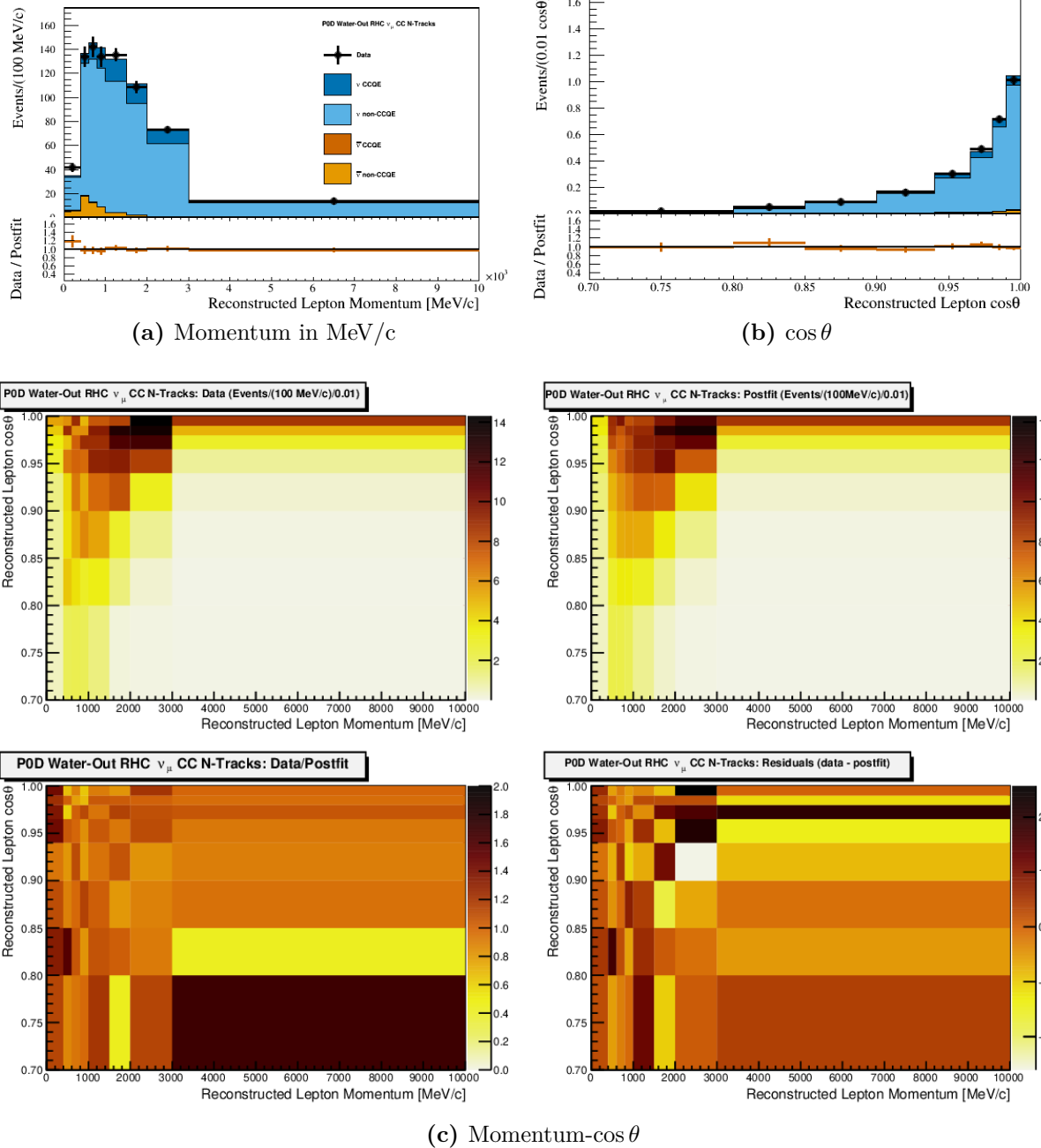


**Figure 6.25:** Data and postfit for the PØD Water-Out  $\nu_\mu$  in RHC CC N-Tracks sample. Sub-figure (a) shows the momentum one-dimensional profile in all but the highest momentum fit bin. Sub-figure (b) shows the  $\cos\theta$  one-dimensional profile in all but the highest angle fit bin. Shown in both (a) and (b) is the ratio between data and the postfit value. Sub-figure (c) shows a grid of two-dimensional data and postfit distributions in the same phase space as (a) and (b). Moving from top-left to bottom-right in (c) is the data, postfit, data to postfit ratio, and data to postfit difference.



**Figure 6.26:** Legend used to compare PØD-only and FGD-only fit results.

Detector	(kg)	Fiducial volume mass			POT ( $10^{20}$ )		kg POT ( $10^{24}$ )	PØD-to-FGD (kg POT)		
		$^{12}\text{C}$ (%)	$^{16}\text{O}$ (%)	other (%)	FHC	RHC		$^{12}\text{C}$	$^{16}\text{O}$	other
PØD Water-out FGD1	3570	70	0.67	19.33	7.872	-	2.81	3.99	-	9.21
	985	86	3.7	10.3	5.81	-	0.572			
PØD Water-In FGD2	5470	45	30	25	3.657	-	2.00	10.63	1.43	8.05
	972	15	74	11	5.81	-	0.565			
PØD Water-out FGD1	3570	70	0.67	19.33	-	3.382	1.207	3.513	-	8.10
	985	86	3.7	10.3	-	2.84	0.280			
PØD Water-In FGD2	5470	45	30	25	-	2.852	1.56	16.9	2.29	12.8
	972	15	74	11	-	2.84	0.276			

**Table 6.1:** Neutrino-nucleon exposure on target elements in the PØD-only and FGD-only analyses. The FGD1 and FGD2 masses were calculated using the following sources [14, 50, 51]. The PØD mass was taken from the following source [67]. The other mass elements include hydrogen, copper, and heavier elements.

---

There is good visual agreement between the PØD-only and FGD-only BANFF parameter values. The flux parameters follow the same shape trends with the PØD-only fit, but with the PØD-only parameters having a higher expectation comparatively. If we examine the bin normalization parameters for the PØD-only fit in Figure 6.30 on page 183, they are suggesting a reduction in the event rate across most bins. This high flux, low bin normalization result is likely due to the anticorrelated relationship between them as indicated in the correlation matrix shown in Figure 6.32 on page 185. This has been observed in previous BANFF analyses. Also, the magnitude of the flux uncertainties is similar between the two, which suggests the two configurations are statistically similar.

The cross section parameters are also quite similar between the two fits, with some larger uncertainties in the PØD-only result. The CCQE and BeRPA parameters are in very good agreement with both fits preferring a significant increase in the BeRPA B scale parameter. There is tension in the fits with the  $M_A^{\text{Res}}$  parameter which is not currently understood. However, if the difference in the postfit parameters is distributed according to a chi-squared distribution, then a deviation such as this is not unexpected. We will explore this idea further with a hypothesis test in the next section.

A couple of interesting features are observed in the 2p2h parameters. Firstly is the 2p2h  $\nu$  normalization on carbon which is about two-times larger in the PØD-only fit than the FGD-only fit. This normalization result is currently an unknown phenomenon. It could be explained by the fact that the PØD has nearly twice as much non-carbon and non-oxygen elements, which is mostly brass, by mass fraction as the FGD (see Table 6.1 on page 177). The second feature involves the 2p2h shape parameters, *both of which have postfit values at the physical limit of +1, or +2 as shown graphically*. This sets the 2p2h model to fully pionless-Delta-decay-like with the same event normalization. This result is also shared with the FGD result and is being addressed in the next generation BANFF analysis. To provide an uncertainty on those shape parameters, even though they are situated at a discontinuity in the derivative, a “mirrored” spline was implemented as shown in Figure 6.31 on page

---

184. The mirrored spline was shown to not affect the fit result while providing a calculable uncertainty in MINUIT for the Hessian matrix [18].

The postfit correlations are shown in Figure 6.32 on page 185. The full matrix shows large anticorrelations between the systematic parameters sets. Largest in magnitude are the flux and cross section parameters. To better see the correlations for those sets, they are zoomed into on Figure 6.33 on page 186. For the cross section parameters only, they are shown in Figure 6.34 on page 187.

### 6.2.3 P-Value Between PØD and FGD Fits

We can now provide a quantification of the agreement between the PØD-only BANFF fit and that of the FGD-only BANFF fit. As a starting assumption, let the FGD-only result be the expectation of the result. We wish to test the hypothesis,  $H_1$ , that the PØD-only data and FGD-only data are sampling from two different neutrino interaction populations. We can also call this the alternative hypothesis. The null hypothesis,  $H_0$ , is that PØD-only and FGD-only data are sampled from the same interaction population. For each measurement  $X_i$  that is independently and identically distributed from a standard normal  $\mathcal{N}(\mu = 0, \sigma^2 = 1)$ , then the following function

$$\chi^2 = \sum_i X_i^2, \quad (6.1)$$

is distributed according to a chi-square distribution

$$F(\chi^2, r) = \frac{1}{2^{r/2}\Gamma(r/2)} (\chi^2)^{(r/2-1)} e^{(-\chi^2/2)}, \quad (6.2)$$

where  $r$  is the number of degrees of freedom (NDOF) and  $\Gamma(x + 1) = x!$  is the Gamma function. We can calculate a p-value to reject the null hypothesis at the  $\alpha$ -level.

If we let  $p_i^{\text{PØD}}(p_i^{\text{FGD}})$  represent the measurement of the  $i$ th parameter for the PØD-only (FGD-only) BANFF fit, then our test statistic can be formally defined as

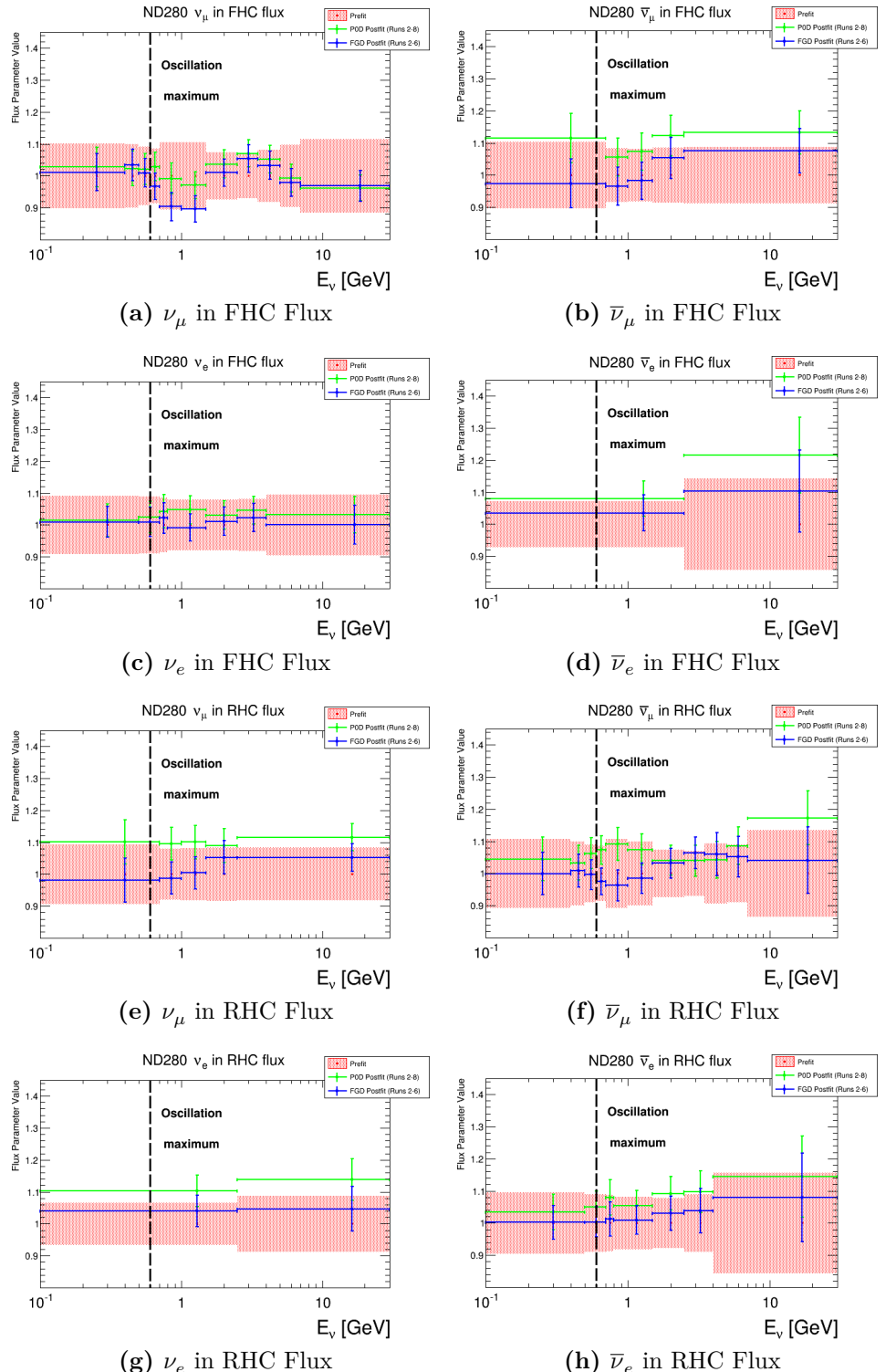


**Figure 6.27:** Postfit ND280 flux parameters for the PØD-only (green) and FGD-only (blue) BANFF fit as functions of neutrino energy. The energy that maximizes the  $\nu_\mu \rightarrow \nu_e$  oscillation (0.6 GeV) is shown with a dashed, black line.

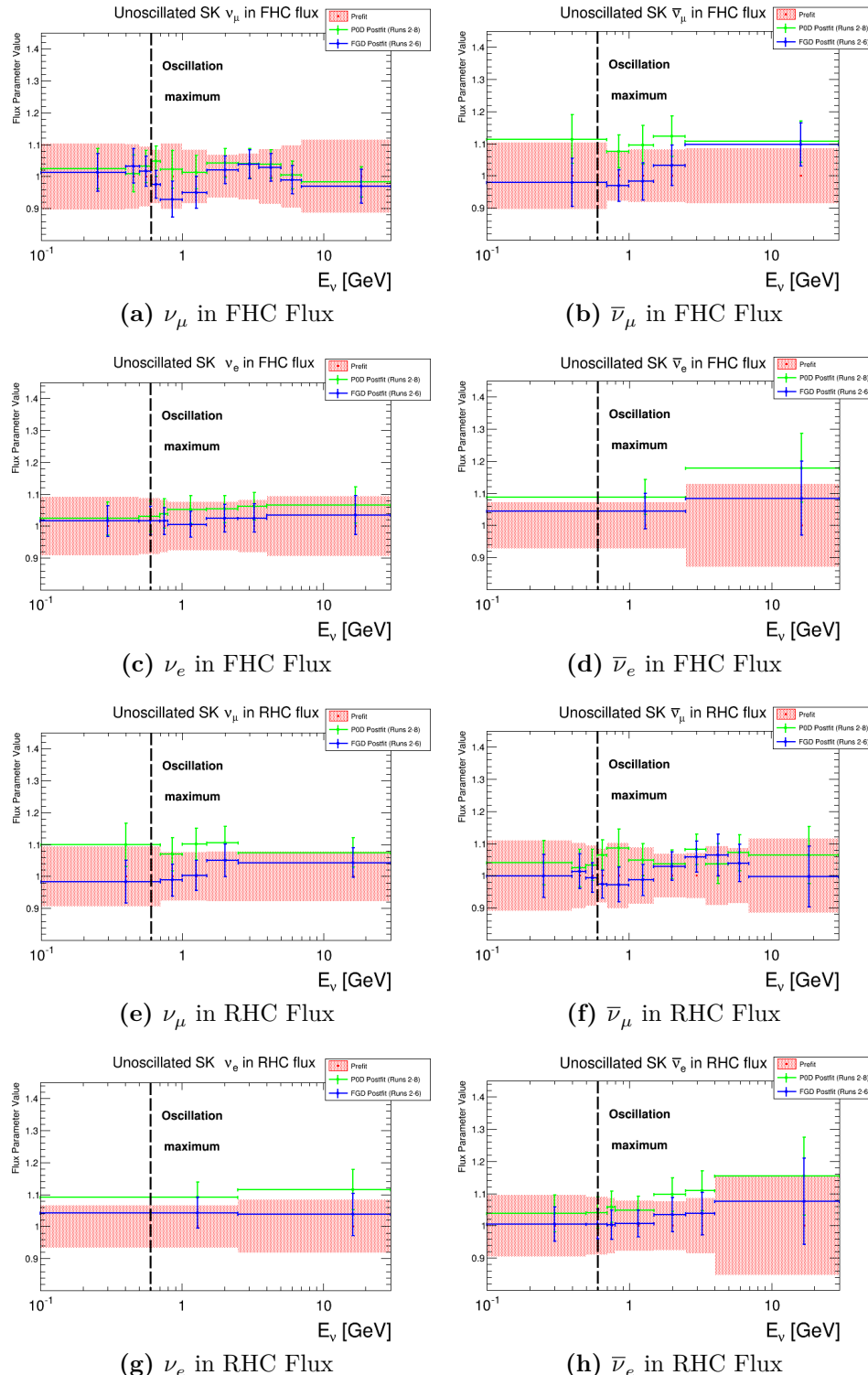


**Figure 6.28:** Postfit Super-K flux parameters for the PØD-only (green) and FGD-only (blue) BANFF fit as functions of neutrino energy. The energy that maximizes the  $\nu_\mu \rightarrow \nu_e$  oscillation (0.6 GeV) is shown with a dashed, black line.

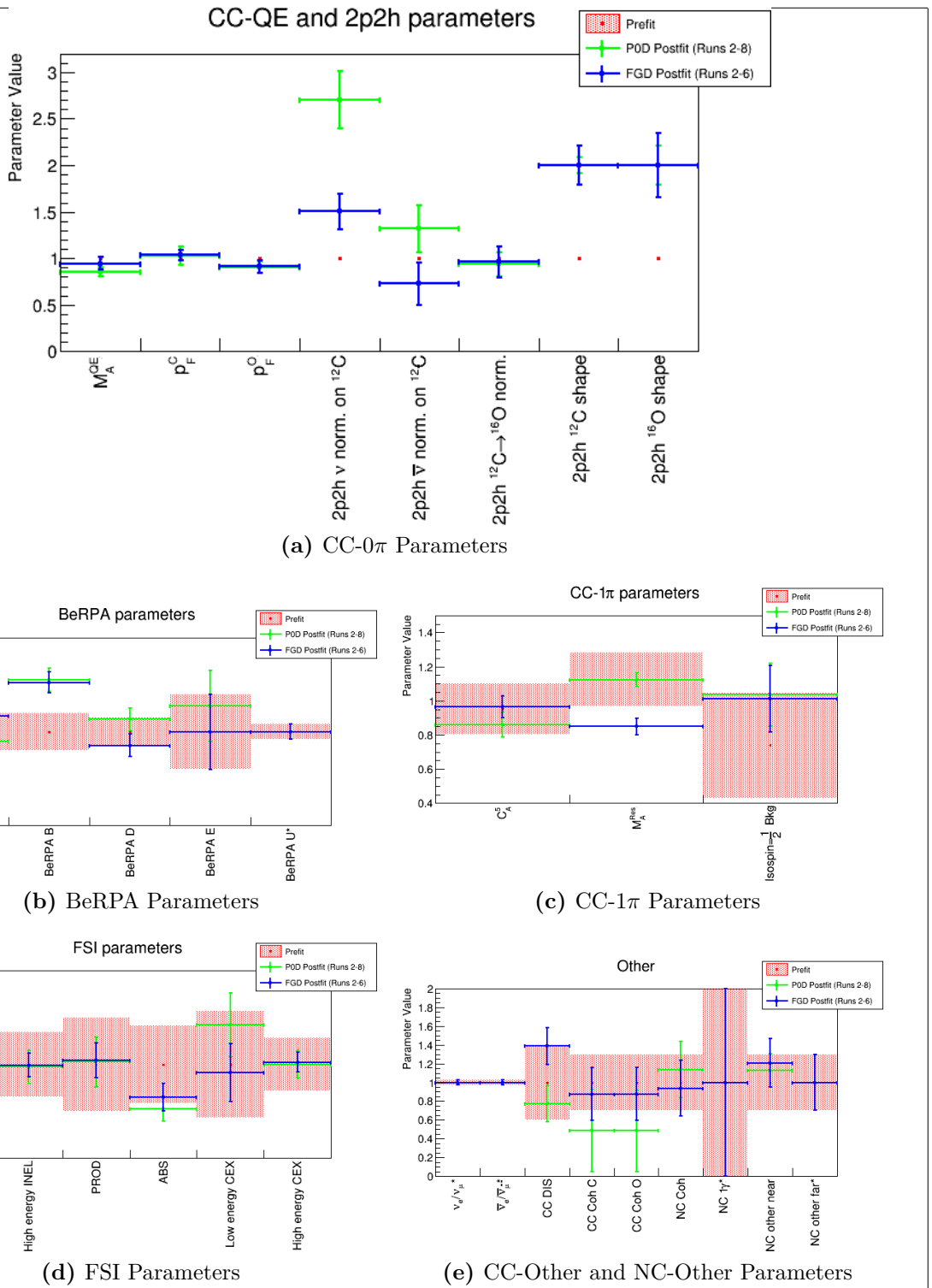
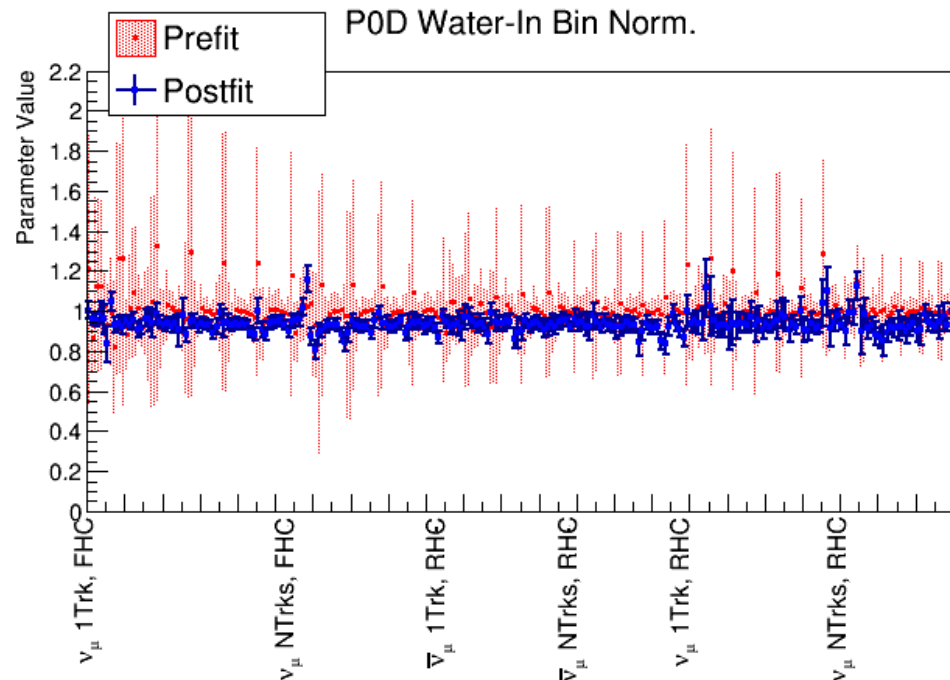
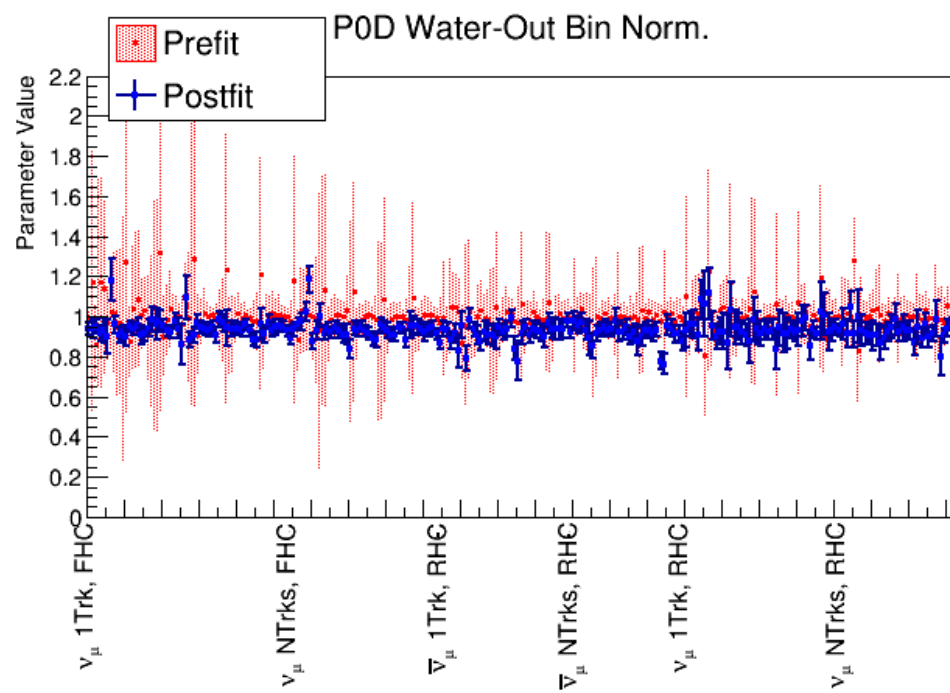


**Figure 6.29:** Postfit cross section parameters for the PØD-only (green) and FGD-only (blue) BANFF fit. In these figures, all shape and scale factor parameters are adjusted to 1 to provide a consistent graphical representation of all fit parameters. Shape parameters always have a prefit value of 0. Parameters without prefit uncertainties had a flat prior applied to them and an asterisk (\*) represents a fixed parameter.



(a) Water-In



(b) Water-Out

**Figure 6.30:** Prefit and postfit PØD bin normalization parameters.

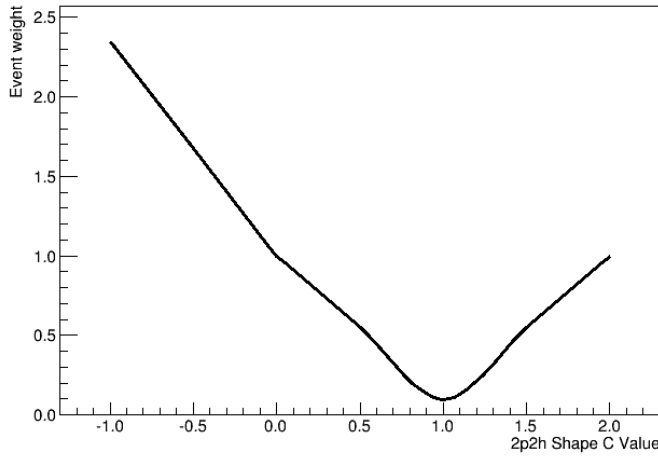


**Figure 6.31:** The “mirrored” spline for a single event. The spline represents an event weight and variations from the prefit value of 0 alters the event weight. The 2p2h shape splines are mirrored about the value of +1 to provide an uncertainty in the postfit result.

$$\chi^2_{\text{PØDvsFGD}} = \sum_i \sum_j \frac{(p_i^{\text{PØD}} - p_i^{\text{FGD}})(p_j^{\text{PØD}} - p_j^{\text{FGD}})}{V_{i,j}^{\text{PØDvsFGD}}} \quad (6.3)$$

where  $V_{i,j}^{\text{PØDvsFGD}}$  is the covariance of measurement  $i, j$ . Since the purpose of the BANFF fit is to provide a constraint on the Super-K flux and cross section models, we will ignore the ND flux bins and  $(p, \cos \theta)$  bin normalization parameters. Also assume for simplicity that the PØD and FGD data are completely uncorrelated. This simplifies the test statistic to

$$\chi^2_{\text{PØDvsFGD}} = \sum_i \frac{(p_i^{\text{PØD}} - p_i^{\text{FGD}})^2}{V_{i,i}^{\text{PØD}} + V_{i,i}^{\text{FGD}}}, \quad (6.4)$$

where  $V_{i,i}^{\text{PØD}}/V_{i,i}^{\text{FGD}}$  is the variance of the  $i$ th parameter from the PØD-/FGD-only BANFF fit measurement. We can calculate a p-value,  $p$ , of observing a test statistic at least as extreme in a chi-square distribution by integrating the right-hand tail of the chi-square distribution using the inverse cumulative distribution function (ICDF)

$$p(\chi^2, r) = \int_{\chi^2}^{\infty} F(x', r) dx', \quad (6.5)$$

---

---

### Postfit Correlation Matrix

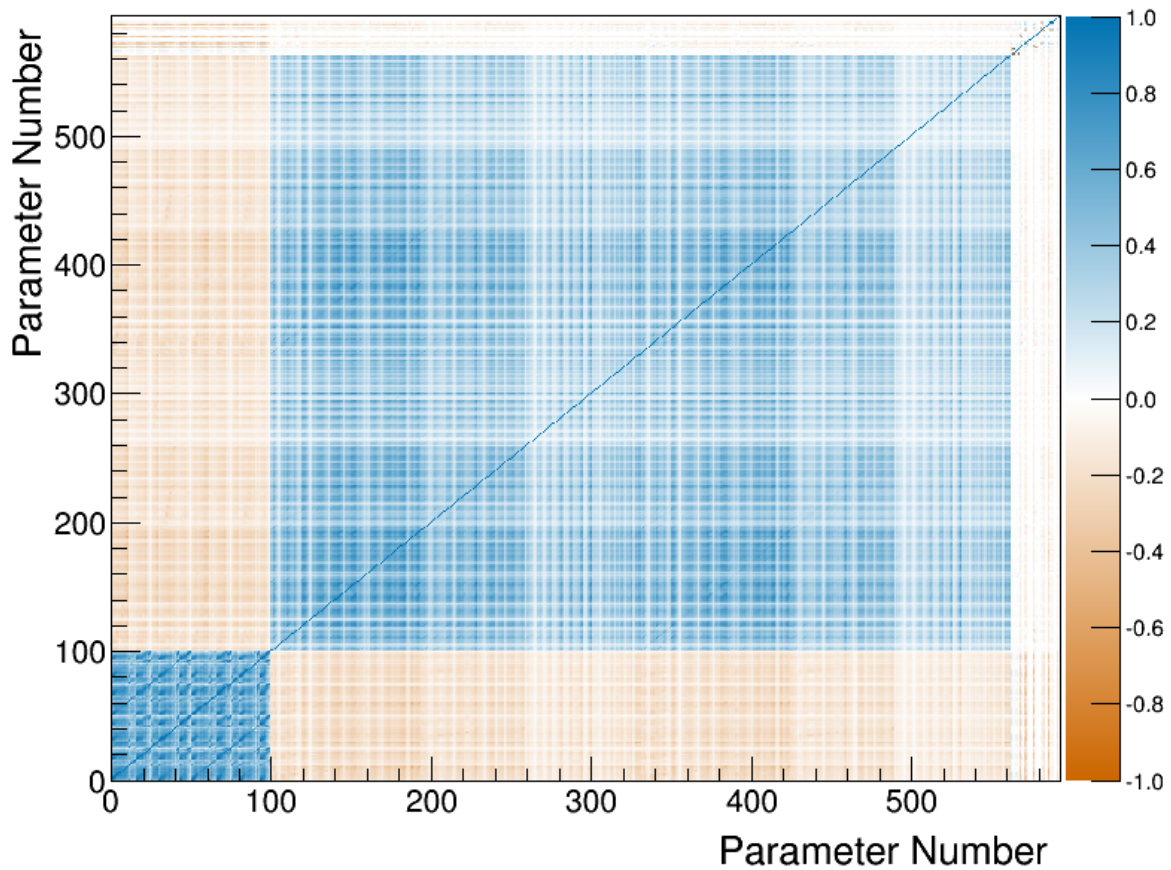
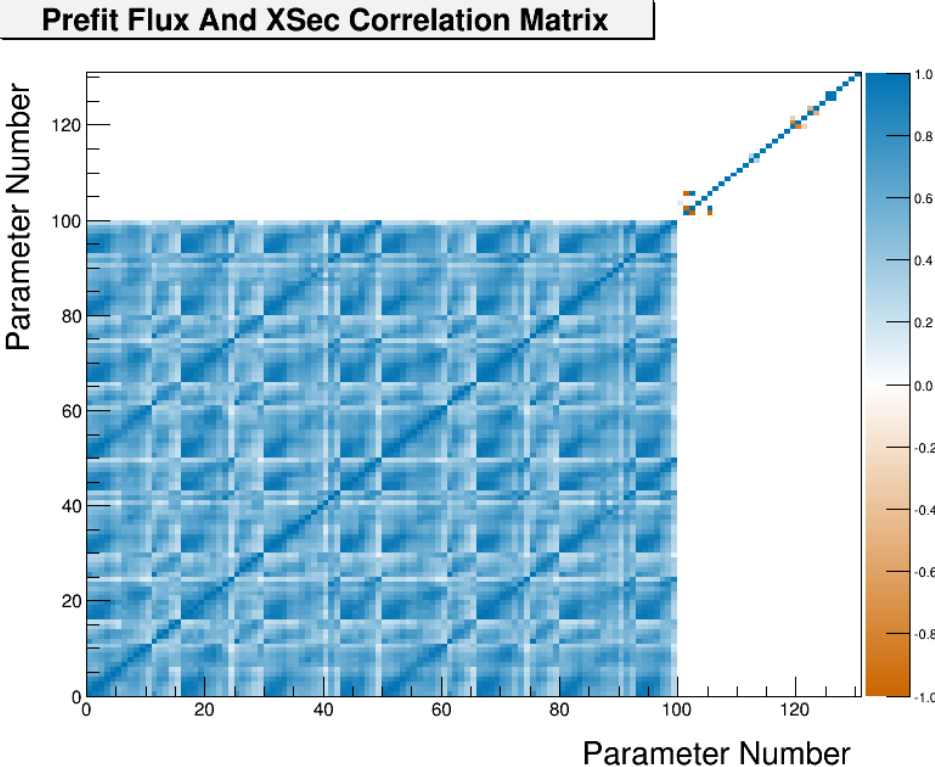
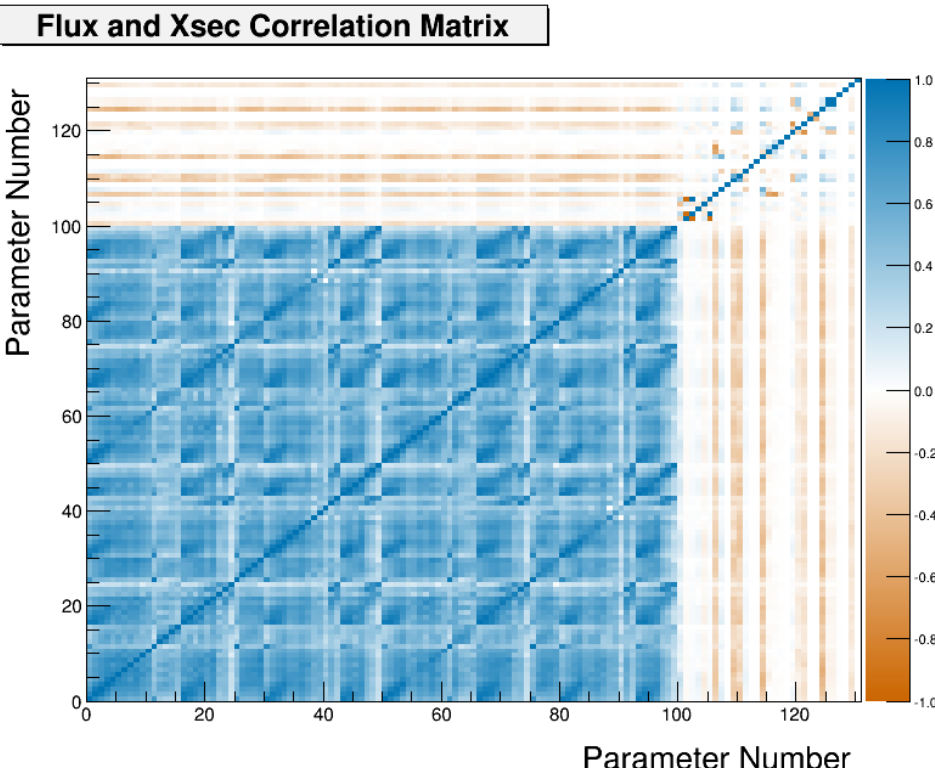


**Figure 6.32:** Postfit correlation matrix. The first 100 parameters are the flux parameters with the first 50 corresponding to ND280 and the last 50 with Super-K. Between 100 and 561 are the bin normalization parameters. The last 31 are the cross section parameters.

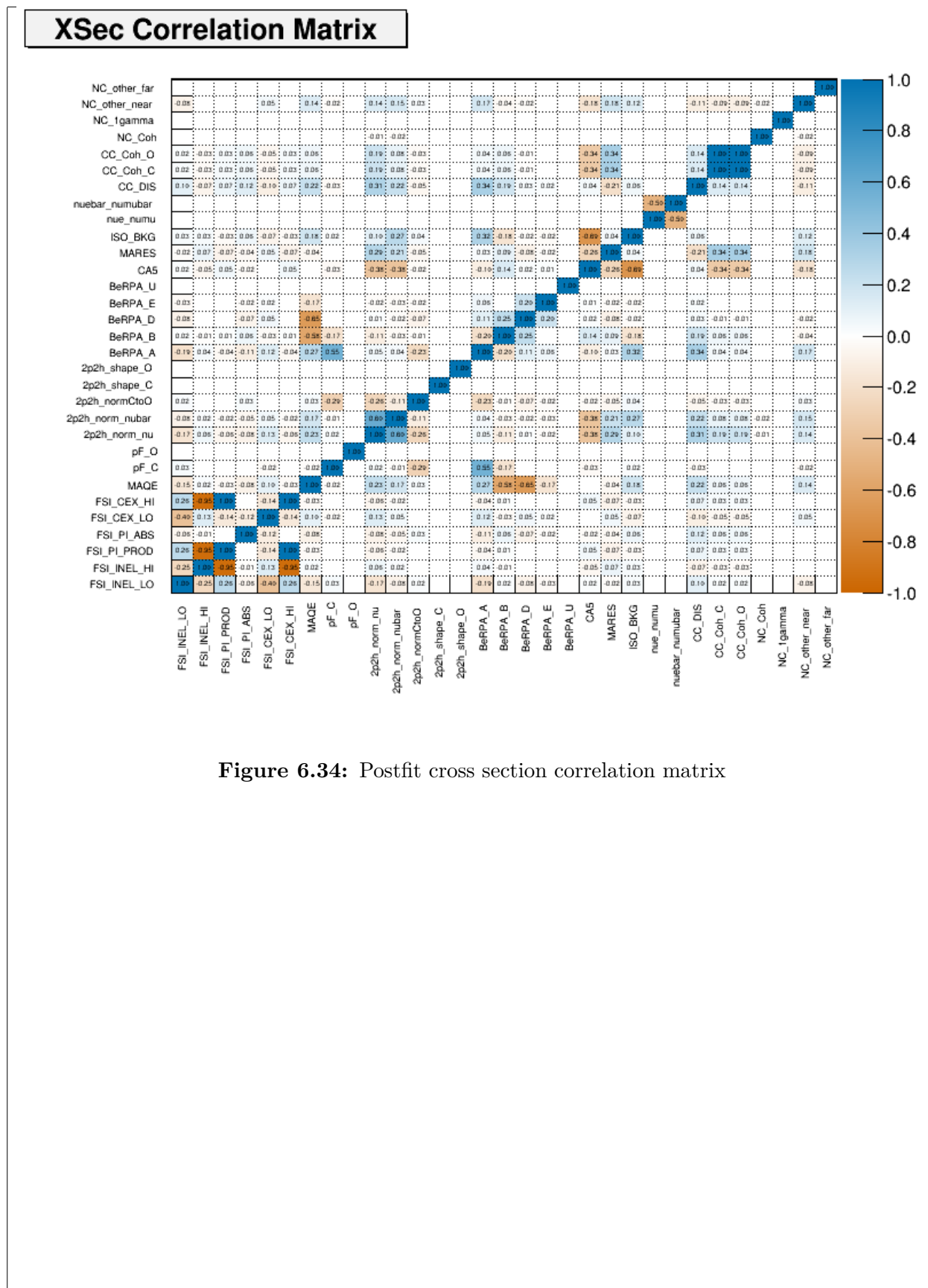


(a) Prefit flux and cross sections correlations



(b) Postfit flux and cross section correlations

**Figure 6.33:** Prefit and post fit flux and cross section parameter correlations. In sub-figures (a) and (b), the prefit and postfit, respectively, correlation matrices for the flux and cross section parameters are shown. In both (a) and (b), the first 100 parameters are the flux parameters with the first 50 corresponding to ND280 and the last 50 with Super-K. The last 31 are the cross section parameters.



---

where  $\chi^2$  is the test-statistic from 6.4.

Now let us count the NDOF for the p-value calculation. There are 50 SK flux parameters and 31 cross section parameters. However, five of cross section parameters are fixed. Additionally, we have assumed the FGD-only result is our expectation, and so we have one less NDOF. This leaves us with

$$r = \underbrace{50}_{\text{SK Flux}} + \underbrace{(31 - 5)}_{\text{XSec}} - 1 = 75 \text{ NDOF}.$$

If we wish to reject the null hypothesis at the 5% level, this requires a chi-squared value of 96.21 or greater.

If we calculate the test statistic as defined above, we find that

$$\tilde{\chi}_{\text{PØDvsFGD}}^2 = \frac{\chi_{\text{PØDvsFGD}}^2}{r} = \frac{81.41}{75} \approx 1.085,$$

of which indicates good agreement between the two measurements for the ND constraint since  $\tilde{\chi}^2 \sim 1$ . This corresponds to a p-value of 0.2865 or a 28.65% probability of obtaining a larger test statistic. This result is visualized in Figure 6.35 on page 189. Since this is not sufficiently close to the 5% level, we fail to reject the null hypothesis. *We can conclude the PØD-only and FGD-only samples and subsequent BANFF fits describe the same data in T2K.*

We must qualify the above conclusion given the flaws of the test statistic definition. The PØD-only flux parameters are clearly skewed above the FGD-only flux parameters, and, therefore, their difference is not normally distributed about zero. This indicates a large, positive correlation between the two measurements, and breaks the uncorrelated uncertainties assumption. Given this correlated result, we expect better agreement between the PØD-only and FGD-only fits as indicated with the above test statistic using a more accurate covariance matrix.

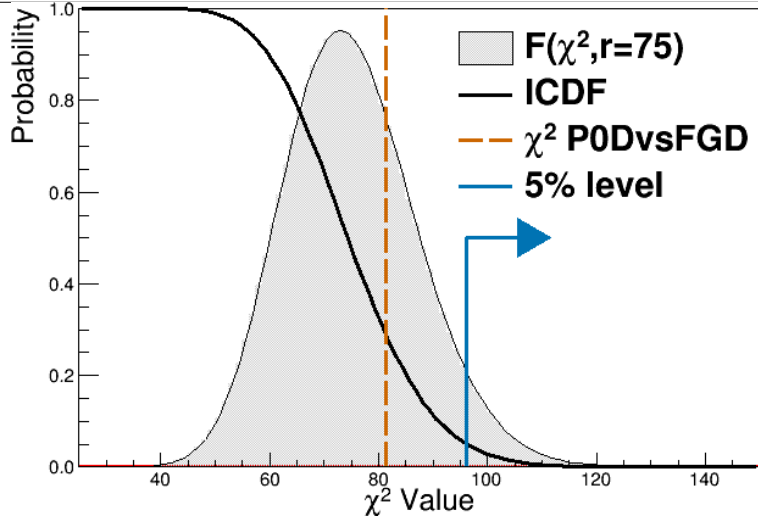


**Figure 6.35:** P-value for the PØD vs FGD ND constraint. Shown in solid black is the inverse cumulative distribution function (ICDF) with 75 NDOF. The chi-squared PDF is shown in gray with arbitrary normalization. The obtained value of the test statistic, shown as a dashed, red line, is 81.41 which is below the 5% level, shown as a solid, blue arrow.

## 6.3 Summary

In this chapter, we have explored the postfit results for the PØD-only data set and compared it against the FGD-only fit. While the FGD-only data samples have about twice as many more neutrino-oxygen events than the PØD-only data, which helps with the sensitivity to oxygen cross section parameters that affect Super-K more, the accumulated neutrino exposures are similar. We observe a good level of agreement between the two fits with moderate differences in some parameters. A hypothesis test was performed to test if the PØD-only and FGD-only data are similar or not. In order to reject the null hypothesis, which is that the two sets are similar, at the 5% level, a  $\chi^2$  of 96.21 or greater was needed. A  $\chi^2$  of 81.41 was obtained, corresponding to a p-value of 28.65, which is insufficient to reject the null hypothesis. Therefore, using the BANFF fit method with the current PØD samples and cross section parameterization, the ND280 constraint is expected to be largely similar if propagated to the next stage in the oscillation analysis.

# Chapter 7

## Discussion

This chapter serves to summarize the methods and results shown in this thesis. The Tokai to Kamioka (T2K) experiment is a long baseline, neutrino oscillation experiment designed to observe a  $\nu_\mu$  beam oscillate into  $\nu_e$ . With the aid of the world class Japan Proton Accelerator Research Complex (J-PARC), a dedicated near detector called ND280 is located downstream of the neutrino production source to observe the beam before oscillations occur. Since starting operations, the fine grain detector (FGD) in ND280 has provided constraints on the neutrino flux and neutrino-water interaction modes important in the oscillation analysis. This thesis is an analysis of an independent measurement of the ND280 constraint using a maximum likelihood estimate in the Beam and Near Detector Flux Task Flux (BANFF) framework with samples from the Pi-Zero Detector (PØD).

Analysis samples have been developed with the PØD to capture a wide variety of interaction modes in T2K, importantly interactions classified as charged current quasi-elastic (CCQE) which constitute the highest cross section in the T2K neutrino energy spectrum. While the PØD has a larger volume compared to the FGD, which means it has more neutrino interactions to choose from, the PØD is less sensitive to harder to measure phenomena like CC single pion production. This limitation is largely due to the design of the detector and sample cuts which reduce its  $(p, \cos \theta)$  sensitivity to the lower energy outgoing muons. The

---

systematic uncertainties inherent in the samples were controlled for in a similar manner with previous BANFF analyses.

The PØD-only data fit shows very good agreement with the FGD-only result using the same flux and cross section parameters. Trends in the data like shape dependence on the flux and accounting for quantum mechanical correlation effects the observable cross section where observed in both sets of fits. A hypothesis test was conducted to test if the PØD-only and FGD-only data fits are consistent with one another. The test produced

$$\tilde{\chi}^2 = \frac{\chi^2}{\text{NDOF}} = \frac{81.41}{75}, \quad p = 0.2865,$$

which indicates the test failed to reject the null hypothesis. *This is another way of saying the PØD provides a similar ND280 constraint compared to the FGD.*

## 7.1 Potential Impacts on the T2K Oscillation Analysis

## 7.2 Analysis Improvements

First is a discussion on applying a different regularization strength. The next topic is a method to reduce the number of effective bin normalization parameters using a different penalty function called the Lasso.

### 7.2.1 Regularization Strength

Recall that the BANFF ND constraint test statistic is defined as

$$\Delta\hat{\chi}_{\text{ND280}}^2 = \underset{\Delta\vec{y} \in \mathbb{R}^d}{\text{argmin}} \left\{ \Delta\chi_{\text{LLR}}^2 (\vec{N}^d, \vec{N}^p) + \Delta\chi_{\text{Penalty}}^2 (\Delta\vec{y}) \right\}$$

where  $\vec{N}^d$  and  $\vec{N}^p$  are the binned data and prediction measurements, respectively, and  $\Delta\vec{y}$  is the difference between postfit and prefit parameter values in the fit. This equation is similar

to the general class of parameter regression using regularization [43]

$$\operatorname{argmin}_{f \in \mathcal{F}} \left\{ L(\eta, f(\vec{\beta})) + \lambda J(f) \right\}, \quad (7.1)$$

where  $L$  is a loss function of measurements  $\eta$ ,  $J(f)$  is a penalty function,  $f(\vec{\beta})$  is a  $d$ -dimensional function of parameters  $\vec{\beta}$  in  $\mathbb{R}^d$ ,  $\lambda$  is the regularization parameter, and  $\mathcal{F}$  is a space of function on which  $J(f)$  is defined. In regularized regression problems, the penalty term serves to solve an ill posed problem by adding external information. Similarly, the regularization parameter controls the importance of the penalty. We recognize that the loss function  $L$  is the log-likelihood ratio term  $\Delta\chi_{\text{LLR}}^2$ , and penalty term is  $J = \Delta\chi_{\text{Penalty}}^2$  with regularization strength  $\lambda = 1$ .

In defining the BANFF test statistic in Chapter 2, the regularization term  $\lambda$  was set to 1 without justification. We can test the effectiveness of this choice using cross-validation. Cross-Validation provides an estimate on the prediction error as well as determines the “optimal” choice of regularization. In cross-validation, the input data is randomly split into  $K$  equal sized partitions. For the  $k \in K$  data partition, we fit the model to the other  $K - 1$  parts of the data and calculate a prediction error  $P$ .

In this verification of the regularization strength, the test statistic is altered to include a regularization term

$$\begin{aligned} \Delta\hat{\chi}_{\text{ND280}}^2 &= \operatorname{argmin}_{\Delta\vec{y} \in \mathbb{R}^d} \left\{ \Delta\chi_{\text{LLR}}^2 + \lambda \times \Delta\chi_{\text{Penalty}}^2(\Delta\vec{y}) \right\} \\ &= \operatorname{argmin}_{\Delta\vec{y} \in \mathbb{R}^d} \left\{ \Delta\chi_{\text{LLR}}^2 + \lambda (\Delta\vec{y})^T \cdot V^{-1} \cdot (\Delta\vec{y}) \right\}, \end{aligned} \quad (7.2)$$

and the data is split into  $K = 5$  partitions. The prediction error  $P$  in this analysis is defined as

$$P_k \left( \left( \Delta\chi^2 \right)_{\text{train}}^{-k}, \left( \Delta\chi^2 \right)_{\text{test}}^k \right) = \left| \left( \Delta\chi^2 \right)_{\text{train}}^{-k} - \left( \Delta\chi^2 \right)_{\text{test}}^k \right|$$

where  $(\Delta\chi^2)_{\text{train}}^{-k}$  is the fitted model statistic on all but the  $k$ th partition, and  $(\Delta\chi^2)_{\text{test}}^k$  is prediction from the fitted model on the  $k$ th partition. This definition of  $P$  is useful since the penalty terms cancel leaving only the difference in log-likelihood terms. The optimal regularization strength is determined by minimizing the cross-validation error,

$$\text{CV} = \frac{1}{5} \sum_{k=1}^5 P_k \left( (\Delta\chi^2)_{\text{train}}^{-k}, (\Delta\chi^2)_{\text{test}}^k \right) \quad (7.3)$$

### 7.2.2 Alternative Penalty

Consider solving the linear regression problem

$$\vec{\eta} = X \cdot \vec{\beta} \quad (7.4)$$

where  $X$  is a  $p \times d$  matrix of  $d$  model features from  $p$  measurements,  $\vec{\beta}$  is a vector of regression weights with  $p$  rows, and  $\vec{\eta}$  is a response vector. There are many approaches to solving ( 7.4) using ( 7.1). A popular solution is the  $l_2$ -regularization constraint [43]

$$\underset{\vec{\beta} \in \mathbb{R}^d}{\operatorname{argmin}} \left\{ L(\vec{\eta}, \vec{\beta}) + \lambda \sum_i |\beta_i|^2 \right\} \quad (7.5)$$

where the sum of squares of the weights  $\beta_i$  sets the constraint and  $L$  is the loss function. The usual choice of  $L$  is using ordinary least squares

$$L(\vec{\eta}, \vec{\beta}) = \sum_j |\vec{\eta} - X\vec{\beta}|^2,$$

which provides the lowest variance in parameter weights.

With some algebra, we can rewrite the BANFF test statistic ( 2.14) into the form of ( 7.5). We again recognize  $\Delta\chi^2_{\text{LLR}}$  is the loss function  $L$  which leaves the penalty term to be tackled. The (inverse) covariance matrix is symmetric and real and can be decomposed as

$$V^{-1} = U\Lambda U^T$$

where  $U$  and  $V$  are the matrix of the eigenvectors and eigenvalues, respectively, of  $V^{-1}$ . Since the eigenvalues are real and positive, the matrix  $\Lambda$  can be expressed as the square of a diagonal matrix  $\Gamma$

$$\Lambda = \Gamma^2.$$

We can now rewrite the penalty term as an inner product of two vectors.

$$\begin{aligned}\Delta\chi_{\text{Penalty}}^2 &= (\Delta\vec{y})^T \cdot V^{-1} \cdot (\Delta\vec{y}) \\ &= (\Delta\vec{y})^T \cdot U\Gamma^2 U^T \cdot (\Delta\vec{y}) \\ &= [\Gamma U^T \cdot \Delta\vec{y}]^T \cdot [\Gamma U^T \cdot \Delta\vec{y}].\end{aligned}$$

If we let  $\vec{\psi} = \Gamma U^T \cdot \Delta\vec{y}$ , then the penalty term becomes

$$\Delta\chi_{\text{Penalty}}^2 = \sum_j |\psi_j|^2$$

and test statistic is now

$$\hat{\Delta\chi}_{\text{ND280}}^2 = \underset{\vec{\psi} \in \mathbb{R}^d}{\operatorname{argmin}} \left\{ \Delta\chi_{\text{LLR}}^2(N^d, N^p) + \|\psi\|_2^2 \right\}, \quad (7.6)$$

where  $\|\cdot\|_2^2$  is shorthand for the  $l_2$ -regularization constraint sum of squares. We see that the BANFF test statistic is indeed a  $l_2$ -regularized solution with  $\Delta\vec{y}$ , recast as  $\vec{\psi}$ , acting as the parameter weight vector and has the regularization strength  $\lambda = 1$ .

Consider now another solution to (7.4) using the  $l_1$ -regularization constraint or least absolute shrinkage and selection operator (Lasso)<sup>14</sup>

---

<sup>14</sup>The Lasso or  $l_1$ -regularization constraint is commonly employed in parameter estimation problems. For example, the method has been used in cancer class prediction with gene expression profiling in the “PAM” package [71]. The Lasso has also been implemented for Poisson likelihood models using the “glmnet” package [35].

$$\operatorname{argmin}_{\vec{\beta} \in \mathbb{R}^d} \left\{ L(\vec{\eta}, \vec{\beta}) + \lambda \|\beta\|_1 \right\}, \quad (7.7)$$

where  $\|\cdot\|_1$  indicates the sum of absolute values of the parameter weight terms. What is unique about the Lasso is its ability to promote model solutions with few nonzero coefficient weights, sometimes called sparse solutions. In other words, predictor parameters with no model impact are excluded in the solution using the  $l_1$ -regularized constraint. Thus the Lasso has the advantage of providing an interpretable model in situations with very high parameter spaces. However, the Lasso does not handle highly correlated variables very well. This is overcome by combining the Lasso with  $l_2$ -regularization which is called the elastic net constraint

$$\operatorname{argmin}_{\vec{\beta} \in \mathbb{R}^d} \left\{ L(\vec{\eta}, \vec{\beta}) + \lambda \left[ \frac{1}{2} (1 - \alpha) \|\beta_i\|_2^2 + \alpha \|\beta_i\|_1 \right] \right\},$$

where  $\alpha$  is the “budget” between the Lasso and  $l_2$ -regularization. The results of using the Lasso and elastic net with highly correlated variables is shown in Figure 7.1 on page 196. The elastic net controls for strong within-group correlations and has a unique solution. Further details about the Lasso and elastic net can be found in the following reference [44].

We can potentially reduce the dimensionality of the ND constraint by utilizing the elastic net. Using the elastic net constraint provides a data-driven method to determine the number of important bin normalizations in the analysis. The method to define the fit binning described in Chapter 4 would be unchanged. What changes is that instead of merging fit bins prior to the fit, the elastic net determines which bin normalizations are important or not important. Along with cross-validation, fit bins with minimal to no impact on the fit can be excluded or combined with important fit bins. Then the best fit parameters and covariance matrix using the current BANFF machinery can still be found.

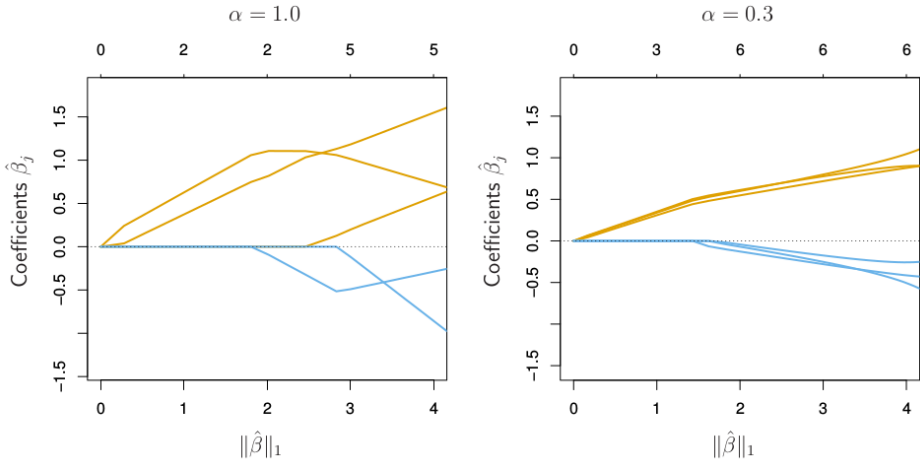


**Figure 7.1:** The Lasso vs elastic net constraint with six variables, highly correlated in groups of three. The Lasso ( $\alpha = 1$ ), left, estimate exhibits erratic behavior as the regularization strength  $\lambda$  is varied. The elastic net ( $\alpha = 0.3$ ), right, pulls highly correlated variables together. In both panels, the vertical axis is the magnitude of the parameter weights (coefficients), the bottom horizontal axis is the regularization strength as measured by  $\|\beta\|_1$ , and top horizontal axis is the count of number non-zero parameter weights.

### 7.3 Future Prospects

There are potential improvements in a “joint” PØD+FGD BANFF fit for the T2K experiment. As shown in the previous chapter, the number of neutrino-carbon and neutrino-oxygen events can be increased by including the PØD data. However, since the fits were performed on different T2K run periods, an equal POT exposure comparison is useful here. Proposing to run a “joint” PØD+FGD ND constraint using T2K runs 2 - 8, the updated neutrino-nucleus exposures are given in Table 7.1 on page 198. We see that while the number of neutrino-carbon events is still larger in the PØD. However, the PØD has 25% fewer neutrino-oxygen events in FHC mode and 9% more in RHC mode. We can estimate the fractional statistical error ( $\delta N$ ) reduction in a joint fit using the data from Table 7.1 on page 198 assuming the FGD fit is the nominal ND constraint. The fractional errors decrease approximately by

$$\begin{aligned}
\delta N_{^{12}C}^{\text{FGD1-FHC}} &= \frac{1}{\sqrt{N_{^{12}C}^{\text{FGD1-FHC}}}} \xrightarrow{+\text{PØD Air}} \frac{1}{\sqrt{(1 + 2.01)N_{^{12}C}^{\text{FGD1-FHC}}}} \sim \frac{1}{\sqrt{3.0}} \\
\delta N_{^{16}O}^{\text{FGD2-FHC}} &= \frac{1}{\sqrt{N_{^{16}O}^{\text{FGD2-FHC}}}} \xrightarrow{+\text{PØD Water}} \frac{1}{\sqrt{(1 + 0.72)N_{^{12}C}^{\text{FGD1-FHC}}}} \sim \frac{1}{\sqrt{1.7}} \\
\delta N_{^{12}C}^{\text{FGD1-RHC}} &= \frac{1}{\sqrt{N_{^{12}C}^{\text{FGD1-RHC}}}} \xrightarrow{+\text{PØD Air}} \frac{1}{\sqrt{(1 + 1.60)N_{^{12}C}^{\text{FGD1-RHC}}}} \sim \frac{1}{\sqrt{2.6}} \\
\delta N_{^{16}O}^{\text{FGD2-RHC}} &= \frac{1}{\sqrt{N_{^{16}O}^{\text{FGD2-RHC}}}} \xrightarrow{+\text{PØD Water}} \frac{1}{\sqrt{(1 + 1.04)N_{^{12}C}^{\text{FGD2-RHC}}}} \sim \frac{1}{\sqrt{2.0}},
\end{aligned}$$

where combinations of FGD1/2 and FHC/RHC represent the FGD in the different beam modes, and an right-point arrow indicates adding the PØD data. These results indicate a fractional statistical error reductions around  $1/\sqrt{2}$  for both neutrino-oxygen events and also potentially stronger flux constraint from higher statistics.

Detector		POT ( $10^{20}$ )		kg POT ( $10^{24}$ )	PØD-to-FGD (kg POT)		
		FHC	RHC		$^{12}\text{C}$	$^{16}\text{O}$	other
PØD	Water-out	7.872	-	2.81	2.01	-	4.64
	FGD1	11.529	-	1.14			
PØD	Water-In	3.657	-	2.00	5.36	0.724	4.06
	FGD2	11.529	-	1.12			
PØD	Water-out	-	3.382	1.207	1.60	-	3.69
	FGD1	-	6.234	0.614			
PØD	Water-In	-	2.852	1.56	7.72	1.04	5.85
	FGD2	-	6.234	0.606			

**Table 7.1:** Neutrino-nucleon exposure on target elements in a joint PØD and FGD analysis using T2K runs 2 - 8. The original numbers can be found in Table 6.1 on page 177.

---

---

Employing both the FGD and PØD in a joint BANFF fit has been attempted during the validation of the results. This requires updating to the newer canonical T2K 2018 cross section parameterization which impairs the ability to compare between fits. Also including both detectors more than doubles the number of parameters and events than for a single detector-only fit. The FGD run periods are also expanded to runs 7 and 8. With more events and parameters, computational limits are already occurring. On a modest high performance computing setup, the fit time for the “Asimov” fit which starts at the likelihood minimum already, required two weeks to complete, or about 10 times longer than the PØD-only Asimov fit. *The joint data fit also did not converge since it ran into machine precision limits.* So possible improvements must be considered if both computational speed and maximum statistical power are desired in the BANFF fit.

Looking forward into the future, this analysis can be improved on significantly. Firstly, the selections are simplistic compared to the recent developments in the T2K experiment. The author was a part of the second generation cross section analysis of single pion production in the PØD, which utilized deep learning techniques, to select a relatively pure CC- $1\pi$  sample. Additionally, the PØD  $\bar{\nu}_\mu$  CC-0 $\pi$  analysis was able to achieve a high-purity CCQE-like sample using almost identical cuts as presented in this thesis. However, both analyses use cuts not yet available in the BANFF framework due to technical difficulties and lack of expertise in the collaboration.

Secondly, more validation studies could be done to understand the sensitivity of the samples. A test of the biases of the fit parameters require fitting an ensemble of “fake data” sets, which are normal variations of the Asimov set. This requires significant amount of computational time to complete, and not to mention the potential carbon footprint left afterwards.

## Bibliography

- [1] K. Abe et al. The T2K Experiment. *Nucl. Instrum. Meth.*, A659:106–135, 2011. 26, 29, 31, 34, 37, 41, 45, 46
- [2] K. Abe et al. Measurements of the T2K neutrino beam properties using the INGRID on-axis near detector. *Nucl. Instrum. Meth.*, A694:211–223, 2012. 36, 38
- [3] K. Abe et al. Observation of Electron Neutrino Appearance in a Muon Neutrino Beam. *Phys. Rev. Lett.*, 112:061802, 2014. 27
- [4] K. Abe et al. Measurement of neutrino and antineutrino oscillations by the T2K experiment including a new additional sample of  $\nu_e$  interactions at the far detector. *Phys. Rev. D*, 96(9), NOV 21 2017. 49, 97, 104, 105, 135
- [5] K. Abe and Others. Measurement of Coherent pi(+) Production in Low Energy Neutrino-Carbon Scattering. *Phys. Rev. Lett.*, 117(19), NOV 4 2016. 123
- [6] K. Abe and Others. Measurement of  $\nu_\mu$  and  $\bar{\nu}_\mu$  charged current inclusive cross sections and their ratio with the T2K off-axis near detector. *Phys. Rev. D*, 96(5), September 2017. 44, 60, 62
- [7] K. Abe and Others. First measurement of the  $\nu_\mu$  charged-current cross section on a water target without pions in the final state. *Phys. Rev. D*, 97:012001, January 2018. 60, 61, 62, 65, 116, 117

- 
- [8] K. Abe and Others. Search for  $CP$  Violation in Neutrino and Antineutrino Oscillations by the T2K Experiment with  $2.2 \times 10^{21}$  Protons on Target. *Phys. Rev. Lett.*, 121:171802, October 2018. 27, 120
- [9] K. Abe and Others. First Measurement of the Anti-NuMu Charge Current Double Differential Cross Section on Water without Pions in the Final State. *Phys. Rev. D.*, Forthcoming. 60
- [10] N. Abgrall and Others. Measurements of  $\pi^\pm$ ,  $K^\pm$ ,  $K_S^0$ ,  $\Lambda$  and proton production in proton-carbon interactions at 31 GeV/c with the NA61/SHINE spectrometer at the CERN SPS. *Eur. Phys. J. C*, 76:84, 2016. 50, 97
- [11] M. A. Acero and Others. New constraints on oscillation parameters from  $\nu_e$  appearance and  $\nu_\mu$  disappearance in the NOvA experiment. *Phys. Rev. D*, 98:032012, Aug 2018. 26
- [12] C. Adams et al. The Long-Baseline Neutrino Experiment: Exploring Fundamental Symmetries of the Universe. 2013. arXiv:1307.7335. 3, 22, 25
- [13] S. Agostinelli et al. GEANT4: A Simulation toolkit. *Nucl. Instrum. Meth.*, A506:250–303, 2003. 68
- [14] P. A. Amaudruz et al. The T2K Fine-Grained Detectors. *Nucl. Instrum. Meth.*, A696:1–31, 2012. 177
- [15] Jiro Arafune, Masafumi Koike, and Joe Sato. CP violation and matter effect in long baseline neutrino oscillation experiments. *Phys. Rev. D*, 56:3093–3099, September 1997. 24
- [16] S. Baker and R. D. Cousins. Clarification of the use of Chi-Square and Likelihood Functions in Fits to Histograms. *Nucl. Instrum. Meth.*, A221:437–442, 1983. 55
- [17] Ch. Berger and L. M. Sehgal. Lepton mass effects in single pion production by neutrinos. *Phys. Rev. D*, 76:113004, December 2007. 123

- 
- [18] S. Bienstock, A. Kaboro, M. Scott, and C. Wret. Constraining the Flux and Cross Section Models with Data from the ND280 Detector using FGD1 and FGD2 for the 2017 Joint Oscillation Analysis, 2017. T2K-TN-324. 179
- [19] R. Bradford and Others. A new parameterization of the nucleon elastic form factors. *Nucl. Phys.*, B159(127), 2006. 121
- [20] T. Campbell. *Measurement of the muon anti-neutrino charged current double differential cross section with no pions in the final state on water using the pi-zero detector at T2K*. PhD thesis, Colorado State University, Fort Collins, Colorado, USA, 2018. 60, 61
- [21] T. Campbell and Others. Analysis of  $\nu_\mu$  Charged Current Inclusive Events in the PØD in Runs 1+2+3+4, March 2014. T2K-TN-80 v4. 63
- [22] T. Campbell, E. Reinherz-Aronis, and W. Toki. The ANuMu/NuMu Cross Sections Ratio With the P0D+TPC Samples, 2017. 63, 117, 118
- [23] J-PARC Center. What is J-PARC?, January 2019. <https://j-parc.jp/researcher/en/about/what/index.html>, Accessed on 26 January 2019. 28
- [24] L. H. Chan, K. W. Chen, J. R. Dunning, et al. Nucleon Form Factors and Their Interpretation. *Phys. Rev.*, 141:1298–1307, January 1966. 121
- [25] A. Chulliat and Others. The US/UK World Magnetic Model for 2015-2020. Technical report, National Geophysical Data Center, NOAA, 2015. 38
- [26] B. T. Cleveland and Others. Measurement of the Solar Electron Neutrino Flux with the Homestake Chlorine Detector. *Astronomical Journal*, 496:505–526, March 1998. 13
- [27] Giampaolo Co'. Random phase approximation and neutrino-nucleus cross sections. *Acta Phys. Polon.*, B37:2235–2242, 2006. 121

- 
- [28] Glen Cowan, Kyle Cranmer, Eilam Gross, and Ofer Vitells. Asymptotic formulae for likelihood-based tests of new physics. *Eur. Phys. J.*, C71:1554, 2011. [Erratum: Eur. Phys. J.C73,2501(2013)]. 130
- [29] R. Das. *Measurement of NuMu induced charged current inclusive cross section on water using the near detector of the T2K experiment*. PhD thesis, Colorado State University, Fort Collins, Colorado, USA, 2016. 60, 62
- [30] A. de Gouvea et al. Working Group Report: Neutrinos. In *Proceedings, 2013 Community Summer Study on the Future of U.S. Particle Physics: Snowmass on the Mississippi*, 2013. arXiv:1310.4340. 22
- [31] I. Esteban et al. Global analysis of three-flavour neutrino oscillations: synergies and tensions in the determination of  $\theta_{23}$ ,  $\delta_{\text{CP}}$ , and the mass ordering. 2018. arXiv:1811.05487. 23
- [32] Rida T. Farouki. The Bernstein polynomial basis: A centennial retrospective. *Computer Aided Geometric Design*, 29(6):379–419, 2012. 122
- [33] A. Ferrero. The ND280 Near Detector of the T2K Experiment. *AIP Conference Proceedings*, 1189(1):77–82, 2009. 26
- [34] J. A. Formaggio and G. P. Zeller. From eV to EeV: Neutrino Cross Sections Across Energy Scales. *Rev. Mod. Phys.*, 84:1307–1341, 2012. 50, 51
- [35] Jerome Friedman and Others. Regularization Paths for Generalized Linear Models via Coordinate Descent. *Journal of Statistical Software, Articles*, 33(1):1–22, 2010. 194
- [36] S. Fukuda et al. The Super-Kamiokande detector. *Nucl. Instrum. Meth. A*, 501(2):418–462, 2003. 26
- [37] Tomasz Golan, Cezary Juszczak, and Jan T. Sobczyk. Final State Interactions Effects in Neutrino-Nucleus Interactions. *Phys. Rev. C*, 86:015505, 2012. 124

- 
- 
- [38] K. M. Graczyk, D. Kielczewska, P. Przewlocki, and J. T. Sobczyk.  $C_A^5$  axial form factor from bubble chamber experiments. *Phys. Rev.*, D80:093001, 2009. 123
  - [39] Krzysztof M. Graczyk, Jakub Źmuda, and Jan T. Sobczyk. Electroweak form factors of the  $\Delta(1232)$  resonance. *Phys. Rev. D*, 90:093001, November 2014. 123
  - [40] Krzysztof M. Graczyk and Jan T. Sobczyk. Form factors in the quark resonance model. *Phys. Rev. D*, 77:053001, March 2008. 123
  - [41] Krzysztof M. Graczyk and Jan T. Sobczyk. Lepton mass effects in weak charged current single pion production. *Phys. Rev. D*, 77:053003, March 2008. 123
  - [42] M. Hartz and Others. Constraining the Flux and Cross Section Models with Data from the ND280 Detector for the 2014/15 Oscillation Analysis. Technical report, T2K Collaboration, May 2015. T2K-TN-220 v4. 53, 56
  - [43] T. Hastie and Others. *The Elements of Statistical Learning: Data Mining, Inference, and Prediction*. Springer Series in Statistics. Springer New York, New York, NY, 2009. 192, 193
  - [44] T. Hastie and Others. *Statistical Learning with Sparsity: The Lasso and Generalizations*. Chapman and Hall/CRC monographs on statistics and applied probability. CRC Press, Taylor and Francis Group, Boca Raton, 2015. 195
  - [45] Y. Hayato. A neutrino interaction simulation program library NEUT. *Acta Phys. Polon.*, B40:2477–2489, 2009. 50
  - [46] C. Jarlskog. A Basis Independent Formulation of the Connection Between Quark Mass Matrices, CP Violation and Experiment,. *Z. Phys.*, C29:491–497, 1985. 23
  - [47] T. Kitagaki and Others. Charged-current exclusive pion production in neutrino-deuterium interactions. *Phys. Rev. D*, 34:2554–2565, November 1986. 123

- 
- [48] E. Komatsu and Others. Seven-year Wilkinson Microwave Anisotropy Probe (WMAP) Observations: Cosmological Interpretation. *Astrophys. J.*, 192:18, February 2011. 25
- [49] C. H. Llewellyn Smith. Neutrino Reactions at Accelerator Energies. *Phys. Rept.*, 3:261–379, 1972. 121
- [50] F. Lodovico and P. Martins. Measurement of the Charged Current CoherentPion Production Cross-Section on Carbon andOxygen using the ND280 tracker. Technical report, T2K Collaboration, 2017. T2K-TN-290. 177
- [51] A. Longhin and Others. Measurement of the inclusive charged-current numu cross section in plastic using the ND280 tracker Run 5c data. Technical report, T2K Collaboration, 2016. T2K-TN-249v8. 177
- [52] Z Maki, M. Nakagawa, and S. Sakata. Remarks on the Unified Model of Elementary Particles. *Progr. Theor. Exp. Phys.*, 28(5), 1962. 18
- [53] M. Martini, M. Ericson, G. Chanfray, and J. Marteau. A Unified approach for nucleon knock-out, coherent and incoherent pion production in neutrino interactions with nuclei. *Phys. Rev.*, C80:065501, 2009. 121
- [54] J. Nieves, I. Ruiz Simo, and M. J. Vicente Vacas. Inclusive Charged–Current Neutrino–Nucleus Reactions. *Phys. Rev.*, C83:045501, 2011. 121, 122
- [55] Kajetan Niewczas and Jan T. Sobczyk. Search for nucleon-nucleon correlations in neutrino-argon scattering. *Phys. Rev.*, C93(3):035502, 2016. 121
- [56] B. Pontecorvo. Inverse Beta Processes and Nonconservation of Lepton Charge. *J. Exp. Theor. Phys.*, 28(5), 1957. 18
- [57] B. Pontecorvo. Mesonium and Anti-Mesonium. *Sov. Phys. JETP*, 6:429, 1957. 14
- [58] G. M. Radecky and Others. Study of single-pion production by weak charged currents in low-energy  $\nu d$  interactions. *Phys. Rev. D*, 25:1161–1173, March 1982. 123

- [59] Dieter Rein and Lalit M Sehgal. Neutrino-excitation of baryon resonances and single pion production. *Ann. Phys.*, 133(1):79–153, 1981. 123
- [60] Dieter Rein and Lalit M. Sehgal. Coherent  $\pi^0$  production in neutrino reactions. *Nucl. Phys. B*, 223(1):29–44, 1983. 123
- [61] Glenn Rowe, Martin Salomon, and Rubin H. Landau. Energy-dependent phase shift analysis of pion-nucleon scattering below 400 MeV. *Phys. Rev. C*, 18:584–589, July 1978. 124
- [62] P. K. Saha et al. Simulation, measurement, and mitigation of beam instability caused by the kicker impedance in the 3-GeV rapid cycling synchrotron at the Japan Proton Accelerator Research Complex. *Phys. Rev. Accel. Beams*, 21:024203, February 2018. 30
- [63] Andrei D Sakharov. Violation of CP invariance, C asymmetry, and baryon asymmetry of the universe. *Soviet Physics Uspekhi*, 34(5):392, 1991. 25
- [64] L.L. Salcedo, E. Oset, M.J. Vicente-Vacas, and C. Garcia-Recio. Computer simulation of inclusive pion nuclear reactions. *Nucl. Phys. A*, 484(3):557–592, 1988. 124
- [65] J. Schechter and J. W. F. Valle. Neutrinoless double- $\beta$  decay in  $SU(2) \times U(1)$  theories. *Phys. Rev. D*, 25:2951–2954, 1982. 20
- [66] N. Schmitz. *Neutrinophysik*. Teubner, Stuttgart, 1997. 19
- [67] Jaclyn Schwehr. *Measurement of the Differential Charged Current Single Pion Cross Section Using the Muon Momentum and Muon Angle In the Pi Zero Detector of the T2K Experiment*. PhD thesis, Colorado State University, Fort Collins, Colorado, 2018. 177
- [68] T. Sekiguchi et al. Development and operational experience of magnetic horn system for T2K experiment. *Nucl. Instrum. Meth. A*, 789:57–80, 2015. 31

- 
- [69] R.A. Smith and E.J. Moniz. Neutrino reactions on nuclear targets. *Nucl. Phys. B*, 43:605–622, 1972. 121
- [70] M. Tanabashi et al. The Review of Particle Physics. *Phys. Rev. D*, 98(030001), 2018. 20, 23
- [71] R Tibshirani and Others. Diagnosis of multiple cancer types by shrunken centroids of gene expression. *Proceedings of the National Academy of Sciences of the United States of America*, 99(10):6567–6572, MAY 14 2002. 194
- [72] Peter von Ballmoos. Antimatter in the Universe: constraints from gamma-ray astronomy. *Hyperfine Interact.*, 228(1):91–100, October 2014. 24
- [73] G. Welch and G. Bishop. An Introduction to the Kalman Filter. Technical Report 95041, University of North Carolina at Chapel Hill, Chapel Hill, NC 27599-3175, July 2006. A description of the mathematics involved in the Kalman filer. 61
- [74] L. Wolfenstein. Neutrino oscillations in matter. *Phys. Rev. D*, 17:2369–2374, May 1978. 24
- [75] Carl Vincent Clarence Wret. *Minimising Systematic Uncertainties in the T2K Experiment Using Near-Detector and External Data*. PhD thesis, Imperial College London, 2019. 107, 120, 121, 123, 124
- [76] Y. Yamazaki. Accelerator technical design report for high-intensity proton accelerator facility project, J-PARC. Report 2002-013, KEK, 2003. 30
- [77] Kai Zuber. *Neutrino Physics*. CRC Press, Boca Raton, FL., 2nd edition, 2012. 1, 14, 18, 26